



UNIwersytet Jagielloński  
w Krakowie

Wydział Fizyki, Astronomii i Informatyki Stosowanej

Instytut Fizyki im. Mariana Smoluchowskiego

**Development of novel methods to study  
various biophysical characteristics of living cells**

Tomasz Jaromir Kołodziej

Rozprawa doktorska wykonana pod opieką

Dr hab. Zenona Rajfura, prof. UJ

w Zakładzie Biofizyki Molekularnej i Międzyfazowej

Kraków 2023



*Chciałbym wyrazić serdeczne podziękowania mojemu Promotorowi  
doktorowi habilitowanemu Zenonowi Rajfurovi profesorowi UJ  
za opiekę naukową i wieloletnią współpracę*

*Dziękuję także moim Rodzicom: Danucie i Januszowi Kołodziejom,  
którzy swoją ciężką pracą i wychowaniem mnie, pozwolili mi na zgłębianie ścieżki naukowej*

*Ponadto chciałbym podziękować:*

*Mojej Rodzinie i Przyjaciołom, od których zawsze mogłem uzyskać wsparcie, radę i chwilę rozmowy,  
Danielowi Dziobowi, który nieraz mi pomagał w poskładaniu różnych elementów pracy w całość,  
a także moim współpracownikom z Zakładu Biofizyki Molekularnej i Międzyfazowej,  
Zakładu Fotoniki i innych miejsc – praca z Wami była wielką przyjemnością.*

*Przede wszystkim jednak, ogromne podziękowania kieruję do Mojej Pięknej – Kasi Janowskiej,  
która przez te wszystkie lata była obok mnie, zawsze zapewniając ogromne wsparcie.*

*This work was supported by the Foundation for Polish Science TEAM-NET Programme  
co-financed by the EU under the European Regional Development Fund,  
grant no. POIR.04.04.00-00-1644/18.*

Wydział Fizyki, Astronomii i Informatyki Stosowanej

Uniwersytet Jagielloński

## Oświadczenie

Ja niżej podpisany Tomasz Jaromir Kołodziej (nr indeksu: 1067377) doktorant Wydziału Fizyki, Astronomii i Informatyki Stosowanej Uniwersytetu Jagiellońskiego oświadczam, że przedłożona przeze mnie rozprawa doktorska pt. „Development of novel methods to study various biophysical characteristics of living cells.” jest oryginalna i przedstawia wyniki badań wykonanych przeze mnie osobiście, pod kierunkiem dra hab. Zenona Rajfura prof. UJ. Pracę napisałem samodzielnie.

Oświadczam, że moja rozprawa doktorska została opracowana zgodnie z Ustawą o prawie autorskim i prawach pokrewnych z dnia 4 lutego 1994 r. (Dziennik Ustaw 1994 nr 24 poz. 83 wraz z późniejszymi zmianami).

Jestem świadom, że niezgodność niniejszego oświadczenia z prawdą ujawniona w dowolnym czasie, niezależnie od skutków prawnych wynikających z ww. ustawy, może spowodować unieważnienie stopnia nabytego na podstawie tej rozprawy.

Kraków, dnia .....

.....

*podpis doktorantki/doktoranta*

# Table of contents

1. List of abbreviations and symbols: .....	4
2. Streszczenie.....	5
3. Abstract.....	7
4. Introduction .....	8
4.1. Motivation and aims. ....	8
4.2. The interdisciplinary history of cell observations. ....	9
4.3. Application of elastic polymer substrate in <i>in vitro</i> studies of cells.....	14
4.3.1. Quantification of cellular forces. ....	14
4.3.2. Elastic substrates mimic the mechanical properties of cellular microenvironment...20	
4.4. Observations of cellular dynamics.....	24
4.4.1. Applications of time-lapse microscopy .....	24
4.4.2. Cell migration.....	25
4.4.3. The role of cell migration in cancer metastases .....	29
4.4.4. Analytical description of cell migration and morphology.....	33
4.5. Measuring relative temperature using NV <sup>-</sup> diamonds.....	36
4.5.1. Cellular microthermometry .....	36
4.5.2. NV <sup>-</sup> diamonds as cellular microthermometers .....	38
5. Materials and methods. ....	43
5.1. Elastic substrate preparation.....	43
5.2. Functionalization of diamond surface and particle size characterization. ....	44
5.3. Characterization of ODMR-TFM substrates. ....	45
5.4. ODMR registration setup. ....	45
5.5. Optimization of ODMR experiments .....	46
5.6. Temperature calibration of ODMR-TFM substrates .....	47
5.7. Cell culture.....	47
5.8. Observation of cellular dynamics.....	48
5.9. Analysis of cell migration and shape.....	49
5.9.1. Inclusion criteria.....	49
5.9.2. Obtaining binary masks from time-lapse sequences.....	49
5.10. Subpopulation analysis of WC256 line.....	50
5.10.1. Dynamic classification of WC256 subpopulations.....	50
5.10.2. Statistical analysis of WC256 cells.....	51

5.11. ODMR-TFM experiment .....	51
6. Results: .....	53
6.1. Application of time-dependent observations and elastic polymer substrates to study cancer heterogeneity.....	53
6.1.1. Heterogeneity of adherent subline of WC256 cell line. ....	53
6.1.2. Adherent subline of WC256 cells exhibits spontaneous subpopulational transitions.....	54
6.1.3. Elastic substrate affects the duration and frequency of subpopulational transitions.....	57
6.1.4. Elastic substrate modifies the occurrence of specific subpopulations.....	59
6.1.5. Elastic substrate influences the biophysical parameters of cell migration and morphology of WC256 cells.....	62
6.1.6. Summary of WC256 cell heterogeneity investigation. ....	68
6.2. Development of new analytical description for coupling cell migration and morphology.....	69
6.2.1. Introducing the idea of unsigned morphomigrational angle (uMM), signed morphomigrational angle (sMM), and major axis dynamics (M.A. dynamics) – examples and rationale.....	70
6.2.2. Building blocks of morphomigrational description. ....	75
6.2.3. Morphomigrational description of selected cellular behaviors.....	78
6.2.4. Summary of morphomigrational description.....	96
6.3. Development of new experimental method for hybrid sensing of cellular traction forces and local temperature changes.....	97
6.3.1. Experimental setup .....	97
6.3.2. Preparation and characterization of ODMR-TFM substrate.....	99
6.3.3. Optimization of ODMR experimental conditions.....	103
6.3.4. Proof-of-principle ODMR-TFM experiments .....	107
6.3.5. Summary of the ODMR-TFM technique development.....	110
7. Discussion .....	111
7.1. Application of time-lapse microscopy and biomimetic elastic substrates in cancer heterogeneity studies.....	111
7.2. Development of morphomigrational description.....	115
7.3. Development of ODMR-TFM technique for parallel measurements of temperature and cellular tractions.....	120
8. Conclusions. ....	125
9. Literature.....	127





## 1. List of abbreviations and symbols:

$\alpha$	– turning angle
AI	– amoeboid Interconversion
AMT / MAT	– amoeboid-to-mesenchymal transition / mesenchymal-to-amoeboid transition
APD	– avalanche photodiode
BSA	– Bovine Serum Albumin
CAT / ACT	– collective-to-amoeboid transition / amoeboid-to-collective transition
DI water	– deionized water
DIC	– Differential Interference Contrast
DLS	– Dynamic Light Scattering
DMEM	– Dulbecco's Modified Eagle's Medium (cell medium)
DMSO	– dimethyl sulfoxide
$\epsilon$	– cell elongation
E	– Young's modulus
ECM	– extracellular matrix
EMT / MET	– epithelial-to-mesenchymal transition / Mesenchymal-to-epithelial transition
FA / FAs	– focal adhesion / focal adhesions
FBS	– Fetal Bovine Serum
HEK 293	– Human Embryonic Kidney 293 (cell line)
M.A.	– major axis of the ellipse or shape
M.A. dynamics / $\Delta\phi$	– major axis dynamics
MEF 3T3	– Mouse Embryonic Fibroblast 3T3 (cell line)
MW	– microwave / microwaves
nDs / $\mu$ Ds	– nanodiamonds / microdiamonds
NV <sup>-</sup> center	– negatively-charged nitrogen-vacancy center
ODMR	– Optically-Detected Magnetic Resonance
PA	– polyacrylamide
PBS	– phosphate-buffered saline
PS	– penicillin-streptomycin
RPMI 1640	– Roswell Park Memorial Institute 1640 (cell medium)
sMM / sMM angle	– signed morphomigrational angle
TLM	– time-lapse microscopy
uMM / uMM angle	– unsigned morphomigrational angle
WC 256	– Walker Carcinoma 256 (cell line)

## 2. Streszczenie

Zarówno prawidłowe funkcjonowanie organizmu jak i procesy chorobotwórcze zależą od sposobu funkcjonowania komórek i tkanek. Dlatego też zrozumienie procesów zachodzących na poziomie komórkowym pozwala wnioskować o przyczynach zjawisk zachodzących w skali całego organizmu. Procesy komórkowe mogą być badane za pomocą wielu różnych technik eksperymentalnych w tym mikroskopowych, z których każda uwzględnia inny aspekt funkcjonowania komórek i tkanek. Właśnie z powodu różnorodności podejść badawczych, rozwój metod eksperymentalnych pozwala na dynamiczny rozwój nauki, a przez to na zrozumienie działania ludzkiego organizmu.

Niniejsza praca doktorska prezentuje rozwój trzech nowych metod eksperymentalno-analitycznych wykorzystujących techniki mikroskopii optycznej w badaniach zachowania żywych komórek. Pierwsza część pracy pokazuje, jak połączenie mikroskopowej fotografii poklatkowej (ang. *time-lapse*) i dynamicznej analizy stanu komórek pozwoliło wzbogacić opis heterogenności komórek nowotworowych adherentnej sublinii komórek szczurzego mięsakoraka WC256. W celu określenia heterogenności badanych komórek opracowano nową klasyfikację subpopulacji, która oparta została na obserwacji dynamiki zachowania komórek. Pozwoliła ona na odkrycie spontanicznych, nieindukowanych przejść pomiędzy subpopulacjami komórek linii WC256. Wyniki te są pierwszymi takimi doniesieniami o dynamicznej naturze heterogenności komórek, rzucając nowe światło na mechanizmy funkcjonowania komórek nowotworowych. Ponadto, zachowanie komórek porównano w kontekście ich hodowli na podłożach wykonanych z twardego szkła oraz z elastycznego polimeru o module Younga  $E = 40$  kPa. Obserwacje wykazały, że częstość występowania subpopulacji, ich charakterystyka biofizyczna oraz obecność i liczba przejść subpopulacyjnych zależały od zastosowanego podłoża elastycznego, co pokazuje, że właściwości mechaniczne mikrośrodowiska mają znaczący wpływ na funkcjonowanie komórek rakowych. Druga część rozprawy przedstawia nową metodologię analizy kształtu i przemieszczenia (migracji) komórek. Dotychczasowe opracowania traktowały migrację i morfologię jako dwie oddzielne cechy komórek. W tej pracy zaproponowano jednak ich połączenie w jeden dynamiczny stan nazwany *zachowaniem morfomigracyjnym*. W celu ilościowego opisu zachowania morfomigracyjnego opracowano dwa nowe parametry geometryczne: znakowany kąt morfomigracyjny (ang. *signed morphomigrational angle*, SMM) i dynamikę osi długiej (ang. *major axis dynamics*, M.A. dynamics). Następnie połączono je z już istniejącymi parametrami opisu migracji komórkowej, takimi jak odchylenie kątowe drogi oraz wydłużenie komórki, co pozwoliło na stworzenie nowej metody opisu zachowania komórki, nazwanej tutaj *opisem morfomigracyjnym*. Wspomniany opis morfomigracyjny pozwala na przypisanie różnym zachowaniom komórkowym zestawu wartości liczbowych, klasyfikując

je ilościowo. Trzecia część pracy doktorskiej prezentuje połączenie dwóch istniejących metod eksperymentalnych: Optycznie Wykrywanego Rezonansu Magnetycznego (*ang. Optically-Detected Magnetic Resonance, ODMR*) oraz Mikroskopii Sił Trakcyjnych (*ang. Traction Force Microscopy, TFM*) w celu stworzenia metody dokonywania lokalnych pomiarów temperatury podczas badań mechanobiologicznych. W ramach przeprowadzonych prac dokonano optymalizacji obu technik w celu ich późniejszego zastosowania do obserwacji żywych komórek a następnie wykonano przykładowe eksperymenty ODMR-TFM dla pojedynczych komórek osadzonych na poliakrylamidowym podłożu elastycznym. Pokazano, że technika ODMR-TFM pozwala na pomiar lokalnej temperatury z dokładnością  $\sim 1$  K, przy jednoczesnym pomiarze trakcji komórkowych.

Nowe podejścia metodologiczne zaprezentowane w tej pracy pozwalają na lepsze poznanie procesów komórkowych. Dzięki temu mają szansę otworzyć nowe perspektywy w mikroskopowych badaniach biofizyki komórki.

### 3. Abstract

Understanding human physiology and mechanisms of various diseases is conditioned by the knowledge of cellular processes that occur in the organism. These processes can be investigated with various types of microscopy techniques which deliver substantial information about the cell functions. Therefore, the development of experimental and analytical techniques is among the most crucial factors that constitute the scientific understanding of living cells.

This thesis is focused on developing new microscopy methods as well as application of already existing methods in novel subjects of cell biophysics. The first part demonstrates the application of time-lapse experiments and polymer elastic substrates in studies of cancer cells heterogeneity. This combination resulted in a novel, dynamic method of classification of adherent subline of WC256 cells and revealed spontaneous transitions between its subpopulations. To the author's knowledge it is the first such observation that gives a new insight into the cancer heterogeneity phenomenon. What is more, the occurrence of subpopulations, their properties and transitions between them were altered in the mechanically more relevant, elastic environment. The second part of the thesis is focused on developing a new analytical technique that links cell morphology and displacement direction. While until now, cell morphology and migration were treated as separate phenomena, in this work they are treated as the one dynamic state of the cell, called *morphomigrational behavior*. The development of novel quantitative descriptors and their combination with already existing ones resulted in creation of a new method called *morphomigrational description* that allowed to assign quantitative values in order to describe various cellular behaviors. The third part of the thesis presents the combination of two already existing methods: *Optically-Detected Magnetic Resonance* (ODMR) and *Traction Force Microscopy* (TFM) in order to introduce the local temperature measurement in the mechanobiology studies. This part consisted of the optimization of both techniques in order to apply them for the parallel observation of relative temperature and traction forces of living cells. These optimizations are summarized with the proof-of-principle ODMR-TFM experiments performed for heating, cooling and constant temperature.

The new methodological approaches shown in this work provide a better understanding of cellular processes, opening new perspectives in cell biophysics.

## 4. Introduction

### 4.1. Motivation and aims.

One of many factors that constitute the well-being of humanity is the progress of medicine and healthcare. This is provided by the understanding of the physiological and pathological processes that occur in our organisms. Cells and tissues receive external stimulations and react to them in many ways, such as cell division, growth, physical adaptation, or secretion of chemical agents. These biochemical and biophysical processes can be examined in the cellular scale using a great variety of microscopy techniques, which provide their understanding on different levels: from just a simple observation, to its quantification, analysis, or even the modification of the examined phenomena. Therefore, the development of new research techniques is a significant factor that allows a better understanding of the great complexity of phenomena that rules our daily functioning.

The several fundamental aspects of developing new research techniques were elegantly presented by a Dutch physicist, the Nobel Prize in Physics laureate, Frits Zernike. With his invention of phase contrast microscopy, he has revolutionized the live-cell observations, creating the method that is used up to these days. During his Noble Lecture on 11 December 1953, he said:

*On looking back to this event, I am impressed by the great limitations of the human mind. How quick we are to learn – that is, to imitate what others have done or thought before – and how slow to understand – that is, to see the deeper connections. Slowest of all, however, are we in inventing new connections or even in applying old ideas in a new field <sup>1</sup>.*

In this quote, we can find several important points about the key factors of developing scientific methods. While it is easy to apply a known method to a subject that is similar to previously studied ones, it is much more difficult to come up with a completely new method. However, the creation of a novel technique from scratch is not the only way to push forward our scientific understanding: one can also combine existing methods to provide a better insight into the research subject, or even apply some already known methods to the research subject that was not investigated in such a way, to observe new aspects of its functioning. These three approaches create those “new connections” or “apply old ideas in a new field” as mentioned by Zernike. This way of doing science is definitely not the easiest, although, in my opinion, it provides a fascinating sense of understanding of how the world works, allowing for new and yet unknown discoveries.

***In this thesis I aimed to develop new research methods in order to better understand cancer cells heterogeneity and the behavior of migrating cells, as well as to introduce local temperature measurements in the field of mechanobiology.***

In the first chapter of results, I present a new insight into the studies of cellular heterogeneity by the application of elastic substrates and dynamic, time-dependent analysis of cell state (*“apply old ideas in a new field”*). In the second chapter of results, I introduce a new technique for the quantitative description of cell migration and morphology called “morphomigrational description” (*“inventing new connections”*). The last chapter of results presents the combination of two techniques: Optically Detected Magnetic Resonance (ODMR) and Traction Force Microscopy (TFM) that were paired in order to improve the mechanobiology experiment by introducing there the local temperature measurements (*“see the deeper connections”*). The key factor linking those three branches is the deep desire to understand the biophysics behind the physiological and pathological cellular processes.

#### **4.2. The interdisciplinary history of cell observations.**

Frits Zernike, introduced in the previous section, was not a biologist but a physicist who applied his expertise in microscopy studies. Similarly, many already existing methods came from the combination of biology with physics, mathematics, chemistry, or even material engineering. In this section I would like to briefly show the history of microscopy methods, highlighting the significance of interdisciplinarity in their development.

Light microscopy as the observation technique started from simple magnifying glasses. The first object that is believed to be a magnifying glass, was found in the Assyrian palace of Nimrud (modern-day Iraq) and consisted of a piece of a polished, plano-convex rock crystal, dated no later than 721-705 BC <sup>2</sup>. However, the idea of magnifying glasses did not gain much popularity over several hundreds of years, until the glass spectacles were “reinvented” in Florence around 1280 AD. Those early lenses were used as basic optical elements of early telescopes and microscopes that were consecutively improved with a better understanding of geometrical optics.

The word ‘microscope’ was coined for the first time by Giovanni Faber in 1625 to describe an instrument invented by Galileo in 1609, but it was not the first microscope ever created. The first described compound microscope, i.e. the microscope consisting of at least two lenses, was created by Hans and Zacharias Janssen around 1590 in the Netherlands <sup>3</sup>. However, observations from these microscopes were not published until the times of Robert Hooke and Antoni van Leeuwenhoek. In 1665, an English experimenter Robert Hooke created his work “Micrographia” in which he described the eye of the common fly and the fruiting structure

of molds. His other observations also included seeds, plants, the structure of cork, and many others. What is more, he was the first to use the term “cells” to describe the pores inside the cork, which is the origin of the contemporary meaning of this term in biology<sup>3,4</sup>. At the same time, Antoni van Leeuwenhoek – a Dutch draper who had no complex scientific education, started to produce early microscopes that were based on the small double-convex lens with a maximum magnification of about 270×<sup>5,6</sup>. In his works, he focused on microbiology and microscopic structure of seeds, bones, skin, fish scales, and oysters, as well as nerves, muscle fibers, fish circulatory system, insect eyes, and numerous other objects. He can also be arguably credited with the discovery of protists, bacteria, cell vacuoles, and spermatozoa<sup>3,7</sup>. The work of Hooke and Leeuwenhoek introduced the microscopy observation method into the field of biology, giving the foundations of current microscopic observations of biological objects.

In the XVII and XVIII centuries, the early microscopes started to be popular in biological observations. At the same time as Leeuwenhoek and Hooke, a Dutch doctor Jan Swammerdam observed red blood cells, and Marcello Malpighi, an Italian biologist and doctor, discovered the blood capillaries in brain, tongue, and retina<sup>8</sup>. In the first half of the XIX century, two German scientists: Matthias Schleiden and Theodor Schwann postulated the cell theory, stating that organisms are made of cells<sup>5</sup>. Further microscopy experiments of Rudolf Virchow improved the understanding of the cellular nature of organisms. In this famous work from 1858, he stated that “*Omnis cellula e cellula*” (all cells from cells), which applies equally to the proper embryological development, as well as to pathological processes<sup>9</sup>. Furthermore, in 1857 the French scientist Louis Pasteur discovered the lactic acid bacteria as well as performed several other observations using the microscope, which gave the foundations of modern microbiology and immunology<sup>10</sup>.

However, the compound microscopes of that time significantly suffered from spherical and chromatic aberration. Further studies on optical lenses allowed Joseph Lister in 1830 to demonstrate that by combining several lenses, spherical aberration can be minimized. This elegant application of physics allowed for constructing the objectives with lower spherical aberration, higher numerical apertures, and thus better resolution<sup>5</sup>. The chromatic aberration was greatly reduced by Fraunhofer in 1816 by the invention of a single lens made of two different types of glass that were fused one into another. This early application of material engineering allowed for getting rid of the colorful halo around the examined subject which was a common artifact in the early microscopes. In 1850, the Italian botanist Giovanni Batista Amici used the water objective that increased the resolution of the observed image. These advances gave significant input into microscopic observations, because the optical quality of microscopic images

up to the 1830s, was not much better than the ones observed with the simplest single-lens microscope <sup>5</sup>.

The next great advancement in microscopy studies came directly from physics, with the experiment on electric and magnetic fields performed by Michael Faraday and further quantitative description of electromagnetism by James Clerk Maxwell <sup>11</sup> that eventually built the understanding of light as an electromagnetic wave. At the same time, microscopic observations were revolutionized by Ernst Abbe who worked at Carl Zeiss AG. His diffraction theory of the image demonstrated that resolution of the image, i.e., the minimum distance in which two points can be resolved, depends on the wavelength of light and the numerical aperture of the objective. He showed, that for the best possible image resolution, it is crucial to collect the light cone that is as wide as possible <sup>2,5</sup>. This physical theory paved the way for creating immersion objectives and observation of more detailed images, which has the profound consequences of biological observations. Parallely, Max Planck introduced his theory of quanta (1901) which was later developed by Einstein who proposed the understanding of light behaving as particle-like quanta of energy (1905, 1906). The understanding of the nature of light and principles of objective optics allowed for further improvements in microscopy techniques.

Many of the biological samples observed that time suffered from significantly poor contrast, which could be increased by staining methods, introducing chemistry into the microscopy studies. One of the earliest methods was provided in 1858 by Joseph von Gerlach who demonstrated the staining of the nucleus and cytoplasm in human brain tissue by contrast agent carmine. Fifteen years later in 1873, Camillo Golgi visualized nervous tissue by silver staining <sup>3,5</sup>. Nonetheless, one of the most known methods of staining came from Danish physician Christian Gram who used gentian violet and potassium iodide, to separate bacteria depending on the presence or absence of the cell envelope as well as the presence of the thick murein layer. This method is used up to this time in microbiological tests <sup>12</sup>.

Unfortunately, all of the staining methods mentioned above required cell fixation, which is just a more sophisticated phrase for killing the cell while keeping its form. Many of the living samples were still poorly visible under the microscope and even the extensive work on new objectives did not solve this problem at that time. This poor contrast comes from the physical properties of light and the observed biological samples. While light passes through any medium, it can change its amplitude or phase. The change of the amplitude (caused by the light absorption in the sample) can be easily recognized by the eye but we are not able to recognize the phase shift. Unfortunately, it is mostly the phase that is changed by the biological samples, which causes the poor visibility of living cells under the simple microscope <sup>5,13</sup>. This problem was solved in 1938 by Frits Zernike who invented the *phase contrast microscope* that was able to translate the phase



shift into changes in light intensity. What is interesting is that he did not discover this technique while working with microscopes but in a different field of optics <sup>1</sup>. Since then, biological objects started to be properly visible by the eye, providing sharp images of thin living cells. Another significant improvement was introduced by Francis Hughes Smith in 1947 and subsequently by the Polish physicist Jerzy (Georges) Nomarski in 1952. The first of them proposed and patented the first differential interference contrast (DIC) microscope, while the latter developed it by providing the proper physical theory behind it and proposed many of its potential variants <sup>13</sup>. The application of additional prisms and polarizers resulted in very sharp images that looked like a relief. Those images presented much more detail, making the DIC the standard microscopic method used for life-cell imaging until today. The phase and DIC contrasts are one of the most brilliant applications of physics in biology, revolutionizing the observation of living biological samples.

The next great breakthrough was enabled by the discovery and application of fluorescence, especially in live cell microscopy. The fluorescence was initially described by Stokes in 1852 when he observed the excitation of quinine solution. It opened a new field in observations of natural fluorescence, which were performed on bacteria, protozoa, proteins, and hemoglobin by Hans Stübel in 1911 as well as the development of the first fluorescent dye called *fluorescein* by Bayer in 1871 <sup>3,5</sup>. The understanding of the fluorescence phenomenon was improved by Niels Bohr who constructed the model of atom in 1913, as well as by Heisenberg in 1925 and Schrödinger in 1926 who developed quantum mechanics. The further study of Aleksander Jabłoński proposed the mechanism of fluorescence <sup>14</sup> and gave the foundation for creating many novel fluorescent dyes.

The widespread application of fluorescence microscopy was enabled by two significant inventions: the method of immunofluorescence staining by Albert Coons in 1941 and fluorescence cubes with filters and dichroic mirrors by E.M. Brumberg in 1959 <sup>3,5</sup>. The first allowed the specific staining of cellular organelles with the immensely increased contrast and the second proposed the prototype of most of the fluorescence microscopes that are used nowadays. Fluorescence microscopes were then subsequently improved in 1957 by Marvin Minsky, who developed an early design of a confocal microscope that would work with the fluorescence illumination and mechanical scanning of the sample <sup>15</sup>. In contrast to the fluorescence microscope in which the observed light comes also from the out-of-focus positions, confocal imaging allowed for the optical sectioning of the sample increasing the contrast of the resulting image. Even nowadays, the further improved confocal microscopes are among the most common tools in cell biology and biophysics <sup>5</sup>.

The next significant point in the history of fluorescence microscopy occurred in 1962 by Shimomura et al., who first isolated the *Green Fluorescent Protein* (GFP) from the *Aequorea Victoria* jellyfish <sup>16</sup>. The use of GFP was however limited until 1994 when GFP was demonstrated to be expressed outside of the jellyfish <sup>17</sup>, which allowed for the targeted fluorescence of cellular organelles in living cells. Other derivatives of GFP were designed for different excitation and emission wavelengths, creating blue, cyan, yellow, and many other fluorescent proteins for live-cell imaging <sup>18</sup>.

The fluorescence and confocal microscopes do not need to be used only as simple imaging equipment but can employ spectroscopy techniques as well. Among the most popular methods I would like to mention are *Förster Resonance Energy Transfer* (FRET), *Fluorescence Lifetime Imaging Microscopy* (FLIM), and *Fluorescence Recovery After Photobleaching* (FRAP). FRET was proposed in 1946 by Theodore Förster and relies on the nonradiative energy transfer in case of the close distance between two properly tailored fluorophores <sup>3,19</sup>. Even nowadays, this technique is used to measure the interactions inside the cells, as well as to investigate protein folding <sup>20</sup>. However, the introduction of this method would not be possible without prior studies on electromagnetism, including the early works of Hertz who was working on dipole fields (Hertzian dipole), Bohr's atom theory, van der Waals investigations of dipole and works of London, Kalman and Perrin who worked on the energy transfer in gases <sup>19</sup>. Therefore, the physics theories and experiments allowed the new types of spectroscopic studies in cell biology and biophysics to be carried out. However, the FRET intensity depends also on the concentration of fluorophores. Therefore, the improved approach assumes the measurements of fluorescence protein lifetimes (FLIM). This method required more sophisticated engineering and application of the time-correlated single photon counting (TCSPC) detectors which have to be introduced in microscope setup, which nowadays is done without any major problem, allowing for an even better understanding of the cell biophysics <sup>21</sup>. Different parameters are measured by the FRAP method, which is used to measure the diffusion of biomolecules inside the cells. It relies on the photobleaching of some defined region and observations of its fluorescence signal recovery. In this technique, the combination of mathematics, physics, and biology gives a better understanding of cellular biophysics <sup>22,23</sup>.

Other advancements in microscopy studies were done due to the invention of superresolution microscopy. It consisted of different strategies that aimed at circumventing the optical diffraction limit of optical microscopy. One of the first methods, called 4Pi microscopy, consisted of the application of two high-aperture objectives that were used to double the resulting numerical aperture <sup>24</sup>. Another technique, called STED, used the intensive donut-shape laser beam to physically deplete the fluorescence of the surrounding molecules in the confocal microscope

setup <sup>25</sup>. Three other approaches, called PALM, STORM and dSTORM, were focused on making fluorescent markers blink which led to the further image reconstruction of the image <sup>26-28</sup>. The blinking was induced by interaction either with light, other fluorescent proteins, or the chemical environment. All superresolution methods utilize either physical or chemical approaches to enhance the quality of microscopy studies. These improvements were significant enough to earn the authors of STED, PALM and STORM the Nobel Prize in chemistry in 2014.

However, the understanding of cell biology and biophysics does not only depend on the observation techniques but is also dependent on the conditions in which cells are observed. The modified cellular environment can deliver specific signals that can influence cellular processes, helping to understand them. One of many ways for delivering the stimulation is an application of biomaterials, which are a branch of materials science. Biomaterials can be designed to deliver different chemical composition, mechanical properties, topography and structure, viscoelasticity properties, dimensionality, etc. <sup>29</sup>. They can be used to deliver mechanical signals in various forms, such as substrate elasticity, tensile forces, dimensional constraints in the form of cell patterning, as well as the shear stress created in the microfluidic devices <sup>30</sup>. What is more, biomaterials are widely used in the context of stem cells and their regenerative potential <sup>31</sup>. They can be also designed to actively respond to external stimulation, such as light, biochemical ligands, pH, or temperature, modifying their biological properties <sup>32</sup>. Therefore, the application of material science paves the way to actively modify cellular conditions to better understand cellular processes.

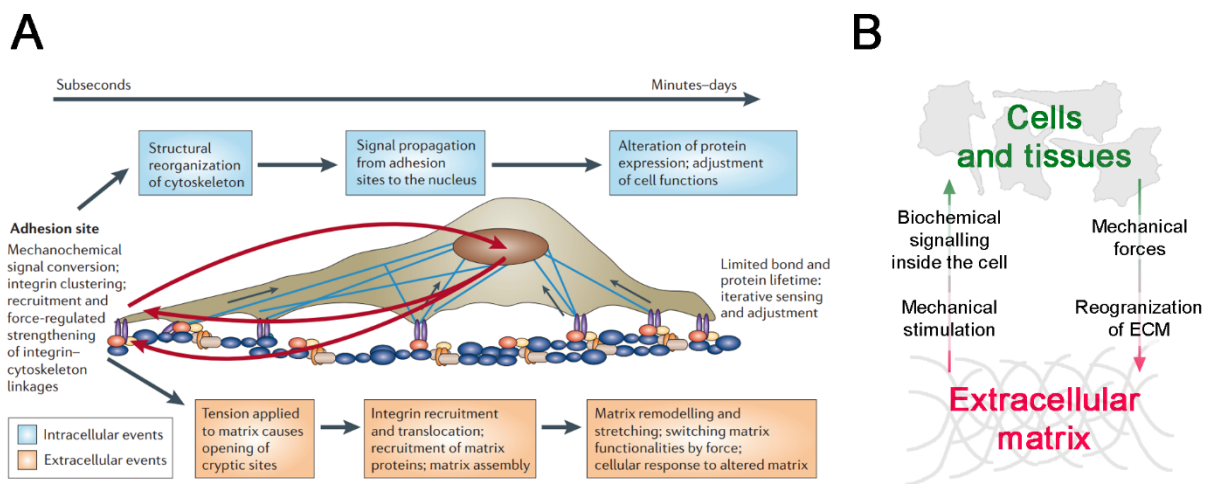
Therefore, the wide range of the currently existing microscopy methods help in investigating cell biophysics and provide an immensely broad insight into cell function. Its development throughout the centuries was provided by the application of principles of physics, mathematics and chemistry in the field of biology. The interdisciplinary combination of an existing knowledge paved the path for the new ways of exploring the complexity of living cells.

### **4.3. Application of elastic polymer substrate in *in vitro* studies of cells**

#### **4.3.1. Quantification of cellular forces.**

The functioning of organism depends on the proper regulation of cells and tissues that build our organs, providing the physiological state of the body. These regulatory processes are based on various biochemical and biophysical stimulations of cells, determining their functions and behavior. Biochemical stimulation encompasses the delivery of basic nutrients, vitamins and salts, as well as growth factors, cytokines, transcription factors, and many other chemical compounds. It provides the proper cellular activity by altering the metabolism, gene

expression as well as shape and movement. What is more, it is crucial for cell survival, growth and division, differentiation, secretion of other chemical compounds, or even cell death<sup>33</sup>. Those processes have been extensively studied over the past several decades which resulted in a deeper understanding of biochemical signaling and many of them are already reviewed in many excellent cell biology books, such as *Molecular Biology of the Cell*<sup>33</sup>. Besides biochemical stimulation, cells receive biophysical signals as well. Biophysical stimulation can be delivered in many forms, such as electric field, light, ultrasounds, mechanical interaction with the environment, or even its dimensionality<sup>34–39</sup>. However, one of the most commonly investigated physical factor is the mechanical interaction between cells and their environment as well as between cells and other cells. The large variety of mechanical interactions that occur in living cells inspired the creation of a separate scientific discipline called “mechanobiology”<sup>40</sup>.



*Figure 1. A: Mechanical response of adherent cells; blue: intracellular events; orange: extracellular events. From Vogel and Sheetz 2006, with permission from Springer Nature. B: The idea of cell-matrix dynamics*

The mechanical stimulations might be delivered to cells in several different ways, including the elasticity of substrate or extracellular matrix, local substrate topography, direct application of compressive and tensile forces, as well as the shear stresses<sup>35,37,41</sup>. The process of sensing physical forces by cells is called “mechanotransduction” and relies on the translation of the mechanical signal into the biochemical action of the cell (Figure 1 A). Depending on the biosensory path and its elements, the mechanical signal might be delivered in two ways: I) can be converted into the biochemical cascades inside the cell or II) can be directly transduced to the cell organelles by the internal structures. Among the mechanosensitive structures one can describe the membrane structures (ion channels, primary cilia, focal adhesions), cytoskeleton and cell nucleus<sup>42</sup>. After receiving the signal, the cell adapts itself to the received stimulation and actively answers to it by remodeling the internal structures. In the case of adherent cells, the remodeling of internal structures results in traction forces, which is the name of the forces that

cell exerts back on the cellular environment. These forces arise from two sources: the contraction of the actomyosin skeleton and the extension of the actin cytoskeleton in the cell's edge <sup>43</sup>. The cytoskeleton is connected to the structures called focal adhesions (FAs) that create the cell-substrates adhesion sites. On the intracellular side, they are composed of the proteins attached directly to the cytoskeleton, which are further connected to the integrin transmembrane receptors that connect the cell with the substrate <sup>44</sup>. Because of the connection between the cytoskeleton and the adhesion sites, the contractile forces can be transmitted outside the cell, directly onto the substrate, as shown in Figure 1A. Therefore, as can be seen in Figure 1 B cells constantly adapt themselves to the mechanical microenvironment and can remodel it back in a constant dynamic process. Therefore, the traction forces are vital for cellular homeostasis, regulating cellular functions as well <sup>41,45,46</sup>.

Traction forces can be quantified by the method called Traction Force Microscopy <sup>47</sup>. It relies on the observation of the elastic substrate deformations, which due to its elastic properties, can be recalculated into the exerted force. One of the first simple registrations of cellular tractions was made by Harris in 1980 and consisted of the observation of wrinkles formed on the thin silicone rubber by the cell cultured on that substrate <sup>48</sup>. However, the quantitative estimation of cellular forces from wrinkles was an extremely difficult task and another few years were needed to find a more robust and quantitative method to assess the cellular traction forces. The revolution in that matter was made by Pelham and Wang in 1997 who introduced the elastic substrates made of polyacrylamide (PA). They found that by changing the ratio of monomer (acrylamide) to cross-linker (bis-acrylamide) it is possible to produce the polymer substrates of varying elasticities <sup>49</sup>. What is even more important, those substrates had similar Young's moduli to the ones that can be found in tissues. Their other property, i.e., the linear deformation in case of application of the force, was used two years later by Dembo and Wang. In their seminal paper in *Biophysical Journal* <sup>50</sup>, they presented the method for quantification of cellular traction forces exerted by the locomoting fibroblast. To perform those observations, they made the polyacrylamide substrate with fluorescent latex beads and then observed the translocation of fluorescent beads that marked the deformation of a substrate caused by the exerted traction forces. However, this method relied on extensive calculations employing Boundary Elements Method (BEM) and was available to a limited number of users. In 2002 another advancement was introduced by Butler et al. by presenting the Fourier Transform Traction Force Microscopy (also called Fourier Transform Traction Cytometry - FTTC) <sup>51</sup>. The development of Fourier Transform TFM made this method to be less computationally complicated, and the mathematical assumptions were explained more clearly, making this method easier to adapt in other laboratories.

In this thesis, the latter method utilizing the Fourier Transform method was used to compute cellular tractions. While calculating tractions one should consider the so-called forward problem, which considers the displacement of the surface of the substrate (treated here as the infinite half-sphere) that was loaded with a point surface load. This problem has a well-known Boussinesq solution <sup>52</sup> saying that the expected displacement in any point  $p_i$  due to the various cellular traction forces can be expressed as the discrete convolution <sup>43</sup>. Here,  $\vec{d}_i$  marks the displacement vector at a point  $p_i$ . This displacement occurs due to the  $m$  force vectors  $\vec{F}_j$  that are exerted in point  $p_j$ . Then, the solution can be presented in the following form of Eq. 1. (Wang 2006):

$$\vec{d}_i = \sum_{j=1}^m \mathbf{G}(\vec{r}_{ij}) * \vec{F}_j \quad \text{Eq. 1}$$

In this form, vectors  $\vec{d}_i$  and  $\vec{F}_j$  contain the  $x$  and  $y$  components, and  $\vec{r}_{ij} = p_i - p_j$  is the vector between the place in which the force was applied ( $p_j$ ) and the place in which displacement was observed ( $p_i$ ). The Boussinesq solution for calculating displacement at the distance  $r$  away from the force can be expressed as Eq. 2:

$$G(\vec{r}) = \frac{1 + \sigma}{\pi * E * r^3} * \begin{bmatrix} (1 - \sigma) * r^2 + \sigma * r_x^2 & \sigma * r_x * r_y \\ \sigma * r_x * r_y & (1 - \sigma) * r^2 + \sigma * r_y^2 \end{bmatrix} \quad \text{Eq. 2}$$

where  $r = |\vec{r}|$ ,  $E$  is a Young's modulus of the substrate and  $\sigma$  is the Poisson's ratio of the substrate. However, the solution of the forward problem is not much helpful if anyone wants to calculate cellular tractions from the displacement. To find the cellular traction one should solve the so-called *inverse problem* that is defined in the opposite way. Solution of the inverse problem was presented by Butler and coworkers <sup>51</sup> who shown that Eq. 1 can be processed by the Fourier Transform, which results in Eq. 3:

$$\tilde{d}(k) = \tilde{G}(k) * \tilde{F}(k) \quad \text{Eq. 3}$$

where the tilde denotes a Fourier Transform quantities and  $k$  denotes the radial wave vector. The Fourier Transformed Boussinesq solution of Eq. 3 is expressed as follows (where  $k = |\vec{k}|$ ):

$$G(\vec{k}) = \frac{2 * (1 + \sigma)}{E * k^3} * \begin{bmatrix} (1 - \sigma) * k^2 + \sigma * k_y^2 & \sigma * k_x * k_y \\ \sigma * k_x * k_y & (1 - \sigma) * k^2 + \sigma * k_x^2 \end{bmatrix} \quad \text{Eq. 4}$$

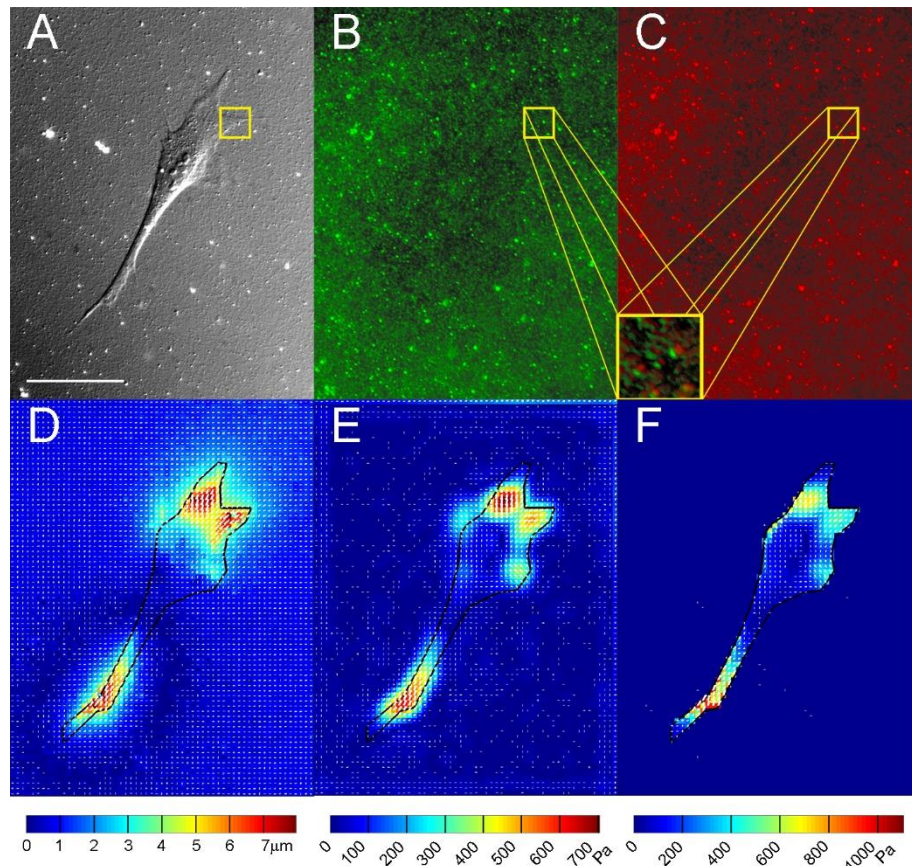
In the Fourier space, the transformed cellular tractions can be simply calculated from Eq. 3 in the following form:

$$\tilde{F}(k) = \frac{\tilde{d}(k)}{\tilde{G}(k)} \quad \text{Eq. 5}$$

Therefore, the result of the inverse Fourier Transform of Eq. 5 simply delivers the cellular tractions that cell exerts on the substrate.

During the next 20 years other scientists introduced further advancements in TFM microscopy<sup>53-55</sup>, however all those methods relied on the same scheme of experiment and data processing (either BEM and similar methods or Fourier Transform TFM). The model TFM experiment using polyacrylamide substrates is done as follows: at each timepoint of the experiment, one should collect the image of fluorescent beads (in fluorescent channel) and the cell itself (in transmitted light channel). After the experiment, the cell has to be detached from the substrate (for example by application of trypsin) and another image of fluorescent beads has to be collected. This image serves as a reference because at that moment no traction forces were exerted in this place. By comparing the bead arrangement of the relaxed substrate to the substrate with the cell attached, one can calculate the bead displacement and then the traction forces using the aforementioned formulas.

Exemplary images obtained from TFM experiment are presented in Figure 2. Panel A shows an exemplary image of a MEF 3T3 cell in DIC contrast, while next panels represent the images of fluorescent beads in the substrate with the cell attached (B) and after the cell detachment (C). The magnified image shows the substrate deformation, marked by the beads' displacements. In the bottom row, we can see the map of displacements (Fig. D), and the map of *unconstrained traction forces* that are calculated straightly from the displacements. However, one can see that the unconstrained traction forces, in this case, are also present outside of the cell boundary, which is counterintuitive. It seems quite clear that the cell simply cannot exert forces in the place where it is not present at all. Therefore, the deformations of the substrate outside the cell boundary are the result of the forces exerted inside the cell, which pull a neighboring substrate in the direction of the cell boundary. In order to get the quantitative values of the real traction forces, the *constrained traction forces* are calculated. It is recalculated again with the assumption that traction forces outside of the cell are equal to zero, thus all the forces should act inside the cell boundary, as it is shown in panel E. The constrained traction forces are then used in the further estimations of the mechanical state of the cell<sup>47,51</sup>.



*Figure 2. Consecutive elements of TFM calculations for exemplary MEF 3T3 cell. A: Image of the cell acquired in transmitted light (here: DIC contrast). B: Fluorescent beads in contracted substrate (under the influence of cellular tractions). C: Fluorescent beads in relaxed substrate after cell detachment (without influence of cellular tractions). Enlarged square shows the displacement of beads. D: Map of fluorescent beads displacements. E: Map of calculated unconstrained cellular tractions. F: Map of calculated constrained cellular tractions. Scalebar = 50 $\mu$ m.*

The Traction Force Microscopy calculation method has also one important issue to be addressed as well. Figure 2 E & F illustrate the calculated traction forces in Pascals, not in Newtons which are usually used to quantify the force. This is simply caused by the fact that we are not able to determine the exact starting point of the force vectors. Therefore, traction forces are recalculated into the area on which the force is applied which imposes its quantification in Pascals. In such a case, the name Traction Force Microscopy seems to be obsolete, and therefore in this work I will also use the term “cellular tractions” to describe them.

It is clear that the application of the new material (polyacrylamide) and new computational methods (BEM, Fourier Transform) have resulted in the creation of a new experimental technique. With its help, it was possible to quantitatively evaluate the cellular tractions and thus get an improved insight into the role of mechanical forces in various cellular processes. Nevertheless, the elastic substrate does not only need to serve as the sensor of cellular tractions but has more applications that are described in the next section.



#### **4.3.2. Elastic substrates mimic the mechanical properties of cellular microenvironment.**

It was already mentioned that elastic polyacrylamide substrates can be tuned to achieve similar elasticities to the ones found in mammal tissues. For this reason, a wide range of studies utilize elastic substrates of various types, including polyacrylamide substrates, as biomimetic material. With their use it is possible to deliver to the cell a well-defined mechanical stimulation, mimicking the relevant cellular microenvironment. Among the softest tissues of our organism, one can find the neural brain tissue, which elasticity varies between 0.05 to 1 kPa. Similarly, the lung tissue has ~0.2 kPa elasticity, while skin is a bit stiffer, with elasticity in the range between 1kPa and 10 kPa. The elasticity of breast tissue is reported to have quite a wide range, depending on the exact type of the tissue (fat tissue, mammary gland, or the overall parenchymal tissue) and varies from ~1 kPa to tens of kilopascals<sup>38,56,57</sup>. The endothelial tissue is about 1–2 kPa elastic, stromal tissues can have ~3 kPa while for the smooth muscle cells, we can expect the elasticity of ~5 kPa. Skeletal muscle cells are even stiffer (~12 kPa), being similar to the chondrocytes (~15 kPa). Going further on the stiffness scale, we can also find tendon tissues (~30 kPa) and early (precalcified) bones of ~34 kPa<sup>58</sup>. The stiffest tissues in our organisms are naturally the bone tissues with elasticity measured in gigapascals. It is important to mention that depending on the patient's condition, the physiological state of the organs as well as the patient's age, those values can differ<sup>59</sup>.

Nevertheless, culture dishes that are routinely used in cell biology studies are made of plastic or glass which are much stiffer (in the range of gigapascals). The simple fact that tissues are much softer than plastic and glass does not seem to be taken into account in the majority of in vitro studies, which are performed using standard Petri dishes or multi-well plates. To change the current state, an increasing number of studies use elastic substrates to reflect the more reliable mechanical microenvironment of the cells. These research significantly improve the in vitro cell studies and help to understand the complicated coupling of biophysical and biochemical regulatory pathways in living cells. In this section I would like to highlight the importance of the application of elastic substrates in cell biology research, showing how much relevant information about cellular biophysics and the overall cellular processes they can provide. As an exemplary objects, I describe two groups of cells, for which the influence of micromechanical conditions is the most prominent: stem cells and selected types of cancer cells.

Studies on stem cells are among the most important research in cell biology. They give us information about the basic mechanisms that rule embryonic development and its pathological processes, as well as they form the core of regenerative medicine and novel therapies. One of the most commonly used type of stem cells are the Mesenchymal Stem Cells (known also

as Mesenchymal Stromal Cells - MSCs), which are multipotent stromal cells that can differentiate into various cell types <sup>60</sup>. The seminal work of Engler et al. has shown that substrate elasticity alone can direct the differentiation of MSCs. Cells cultured on the gels of a similar elasticity to brain tissues (0.1-1 kPa), underwent neurogenic differentiation. On the substrates of a similar elasticity to the striated muscle (8 – 17 kPa), the myogenic differentiation was observed, while on the substrates of 25-40 kPa elasticity that were mimicking the precalcified bone, MSCs underwent the osteogenic differentiation <sup>58</sup>. This work has inspired numerous further research that focused on the examination of different types of stem cells in the context of their overall behavior on elastic substrates. In the work of Xu et al., researchers examined similar, umbilical cord mesenchymal stem cells on various elasticities, between 13 and 68 kilopascals, showing that the elasticity has a significant influence on the proliferation, morphology and differentiation of those cells <sup>61</sup>. The adipogenic differentiation, driven by the soft substrates was presented in the work of Young et al., who also demonstrated its correlation with the increased cell spreading and modified shape <sup>62</sup>. Another study of differentiation was made on much stiffer substrates that were made of methyl acrylate/methyl methacrylate polymer substrate and showed that the chondrocytic and osteoblastic differentiation depends on the substrate stiffness, however, the intensity of osteogenic differentiation did not simply increase with the elasticity <sup>63</sup>. The shapes and secretory profiles of the bone marrow-derived MSCs seeded on 2 and 20 kPa substrates were examined in the work of Seib et al. <sup>64</sup>. They have shown that the mechanical microenvironment alters not only the cell shapes but also the secretory profile as well, which can have a significant influence on the potential therapies that use similar cell types *in vivo*. However, substrate elasticity does not need to be the only factor that is considered in stem cell studies. The importance of substrate elasticity, the presence of neighboring cells, and cell-cell contacts were shown in the work of Mao et al., <sup>65</sup>. In that work, cells were observed on the various elastic substrates that were additionally patterned in order to introduce dimensional constraints. Similarly, the substrate elasticity coupled with dimensional constraints introduced by local topography was shown to influence the preservation of the stemness of mouse embryonic stem cells <sup>66</sup>. The various differentiation was also observed for Neural Stem Cells seeded on substrates of 12-750 kPa made of different type of elastic substrate called polydimethylsiloxane (PDMS). In that study, the softer substrates lead to the neural differentiation, especially to the astrocytes <sup>67</sup>. The described examples of stem cell reaction to substrate elasticity are definitely not an exhaustive review of all existing advancements in this field. Nevertheless, they highlight the significance of studies of different types of stem cells in the context of their mechanical microenvironment.

Another type of cells that is extensively studied in the context of mechanical microenvironment are cancer cells, which is caused by the fact that various types of cancer are among the most serious health problems around the world. The understanding of clinical aspects of cancer biology requires prior studies performed on isolated cancer cell lines in order to examine the basic biochemical and biophysical processes first. One of the first well-known studies on this subject compared several cancer cell lines to examine their proliferation on the elastic substrates<sup>68</sup>. The elasticity ranged from 0.15 to 9.6 kPa and included several cell lines, such as breast, lung, prostate, pancreatic, melanoma, and stromal cancer cells both from primary tumors and metastatic sites. They demonstrated that the proliferation of certain cell lines (mechanosensitive cells) was influenced by substrate elasticity, but there were also cell lines whose behavior was not altered by substrate elasticity at all. Further studies conducted in the same research group were focused on the three cell lines: MDA-MB-231 (breast cancer), A549 (lung cancer) and mPanc96 (pancreatic cancer) to find the reason for their mechanosensitivity. They found that substrate elasticity modifies the length of the cell cycle and cell metabolism in the G1 phase as well as the expression of selected proteins, including the ones engaged in regulation of cytoskeleton, glycolysis, and key metabolic pathways required for cancer cell survival<sup>69</sup>. The lung cancer cells were also examined in the context of their behavior on elastic substrates. The work of Shukla et al. showed that substrate elasticity influences cell migration, however, it did not influence the expression of the epithelial-to-mesenchymal transition (EMT) that causes migration of initially non-migrating cancer cells, being crucial for cancer metastasis<sup>70</sup>. Another study demonstrated that on the softer substrates, the expression of metalloproteinases MMP2, MMP3, MMP7 and MMP14 decreased, while the expression of TIMP inhibitors of those metalloproteinases increased. The mentioned metalloproteinases are an extremely important indicator of cancer progression, since they are responsible for degradation of extracellular matrix, allowing cancer cells to get into the circulatory system<sup>71</sup>. Another type of cancer investigated in the mechanobiological context are various types of gliomas. Five different glioma lines (U373-MG, U87-MG, U251-MG, SNB19, C6) were examined on soft, medium, and stiff substrates (0.08 kPa, 0.8 kPa, 19 kPa and 119 kPa) showing that the increased substrate stiffness promotes cell spreading, proliferation and migration. Those processes were induced by the modified contractility of the actomyosin cytoskeleton<sup>72</sup>. A deeper view on the mechanobiology of glioma cells was provided by Pogoda and her co-workers who demonstrated that glioma cells are sensitive to the interplay of substrate stiffness and the composition of extracellular matrix (ECM). The substrate elasticity and ECM type influenced the cell area, cortical stiffness, movement persistence and overall cell motility. They also altered the proliferation rate and production of the interleukin IL-8 which acts as a proinflammatory molecule<sup>73</sup>. Another investigated type of cancer is ovarian cancer which

seems to become more aggressive on softer substrates, which stands in opposition to the aforementioned cancer types. While the study of McGrail et al. showed that the malignancy of the ovarian cancer cells (SKOV-3 line) increased on softer substrates <sup>74</sup>, the study of Fan et al. demonstrated that the proliferation of the same cell line increased on the stiff substrates, but the softer substrates promoted the early markers of epithelial-to-mesenchymal transition (which is co-responsible for tumor metastasis), and the resistance to chemotherapeutics <sup>75</sup>. The mechanical microenvironment is also immensely important in the context of breast cancer. One of the very first findings on the influence of elastic substrates on breast cancer showed that the number of invadopodia as well as their activity increased on the stiffer substrates <sup>76</sup>. This finding was especially important since invadopodia are the cellular structures that, by secretion of metalloproteinases, dissolve the extracellular matrix, causing the migration of cancer cells into the circulatory system. The work of Peng et al. was done on MDA-MB-231 cells, demonstrating that the substrate stiffness regulates the motility of cancer cells, contractility of actomyosin cytoskeleton and exerted traction forces <sup>77</sup>. The interplay of substrate elasticity and biochemical signaling was also found to affect the migration of single cells and cell sheets as well as cancer malignancy <sup>78</sup>. Another work demonstrated that the increased substrate elasticity affects breast cancer cell morphology, spreading, and proliferation. However, the softer substrates increased the drug resistance, which means that more cancer cells did not die when the chemotherapeutics were applied <sup>79</sup>. This finding is in line with the work of Qin et al. who showed that among the culture substrates between 10 and 57 kPa, the medium elasticity increases the drug resistance as well <sup>80</sup>. Another work analyzed the adaptation of cancer cells to different substrates, comparing their initial mechanical microenvironment. The prolonged culture of breast cancer cells on elastic substrates modified their spreading area, circularity, attachment efficiency, proliferation, and overall cell adaptation to the different substrate elasticity<sup>81</sup>.

Those briefly described studies present only the fragment of the current methods that incorporate the elastic substrate as the biomimetic environment. With the help of elastic substrate, it is possible to dissect the different signaling pathways, determining which processes are connected with the mechanical interactions, increasing our knowledge of cancer behavior. It is also visible that different research groups were using substrates made of different materials (PA, PDMS and others) that varied in substrate chemistry and elasticity. Therefore, it is crucial to properly frame the elastic substrate into the research question and research subject, to elucidate the relevant information about cell biology and biophysics.

What is more, in the abovementioned studies, one could spot the cell migratory behavior as one of the factors that was examined in the context of cancer. Cell migration is the crucial

phenomenon that drives the process of cancer metastasis, influencing the lives of patients all around the world. This process is described in the next sections to illustrate yet another aspect of cellular biophysics and the methods that are used for its observation and description.

#### **4.4. Observations of cellular dynamics**

In the previous section, I described elastic substrates as tools for quantifying cellular forces and investigating various cellular processes in the relevant micromechanical conditions. However, cellular processes are not static events, but dynamic actions that regulate the activity of organisms. In this section, I would like to describe the importance of time-lapse microscopy in investigations of dynamic cellular processes, with a special emphasis on the phenomenon of cell migration.

##### **4.4.1. Applications of time-lapse microscopy**

The observation of the time evolution of any object simply requires the registration of its state in consecutive timepoints. In the case of microscopic observations, this technique is called time-lapse microscopy (TLM) and consists of capturing the sequence of microscopic images at regular intervals <sup>82</sup>.

Time-lapse microscopy can be basically used to investigate any dynamic phenomenon in the micrometer scale. The early TLM studies in 1950s and 1960s were focused on culturing cells, monitoring blood cells, cell division, or development of the skeletal muscles. Initially, they were coupled with phase contrast and DIC microscopy, however, the development of fluorescence techniques enabled the coupling of TLM with confocal, FRET, and other microscopy techniques <sup>82</sup>. One of the first dynamic phenomena that drew scientific interest were the division and growth of single cells and tissues. Combining TLM with proper fluorescent markers enabled the detailed observation of the cell cycle, meiosis, nucleolar assembly after mitosis, multinucleation of skeletal muscle cells, mitotic synchronization, and many others. Besides the physiological processes, the process of death was also examined in order to investigate its multiple regulatory mechanisms, including apoptosis, phagocytosis of apoptotic cells, phototoxic processes, necrosis and autophagy. The TLM was also used to investigate intracellular dynamics of subcellular organelles, proteins and reporters, for example: movements and changes in mitochondria, Golgi apparatus, centromeres, centrosomes and microtubules <sup>82</sup>. What is more, the observation of cellular dynamics included the intracellular processes, such as interkinetic nuclear migration, dynamics of integrins and F-actin distribution, gene dynamics (using luciferase reporter), clustering of acetylcholine receptors on myotubes, calcium flux dynamics, and many others. One can also investigate the characteristics of cell-cell contacts that are important for stem cells, as well as in tumor environments <sup>82</sup>.

However, one of the most profound application of time-lapse microscopy is the observation of cell migration. This phenomenon regulates various physiological processes in our organism, such as tissue repair and regeneration, immune system functioning, and proper embryonal development. The pathological processes such as arthritis, osteoporosis, atherosclerosis and cancer metastases rely on cell migration as well <sup>83</sup>. Therefore, the time-lapse studies of cell migration are in focus of many researchers, constituting a significant branch of cell biophysics.

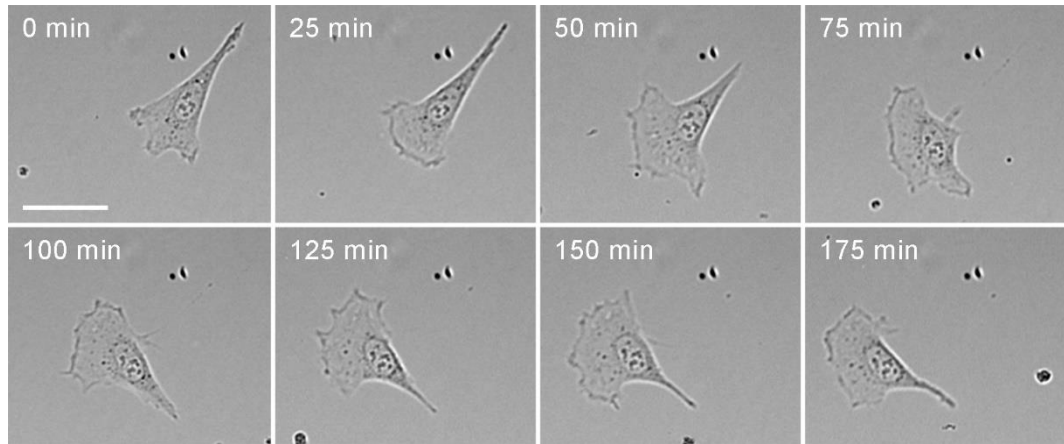
#### **4.4.2. Cell migration**

##### **4.4.2.1. Mesenchymal migration**

Cell migration is a phenomenon relying on the displacement of the cell from one location to another. This deeply technical and yet simplest definition does not reflect the complexity of the whole process at all. Single cells utilize two different types of migration: the mesenchymal and amoeboid modes <sup>84</sup>. The mesenchymal mode consists of several steps, starting from the cell polarization, where the frontal and distal sides of the cell are distinguished. Cell polarization can occur spontaneously <sup>85</sup> or due to the signals that come from the extracellular environment. Those signals can have a form of cell-substrate adhesions, connections with other cells, or the gradient of soluble chemical substances that are often called “chemoattractants” <sup>86,87</sup>. The next migration step relies on creating protrusion, i.e., the membrane extension. This process is mainly caused by the formation of new actin fibers at the leading edge. Depending on the cell type as well as the extracellular conditions, such extension may be produced in different forms. The first type of extension is called *lamellipodium* (from Latin *lamella* – “thin sheet” and Greek *pod* – foot), a broad, sheet-like extension that is constructed from a branched network of actin filaments <sup>88,89</sup>. Another type of extension is filopodium, which is a thin and long protrusion made of parallel actin bundles decorated with tropomyosin and fascin <sup>90</sup>.

However, the cell would not migrate at all, if the created protrusion is not sustained by its attachment to the substrate. Therefore, the next step of cell migration consists of the creation of adhesion sites between the protrusion and substrate. Depending on the physical and chemical properties of the substrate, cell type, phase of migration, and many other factors, we can observe the adhesion sites of different sizes and compositions: from nascent adhesions to focal complexes and mature focal adhesions that are the most solid type of cell-substrate linker. Among different types of adhesions, one can also mention podosomes that are present in fast-migrating cells as well as invadopodia which are the specialized types of adhesions that are expressed by cancer cells to dissolve the extracellular matrix and facilitate the tumor invasion into circulatory system <sup>35,91-96</sup>. The fourth step of migration consists of the contraction of the cell body and the retraction of cell rear. The contraction and translocation of the cell body are driven by the actomyosin

contractile cytoskeleton and de-adhesion of distal adhesion sites. This disassembly can be induced by their targeting by microtubules, the endocytosis of adhesion receptors, or calpain-dependent cleavage of adhesion sites<sup>94</sup>. The example of migrating MEF 3T3 cell is shown in Figure 3. One can see that between 0 and 50 minutes the cell forms and extends the large lamellipodium in the front, while between 50 and 75 minutes one can observe a visible contraction of the cell, which results in the retraction of the distal part. In the next four frames (100-175 min) the same cell changes its polarization which results in its clockwise turn.



*Figure 3. Migrating MEF 3T3 cell which is the one of the most prominent models of cell migration process. Scalebar = 50  $\mu$ m.*

The important feature of mesenchymal migration is that the consecutive phases of cell migration do not need to be separated in time, which is visible in the timepoint of 50 min in Figure 3. The cell extends its lamellipodium and contracts the cell rear at the same time. However, if the cytoskeleton contraction is stronger than the attachment force of adhesion sites, the whole distal part of the cell can be detached, as it is seen in the 75 minutes of this time sequence. There is also a subtype of mesenchymal migration, called gliding motion. In this mode, all migration phases overlap, which results in more smooth migration, which does not cause significant changes in cell shape<sup>97-99</sup>. It also consists of the constant buildup of the actin cytoskeleton in the front, with its constant deconstruction at the cell rear. Such migration mode can be observed for keratocytes (corneal cells) and keratinocytes (skin cells). The exemplary fish epithelial keratinocyte that undergoes the gliding motion is shown in Figure 4, where the stable cell shape is preserved over time.

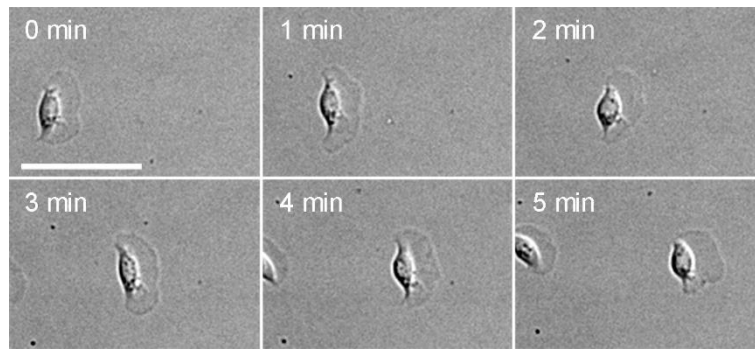


Figure 4. The epithelial fish keratinocyte that utilizes the gliding motion mode of migration. Scalebar = 50  $\mu\text{m}$ .

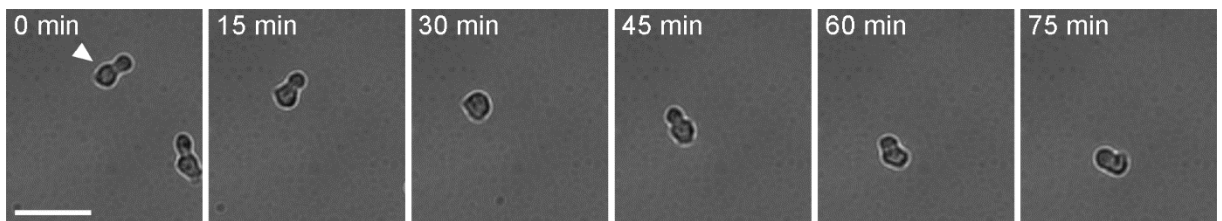
#### 4.4.2.2. Amoeboid migration.

Compared to the mesenchymal mode of migration, the amoeboid mode is less clearly defined. The term “amoeboid” relates to the protozoan *Amoeba proteus* which was named after the Greek: *amoibe* – “change” and *Proteus* – the Greek god of change<sup>100</sup>. Based on the observation of the mentioned archetypic amoebae, this type of migration relies on rounded and poorly adhered protrusions that are not necessarily rich in F-actin<sup>91</sup>. However, the amoeboid group of cells is not uniform and encompasses different cell types (from unicellular eukaryotes and individual metazoans) that differ in their habitat, size, compactness, and other properties. Their one common feature is that during locomotion they constantly change shape by protruding and retracting their extensions<sup>100</sup>. Other additional features that are considered in amoeboid migration are as follows: increased migration speed, creating protrusion mostly as a result of cell contractility than polymerization of the actin cytoskeleton at the front, independence of specific adhesion receptors, and rounded cell shape. However, most amoeboid cells rarely exhibit all of those features at the same time<sup>91</sup>.

The migration of amoeboid cells is caused by the forces that come from the actomyosin cytoskeleton, while other cytoskeletal elements are not much involved in this process<sup>101,102</sup>. The current models assume that cellular displacement is generated by two types of forces. One is the expansion of the actin cytoskeleton that creates less organized protrusions, compared to the mesenchymal migration mode. The second type consists of the contraction of the cell rear that depends on type II myosins. This mechanism causes the local rise of hydrostatic pressure that can either cause the cracking of the cortical actin network in the front of the cells or the detachment of the cell membrane from the cortical actin cytoskeleton. In both cases, the flow of the cytosol caused by the contraction of cell rear, creates the spherical bleb in the cell front<sup>103-105</sup>. The bleb creation is followed by the equilibration of internal pressure and actin recruitment into the bleb which causes further bleb retraction<sup>106</sup>. The exact interplay between the two mentioned models: actin network expansion and actomyosin contraction, depends on the cell



type, adhesive environment, as well as protein expression. Therefore, even the same cell type can balance these two processes, depending on the current conditions <sup>100</sup>. This interplay is reflected in many types of intermediate forms of amoeboid migration. The neutrophils that are considered amoeboid type cells are equipped with lamellipodium with actin-rich protrusions, that in their structure are similar to lamellipodia (and thus to the mesenchymally migrating cells) <sup>107</sup>. Also, the mixed amoeboid-filopodial migration mode was found at some stages of cancer cell invasion <sup>108</sup>. Therefore, it is possible to observe the intermediate stages between mesenchymal and amoeboid migration. On the other hand, the most extreme way of amoeboid migration is the blebbing mode, which is predominantly driven by the contraction mechanism, and independent from the specific receptor-based adhesions to the environment <sup>91</sup>. In this mode, cells exhibit the leading bleb protrusion that changes in size and shape, as shown in Figure 5.



*Figure 5. Migrating blebby cell from WC256 cell line. Scalebar = 50  $\mu$ m.*

The current state of knowledge suggests that the mode of migration depends, among the others, on the extracellular environment. For example, the dense extracellular matrix can induce mesenchymal movement, while the lower availability of adhesion ligands and the sparse extracellular matrix (ECM) can cause amoeboid migration. Similarly, softer substrates can influence amoeboid movement, while stiffer ones can promote mesenchymal arrangement <sup>39</sup>. It is in line with the reports that were already mentioned in this introduction, demonstrating that stiffer substrates promote cell spreading of many cell types. Other extracellular factors that regulate migration and morphology are: cell-cell adhesions (mostly from the cadherins family), cell-ECM adhesions (integrins), the balance between the cytoskeletal protrusion and contraction, the balance between traction forces and propulsive forces as well as the proteolytic activity <sup>39</sup>. Combination of these factors with time-lapse microscopy can help to get a better insight into cellular biophysics, being of special importance in the context of cancer cells, since the migration of cancer cells leads to metastases, as it is elaborated more in the further sections.

#### **4.4.2.3. Collective migration**

Collective cell migration is the movement of multiple cells that are connected by cell–cell contacts. Because of that, they can coordinately migrate in a defined direction as a group <sup>109,110</sup>. Collective migration is the prevalent mode in the process of embryonic development, wound healing, and tissue regeneration <sup>109</sup>. Migrating cell clusters and tissues behave similarly to single migrating cells, so the cell cluster has to subsequently: polarize, protrude, adhere to the substrate, and implement contraction, to execute the successful displacement. To do so, they need to produce both: cell-cell adhesions that provide cohesiveness of the group, and cell-ECM adhesions that provide the anchoring to the substrate. Among the cell-cell adhesions, one can mention: adherens junctions, tight junctions, desmosomes and gap junctions that are made of different protein types and bind to different cellular structures. They are responsible for the maintenance of the cell-cell connections, provide the mechanical durability of the tissue or facilitating intercellular communication <sup>109</sup>.

The important characteristic of collective cell migration is that each cell along the cell sheet can express different behavior. Its activity depends on the position in the cell aggregate and therefore determines its migratory function. In the front of a migrating cell sheet, we can identify the so-called “leader cells” which exhibit mesenchymal-like phenotype with lamellipodia and filopodia, that enable the cellular movement. Creation of migratory structures is paired with the upregulation of cell-ECM adhesions and downregulation of cell–cell contacts. Therefore, the leader cells change their initial apico-basal polarity of epithelial tissue, to the migratory phenotype with the front-end polarization, which process is regulated by the actin and microtubule cytoskeleton <sup>109</sup>. Such modified leader cells are able to guide the larger groups of the follower cells, that are behind the tissue front. The collective migration may be initiated due to the extracellular cues: chemoattractants, changes in ECM adhesion, elasticity and dimensionality, as well as from the intrinsic tissues' factors <sup>109</sup>. Because of that, the collectively migrating cells can serve their functions in the aforementioned physiological and pathological processes.

#### **4.4.3. The role of cell migration in cancer metastases**

Cell migration phenomenon plays a central role in the process of tumor progression and creation of metastases. In fact, cancer metastases are the major cause of death in oncology patients <sup>111</sup>. For creating the metastasis, cancer cells have to detach from the primary tumor and migrate to other organs. Therefore, the migration of cancer cells is one of the most extensively investigated subject in cancer biology.

The main modes of cancer migration are shown in Figure 6. The first important migration strategy is collective migration which plays a major role in squamous cell carcinoma, colon, breast, and many different types of cancers. During this process, the cell-cell contacts drive the polarization of migrating tumor sheet, creating the multicellular functional unit. The leader and follower cells create the cell-ECM adhesions for two reasons: firstly, to generate traction forces that enable migration and secondly to actively remodel the ECM through the proteolytic dissolving, mainly by metalloproteinases. The ECM remodeling is performed to get rid of tissue barriers and create the path of the least resistance to ease the movement<sup>108</sup>. Collective cell invasion might be done in several forms presented in Figure 6: collective sheets or strands that are still attached to the tumor<sup>112</sup>, isolated clusters that are detached from the original lesion<sup>113</sup>, neuronal-like networks of connected cells<sup>114</sup>, or as collective cohorts that are “jammed” due to the dimensional confinement, but not express strong intercellular connections<sup>115</sup>. The collective migration of cancer cells might be preferred due to three important reasons: (a) the collective environment that induces migration and cell survival of connected cells, (b) the passive displacement of nonmigratory cells that can actively divide, although would not be transported during single-cell migration and (c) better protection of the internally localized cells from the immune cells, shear stress and nuclear damage<sup>116,117</sup>.

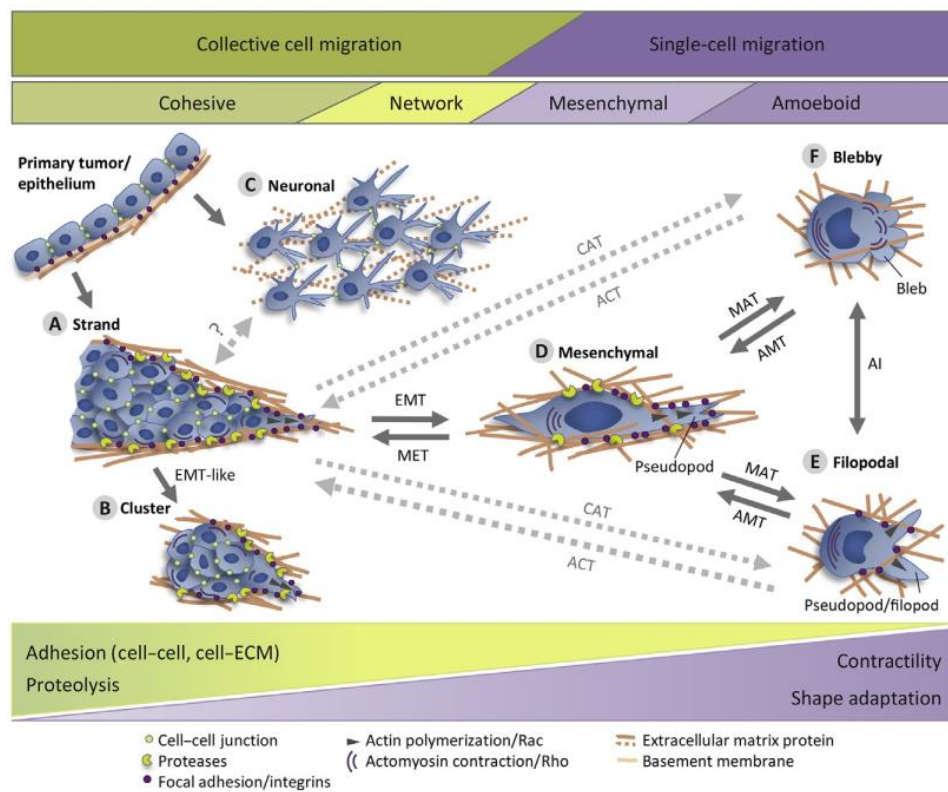


Figure 6. Main modes of cancer cell migration and the migratory transitions. The collective migration occurs when cell-cell adhesions and proteolytical activity dominates, while the single cell migration occurs when the cell contractility and shape adaptation play more dominant role. From<sup>108</sup> with permission from Elsevier.

However, the cancer cells can also detach from the nonmigratory tumor or from collectively migrating cells under certain conditions. In fact, such transition from collective to single-cell mesenchymal migration frequently occurs if the cell-cell adhesions are downregulated. Such transition can also take place in the situation of rapid loss of dimensional constraints of the microenvironment, i.e., where the cells from a tightly packed environment translocate into wider spaces <sup>108</sup>. This phenomenon is called *epithelial-to-mesenchymal transition* (EMT) and is connected with both: conversion from collective to single-cell migration as well as transition from nonmigratory epithelial tumor morphology to collectively migrating cells as well. In this process, the epithelial features: cell-cell junctions and apicobasal anchorage to the basal membrane are downregulated, while the stromal-type adhesions and dynamics of the cytoskeleton increase <sup>118,119</sup>. This process is involved in the invasion of many epithelial cancers, such as colon, lung, prostate, and breast cancers <sup>120</sup>. Depending on the intensity of EMT, the collective cell agglomerates can weaken or even get rid of intercellular junctions and increase the cell-ECM adhesions. The adhesion remodeling is combined also with changes in actomyosin contractility from cell-cell junctions to the migratory cytoskeletal arrangements that prefer the cell-ECM interactions. All these actions result in the loss of apico-basal polarity (present in non-migratory epithelial cell clusters) and establishing the front-rear polarity of migratory cells. The current studies suggest that EMT is neither a linear nor binary process but has rather the form of continuous change with the intermediate states in which cells can exhibit both the epithelial and mesenchymal features <sup>121,122</sup>.

EMT occurs mainly due to the chemical stimulation by growth factors and cytokines which modify Rho/Rac signaling pathway, inducing the migratory cell profile and activating several other signaling cascades. The chemical stimulation of EMT might be received directly from the blood vessels, as well as from the cancer-associated cells <sup>123</sup>. The latter mechanism comes from the transformation of physiological cells from the tumor surrounding, into the modified cells that chemically induce tumor expansion and aggression. It was shown that so-called cancer-associated fibroblasts can release transforming growth factor  $\beta$  (TGF $\beta$ ) and platelet-derived growth factor (PDGF) that induce EMT <sup>124</sup>. Another study found that the cancer-activated adipocytes can secrete prometastatic cytokines such as TNF $\alpha$ , leptin, and IL-6, causing an increased production of metalloproteinases that induce migratory behavior and cancer invasiveness <sup>125</sup>. The modified macrophages in the breast tumor proximity can also create a paracrine loop that guides the cancer cell to nearby blood vessels <sup>126,127</sup>. What is more, the EMT transition can occur in a reversed direction. This process is called mesenchymal-to-epithelial transition (MET) and occurs when the collective migration or epithelial phenotype is preferred. For example, the linear, dimensional confinement of the jammed cells can cause the creation of adhesions between non-connected cells

<sup>115</sup>. A similar situation can also occur if the cells are guided by the structured, parallel ECM fibers<sup>128</sup>.

Another transition from the collective mode is *collective-to-amoeboid transition* (CAT), which is observed only in specific cancer types. One of the first observations of CAT was done by inhibiting  $\beta 1$  integrin in clusters of melanoma cells <sup>129</sup>. The exact mechanism of CAT is not well known, however, the cells undergoing such transitions need to get rid of both: cell-cell and cell-ECM adhesions and might do it to squeeze into the constrained environment of ECM fibers <sup>111</sup>. Therefore, further studies are needed to find the occurrence, importance, and mechanism of this transition.

Cancer cells can also change their form from mesenchymal to amoeboid and reverse. These processes are called *mesenchymal-to-amoeboid transition* (MAT) and *amoeboid-to-mesenchymal transition* (AMT), respectively, as shown in Figure 6. The aforementioned EMT transition required the upregulation of cell-ECM adhesions and downregulation of cell-contacts, which is the result of the previous alterations of gene expression pattern. Alternatively, MAT occurs faster than gene expression <sup>130,131</sup>. There are several ways to induce the MAT transition. The first one is to interfere with small GTPases that are responsible for extension of actin protrusions and increase actomyosin cortical contractility. The second way affects the actin network organization and actin-plasma interactions in various manners: weakening or even disrupting cortical actin, reducing the attachments of the plasma membrane to the actin cortex, or even creating the myosin II-dependent local contraction that causes the increase of hydrostatic pressure. The third way of inducing MAT transition interferes with the crosstalk between cell adhesions and ECM. This can be done by downregulation of focal adhesions (FAs) proteins, reduction of integrin receptors strength, inhibition of metalloproteinases expression, creation of a retrograde flow of actin cortex, altering the adhesiveness of ECM, and many others <sup>91</sup>. Therefore, in the MAT transition, the cell should acquire the ability to change shape, as well as obtain more spherical morphology. This can be directed by the following cues: (a) reduced cell-ECM adhesion, (b), loss of ECM proteolysis, (c) increase of the RhoA and myosin II-dependent contractility of actomyosin cytoskeleton, and (d) microtubule destabilization <sup>108</sup>. Obtaining the amoeboid morphology can potentially help in cancer invasion by the more efficient migration through dimensional obstacles, as well as the more efficient migratory behavior overall <sup>91</sup>. Among the amoeboid transitions, one can also distinguish the amoeboid interconversion (AI) that occurs between pseudopodal and blebbing cells. It provides the flexibility of the cell that migrates through different cell types and barriers such as vascular walls and basal membranes. While the exact mechanism and function of amoeboid interconversion are not yet fully understood <sup>108</sup>,

it is proposed that it might be connected with cell stemness and altered ability of metastasis formation<sup>132</sup>.

Cancer dynamics and plasticity play a substantial role in oncogenesis and metastasis. Therefore, many of the aforementioned studies were focused on the time-dependent observations coupled with either physical or chemical stimulation to understand the mechanisms of cancer dynamics. The realization of the time-lapse studies of cancer cells seeded on elastic substrates is also shown in this thesis. Section 6.1 of results, presents the spontaneous transitions between the different morphological subpopulations of the heterogenous WC256 line, providing the newly discovered here plasticity of cancer cells that can occur in the absence of external stimulation. As it is shown here, such transition requires modification of migration strategy (movement directionality, velocity, etc.) as well as shape modifications between more spread and rounded morphology.

Such classification of different cell forms can be also done quantitatively. Therefore, the next sections of the introduction are focused on the quantitative methods that can be applied to the classification of cell migration and shape.

#### **4.4.4. Analytical description of cell migration and morphology.**

The quantification of biological phenomena gives significant information about their occurrence and mechanisms, allowing for precise comparisons between different experimental conditions, as well as experimental heterogeneity. Therefore, the quantitative description of cell shape and morphology plays a central role in the description of cell state. In this section, I would like to recapitulate one of the most common quantitative descriptors that are used in cell biology studies in comparisons of different cellular behaviors.

Cell migration phenomenon can be measured in several ways. Quantitative descriptors can characterize either the single displacement vectors or their dynamics, as well as the whole track that the migrating cells experienced during the observation time<sup>133</sup>. The registration of cell migration consists of a time-lapse movie that is constructed of consecutive time frames. The simplest characterization of cellular dynamics can come from the two consecutive frames that are used to calculate displacement and the instantaneous velocity, while the three consecutive frames enable quantification of vectors dynamics in the form of a turning angle between two displacements<sup>134-137</sup>. There are two ways to analyze such descriptors along the time sequence in the context of the cell population. The first relies on the initial averaging of calculated parameter values for each cell and further analysis of those averaged values in order to draw conclusions about cell population. The initially averaged parameters calculated that way are called “cell-based parameters”. An alternative approach called “step-based parameter” assumes the analysis

of information from all available time steps of all cells, regardless to which cellular track each timepoint belonged. Both of these approaches have their advantages: cell-based parametrization is more intuitive in drawing conclusions because it is easier to imagine the behavior of the single cell, instead of the whole cell population. The comparison between cell-based parameters can also show differences between each cell in the population, indicating their potential diversity. However, the cell-based parameters make impossible to trace the cells that leave the field of view and come there back again after some period, which is possible for the step-based analysis. The cell-based parametrization is also prone to several biases that are not present in the step-based parametrization <sup>133</sup>.

Another group of migration descriptors measures the cellular behavior along the whole-time sequence. The most common descriptor comes from the analysis of Brownian motion and calculation of the Mean-Squared Displacement (MSD) which can characterize whether cells migrate in a diffusive, sub-diffusive, or ballistic manner <sup>138</sup>. It is also possible to fit the model of persistent random walk, which gives information about migratory behavior by calculation of persistence time and random motility coefficient. The persistence time illustrates the average time that is needed by the cell to make a significant change in the movement direction, and the random motility coefficient is analogous to the diffusion coefficient <sup>139,140</sup>. The movement effectiveness can be also described by cumulative distance that sums up all displacement vectors of the cell, indicating the total path length <sup>135,141</sup>. Another migratory descriptor that illustrates movement effectiveness is the confinement index that divides the total displacement vector (the vector connecting two ends of the cell track) by the cumulative distance. Therefore, the value of the cumulative index close to 1, suggests that the cell migrated away from the starting point in a straight way, while the value close to 0 illustrates the long cellular displacement that resulted in a similar initial and final cell position, or the chaotic movement in the starting point proximity <sup>133</sup>. Migration persistence can be also defined by the persistence length that couples the total displacement vector with the number of frames and the mean distance that was traveled between them <sup>73</sup>. Another factor able to describe movement directionality is the auto-correlation function of cell velocities, which describes how directional the movement was <sup>142</sup>. The migration can be also quantified in relation to the extracellular cues, such as chemoattractants or the substrate topography. The directionality time describes the time scale required for identifying the directionally biased motion, e.g., due to the chemotactic stimulation <sup>136</sup>, while the tensor of individual moment of inertia, which shows the preferred direction of migration on the 2D plane<sup>143</sup>.

Nevertheless, the displacement of many types of mesenchymal cells requires rearrangement of cell shape <sup>144</sup>. In such cases, cellular morphology is tightly connected with

the migratory properties and therefore is a significant determinant of cellular behavior. The extensive reviews on different morphological descriptors of shape were provided by several authors <sup>145-147</sup> and therefore I would like to recapitulate only a few of them which I found most common. The simplest parameters for describing cell shape are the area, perimeter, and perimeter/area ratio <sup>145,148</sup>, which depend on the cell size. However, the overall cell morphology can be also quantified by its geometry, being independent of the cell size as well. One of them is cell elongation which relies on the fitting the ellipse to the cell shape. When the cell is highly elongated and thus the difference between minor and major axes of ellipses increases, the elongation factor is closer to 1. In contrast, when the cell is rounded and the major and minor axis are of similar lengths, the elongation decreases to 0 <sup>149</sup>. The alternative description is provided by circularity which is also called compactness <sup>150</sup>, describing how much the shape is similar to the circle. It is also possible to use the aspect ratio between minimum and maximum dimensions to describe the geometrical properties of cell shape <sup>151,152</sup>. Alternatively, it is also possible to describe the regularity of cell shape using the solidity parameter which divides the cell area, by the area of convex hull. Therefore, for the ideally smooth shape of regular boundaries, the solidity is close to 1, while for the less regular boundaries and the presence of holes, the solidity decreases towards 0 <sup>153,154</sup>. Similarly to the direction of migration, cell shape can be also considered in the context of the environmental cues in its surroundings. For example, it is possible to measure the angle between the main axis of shape and the direction of extracellular signals <sup>155,156</sup> as well as the orientation of the nucleus regarding the orientation of the whole cell<sup>151</sup>.

However, all of the aforementioned shape descriptors are calculated for static images and do not take into account the neighboring frames, and differences between them. This issue is partially solved by the descriptors of cell shape dynamics, such as DECCA parameter that describes the cell motion over time, linking the cell motility and shape. Due to its characteristics, it however does not distinguish between the membrane ruffling and directional shape displacement, describing rather the sum of cellular dynamics over time <sup>48</sup>. Other approaches rely on the observation of temporal shape dynamics by the TSRVF-PCA method with the VAR model <sup>157</sup>, as well as the evolution of Fourier shape descriptors, which elucidate temporal changes of cell outline <sup>158</sup>.

Even after such a short recapitulation of cell migration and cell shape descriptors, it is clear that current literature provides a wide variety of quantitative descriptors of those aspects of living cells. However, all these parameters treat the cell migration and shape separately, as two independent properties of dynamic cells. In the chapter 6.2 of results, I present the alternative approach for connecting cell migration with morphology, which aims at the mathematical description of cellular actions. The mutual dependence of cell shape and



migration direction is emphasized by introducing new terms in cell biology studies: *morphomigrational behavior of cell* and its proper *morphomigrational description*.

## **4.5. Measuring relative temperature using NV<sup>-</sup> diamonds**

### **4.5.1. Cellular microthermometry**

Temperature is one of the most basic physical quantities describing the thermodynamic state of the molecules that build the system. It also influences cellular functioning on the most basic, molecular levels: DNA replication and RNA translation as well as protein folding and interactions between proteins<sup>159-163</sup>. On the cellular level, temperature was found to affect the proliferation of various types of cells<sup>164,165</sup>. What is more, temperature influences the cell migration phenomenon as well, including migration of neutrophils which play a significant role at inflammation sites<sup>166</sup>, mesenchymal stem cells (MSCs) that are considered in modern therapies of chronic inflammation and autoimmune response<sup>167</sup>, as well as the collective migration of NIH-3T3 fibroblasts during wound healing assay<sup>168</sup>. Temperature also influences the differentiation of CD4 T helper cells<sup>169</sup> as well as many other cell lines<sup>170,171</sup>. On the higher level of organization, temperature was found to be the potential indicator in cancer diagnostics<sup>172</sup> and thyroid disease<sup>173</sup>. The increased body temperature was also measured at the inflammation sites, being involved in the proper immunological response<sup>174</sup>. Because of its profound influence on living cells, temperature is also stabilized in most live-cell microscopy setups by the application of additional incubators that increase the reliability and reproducibility of experimental results.

The branch of science focused on temperature measurements in the microscale is called *microthermometry*. and draws increased attention from researchers. Many different types of microthermometers have been developed until now, although their application depends on the aim of the study, experimental conditions, and the available equipment. The review work of Okabe et al. divides microthermometry probes into 4 main types, depending on the materials which they are made of: small chemical compounds, synthetic polymers, fluorescent proteins, and inorganic particles, as shown in Figure 7. They differ in their overall forms, methods of delivery into the cell as well as the physical parameters that are responsible for temperature readout<sup>175</sup>.

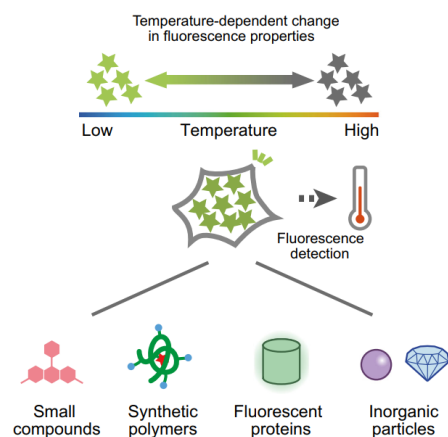


Figure 7. Types of fluorescent microthermometers, depending on the material they are made of<sup>175</sup>. Open Access CC BY 4.0 license.

The europium III thenoyltrifluoroacetate trihydrate (Eu-TTA) is one of the earliest microthermometers and belongs to the group of small compounds. The temperature increase is observed by the decrease of Eu-TTA fluorescence<sup>176</sup>. The method of its delivery was improved over several research and started from its incorporation into liposomes, which resulted in embedding Eu-TTA into the cell membrane<sup>176</sup>. However, the fluorescence of Eu-TTA is also sensitive to the changing pH, which narrows down its application. Another study overcame this issue by placing Eu-TTA in the micropipette, which resulted in its isolation from the chemical surrounding. Nevertheless, such an approach required the precise positioning of the micropipette, and the temperature measurement was performed not in the cell, but at some distance from it<sup>177</sup>. Microthermometers from the group of small compounds can be also targeted to the specific cell organelles, as was done with MitoRTP which specifically binds to mitochondria. Here, the temperature measurement is more sophisticated and relies on the ratiometric measurement of two dyes: the Rhodamine B fluorescence that decreases with elevated temperature, and the CS NIR dye whose fluorescence remains stable<sup>178</sup>.

The second group of microthermometers includes synthetic polymers. The most common ones are made of block copolymers of poly-N-Isopropylacrylamide (NIPAM) or poly-N-n-propylacrylamide (NNPAM) that are equipped with fluorescence units. Depending on the type of polymer, the temperature registration is based on the fluorescence intensity<sup>179,180</sup>, fluorescence ratio<sup>181,182</sup>, or FLIM imaging<sup>183,184</sup>. In the earliest studies, the application of polymer microthermometers required their injection into the cell, which can be considered a significant intervention into cell homeostasis. However, further studies improved this method through the proper modification of the polymer, allowing its spontaneous cellular internalization.

Fluorescent proteins, which are mostly represented by GFP and its derivatives, constitute the third group of microthermometers. The local temperature variations can be measured

by the altered fluorescence intensity <sup>185</sup>, fluorescence anisotropy <sup>186</sup>, or the ratiometric measurement between two excitation maxima. In the ratiometric approach fluorescent proteins are characterized by two emission maxima, where one of them increases with temperature, while the second one decreases <sup>187</sup>. Another exemplary protein microthermometer was made from two coupled fluorescent proteins: mSirius and mT-Sapphire. The fluorescence of the first one depends on the temperature, while the fluorescence of the second one does not, which allows for ratiometric measurements <sup>188</sup>. The great advantage of protein microthermometers is their ability to be expressed in many different cellular structures, only by the proper construction of plasmids. However, the observed cells have to be first transfected, transformed, or injected with mRNA <sup>175</sup>, which might not work well with every cell line. What is more, the fluorescent proteins are also subjected to bleaching and therefore their use may be limited in some microscopy experiments.

The fourth type of microthermometers are inorganic particles that in most cases are spontaneously internalized into the cells. The largest group of such inorganic particles are quantum dots, for which temperature measurement relies on fluorescence or photoluminescence spectral shift <sup>189-191</sup>, as well as fluorescence intensity ratio <sup>192</sup>. Among their advantages, one can mention no need of cell modification as well as the simplicity of their application. However, the temperature readout by recording the spectral shift requires an extensive spectroscopic setup and spectrum registration might consume a substantial amount of time. Therefore, each of the mentioned microthermometer does have its advantages and disadvantages that have to be carefully considered in the context of research design.

#### **4.5.2. NV- diamonds as cellular microthermometers**

Another type of small inorganic microthermometer that has not been mentioned yet are the nanodiamonds (nDs) with negatively-charged nitrogen-vacancy color centers (NV<sup>-</sup>). The nanodiamonds form an inert, carbon-based material of high biocompatibility. Numerous studies have already tested nDs to examine their interactions with cells in the context of their potential toxicity, viability, morphology, cell cycle progression, inflammation, genotoxicity, differentiation, and other aspects of cellular homeostasis. In most cases, the negative effects were not observed, being present only in some specific cell lines cultured with high (250 µg/ml) diamonds concentration <sup>193</sup>. The good biocompatibility makes nDs the perfect candidates for various cellular applications. The fluorescent nDs were used as the staining markers that were visible in both fluorescence and electron microscopy <sup>194,195</sup>. Due to their small size (from tens to hundreds of nanometers), they were also used in single particle tracking experiments, especially in observations of the dynamics of cell membrane receptors <sup>196,197</sup>. Another proposed application of nDs is their usage as the carriers of chemical compounds (e.g., drugs) into the cells.

The already proposed systems were based on various functionalization of diamonds surface that resulted in the surface electrostatic interactions that caused the transient binding and further release of the transported DNA inside the cell <sup>198</sup> or the physical absorption of a transported ligand<sup>199</sup>. Due to the extremely high physical and chemical stability of diamonds and their color centers, nanodiamonds were also used as a tracker of dividing cells. In these experiments, a single cell was initially loaded with a sufficient amount of nanodiamonds that were subsequently passed to the daughter cells, allowing their identification <sup>200,201</sup>. Nanodiamonds were also utilized as the chemical sensor of hydrogen peroxide in living macrophages <sup>202</sup>.

The application of NV<sup>-</sup> nanodiamonds in microthermometry is tightly connected to the electronic structure of NV<sup>-</sup> color centers. Panel A of Figure 8 shows the model of the nitrogen-vacancy diamond color center, while panel B presents the structure of its energy levels.

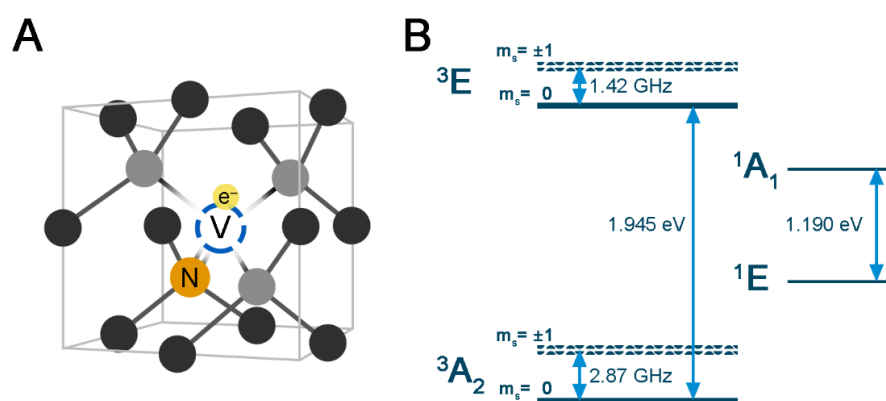


Figure 8. **A:** Model of the negatively-charged Nitrogen-Vacancy (NV<sup>-</sup>) center in diamond. Carbon atoms interacting with vacancy are marked with grey color. **B:** Electronic structure of NV<sup>-</sup> color center.

The NV<sup>-</sup> diamond center consists of the nitrogen atom that is built in the crystal lattice and the neighboring empty site (vacancy). The ground ( ${}^3A$ ) and excited ( ${}^3E$ ) states are triplets that are separated by 1.945 eV which corresponds to 637 nm wavelength. Their magnetic sublevels with the spin projection of  $m_s = 0$  and  $m_s = \pm 1$  are split by 2.87 GHz (ground state) and 1.42 GHz (excited state), respectively. In a zero magnetic field, a small additional splitting of  $m_s = \pm 1$  states is caused by the strains in the crystal lattice. Apart from the aforementioned triplet states, there are also two singlet states. The meta-stable (300 ns lifetime) ground state  ${}^1E$  and excited  ${}^1A$  state are separated by 1.190 eV (1042 nm). Typically, the NV<sup>-</sup> centers are excited with the green light of  $\sim 532$  nm wavelength <sup>203</sup>.

The electronic structure of this color center allows for the observation of the *Optically-Detected Magnetic Resonance* (ODMR) phenomenon, that is utilized in the nanodiamond microthermometry. Briefly, the presence of singlet states with state-dependent inter-system crossing rates allows efficient preparation of NV<sup>-</sup> centers in the  $m_s=0$  state (optical pumping), which exhibits brighter fluorescence. ODMR technique relies on the decrease of fluorescence intensity when NV<sup>-</sup> center interacts with both green light and microwaves of the resonant frequency.

Figure 9 illustrates the mechanism of the ODMR phenomenon. Panel A shows the situation where the diamond interacts with the green light, but the microwave frequency is out of NV<sup>-</sup> resonance. The green light excites electrons, that further undergo the vibrational relaxation to the excited triplet states. From that point, most NVs release their energy in the form of red fluorescence ( $\lambda=637$  nm). The NV<sup>-</sup> spin during deexcitation is conserved and therefore fluorescence can occur only between: (I)  $m_s=+1$  excited and ground states, (II)  $m_s=-1$  excited and ground states, as well as (III)  $m_s=0$  excited and ground states, which is marked by three independent red arrows. However, NVs can also undergo a transition to the singlet state (<sup>1</sup>A), from which can either release a 1042 nm photon or decay nonradiatively and, after  $\sim 300$  ns, relax from the <sup>1</sup>E singlet into the ground triplet state. The probability of intersystem crossing from the excited triplet state (<sup>3</sup>E) is higher from  $m_s=\pm 1$  than from  $m_s=0$ , which is marked by the thicker arrows. Also, the transition from the ground singlet state <sup>1</sup>E occurs preferably to the  $m_s=0$  than  $m_s=\pm 1$  ground triplet state. Both of these facts result in optical pumping of the ground  $m_s=0$  state, which is then more occupied than the  $m_s=\pm 1$  state. Therefore, the  $m_s=0$  state exhibits brighter red fluorescence than the remaining ones <sup>203</sup>.

In the case of the resonant frequency presented in Figure 9 B, some NVs from the  $m_s=0$  state are already excited by microwaves, which place them on the  $m_s=\pm 1$  level of the <sup>3</sup>A ground state. Since the microwaves rebalance the occupation of  $m_s=0$  and  $m_s=\pm 1$  states, the availability of the  $m_s=0$  state is lower than in out-of-resonance conditions, which decreases its brighter fluorescence. That is because the probability of the intersystem crossing from the  $m_s=\pm 1$  excited state is higher than from  $m_s=0$ , which causes more NVs to undergo the intersystem crossing and thus do not exhibit red fluorescence at all. Both of these facts result in the fluorescence intensity decrease at the microwave resonance conditions, which is the core of the ODMR phenomenon. Since the NV<sup>-</sup> electron confinement in the crystal lattice and hence, the energies of the electronic states are dependent on temperature, the ODMR resonant frequency decreases nearly linearly with temperature increase with a slope of  $-74$  kHz/K around room temperature <sup>204</sup>.

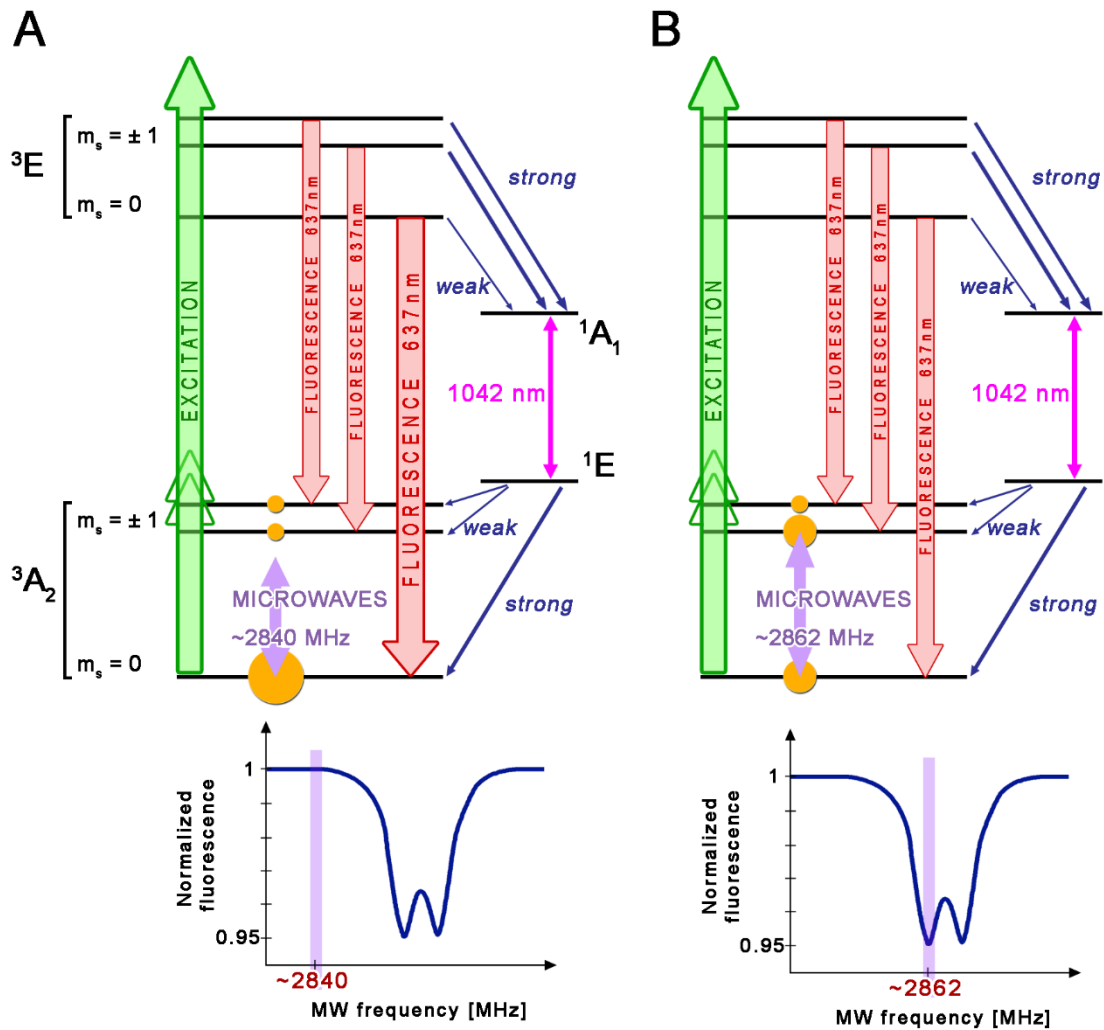


Figure 9. Mechanism of ODMR phenomenon. A: Out-of-resonance case, B: Resonance case.

The application of NV- nanodiamond thermometry was already presented in some studies regarding living cells. In the work from 2013, Kucsko et al. applied nanodiamonds and gold nanoparticles to show that nanodiamonds registered the temperature increase when a nearby gold nanoparticle was heated by the laser light. The measured temperature increase differed, depending on how far the nanodiamond was placed from the heat source <sup>205</sup>. Another temperature observation in living cells was performed on neurons, where single nanodiamonds could measure a temperature difference of  $\pm 1.5K$  <sup>206</sup>. While, in principle, ODMR can be used for recording absolute temperatures, this is not a common approach, because the diamonds have to be initially calibrated to couple the exact resonance frequency with temperature. This fact was however considered by Sekiguchi et al. who demonstrated the exemplary determination of absolute temperature by starting from typical ODMR experiments and then moving to cell fixation and temperature calibration of each diamond <sup>207</sup>. This procedure, however, had to be done on the microscope and required temperature calibration after every single experiment, which generally made

it highly complicated and time-consuming. Because of those obstacles, most NV- thermometry on living cells still relies mostly on the measurements of relative temperature.

The 6.3 section of results describes the optimization and incorporation of temperature measurements into mechanobiology studies. Therefore, the two experimental techniques: ODMR and TFM were combined to find a new paths to better understand cell biophysics, by parallel measurement of traction forces and relative temperature.

## 5. Materials and methods.

### 5.1. Elastic substrate preparation.

Elastic substrates were prepared in two forms: in the glass-bottom dishes for the optical microscope observations (CellVis, #1.5 glass thickness for WC256 cells and #0 glass thickness for ODMR-TFM studies) as well as on standard glass slides for AFM measurements. In both cases, the glass surface was silanized by the mixture of glacial acetic acid (Chempur), 3-(Trimethoxysilyl) propyl methacrylate (Sigma-Aldrich), and 96% ethyl alcohol in a 1:1:14 ratio for 20 minutes. After this process, glass was rinsed three times with 96% ethyl alcohol to wash out the residual chemicals<sup>208</sup>.

A polymerization mixture of 40 kPa substrate for studies of WC256 heterogeneity was prepared by mixing 8% acrylamide with 0.48% bis-acrylamide (Bio-Rad) in a 10mM aqueous solution of HEPES buffer (Gibco). A polymerization mixture of 12 kPa blank substrate was prepared by mixing 7.5% acrylamide and 0.16% bis-acrylamide in DI water. A polymerization mixture of 12 kPa substrate with diamonds was prepared similarly to the blank substrate but with the addition of the pre-sonicated and vortexed NV<sup>-</sup> diamond suspension in 25 µg/ml concentration. The polymerization mixture of ODMR-TFM substrate (substrate for parallel measurement of temperature and cellular tractions) was prepared similarly to the substrate with NV<sup>-</sup> diamonds, but with an addition of 2% of green, fluorescent 200-nm diameter carboxylate-modified polystyrene (PS) beads (excitation: 505 nm, emission: 515 nm, cat. N<sup>o</sup> F8811, Thermo).

Each type of polymerization mixture was mixed with polymerization agents: 0.05% of ammonium persulfate and 0.05% tetramethylethylenediamine (Bio-Rad). 40 kPa and 12 kPa substrates were prepared in slightly different ways. In the case of 40 kPa substrate, 23 µl of polymerization mixture was applied on the silanized glass-bottom dish and covered with the round 18-mm coverslip and left for 1 h to polymerize. After that time the glass-bottom dish was filled with PBS and the coverslip was removed from the substrate. 12 kPa substrates were prepared by upside-down polymerization: the proper amount of polymerization mixture (18 µl for thin, 22 µl for medium, and 26 µl for thick substrates) was placed on the glass coverslip, which was then touched by the inner surface of the glass-bottom dish or the glass slide to allow the upside-down polymerization. This procedure allowed for the sedimentation of microdiamonds. After the 1h polymerization, the upside-down glass-bottom dish was turned orderly and filled with PBS, which allowed for detaching the top coverslip (which was initially in the bottom). After polymerization, each type of substrate (40 kPa and 12 kPa) was left



for 24 hours to dissolve any residual amount of acrylamide in the buffer. Afterwards, the substrate was washed three times with PBS.

## **5.2. Functionalization of diamond surface and particle size characterization.**

Functionalization of microdiamond surface was done with the assistance of Mateusz Ficek, while Dynamic Light Scattering (DLS) experiments were performed and analyzed with Maciej Głowacki (both from the Department of Metrology and Optoelectronics, Faculty of Electronics, Telecommunications and Informatics, Gdańsk University of Technology, Poland). Tests of different surface terminations in various solvents were conducted on nonfluorescent microdiamonds (MSY 0.75-1.25, Microdiamant AG). They have a similar size ( $D_{50} = 1 \mu\text{m}$ ) to the NV<sup>-</sup> microdiamonds while being less expensive. The final suspension used in further experiments was prepared from NV<sup>-</sup> microdiamond powder with  $\sim 3.5$  ppm color centers concentration (MDNV1umHi30mg, Adamas Nano).

Hydrogenated and oxygenated surface terminations were prepared by treatment of diamond powders with hydrogen and oxygen plasma using the plasma cleaner system (Diener ZEPTO). Briefly, the weighed diamond powder was placed in a glass dish and placed in the chamber of the plasma cleaner system. After the air was pumped out, the chamber was filled with hydrogen or oxygen, for hydrogenation or oxidation of the surface, respectively. At a pressure of 0.3 mbar, plasma RF with frequency 13.56 MHz and power of 300 W was employed. The diamond powder was treated with plasma for 10 minutes.

Afterwards, four separate nonfluorescent microdiamonds suspensions were prepared in 0.5 mg/ml concentration using following solvents: (I) deionized water (prefiltered through 0.22  $\mu\text{m}$  PS filter), (II) DMSO, (III) BSA 2.5% w/w in DI water (freshly prepared from lyophilized BSA and prefiltered DI water) and (IV) FBS solution (FBS qualified, Gibco). The further suspension of NV<sup>-</sup> oxygenated microdiamonds was prepared in prefiltered DI water at 0.5 mg/ml concentration as well. Before DLS measurements, samples were sonicated for 5 minutes in an ultrasonic bath and then twice vortexed for 15 seconds at 3000 rpm.

Hydrodynamic diameters were determined using Zetasizer Nano ZS particle analyzer (Malvern Panalytical, UK) equipped with a 632.8 nm laser and a narrowband filter (ZEN9062). For the measurement, every suspension was placed in a disposable, polystyrene cuvette (outer dimensions of 12 × 12 × 45 mm) and measured at 25°C using a backscatter configuration (scattered light collected at 173° angle). Each measurement of the particle size distribution consisted of three measurements. Particles were analyzed in the context of their mean hydrodynamic diameter (Z-Average), standard error of the mean (SEM), as well as 10<sup>th</sup>, 50<sup>th</sup>,

and 90<sup>th</sup> percentiles ( $D_{10}$ ,  $D_{50}$ ,  $D_{90}$ ) derived from intensity-weighted particle size distributions. SEM was calculated from the standard deviation, derived from the polydispersity index <sup>209</sup>.

### **5.3. Characterization of ODMR-TFM substrates.**

The Atomic Force Microscopy (AFM) experiments and their interpretation were performed by Agata Kubisiak from Department of Physics of Nanostructures and Nanotechnology, Institute of Physics, Jagiellonian University. The elasticity measurements were performed using a NanoWizard 3 NanoScience AFM (JPK Instruments) in force mapping mode. Experiments were repeated three times on samples prepared independently on different days and each experimental day consisted of the examination of all types of 12 kPa substrates. For each substrate, force mapping was performed in 5 different areas of the sample. All experiments were performed in a drop of Hanks' Balanced Salt Solution (HBSS, Cat. No. 55037C, Sigma-Aldrich, St. Louis, USA). A spatial map of force vs. distance (FD) curves was measured at a grid of 16x16 points and a square surface of 30  $\mu\text{m} \times 30 \mu\text{m}$ . The position of scan area was controlled by the inverted optical microscope (IX-71, Olympus). Force-distance curves were measured at a speed of 2  $\mu\text{m/s}$  with the maximal applied force 1.2 nN. To evaluate the elastic modulus of substrates, the non-covered spherical polystyrene probe with a radius of 2.5  $\mu\text{m}$  (Novascan) mounted on the triangular cantilever with the spring constant of 0.03 N/m was used. Before each measurement, the cantilever spring constant was calibrated using dedicated software (SPM Software, JPK Instruments). The global elastic modulus of substrates was calculated using the Hertz-Sneddon model was used.

Topographical images were performed using force-distance (FD)-based imaging mode (QI; JPK Instruments), allowing for high-resolution imaging of the image. In this method, a single FD-curve measurement was performed at every pixel of the image and then translated from the selected trigger force into images of substrate topography. The loading force varied from 0,5 to 0,7 nN and was adjusted to obtain a clear contrast of the topography of the substrate. The obtained images of topography were analyzed using JPK Data Processing Software.

Confocal imaging was performed on Zeiss LSM 710 confocal microscope using Zeiss  $\alpha$ -Plan Apochromat 63x/1.46 oil objective.

### **5.4. ODMR registration setup.**

Microwaves were generated by the microwave generator (Rohde & SchwarzSMBV100A) connected to the amplifier (Mini-Circuits ZRL-3500+) which was then connected to the MW antenna in the form of a coaxial cable terminated with a wire loop of  $\sim 1\text{mm}$  diameter made of 0.2 mm copper wire. Registration of wide-field ODMR consisted of a time-lapse sequence

of fluorescent images acquired with a CMOS camera (ORCA-Flash 4.0 V2). The camera was triggered by the signal from the MW generator and therefore, each next frequency of microwave sequence triggered the image acquisition in a time-lapse sequence. To increase camera registration speed, the ODMR spectrum was registered with a field of view limited to 1024 x 1024 pixels. Regular ODMR sweep (*Regular Sweep*) consisted of 201 points (frequencies) sequence, between 2845 and 2895 MHz with 0.25 MHz step. The Irregular Sequence (*Irreg Sequence or Irreg Seq*) consisted of 2864 and 2874 MHz with 0.25 MHz step with 3 out-of-resonance frequencies in the beginning and the end. Frequency was switched every 25 milliseconds, however, due to the camera dead time, fluorescence was registered only for 18 milliseconds. During the whole ODMR registration, the fluorescence illumination was turned on. The MW antenna was positioned ~250 μm above the substrate using the InjectMan® NI 2 (Eppendorf) micromanipulator. Fluorescence of NV<sup>-</sup> diamonds were collected using a custom fluorescence cube built with: Band Pass Filter 470/40 nm (excitation), DMLP 567 nm dichroic mirror, and Long Pass 600 nm filter (emission).

### 5.5. Optimization of ODMR experiments

Optical power density of fluorescence lamp was measured in following way. The LD Plan-Neofluar 40x/0.6 objective (Zeiss) was focused on the top layer of ODMR-TFM substrate to obtain the sharp image of green fluorescent beads. The field diaphragm on the fluorescence path was partially closed to make its borders visible on the image, allowing to measure the area of illuminated field of view. This area was used then to calculate the optical power density. Afterwards, ODMR-TFM substrate was removed from the microscope stage and replaced with the sensor of power meter (PM100D power meter with S120 sensor, Thorlabs). Objective was refocused to register the maximal optical power that indicated the focused light. The optical power was measured between 0 and 100% of fluorescence lamp intensity (HXP120, Zeiss). Optical power registered by the power meter was then divided by area of the field of view measured at the initial stage.

Thickness of the substrate was measured by refocusing between top and bottom surfaces of the substrate, using LD Plan-Neofluar 40x/0.6 dry objective (Zeiss). Because of the differences between refractive index of PA substrate and air, the measured distance ( $\Delta h_{\text{Measured}}$ ) was corrected with the formula Eq. 6 as in <sup>210</sup>. The refractive index of polyacrylamide gel was assumed to be the same as for water.

$$\Delta h_{\text{Corr}} = \Delta h_{\text{Measured}} * \sqrt{\frac{n_{\text{water}} - NA}{n_{\text{air}} - NA}} \quad \text{Eq. 6}$$

ODMR spectra for different substrates were collected at room temperature for three substrates of different thicknesses. They were used to examine 5 places of similar thicknesses, each for three different thickness ranges: thin (20-40 $\mu\text{m}$ ), medium (50-70 $\mu\text{m}$ ), and thick (100-120 $\mu\text{m}$ ).

### **5.6. Temperature calibration of ODMR-TFM substrates**

Temperature calibration of the ODMR-TFM substrate was performed in the range of 17°C – 39°C. ODMR-TFM substrate was placed in the same incubation equipment as shown in Figure 41 A. The type K thermocouple of  $\pm 1.5$  °C accuracy was placed inside the glass-bottom dish, on the left side of its inner well, touching the bottom coverslip. During the experiment, a glass-bottom dish with ODMR-TFM substrate was filled with the cell culture medium without phenol red, to preserve the standard experimental conditions. Then, the temperature inside the dish was increased by 1°C which was confirmed by the stable thermocouple readout for 5 minutes. Therefore, we assumed that the glass-bottom dish with the substrate and cell culture medium have the same temperature. ODMR spectra were collected in three different fields of view. For each timepoint, the reference full sweep and the chosen Irregular Sequence averaged twice (*see: ODMR registration setup*) were measured. To avoid the potential local heating of diamonds, those two measurements were performed in a 1-minute interval.

### **5.7. Cell culture**

The initial cell line of Walker carcinosarcoma cells was obtained from Prof. H. Keller from the University of Bern, Switzerland. The adherent subline examined in this work was derived from the initially non-adherent cells grown in a suspension by Dr. Jolanta Sroka <sup>211</sup>. The WC256 cells were cultured in cell medium RPMI1640 (Euroclone) supplemented with 10% FBS (Gibco) and 1% of Penicillin/Streptomycin in the standard cell culture incubator (temperature 37°C, 5% CO<sub>2</sub> concentration in air, 100% humidity).

Fish epithelial keratinocytes were obtained from golden molly (*Poecilia sphenops*) scales. Live fish were maintained in the Laboratory of Inland Fisheries and Aquaculture at the Department of Zoology of Poznań University of Life Sciences (Unit no. 0091, registered by the National Ethics Commission (Warsaw, Poland)). The Local Ethical Commission for Investigations on Animals in Poznań at Poznań University of Life Sciences was advised about protocols and decided that bioethical permission for the research was not needed. Fish were euthanized by the pre-trained researcher (Mateusz Rawski from the Laboratory of Inland Fisheries and Aquaculture at the Department of Zoology of Poznań University of Life Sciences) with an overdose of tricaine methanesulfonate (MS222, 300 mg L<sup>-1</sup>) by prolonged immersion, then scales were collected postmortem. Afterward, scales were placed for 15 minutes in a cell

medium composed of DMEM High Glucose (BioWest) + 10%FBS (Gibco)+ 1%PS (BioWest). Next, each scale was placed in a separate glass-bottom dish (CellVis, #1.5 thickness), and the 20  $\mu$ l droplet of cell medium was placed on top of each scale. Such prepared scales were covered with a round 18 mm coverslip<sup>99</sup>. A few droplets of sterile distilled water were placed in each dish to prevent the medium evaporation and dishes were sealed with a parafilm for 24-hour incubation at room temperature. Incubation allowed the migration of large epithelial cell clusters from the scale surface onto the glass substrate. After the incubation, cell culture dishes were filled with  $\sim$ 2.5 ml of cell medium and the coverslip was carefully detached from the dish. Dishes that still contained the cells after the coverslip separation, were left for 2 hours to allow the recovery of the cells after the separation procedure. The cellular cluster was partially dispersed to single cells by replacing the cell medium with PBS (without  $\text{Ca}^{2+}$  and  $\text{Mg}^{2+}$ ) for 40 minutes. Afterwards, PBS was replaced again with full cell medium, and the sample was left for the next 1.5 hours for the sample recovery. After this procedure, single keratinocytes were prepared for microscope imaging.

MEF 3T3 and HEK293 cells were cultured in plastic T-25 bottles (NEST Biotechnology) in a standard cell culture incubator. MEF 3T3 were maintained in DMEM Low Glucose medium (Bio West) while HEK293 in DMEM High Glucose medium (Bio West), both supplemented with 10% of FBS (Gibco) and 1% PS (BioWest).

## **5.8. Observation of cellular dynamics**

Prior to microscopy observation of WC256 cells, two types of substrates: a clean glass-bottom dish and 40 kPa PA substrate were functionalized with fibronectin. The PA substrate was treated with Sulfo-SANPAH solution (Thermo) for 5 minutes under ultraviolet light. Afterwards, substrates were washed initially with 10 mM HEPES solution in deionized water and then three times with sterile PBS. Then, the hydrogels were incubated with the fibronectin solution (15  $\mu$ g/ml) at 4°C for 12 hours<sup>212,213</sup>. The glass-bottom dishes were incubated with a similar concentration of fibronectin, in the same conditions, without any chemical pretreatment. After protein conjugation, dishes were washed three times with sterile PBS, and WC256 cells were seeded in the concentration that allowed the single-cell observation. Time-lapse experiments were initiated 1 hour after seeding cells (30 minutes after the cell adhesion was observed) using an inverted Zeiss Axio Observer Z1 microscope, equipped with AxioCam camera (Zeiss), Plan Apochromat 10x/0.45 dry objective (Zeiss) and on-stage mini-incubator (PeCon) used to provide the proper temperature (37°C), gas mixture (air with 5%  $\text{CO}_2$ ) and humidity. The experiment was performed with 90 second intervals for 4 hours. A Definite Focus component (Zeiss) was used to maintain the constant focal plane.

For cell migration experiments on a glass substrate, MEF 3T3 cells and HEK293 cells were seeded on the non-functionalized glass-bottom dishes in the concentration that allowed registration of single-cell migration and left for 10 hours in the cell incubator. Incubation of MEF 3T3 cells lasted 10 hours and HEK293 cells for 18 hours which was caused by different times of proliferation of those cells. After these procedures, MEF3T3 cells and HEK293 cells were ready for imaging. Migration of MEF 3T3 cells was observed at 2.5 minutes interval for 9 hours, HEK293 cells were observed at 2 minutes interval for 5 hours, and both cell lines were kept at 37°C and 5% CO<sub>2</sub>. Keratinocyte migration was observed at 10 seconds interval for 30 minutes in room temperature and atmosphere.

## **5.9. Analysis of cell migration and shape**

### **5.9.1. Inclusion criteria**

To investigate the heterogeneity of an adherent subline of WC256 cells, data from 5 experiments on glass and 5 experiments on PA substrates were pooled together to collect 50 cells for each experimental condition. Cells had to meet the following inclusion criteria in order to be analyzed: (1) the analyzed cell had to be an individual; (2) the analyzed cell must not be in contact with another cell and (3) the cell must not be undergoing division in the current or neighboring frames. Nevertheless, before and after cell division, WC256 cells maintained similar morphology. Therefore, only the frames where cells were round before and after cell division, as well as frames showing cell division were excluded from the analysis.

In the observation of MEF 3T3, HEK293, and fish epithelial keratinocyte cells, the included cells should not be in contact with another cell for at least 80% of the total experiment time, as well as not divide during the experiment.

### **5.9.2. Obtaining binary masks from time-lapse sequences**

Time-lapse analysis of WC256 cells, as well as MEF 3T3, HEK293, and fish keratinocytes in the migration experiments consisted of obtaining cell outlines and their analysis in consecutive frames. WC256 cell outlines were retrieved in two ways: cells exhibiting sharp and regular boundaries were analyzed automatically using the automated software provided by Seroussi et al.<sup>214</sup>. Cells that were not identified by the software were outlined manually using the ROI Tracker plugin<sup>215</sup> in the ImageJ software. Cell perimeters were converted to binary masks using ImageJ software. In the case of MEF3T3 and HEK293 cells, as well as fish epithelial keratinocytes, binary masks were obtained using the ROI manager function of FIJI software.

The binary masks were analyzed by the custom-written MATLAB script (Matlab 2018a, Mathworks Inc. with Image Processing Toolbox). The binary shape properties, such as: centroid, minor and major axis of the ellipse fitted to the shape, orientation of the major axis, cell area

and perimeter were obtained using the *regionprops* function. The displacement vector for the specific frame ( $n$ ) was measured between the currently analyzed ( $n$ ) and the following ( $n+1$ ) frame. Turning angle ( $\alpha$ ) was calculated between the preceding displacement vector (between  $n-1$  and  $n$  frame) and the current displacement vector. The clockwise turn was marked with a positive sign of turning angle. Shape elongation was defined as  $\varepsilon = 1 - (a/b)$ , whereby  $a$  and  $b$  represent the major and minor axis of the ellipse fitted to a binary shape, respectively. The *regionprops* function determined the fitted ellipse by creating the ellipse of the same second-moments as the binary shape. Elongation  $\varepsilon = 0$  indicates a round shape, while  $\varepsilon = 1$  signified an infinitely elongated ellipse.

## 5.10. Subpopulation analysis of WC256 line

### 5.10.1. Dynamic classification of WC256 subpopulations

Subpopulations of adherent subline of WC256 cells were identified similarly as described in previous work <sup>211</sup>, distinguishing mesenchymal, polygonal and bigonal (nonpolar) as well as amoeboid cells. Since the proper quantitative classification of WC256 cells did not exist yet, the qualitative classification was used instead.

- Mesenchymal cells classification criteria: (I) the one-way expansion of cell border that results in directional displacement in the short time-scale (several frames); (II) the movement had to be based on repeated cycles of protrusion, adhesion and retraction of cell rear or be similar to the keratinocyte-like gliding motion <sup>144,216,217</sup>; (III) similar shape (mostly well spread) had to be maintained over time.
- Polygonal and bigonal cells classification criteria: (I) expansion of cell border in more than one direction (cell stretching) that results in the nondirectional displacement in the short time-scale (several frames); (II) there could be only a limited number of moments in which cell tears of adhesions on one side, which can result in the directional displacement in cell centroid. However, this directional movement was rather not the result of the standard migration mode of mesenchymal cells; (III) similar shape (mostly well spread) had to be maintained over time.
- Amoeboid cells classification criteria: (I) the one-way expansion of cell border that results in directional displacement in the short timescale (several frames); (II) unstable shape (mostly poorly spread) with small dynamic protrusions (pseudopodal cells) or migration via spherical protrusion on the leading edge (blebbing cells) <sup>91,130,218</sup>.

However, the expansion of cell border cannot be analyzed using only one (static) image. Therefore, each frame was assigned to proper subpopulation by its comparison with two previous and 2 ensuing frames. This method of dynamic classification allowed for qualitative analysis

of movement directionality and shape dynamics. Frames that were hard to classify by the aforementioned criteria were labeled with “unidentified” subpopulation and were excluded from further analyses of cell migration and shape descriptors.

### **5.10.2. Statistical analysis of WC256 cells**

Statistical analysis was performed using OriginPro 2018 software. The majority of data did not exhibit the normal distribution (as measured by D’Agostino K-squared test), while only the perimeter/area ratio in the mesenchymal subpopulation met the normality criteria. Therefore, we decided to use descriptors of non-normal distribution, i.e., median, quartiles, and interquartile ranges (IQRs). Therefore, the Mann-Whitney test was performed to demonstrate the statistical differences. The distribution widths were described by interquartile ranges (IQRs), which represent the differences between the third and first quartiles ( $IQR = Q3 - Q1$ ).

### **5.11. ODMR-TFM experiment**

Prior to ODMR-TFM experiments, the surface of 12 kPa PA substrate was functionalized with type-I collagen. The polyacrylamide substrate was treated with Sulfo-SANPAH solution (Thermo) for 5 minutes under ultraviolet light. Afterwards, substrates were washed initially with 10 mM HEPES solution in deionized water and then three times with sterile PBS. Then, the hydrogels were incubated with the type-I collagen solution (10  $\mu\text{g}/\text{ml}$ ) at 4°C for 12 hours<sup>212,213</sup>. After protein conjugation, dishes were washed three times with sterile PBS, and MEF 3T3 cells were seeded in the concentration that allowed the observation of single cells and incubated in a cell incubator for the next 12 hours. Cells were seeded in DMEM Low Glucose medium without Phenol Red dye (Bio West). After this procedure, cells were prepared for the ODMR-TFM experiment.

In each experiment, the local temperature was measured every 10 minutes. Each timepoint consisted of three separate measurements: transmitted light (here: DIC contrast) snapshot to locate the cell, time-lapse ODMR signal collection, and acquisition of Z-Stack images of TFM beads. For most of the experiment time, the microwave antenna was placed in the standby position about ~3 mm above the substrate and was approached to ~250 $\mu\text{m}$  distance only for the duration of ODMR signal collection. The Z-Stack (short series of images obtained in different focus positions) of TFM beads was performed due to the lack of focus stabilization in such a custom experiment. Collection of several slices allowed for choosing the proper focus of the TFM image for cellular tractions calculation.

The heating experiment started from a low temperature (28.4°C) which was kept for 7 consecutive time steps. Therefore, the temperature slowly increased, to reach ~1°C difference between each time step. After reaching ~37°C, the temperature was kept at the same level until



the end of the experiment. Heating was done by an on-stage mini-incubator, as well as a large incubation chamber, which both could be heated to the defined temperature. The cooling experiment started at 37°C which was kept for 7 consecutive time steps. However, neither incubator was equipped with cooling equipment. Therefore, in order to achieve the temperature decrease, the heating of both incubators was turned off and the refrigerated icepacks were placed inside the large incubation chamber. Therefore, the microscope environment and thus the observed sample were cooled down. Icepacks were added consecutively to decrease the temperature by  $\sim 1^\circ\text{C}$  every 10 minutes, and the cooling process was observed by the thermocouple readout. The final temperature of  $\sim 28^\circ\text{C}$  was kept until the end of the experiment. The constant-temperature experiment was performed at 37°C and the temperature of cell medium was measured by the thermocouple.

TFM data processing was performed using the software provided by Prof. Xavier Trepats from the Integrative Tissue and Cell Dynamics group, at the Institute for Bioengineering of Catalonia in Barcelona, Spain.

## **6. Results:**

### **6.1. Application of time-dependent observations and elastic polymer substrates to study cancer heterogeneity.**

Results presented in this chapter were collected in the framework of “Impact of Elastic Substrate on the Dynamic Heterogeneity of WC256 Walker Carcinosarcoma Cells”. – Mielnicka et al., 2023 which is already accepted for publication in Scientific Reports journal. I am an equal contribution author with Aleksandra Mielnicka and I have received her permission to use these results in the thesis. I was co-responsible for the experiment design, experimental work and data analysis.

#### **6.1.1. Heterogeneity of adherent subline of WC256 cell line.**

The phenomenon of cell heterogeneity is defined as the presence of cells of different characteristics within a single population. These differences can be related to any aspect of cell behavior and even the populations considered as homogenous can exhibit some level of variability under thorough examination <sup>219,220</sup>. Heterogeneity is especially evident in cancer cells and alters their response to treatment <sup>221-223</sup>. It plays an important role in tumor evolution, being influenced by the interactions of cancer cells with other neighboring cells, patient’s tissues, and applied chemotherapeutics. Up to now, the dynamics of cellular heterogeneity was investigated in a long timescale (days – months) that is necessary for gene mutation and selection of more preferred cell phenotypes <sup>219,224,225</sup>. However, the short time-scale evolution of heterogenous cancer cell lines was not considered until now.

Results presented in this chapter aim to fill this gap by investigating the short timescale (several hours) plasticity of an adherent subline of WC256 cells and combining it with the biomimetic elastic substrate to create the biologically relevant mechanical microenvironment. WC256 cells are the carcinosarcoma rat cells that primarily metastasize to bones, causing their resorption and hypercalcemia <sup>226-230</sup>. This is a model heterogeneous cell line that is composed of cells of different phenotypes and migration strategies. Previous works have already compared adherent and non-adherent sublimes of this cell line in the context of their heterogenous morphology and migration strategy <sup>211,231</sup>. This study analyzes the adherent subline of the WC256 cell line in the context of its dynamics in time, revealing short time-scale plasticity, as well as a modified cellular response on an elastic substrate.

### 6.1.2. Adherent subline of WC256 cells exhibits spontaneous subpopulational transitions.

The application of time-lapse measurements and classification based on cellular dynamics, lead to the modification of WC256 cell classification when comparing to the previous one <sup>211</sup>. As it was mentioned in Materials and Methods, the mesenchymal subpopulation consisted of cells that were properly spread and migrated in some defined direction by the mesenchymal movement or gliding motion. The previously known groups of bigonal and polygonal cells were merged into one type, since both exhibited nondirectional movement and their behavior consisted of stretching the cell body in different directions. The pseudopodal and blebbing cells have been merged into the same group, because of their unstable shape and distinctly faster and directional migration. There was also a small fraction of frames (<5% in total) which was not possible to clearly describe them with the introduced criteria. Cells in those frames were marked as the “unidentified” type. The exemplary time series of each of these groups are shown in Figure 10.

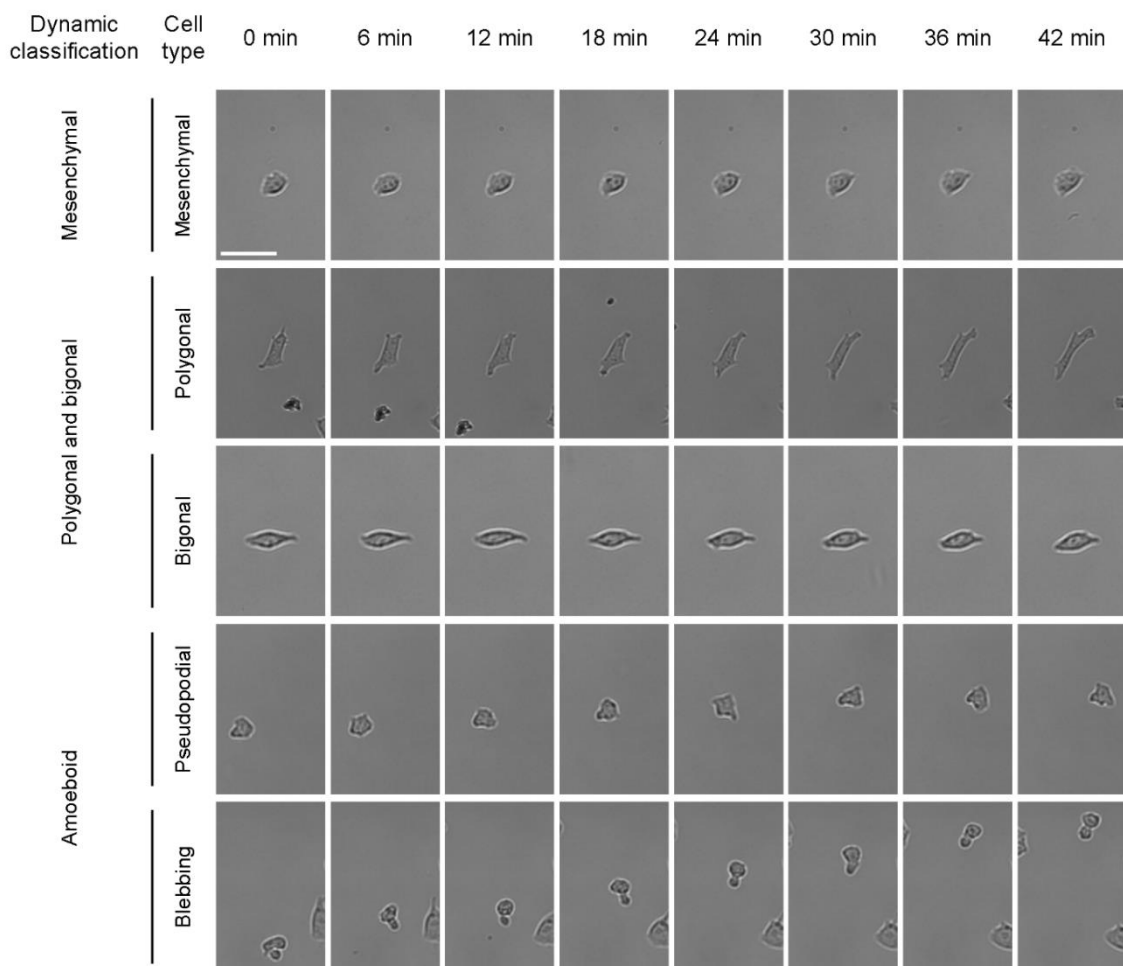
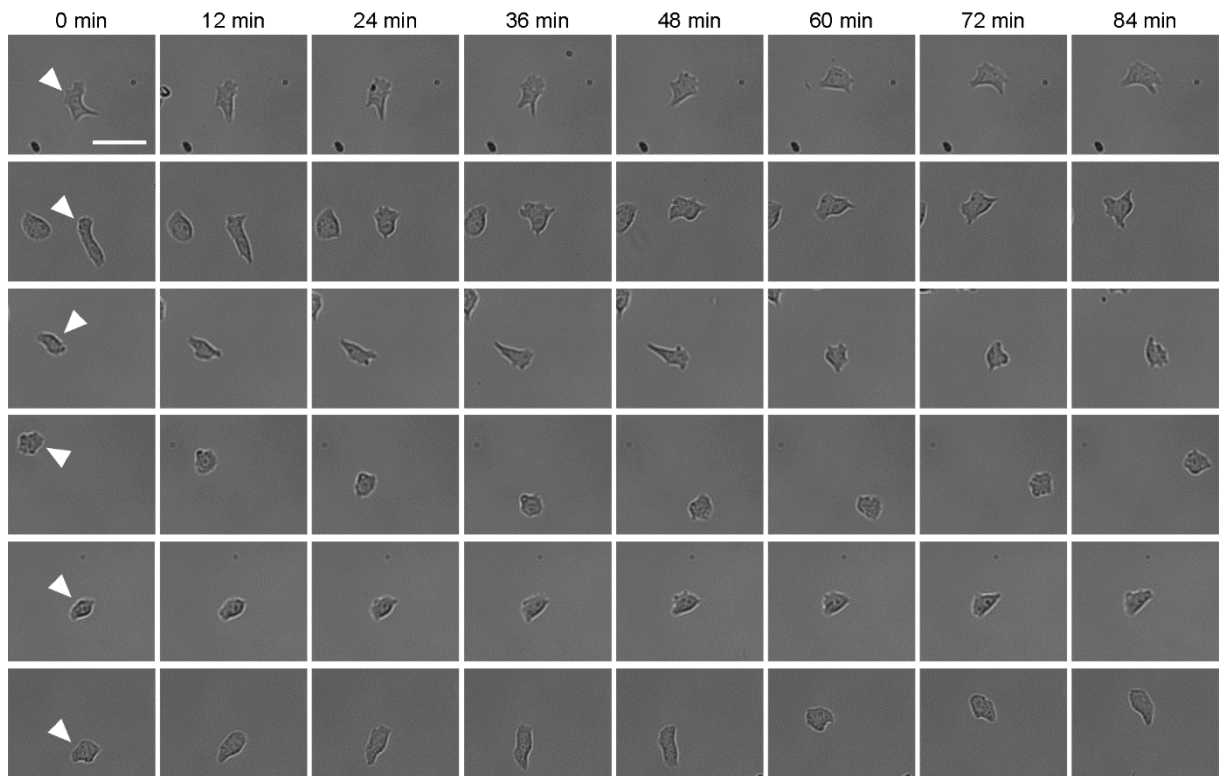


Figure 10. Different subpopulations of WC256 adherent subline: mesenchymal subpopulation, polygonal and bigonal subpopulation (polygonal and bigonal type of cells), amoeboid subpopulation (pseudopodal and blebbing types of cells). Scalebar = 50µm.

It was also observed that the mesenchymal subpopulation itself is highly diverse. It consisted of the cells that differed in the presence of retraction tail, type of protrusions, type of motion (mesenchymal/gliding motion), velocity, etc. However, all those cells met the criteria to account for the mesenchymal subpopulation. Even if the diversity of mesenchymal cells was not a subject of further quantification, it is important in my view to mention this finding for future researchers that could be interested in using WC256 cells as a model heterogeneous cancer cell line. Examples of different mesenchymal cells are shown in Figure 11.



*Figure 11. Variants of mesenchymal cells that were preliminarily identified in this study. Scalebar = 50 $\mu$ m.*

The main result that came from the application of time-lapse measurements (and thus the dynamic classification of subpopulations) was a discovery that a single WC256 cell can change its characteristics over time, by exhibiting properties of different subpopulations. What is even more significant, those changes occurred without any additional physical or chemical stimulation and therefore it was possible to observe the spontaneous transitions during the 4-hours observations. Those transitions could occur directly between subpopulations or through the “unidentified” intermediate state mentioned above. The simple transition between the mesenchymal and amoeboid subpopulations was also observed, however, it was treated rather as a rare exception what is addressed in the further text. These changes in cellular characteristics were called *subpopulational transitions*, the scheme of which is presented in Figure 12.

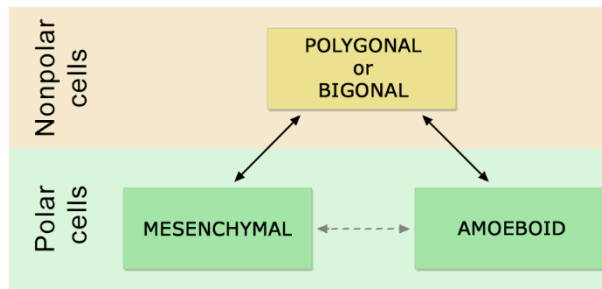


Figure 12. Subpopulational transitions registered for adherent subline of WC256 cells. The most common transitions between polar and nonpolar cells are marked with solid arrows. The direct transition between mesenchymal and amoeboid subpopulations (marked with dashed arrow) was observed rarely (3% of all observed cells).

Most common transitions were observed between mesenchymal and polygonal or bigonal subpopulations, as well as between amoeboid and polygonal and bigonal ones. Those transitions could be performed in both directions and occur several times for the cell. Figure 13 illustrates an exemplary transition between: A) mesenchymal and polygonal subpopulations, and B) amoeboid and polygonal subpopulations.

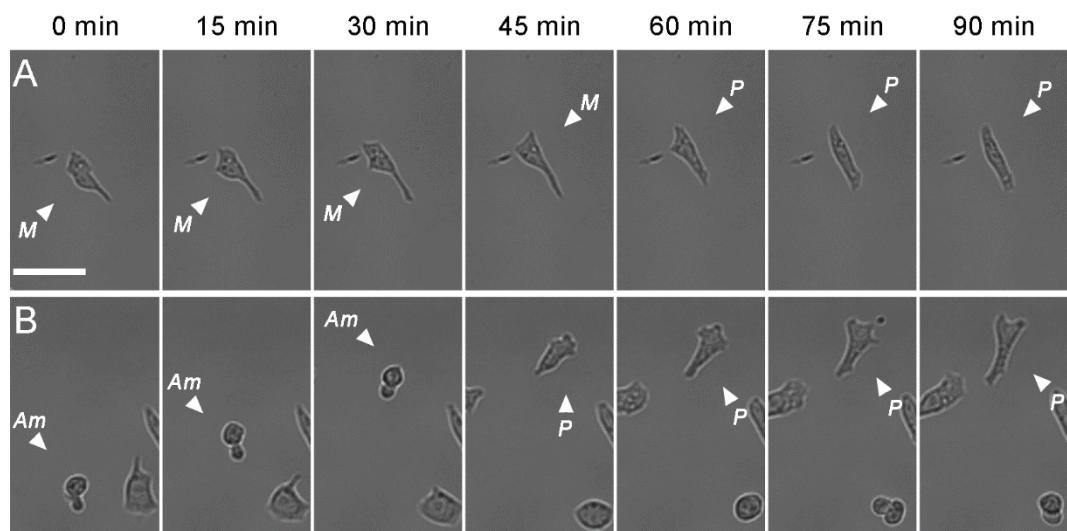


Figure 13. Exemplary subpopulational transitions. **A:** transition between mesenchymal (M) and polygonal (P) form. **B:** transition between amoeboid (Am) and polygonal (P) form. Scalebar = 50 $\mu$ m.

### **6.1.3. Elastic substrate affects the duration and frequency of subpopulational transitions.**

The 40 kPa elasticity of polyacrylamide substrate was chosen due to its biomimetic properties. Since a similar elasticity was found for the breast parenchymal tissue, it should reflect the original mechanical microenvironment of WC256 cell line. The first analyzed parameter was the duration of morphology i.e., for how long cells exhibited properties of certain subpopulations. This parameter was analyzed throughout the entire time of experiments (4 hours) and therefore, the 4 hours is the longest possible duration observed in this study.

Figure 14 shows that the duration of subpopulation differs between the two applied substrates. It is important to mention that one cell could belong to different subpopulations over time and several transitions could occur during the time of experiment. Therefore, the total number of cells in Figure 14 is higher than 50 for each experimental condition. Comparing both substrates, more cells from the glass substrate spent at least some time in the mesenchymal form (35 cells) than cells observed on the 40 kPa substrate (19 cells). The longest duration of the mesenchymal subpopulation (4 hours) was preferred for both substrates, however, the number of cells that belong there for the shortest time (< 1 hour) was higher for the elastic substrate than on glass (5 cells on PA vs 3 cells on glass). This is especially interesting in the context of a lower occurrence of mesenchymal state among the cells seeded on PA.

The number of cells that belonged to the polygonal and bigonal subpopulation is rather similar for both substrates: 29 cells on glass and 34 cells on the elastic substrate. The distribution of polygonal and bigonal subpopulation on PA substrate is rather even, with a slight dominance of the 3 - <4 hours duration (8 cells). On the other hand, the relatively short duration of polygonal and bigonal state (1 - <2 hours - 10 cells) was only slightly preferred by cells seeded on the glass substrate. The most striking difference between the substrates can be observed for the amoeboid subpopulation. On the 40 kPa PA substrate, the fragments of time-lapse sequence assigned to the amoeboid subpopulation occurred 3 times more, compared to the cells seeded on rigid glass (27 cells on 40 kPa vs 9 cells on glass substrate). The cells seeded on PA substrate were spending rather a short amount of time in the amoeboid form (10 cells spent there between 0 and <1 hour), however, the longer durations were also observed (between 3 and 5 cells for each observed duration). On the glass substrate, most of the amoeboid subpopulation lasted less than 1 hour or on the contrary, for the full 4 hours. The remaining durations were very low or were not present at all. However, due to the low number of amoeboid cells observed on glass, it is not possible to discriminate, whether the difference in their durations was caused by the applied substrate, or due to the difference between the overall occurrence of amoeboid subpopulation.

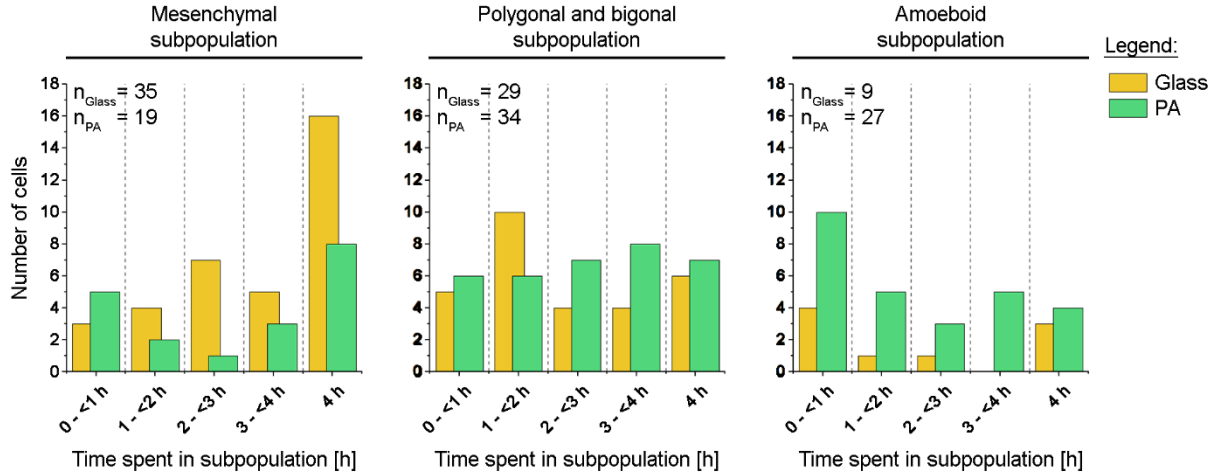


Figure 14. Histograms representing the duration of each subpopulation among cells seeded on rigid glass and elastic PA substrate. Adapted from <sup>148</sup>.

Further analysis was focused on the number of subpopulational transitions that were observed throughout the whole experiment (4 hours). This quantification was made for the two most common transitions presented in Figure 12 and Figure 13. As it can be seen in Figure 15, most of the cells seeded on glass transitioned between mesenchymal and polygonal or bigonal states. They mostly performed such transition once (6 cells) or twice (5 cells), while a higher number of transitions occurred less often (2 cells transitioning 3 times and 2 cells transitioning 4 times). In contrary, fewer cells seeded on 40 kPa substrates were transitioning between mesenchymal and polygonal and bigonal states, however, the lower number of transitions was also preferred (2 cells performing only one or two transitions).

The transitions between amoeboid and polygonal or bigonal cells were most commonly observed on an elastic substrate. In this case, the low number of transitions was also preferred (4 cells of 1 transition and 5 cells of 2 transitions), although the higher number of transitions were also present: 2 cells with three transitions, 3 cells with four transitions, 2 cells with five transitions and also 1 cell with six transitions. Again, it is not possible to determine whether the differences in transition number were caused by the substrate elasticity or occurred due to the differences in the number of cells between both substrates.

What is more, the “full transition” between mesenchymal and amoeboid subpopulation through the polygonal or bigonal intermediate state was also observed, however, its occurrence was very low: it was observed for 2 cells on glass and 2 cells on PA substrate. Also, the direct transition between mesenchymal and amoeboid subpopulation occurred, but was similarly rare to the full transition (2 cells on glass and 1 cell on PA substrate).

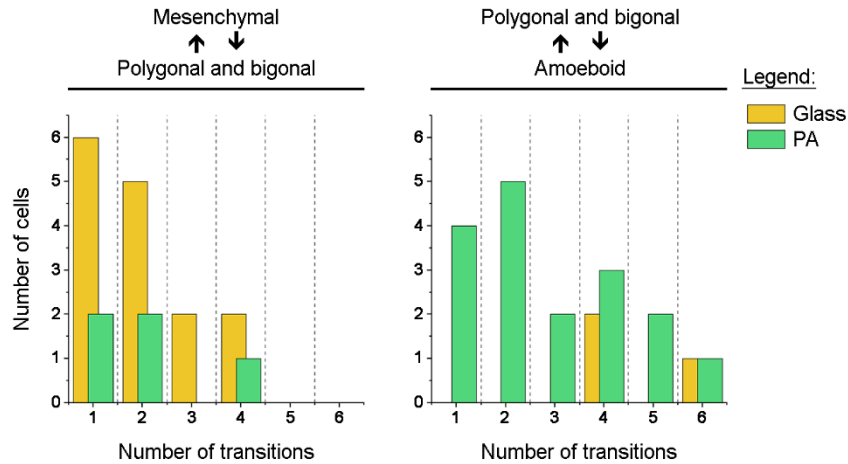


Figure 15. Histograms representing number of most common transitions observed among cells seeded on rigid glass and elastic PA substrate. Adapted from <sup>148</sup>.

#### 6.1.4. Elastic substrate modifies the occurrence of specific subpopulations.

To find the impact of the elastic substrate on the overall distribution of subpopulations, all frames that were assigned to each subpopulation during the experiment were summed and then divided by the total number of frames. As it was mentioned, there was a small portion of frames (<5% in total) that had an unidentified subpopulation. Figure 16 shows the subpopulation distribution observed for the elastic 40kPa PA and glass substrates. Among the cells seeded on a glass substrate, mesenchymal subpopulation was observed most commonly (55% percent of frames), while the same was observed for less than 25% of frames registered for 40 kPa substrate. On the contrary, polygonal and bigonal subpopulation was less common on glass (32% of frames) compared to the elastic substrate (44 % of frames). The significant difference can be also seen for the amoeboid subpopulation, where only 9% of frames were observed for a glass substrate, while 23% of frames were observed for 40kPa substrate. Therefore, it is clear that the type of a substrate has a clear impact on the distribution of the WC256 subpopulations.



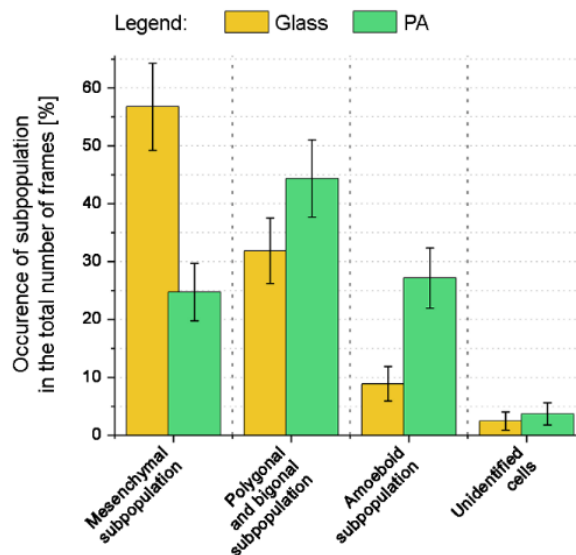


Figure 16. Occurrence of subpopulations observed among cells seeded on rigid glass and elastic PA substrate in the total number of registered frames. Error bars represent the square root of counts. Adapted from <sup>148</sup>.

However, this summative image does not provide a deeper insight into the dynamics of those subpopulations. A time evolution of subpopulations is presented in Figure 17, showing the clear differences between two applied substrates. For the glass substrate, one can see a slight decrease in a mesenchymal subpopulation, which coincides with an increase of the occurrence of a polygonal and bigonal subpopulation. This observation is consistent with the fact that the transitions between those two subpopulations were most commonly observed on this type of substrate, being quantitatively confirmed by the significant anticorrelation in time (Pearson's  $r = -0.8616^*$  and  $p < 0.0001$  as presented in Table 1). The occurrence of remaining subpopulations: amoeboid and unidentified cells remained low and stable during the observation time. A completely different picture can be seen among the cells seeded on the PA substrate. For the mesenchymal subpopulation, one can observe a slight initial increase and further slow decrease over time. Alternatively, the dynamics of polygonal and bigonal cells as well as amoeboid ones are much more interesting. The occurrence of polygonal and bigonal subpopulation rises between 50 and 130 minutes and then drops for a while, to recover shortly thereafter. The inversed trajectory can be observed for the amoeboid subpopulation. It starts from the intensive decrease of the occurrence, followed by the incidental increase (130-106 min), and further quasi-stable fluctuations at the end of the experiment. The interdependence of polygonal or bigonal and amoeboid subpopulation is confirmed by the significant anticorrelation calculated by the Pearson test (Pearson's  $r = -0.8274$ ,  $p < 0.0001$  as shown in Table 1). This is also in line with the high occurrence of transitions between amoeboid and polygonal and bigonal cells on PA substrate.

At this point, it is important to mention that in standard statistical practice, Pearson's test is calculated for two independent variables in order to find if they correlate with each other. However, in this case, the test is performed for samples that are dependent on each other due to the subpopulational transitions. Therefore, Pearson's  $r$  rather discriminates here, which subpopulations are correlated or anticorrelated in time and which ones do not exhibit such coupling. Presumably, the dependence of subpopulations is the cause of the very low  $p$ -values. Besides the already mentioned anticorrelations, Table 1 shows even more results that are statistically significant. For example, the correlation of mesenchymal and polygonal/bigonal cells on PA substrate is statistically significant, however, Pearson's  $r = -0.5151$ , describing a rather weak correlation. Another significant correlations might be also observed between amoeboid and two remaining subpopulations on glass, however, due to the low occurrence of amoeboid cells, this result should not be considered reliable.

Table 1. Results of Pearson's correlation tests for the time evolution of WC256 subpopulations. Adapted from<sup>148</sup>.

	Glass		PA	
	Mesenchymal	Polygonal and bigonal	Mesenchymal	Polygonal and bigonal
<b>Polygonal and bigonal</b>	-0.8616* ( $p < 0.0001$ )	---	-0.5151* ( $p < 0.0001$ )	---
<b>Amoeboid</b>	0.3330* ( $p < 0.0001$ )	-0.4538* ( $p < 0.0001$ )	0.12487 ( $p = 0.1145$ )	-0.8274* ( $p < 0.0001$ )

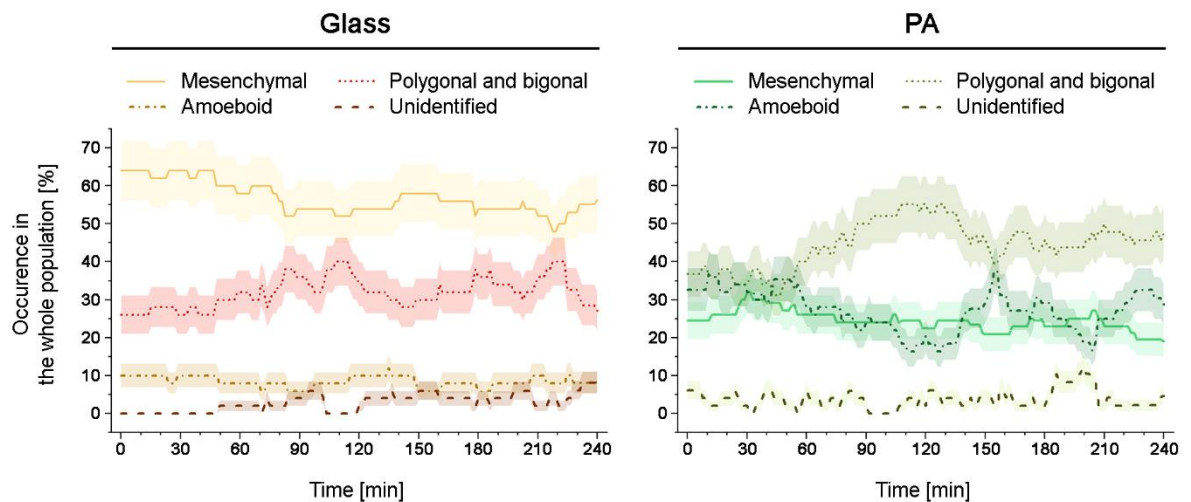


Figure 17. Time evolution of subpopulation occurrence along the experiment time. Error bars represent the square root of counts. Adapted from<sup>148</sup>.

### **6.1.5. Elastic substrate influences the biophysical parameters of cell migration and morphology of WC256 cells.**

Since the application of elastic substrate influenced the subpopulational transitions, occurrence of subpopulations, and subpopulational dynamics as well, the further logical step was to find if the elastic substrate influences the migratory behavior and morphology of cells. The examined biophysical properties of cell migration were as follows: a) instantaneous velocity (calculated between every two frames) and b) turning angles (calculated between each two consecutive displacement vectors, i.e., the three consecutive frames). The biophysical descriptors of cell morphology consisted of cell elongation, area and perimeter/area ratio (see: Materials and Methods). Despite the analysis of each subpopulation separately, all frames regardless of subpopulation were also pooled together to find if the behavior of the whole WC256 population reflects the behaviors of each subpopulation separately.

The very first general observation is that the velocity of amoeboid cells stands out of the other subpopulations (Figure 18 and Table 2), regardless of the substrate type. However, the 40kPa substrate has a significant impact on this subpopulation's velocity as well because even if the median values are affected only moderately (medians:  $v_{\text{AMOEBOID GLASS}} = 1.325 \mu\text{m}/\text{min}$  and  $v_{\text{AMOEBOID PA}} = 1.536 \mu\text{m}/\text{min}$ ), the difference between the 3<sup>rd</sup> quartile is definitely more evident:  $2.186 \mu\text{m}/\text{min}$  of the rigid glass substrate and  $2.717 \mu\text{m}/\text{min}$  on the elastic substrate. The impact of the elastic substrate on mesenchymal subpopulation velocity is quite low (medians:  $v_{\text{MESENCHYMAL GLASS}} = 0.614 \mu\text{m}/\text{min}$  and  $v_{\text{MESENCHYMAL PA}} = 0.518 \mu\text{m}/\text{min}$ ), although the statistical test shows the high significance of this difference. This might be caused by the very large size of the sample, where even very small differences influence the final result. Therefore, even if this difference is statistically significant, one should not consider its practical meaning in the context of cancer biology. The velocity of polygonal and bigonal cells was not affected at all, which was expected from the beginning of the study. This subpopulation does not exhibit directional movement, being rather stretched in multiple directions and performing Lévy flights from time to time. Another interesting observation is the significant difference in velocity calculated for the whole WC256 population. While the median value is affected again only a little (medians:  $v_{\text{ALL GLASS}} = 0.607 \mu\text{m}/\text{min}$  and  $v_{\text{ALL PA}} = 0.655 \mu\text{m}/\text{min}$ ), the 3<sup>rd</sup> quartile rose significantly on the elastic substrate ( $0.988 \mu\text{m}/\text{min}$  on glass compared to  $1.287 \mu\text{m}/\text{min}$  on 40 kPa substrate). It shows that the increase in the occurrence of amoeboid subpopulation paired with their higher velocity has a visible influence on the whole population's velocity.

Table 2. Statistical descriptors of cell velocity of each subpopulation of WC256 cells. Number of stars marks the statistically significant differences calculated by Mann-Whitney test (- stands for no difference, \* stands for  $p < 0.05$ , \*\* stands for  $p < 0.01$ , \*\*\* stands for  $p < 0.001$ ). Adapted from <sup>148</sup>.

Parameter	Subpopulation	Substrate	Median	Q1	Q3	IQR	Statistical difference
Velocity [ $\mu\text{m/s}$ ]	Mesenchymal	Glass	0,614	0,372	0,963	0,591	***
		PA	0,518	0,289	0,989	0,700	
	Polygonal and bigonal	Glass	0,509	0,311	0,795	0,484	-
		PA	0,507	0,306	0,797	0,492	
	Amoeboid	Glass	1,325	0,795	2,186	1,391	***
		PA	1,536	0,899	2,717	1,818	
	All subpopulations together	Glass	0,607	0,364	0,988	0,624	***
		PA	0,655	0,365	1,287	0,922	

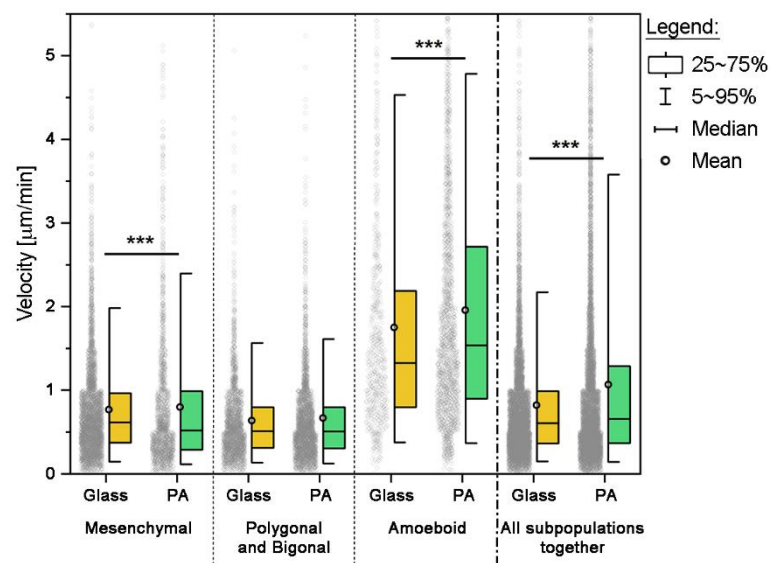


Figure 18. Box plots and data distribution of WC256 cells velocities. Number of stars marks the statistically significant differences calculated by Mann-Whitney test (- stands for no difference, \* stands for  $p < 0.05$ , \*\* stands for  $p < 0.01$ , \*\*\* stands for  $p < 0.001$ ). Adapted from <sup>148</sup>.

The second parameter describing the migratory behavior of cells is the distribution of turning angles (Figure 19, Table 3). The widest distribution was observed for polygonal and bigonal cells ( $> 160$  deg) which were not affected by the application of elastic substrate. Similarly, as in the velocity distribution, this effect was expected due to the chaotic movement of those cells. Furthermore, the mesenchymal cells show narrower distribution of turning angles ( $> 100$  deg) than polygonal and bigonal cells, but there was no significant difference between the substrates as well. It means that the application of elastic substrate does not change whether mesenchymal cells migrate in more or less directionally.

The only significant influence of substrate elasticity among the three subpopulations is visible for the amoeboid cells. The IQRs of the turning angles registered on the glass substrate were 70.9 deg and 46.2 deg on the elastic substrate. It shows that amoeboid cells seeded on elastic

substrate migrate significantly straighter than on rigid glass substrate. Another statistically significant difference can be seen for the whole WC256 population; however, it might be caused again by an increased occurrence of amoeboid subpopulation on an elastic substrate.

Table 3. Statistical descriptors of turning angles of each subpopulation of WC256 cells. Number of stars marks the statistically significant differences calculated by Mann-Whitney test (- stands for no difference, \* stands for  $p < 0.05$ , \*\* stands for  $p < 0.01$ , \*\*\* stands for  $p < 0.001$ ). Adapted from <sup>148</sup>.

Parameter	Subpopulation	Substrate	Median	Q1	Q3	IQR	Statistical difference
Turning angles [deg]	Mesenchymal	Glass	-15,4	-75,7	28,6	104,2	-
		PA	-11,8	-68,9	34,4	103,3	-
	Polygonal and bigonal	Glass	-37,9	-126,1	39,8	166,0	-
		PA	-28,2	-121,3	41,2	162,5	-
	Amoeboid	Glass	-10,4	-49,1	21,7	70,9	**
		PA	-5,3	-29,6	16,6	46,2	**
	All subpopulations together	Glass	-18,6	-91,2	30,2	121,4	**
		PA	-15,4	-75,7	28,6	104,2	**

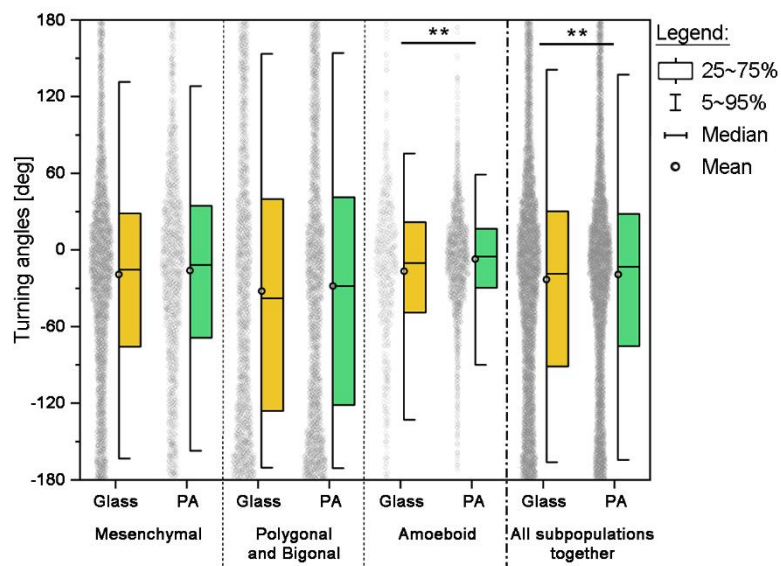


Figure 19. Box plots and data distribution of WC256 cells turning angles. Number of stars marks the statistically significant differences calculated by Mann-Whitney test (- stands for no difference, \* stands for  $p < 0.05$ , \*\* stands for  $p < 0.01$ , \*\*\* stands for  $p < 0.001$ ). Adapted from <sup>148</sup>.

In Figure 20 and Table 4 we can see how the subpopulations of WC256 cells differ from each other in the context of their geometry. It is worth reminding that the elongation parameter calculated here signifies an ideally rounded shape if  $\epsilon = 0$  and the infinitely elongated ellipse for  $\epsilon = 1$ . The mesenchymal and amoeboid cells observed on glass are similarly elongated, however, they are affected by the substrate elasticity in opposite ways. The application of elastic substrate caused the significant rounding of the mesenchymal subpopulation (medians:  $\epsilon_{\text{MESENCHYMAL GLASS}} = 0.365$  and  $\epsilon_{\text{MESENCHYMAL PA}} = 0.267$ ) while for the amoeboid cells we can

observe their slight elongation (medians:  $\epsilon_{\text{AMOEBOID GLASS}} = 0.357$  and  $\epsilon_{\text{AMOEBOID PA}} = 0.385$ ). Polygonal and bigonal cells are remarkably more elongated than the remaining subpopulations and one can spot a slight rounding of this subpopulation on an elastic substrate. The statistical significance of polygonal and bigonal as well as amoeboid cells might be caused again by the large size of the sample and these differences seem to not be significant in the context of cancer biology. A similar situation can be seen for the elongation of the whole population of WC256 cells, for which the statistical difference should not be treated as relevant. On the other hand, it is clearly visible that the elongation distribution of the whole WC256 population poorly reflects the complexity of the subpopulations which underlines the need of analyzing the subpopulations separately from each other.

Table 4. Statistical descriptors of cell elongation of each subpopulation of WC256 cells. Number of stars marks the statistically significant differences calculated by Mann-Whitney test (- stands for no difference, \* stands for  $p < 0.05$ , \*\* stands for  $p < 0.01$ , \*\*\* stands for  $p < 0.001$ ). Adapted from <sup>148</sup>.

Parameter	Subpopulation	Substrate	Median	Q1	Q3	IQR	Statistical difference
Elongation [ normalized ]	Mesenchymal	Glass	0,365	0,258	0,493	0,235	***
		PA	0,267	0,169	0,359	0,190	
	Polygonal and bigonal	Glass	0,615	0,484	0,700	0,216	***
		PA	0,580	0,445	0,681	0,236	
	Amoeboid	Glass	0,357	0,245	0,462	0,217	***
		PA	0,385	0,287	0,480	0,193	
	All subpopulations together	Glass	0,436	0,302	0,601	0,299	***
		PA	0,427	0,288	0,585	0,297	

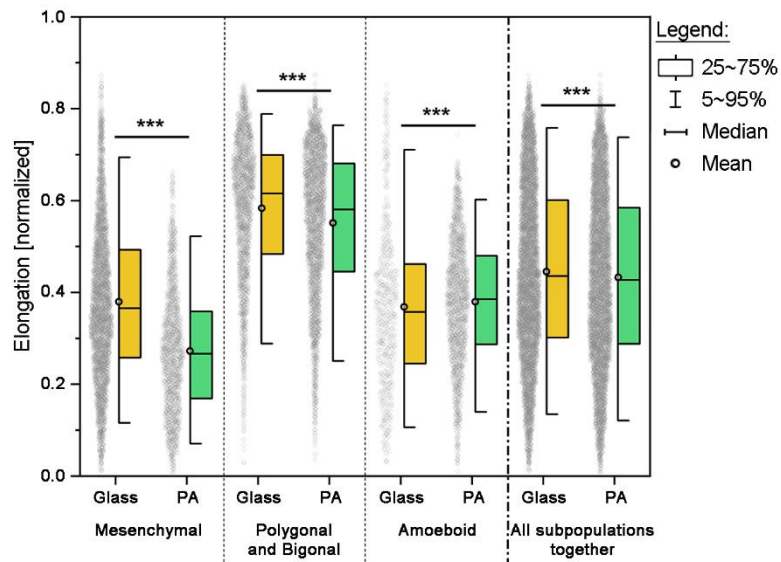


Figure 20. Box plots and data distribution of WC256 cell elongations. Number of stars marks the statistically significant differences calculated by Mann-Whitney test (- stands for no difference, \* stands for  $p < 0.05$ , \*\* stands for  $p < 0.01$ , \*\*\* stands for  $p < 0.001$ ). Adapted from <sup>148</sup>.

While analyzing the cell area, it is important to mention that the analyzed parameter comes from the image of the cell projected onto the 2D plane (projected cell area). Thus, we quantify here the 2D projection of a cell that in fact has a 3D structure. The description of the measured cell area is presented in Figure 21 and Table 5. The areas of mesenchymal as well as polygonal and bigonal cells observed on glass are similar to each other. However, the elastic substrate influences the mesenchymal subpopulation more evidently (medians:  $A_{\text{MESENCHYMAL GLASS}} = 478.9\mu\text{m}^2$  vs.  $A_{\text{MESENCHYMAL PA}} = 338.3\mu\text{m}^2$ ), but the polygonal and bigonal subpopulation decreased its area on the PA substrate as well (medians:  $A_{\text{POLYGONAL AND BIGONAL GLASS}} = 478.9\mu\text{m}^2$  vs.  $A_{\text{POLYGONAL AND BIGONAL PA}} = 338.3\mu\text{m}^2$ ). Compared to the other subpopulations, the amoeboid cells have much smaller area on glass (compared to other subpopulations), but even though their areas decreased on the elastic substrate (medians:  $A_{\text{AMOEBOID GLASS}} = 321.4\mu\text{m}^2$  vs  $A_{\text{AMOEBOID}} = 252.8\mu\text{m}^2$ ). The overall decrease of cell area calculated for the whole population of WC256 cells also reflects the change among subpopulations, since the influence of the elastic substrate is quite similar in the context of cellular area for each subpopulation separately.

*Table 5. Statistical descriptors of cell area of each subpopulation of WC256 cells. Number of stars marks the statistically significant differences calculated by Mann-Whitney test (- stands for no difference, \* stands for  $p < 0.05$ , \*\* stands for  $p < 0.01$ , \*\*\* stands for  $p < 0.001$ ). Adapted from <sup>148</sup>.*

Parameter	Subpopulation	Substrate	Median	Q1	Q3	IQR	Statistical difference
Area [ $\mu\text{m}^2$ ]	Mesenchymal	Glass	478,9	401,5	566,0	164,5	***
		PA	338,3	274,6	381,1	106,5	
	Polygonal and bigonal	Glass	503,9	448,9	568,2	119,3	***
		PA	399,3	323,1	466,3	143,3	
	Amoeboid	Glass	321,4	290,9	399,3	108,4	***
		PA	252,8	226,1	284,9	58,8	
	All subpopulations together	Glass	478,3	401,0	558,4	157,4	***
		PA	326,3	259,9	414,0	154,2	

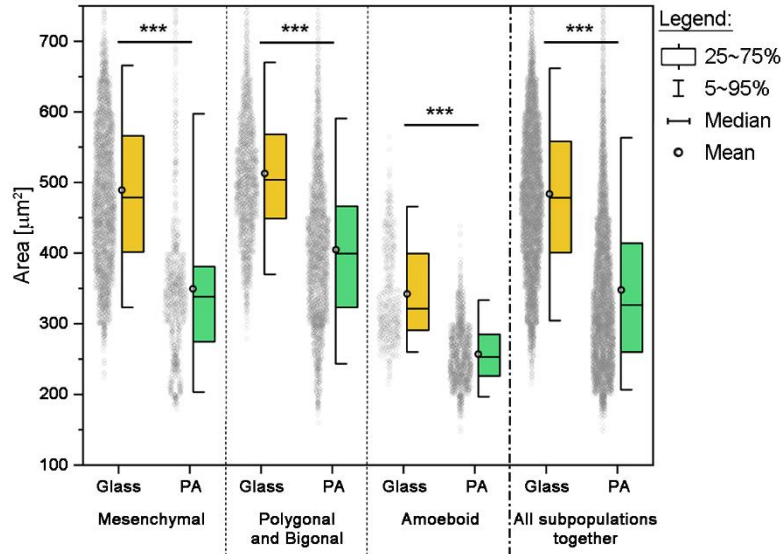


Figure 21. Box plots and data distribution of WC256 cell areas. Number of stars marks the statistically significant differences calculated by Mann-Whitney test (- stands for no difference, \* stands for  $p < 0.05$ , \*\* stands for  $p < 0.01$ , \*\*\* stands for  $p < 0.001$ ). Adapted from <sup>148</sup>.

The last biophysical parameter used for the analysis of cell shape was the ratio of the cell perimeter to its area (Table 6 and Figure 22). Again, it is important to mention that those parameters are calculated for the cell area that is projected onto the 2D plane. Each of the examined subpopulations has a different perimeter/area ratio. However, the influence of the PA substrate is rather similar on each subpopulation, causing this ratio to grow compared to the cells seeded on the rigid glass. The highest increase can be seen for the amoeboid subpopulation (medians:  $P/A_{\text{AMOEBOID GLASS}} = 1.163 \text{ 1}/\mu\text{m}$  vs  $P/A_{\text{AMOEBOID PA}} = 1.180 \text{ 1}/\mu\text{m}$ ). A lower increase of this parameter can be seen for the remaining subpopulations.

What is interesting, the highest increase is observed for the whole population of the WC256 cells (medians:  $P/A_{\text{WC256 GLASS}} = 0.150 \text{ 1}/\mu\text{m}$  vs  $P/A_{\text{WC256 PA}} = 0.169 \text{ 1}/\mu\text{m}$ ). This highest difference is probably caused by the higher occurrence of amoeboid subpopulation among cells seeded on glass. This difference however does not reflect the behaviors of separate subpopulations which again highlights the need for the individual analysis of subpopulations.



Table 6. Statistical descriptors of cell Parameter/Area ratios of each subpopulation of WC256 cells. Number of stars marks the statistically significant differences calculated by Mann-Whitney test (- stands for no difference, \* stands for  $p < 0.05$ , \*\* stands for  $p < 0.01$ , \*\*\* stands for  $p < 0.001$ ). Adapted from <sup>148</sup>.

Parameter	Subpopulation	Substrate	Median	Q1	Q3	IQR	Statistical difference
Perimeter / Area [1 / $\mu\text{m}^2$ ]	Mesenchymal	Glass	0,142	0,134	0,153	0,019	***
		PA	0,149	0,141	0,162	0,021	
	Polygonal and bigonal	Glass	0,158	0,148	0,170	0,022	***
		PA	0,168	0,157	0,183	0,026	
	Amoeboid	Glass	0,163	0,157	0,171	0,014	***
		PA	0,180	0,169	0,191	0,022	
	All subpopulations together	Glass	0,150	0,138	0,162	0,024	***
		PA	0,169	0,155	0,184	0,029	

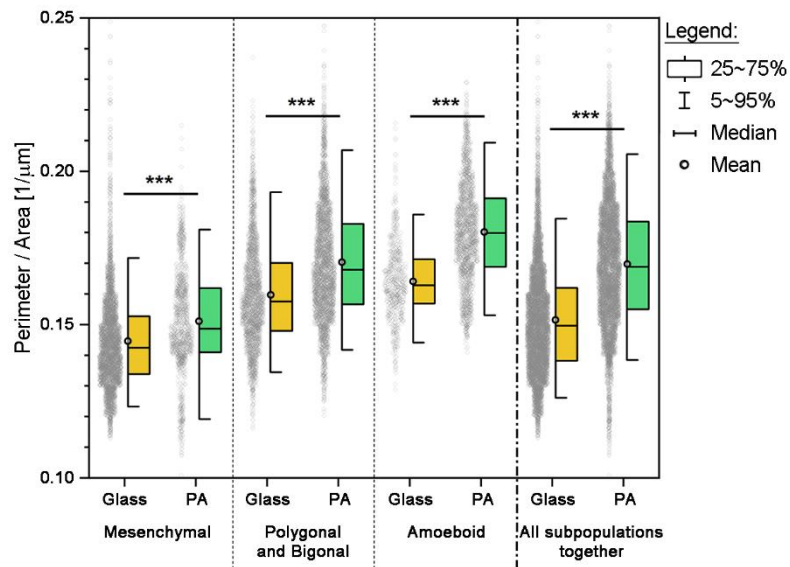


Figure 22. Box plots and data distribution of WC256 cell perimeter/area ratio. Number of stars marks the statistically significant differences calculated by Mann-Whitney test (- stands for no difference, \* stands for  $p < 0.05$ , \*\* stands for  $p < 0.01$ , \*\*\* stands for  $p < 0.001$ ). Adapted from <sup>148</sup>.

### 6.1.6. Summary of WC256 cell heterogeneity investigation.

The aforementioned results show the newly described phenomenon of dynamic subpopulational heterogeneity of adherent subline of WC256 cells. It consisted of the spontaneous (non-induced) modification of cell shape and migratory behavior. This discovery was enabled by the application of time-lapse microscopy and dynamic classification of cell subpopulation, which to my best knowledge, were not utilized in the studies of cancer heterogeneity before this study. What is more, the application of more relevant elastic substrate changed the image of the WC256 subpopulations. It is an important observation for the cancer heterogeneity studies, especially in the context of chemotherapeutics research.


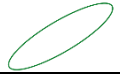



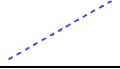

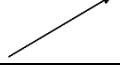




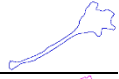


## 6.2. Development of new analytical description for coupling cell migration and morphology.

After reading Chapter 6.1, it is evident that the time-lapse measurements and subsequent dynamic classification of cellular processes can lead to a deeper understanding of cellular behavior. In the analyzed case of WC256 cells, different subpopulations were distinguished by the experimenter who performed the classification procedure by comparing 2 preceding and 2 following frames from the currently evaluated frame and assigned the cellular behavior according to the criteria defined in Materials and Methods. Such a procedure was sufficient in the study mentioned; however, it suffered from some drawbacks as well. The first drawback is that such a method of analysis consumes a great amount of time. Therefore, there might be a practical problem with its wider implementation, especially for the samples consisting of very large datasets. Another drawback is that the description of cells is based on the archetypical understanding of how different cells look like, which was used to construct the behavioral criteria. This is definitely not a problem for the experienced researchers who have already analyzed different types of cells. However, the people who have not been involved in the analysis of migrating cells before, have to be instructed by the more advanced researchers, just as it was done in this study.

The behavioral criteria of WC256 cell classification consisted of the assessment of cellular migration and morphology in a qualitative way. This qualitative approach was employed, since up to now, there was a clear lack of simple quantitative descriptors that combine migration direction and cell shape. On the contrary, those processes were treated separately from one another, even if the type of migration is a consequence of the dynamics of cellular shape and both of them are dependent on various intercellular and extracellular factors<sup>97,232,233</sup>. In this chapter, I introduce the novel concept where cell migration and morphology are treated as a single phenomenon, which I called the *morphomigrational behavior*. For its description, I have constructed two new quantitative parameters (i.e., signed morphomigrational angle and major axis dynamics) and compared them with two already existing descriptors (i.e. turning angle and shape elongation) to build the morphomigrational description – the analytical tool that can be used to quantitatively assess the dynamic cellular behaviors.

To properly illustrate all geometrical parameters in Figures Figure 23–Figure 39 each specific parameter is represented by the same graphic item, as shown in the visual legend presented in Table 7.

Table 7. Components of morphomigrational description with their abbreviations and graphical symbols. Adapted from <sup>234</sup>.

Component of description	Abbreviation or symbol	Graphical symbol	Component of description	Abbreviation or symbol	Graphical symbol
Signed morphomigrational angle	sMM / sMM angle		Ellipse fitted to current frame $n$	-	
Unsigned morphomigrational angle	uMM / uMM angle		Major Axis of ellipse fitted to current mask $n$	-	
Turning angle	$\alpha$		Major Axis of ellipse fitted to following mask $n+1$	-	
Major Axis dynamics	$\Delta\varphi$		Current direction of displacement ( $n \rightarrow n+1$ )	-	
Major Axis (general meaning)	M.A.	-	Preceding direction of displacement ( $n-1 \rightarrow n$ )	-	
Elongation	$\epsilon$	-	Centroid in current frame $n$	-	
Mask in current frame $n$	-		Centroid in following frame $n+1$	-	
Mask in following frame $n+1$	-		Centroid in preceding frame $n-1$	-	
Mask in preceding frame $n-1$	-				

Results presented in this chapter are published in the work entitled “Morphomigrational description as a new approach connecting cell’s migration with its morphology” – Kołodziej et al., 2023, that is already accepted for publication in Scientific Reports journal (Springer Nature). In that work I proposed and developed the idea of morphomigrational description, performed the main part of experimental work, analysis, and interpretation of experimental data.

### 6.2.1. Introducing the idea of unsigned morphomigrational angle (uMM), signed morphomigrational angle (sMM), and major axis dynamics (M.A. dynamics) – examples and rationale.

The first step of building a morphomigrational description was the introduction of an *unsigned morphomigrational angle* (uMM or uMM angle). The uMM is the angle between the major axis (M.A.) of the ellipse fitted to the binary mask of cell shape in current ( $n$ ) frame, and the displacement vector between centroids in current ( $n$ ) and following ( $n+1$ ) frame, as shown in Figure 23. To keep the further description clearer, the shorter phrase “major axis of shape” instead of “major axis of an ellipse fitted to the binary mask of the shape” is used in the further text.

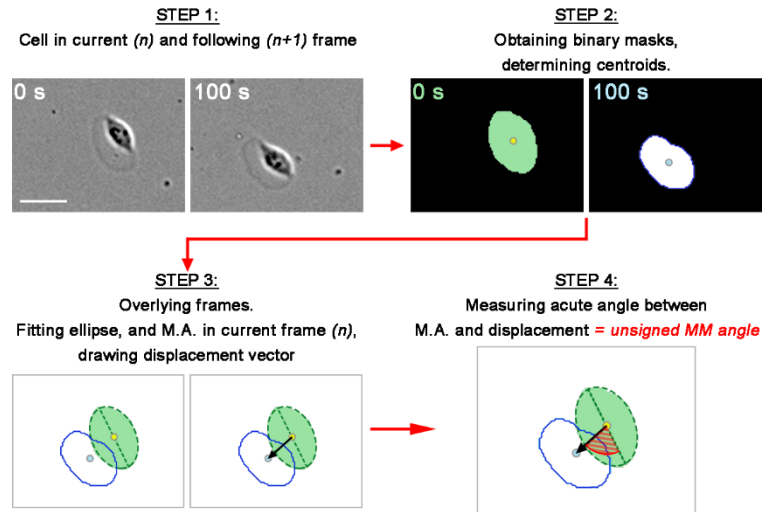


Figure 23. Procedure of calculation of unsigned morphomigrational angle (uMM angle). Scalebar =  $20\mu\text{m}$ . Adapted from <sup>234</sup>.

The uMM angle is designed to be an acute angle, thus it can have a value between  $0^\circ$  and  $90^\circ$ . However, it does not differentiate whether the displacement vector points more to the right or left side of the M.A., which is shown in Figure 24 Both rows represent the very same keratinocyte observed at different timepoints. In each row, the left image shows the current frame, the middle image shows the following frame, and the right image depicts the uMM angle constructed using these two frames. In the top row, the displacement vector points more to the right side of M.A. On the contrary, the displacement vector in the bottom row points to the left side of M.A. However, the uMM values for these two cases are almost the same:  $71^\circ$  and  $70^\circ$ , respectively. Therefore, it is clear that uMM angle does not carry the information about the turning direction but links the spatial arrangement of the cell on a 2D plane with the displacement direction. This clear example presents how the uMM angle differs from the turning angle that is calculated between two consecutive displacement vectors.

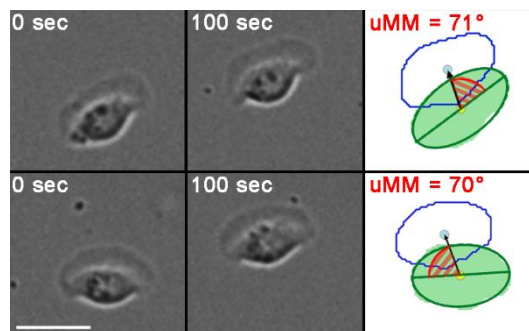


Figure 24. Unsigned morphomigrational angle calculated for two different migration moments of the same keratinocyte. Values of uMM angle are almost the same, even if in the top row uMM angle is constructed on the right side of the displacement vector and in the bottom row on the left side of the displacement vector. Scalebar =  $20\mu\text{m}$ . Adapted from <sup>234</sup>.

However, looking at Figure 24 it is easy to imagine four significantly different situations which would result in the same value of uMM angle: when the displacement vector points to the left and right side above the M.A. and two similar cases where displacement vectors are below the M.A. All of those four cases would represent different morphomigrational behaviors while being described by the same quantitative value. To overcome this ambiguity the unsigned morphomigrational angle was developed into the signed morphomigrational angle (sMM).

The positive sign of sMM is assigned while the angle is constructed on the same side of M.A. as in the first frame and the negative sign when the sMM is constructed on the other side of M.A. The idea of sMM angle is shown in Figure 25 where in the second and third frames sMM has a negative sign because the displacement vector pointed to the other side of M.A. than in the 1<sup>st</sup> frame.

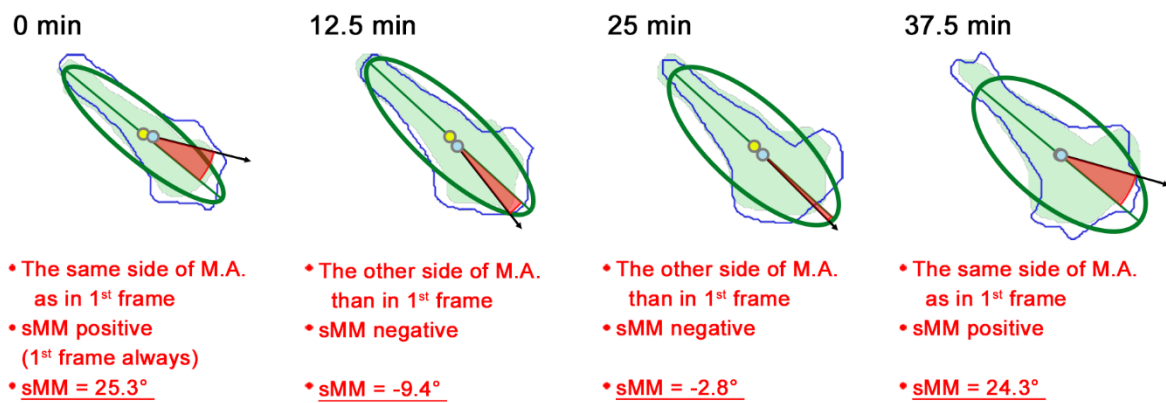


Figure 25. Idea of sMM angle presented for MEF 3T3 cell. The sMM angle is positive in the first frame (as always) and negative if the sMM angle is constructed on another side of M.A. Adapted from <sup>234</sup>.

Such concept of sMM angle requires tracing the arrangement of M.A. along the whole time sequence, which is shown in Figure 26 and Figure 27. The procedure starts from calculating uMM angle from two consecutive time frames (steps 1-4). Then, it is followed by the image rotation to the horizontal position of M.A. This rotation is performed around one of the ends of the major axis. After this procedure, the displacement vector always points above or below the rotated major axis. The value of sMM angle is always positive in the first frame and the location of the displacement vector determines the sMM sign in further frames. Therefore, if the displacement vector in the first frame points upwards, the other frame in which the displacement vector points upwards will have a positive sign as well, while frames in which the displacement vector points downwards will be marked by a negative sign. Alternatively, if the displacement vector in the first frame points downwards, all similar frames will be marked with a positive sign, while frames with displacement vector pointing upwards will result

in negative sMM. Therefore, the signed morphomigrational angle can have a value between  $-90^\circ$  and  $90^\circ$ . For the case of displacement vector lying on the M.A., the  $sMM = 0^\circ$ .

Another important subject of the procedure is the rotation of the image. To keep the procedure consistent, the image in the first frame is rotated always clockwise, and always around the lower end of M.A. In the remaining frames, the rotation angle  $\varphi$  is calculated to minimize its value between consecutive frames. In the first frame in Figure 26, the image is rotated clockwise around the lower end of M.A. Therefore, the displacement vector after rotation points upwards which sets the positive sign in this image sequence. Also, in the next frame, the image is rotated around the lower end of M.A. which results in a positive sign of sMM as well. However, it changes in the third and fourth frames where the image is rotated anti-clockwise around the upper end of M.A., which again results in the positive sign of sMM. Positive signs in all frames in Figure 26 are the proper results of calculations because the displacement vector did not change the side of M.A. Therefore, it demonstrates that the procedure of assigning the sMM sign works properly, even if the first and second images are rotated clockwise, while the third and fourth images are rotated anti-clockwise.

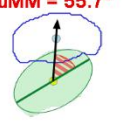
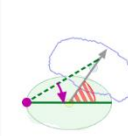
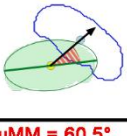
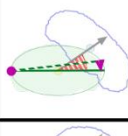
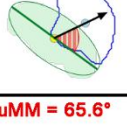
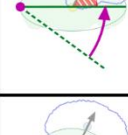
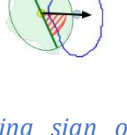

STEP 1: Cell in current ( $n$ ) and following ( $n+1$ ) frame		STEP 2 - 4: Masks overlay, uMM angle calculation	STEP 5: Image rotation for horizontal M.A. alignment	STEP 6: Final decision of sMM angle sign
0 s	100 s	uMM = $55.7^\circ$ 		$\varphi = 30.8^\circ$ (clockwise, 1 <sup>st</sup> frame) M.A. rotation: about lower end (1 <sup>st</sup> frame) uMM location: above M.A. sMM sign: positive (1 <sup>st</sup> frame) sMM = $55.7^\circ$
100 s	200 s	uMM = $34.7^\circ$ 		$\varphi = 6.2^\circ$ (clockwise) M.A. rotation: about lower end uMM location: above M.A. sMM sign: positive sMM = $34.7^\circ$
200 s	300 s	uMM = $60.5^\circ$ 		$\varphi = -36.2^\circ$ (anti-clockwise) M.A. rotation: about higher end uMM location: above M.A. sMM sign: positive sMM = $60.5^\circ$
300 s	400 s	uMM = $65.6^\circ$ 		$\varphi = -65.9^\circ$ (anti-clockwise) M.A. rotation: about higher end uMM location: above M.A. sMM sign: positive sMM = $65.6^\circ$

Figure 26. The algorithm of calculating sign of sMM angle presented for migrating keratinocyte. Scalebar =  $20\mu\text{m}$ . Adapted from <sup>234</sup>.

Figure 27 shows the sMM calculation algorithm in the case of the changing sign of sMM. As mentioned previously, the image in the first frame is rotated clockwise around the lower end of M.A. In this case, the displacement vector points downwards after the rotation procedure. Its position determines that the remaining frames with the similar arrangement will have a positive sMM sign, while the frames with displacement vector pointing upwards have to be assigned with a negative value of sMM. The latter situation is presented in the third frame (40-60 minutes) when the displacement vector after image rotation points upwards, which resulted in the negative sign of sMM angle. It shows that regardless of the initial arrangement of the rotated displacement vector: upwards or downwards of the image, the first frame has always a positive sign of sMM, and the sign in the remaining frames is calculated relating to the first frame.

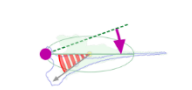
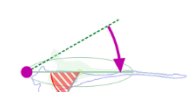
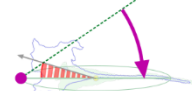

STEP 1: Cell in current ( $n$ ) and following ( $n+1$ ) frame		STEP 2 - 4: Masks overlay, uMM angle calculation	STEP 5: Image rotation for horizontal M.A.	STEP 6: Final decision of sMM angle sign
0 min	20 min	uMM = 37.2°		$\varphi = 19.8^\circ$ (clockwise, 1 <sup>st</sup> frame) M.A. rotation: about lower end (1 <sup>st</sup> frame) uMM location: below M.A. sMM sign: positive (1 <sup>st</sup> frame) sMM = 37.2°
20 min	40 min	uMM = 60.3°		$\varphi = 29.7^\circ$ (clockwise) M.A. rotation: about lower end uMM location: below M.A. sMM sign: positive sMM = 60.3°
40 min	60 min	uMM = 16.9°		$\varphi = 34.2^\circ$ (clockwise) M.A. rotation: about lower end uMM location: above M.A. sMM sign: negative sMM = -16.9°
60 min	80 min	uMM = 3.4°		$\varphi = 27.7^\circ$ (clockwise) M.A. rotation: about lower end uMM location: below M.A. sMM sign: positive sMM = 3.4°

Figure 27. The algorithm of calculating the sign of sMM angle presented for migrating MEF 3T3 cell. Scalebar = 20 $\mu$ m. Adapted from <sup>234</sup>.

Besides the sMM angle, it is useful to introduce one more dynamic parameter. It is the dynamics of major axis ( $\Delta\varphi$ ) that shows how much the major axis rotates between the current and the following frame. The high M.A. dynamics represents the rapid changes of shape arrangement, or the rounded shape, while M.A. remains low for the shape that is stable along the image sequence. The application of M.A. dynamics as well as the limitation of sMM angle is discussed in further text.

### 6.2.2. Building blocks of morphomigrational description.

The sMM angle is a novel quantitative descriptor that unifies the cellular arrangement with migration direction. However, this parameter alone is not sufficient to describe such complex objects as living cells. Therefore, we have constructed the morphomigrational description that is based on four quantitative parameters that describe different aspects of cellular behaviors, calling them the “building blocks”. Two of them: sMM angle (sMM) and M.A. dynamics ( $\Delta\phi$ ) were introduced in the previous section. The remaining two quantitative parameters: turning angle ( $\alpha$ ) and elongation ( $\epsilon$ ) already exist in the literature and were used in the analysis of WC256 cells in the previous chapter. This section explains the reasons behind coupling those four parameters in morphomigrational description, showing how they complement each other in the quantitative image of cellular behavior.

The process of creation of morphomigrational description started with the visual assessment of cellular behaviors and manual analysis of building blocks. However, while numbers are well understood by computers, they still might not be very intuitive for human minds. Therefore, in this work, we have bound the quantitative values with the coarse-grain descriptions (very low, low, moderate, high, very high) to better understand the morphomigrational description of cells. Those coarse-grain descriptors are presented in Table 8.

*Table 8. The coarse-grain description of building blocks of morphomigrational descriptions used in this work. Adapted from <sup>234</sup>.*

Parameter	Values		Coarse-grain description	Parameter	Values		Coarse-grain description
	from	to			from	to	
sMM angle (sMM)	-15° ≤	≤ 15°	sMM very low	M.A. dynamics ( $\Delta\phi$ )	-10° ≤	≤ 10°	$\Delta\phi$ very low
	-45° ≤	< -15°	sMM low		-20° ≤	< -10°	$\Delta\phi$ low
	15° <	≤ 45°			10° <	≤ 20°	
	-70° ≤	< -45°	sMM moderate		-45° ≤	< -20°	$\Delta\phi$ moderate
	45° <	≤ 70°			20° <	≤ 45°	
	-90° ≤	< -70°	sMM high		-60° ≤	< -45°	$\Delta\phi$ high
	70° <	≤ 90°			45° <	≤ 60°	
Turning angle ( $\alpha$ )	-60° ≤	≤ 60°	$\alpha$ low	-90° ≤	< -60°	$\Delta\phi$ very high	
	-90° ≤	< -60°	$\alpha$ moderate	60° <	≤ 90°		
	60° <	≤ 90°		$\alpha$ high	0 ≤	≤ 0.1	$\epsilon$ low
	-135° ≤	< -90°	$\alpha$ very high		0.1 <	≤ 0.6	$\epsilon$ moderate
	90° <	≤ 135°		0.6 <	≤ 1.0	$\epsilon$ high	
	-180° ≤	< -135°	$\alpha$ very high				
	135° <	≤ 180°					



### 6.2.2.1. Complementary functions of sMM angle and turning angle

Because of their complementary function, sMM angle (sMM) and turning angle ( $\alpha$ ) were coupled together as two of four building blocks of morphomigrational description. Figure 28 presents the migration of an exemplary MEF 3T3 cell. For the first two frames (0 min and 10 min), the cell moves almost straight, which is described by low  $\alpha$ . Cell movement is also performed along the major axis which is described by very low sMM. However, between the third and fourth frames, the cell turns back. Such rapid change of direction is described by the very high value of  $\alpha$ . At the same time, sMM angle remains very low since this movement is still performed along the major axis. In the last frame, the cell moves again along its major axis in some defined direction that is described by the low  $\alpha$  and low sMM, just as in the first two frames. Therefore, the combination of turning angle and sMM angle allowed to quantitatively describe the lateral migration as well as the lateral U-turn of the cell.

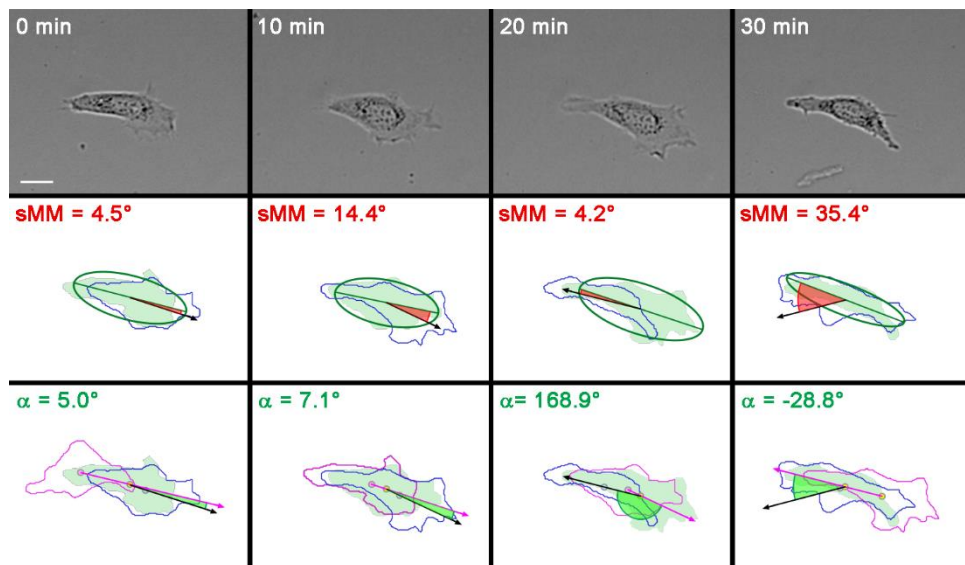


Figure 28. Complimentary role of sMM angle and turning angle presented on the example of migrating MEF 3T3 cell that performs a U-turn. Scalebar = 20 $\mu$ m. Adapted from <sup>234</sup>.

### 6.2.2.2. Complementary functions of sMM angle, M.A. dynamics and elongation.

#### Limitation of sMM angle.

The turning angle is constructed by employing the major axis of the shape. Therefore, its stability, described by M.A. dynamics ( $\Delta\phi$ ), is crucial in the interpretation of the morphomigrational description. In Figure 29 the HEK 293 cell starts from changing its spatial arrangement. In the first frame (0 min) elongation is moderate ( $\varepsilon = 0.14$ ) and M.A. dynamics is moderate ( $\Delta\phi = -28.8^\circ$ ) as well. In the second frame, the cell becomes more round which is marked by the low elongation. Such a rounded shape imposes the random orientation of the major axis, which results in an increase of M.A. dynamics ( $\Delta\phi = 44.6^\circ$ ). Therefore,

due to the random orientation of M.A., the sMM angle does not provide significant information. In the third frame (4 min) the cell extends a new protrusion on one side and in the fourth frame (6 min) detaches the protrusion on the other side and thus translocates the cell body (6 min). This behavior, the detachment of the “rear protrusion”, is described by a specific set of values of building blocks. Cell movement in the third frame is performed laterally to the major axis which is described by a very low value of sMM. However, the detachment of the cell rear results in the change of cell geometry to a perpendicular one, which is described by the very high value of M.A. dynamics ( $\Delta\varphi = -75.9^\circ$ ). This geometry is then preserved in the last frame where the cell moves perpendicularly to its major axis (sMM =  $76.5^\circ$ ) and the shape turns only slightly in the anti-clockwise direction ( $\Delta\varphi = -19.7^\circ$ ).

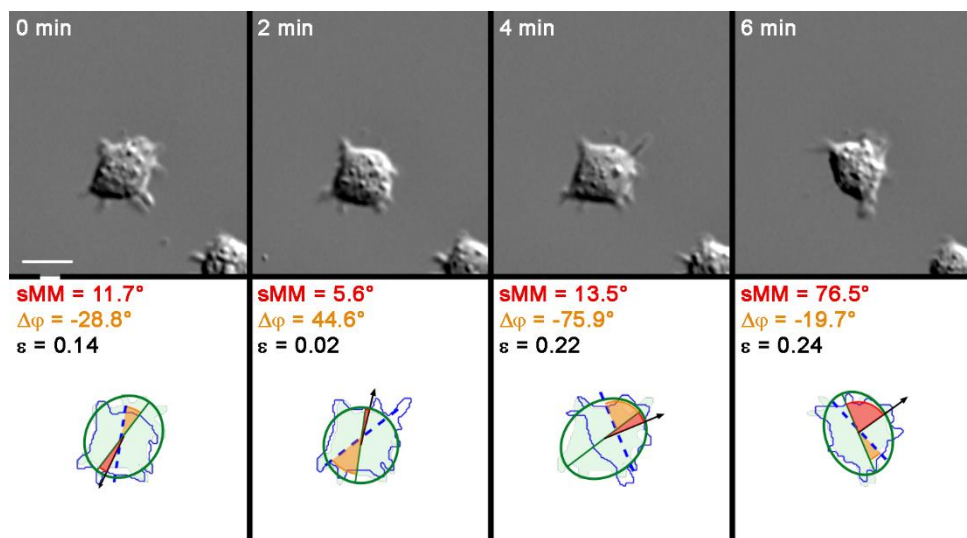


Figure 29. Complimentary role of sMM angle and M.A. dynamics presented for exemplary HEK293 undergoing tail retraction. Scalebar =  $20\mu\text{m}$ . Adapted from <sup>234</sup>.

The next example elaborates more on the limitations of the application of sMM angle. Figure 30 presents the migration of MEF 3T3 cell. This cell represents a very regular shape, which is described by the very low elongation ( $\varepsilon$  is up to 0.05). It results in moderate, high, and very high values of M.A. dynamics, due to the random orientation of M.A. In the third frame (20 min) the cell extends slightly its rear which results in the negative value of sMM angle, while in the fourth frame (30 min) displacement vector slowly recovers to the previous direction. However, due to the constant rotation of M.A. in the third and fourth frames, the sign of sMM remains negative, even if the displacement direction in the first, third, and fourth frames is rather similar. It shows that for the rounded shapes, the sMM angle might assume random values and therefore, the morphomigrational description benefits more from the remaining building blocks.

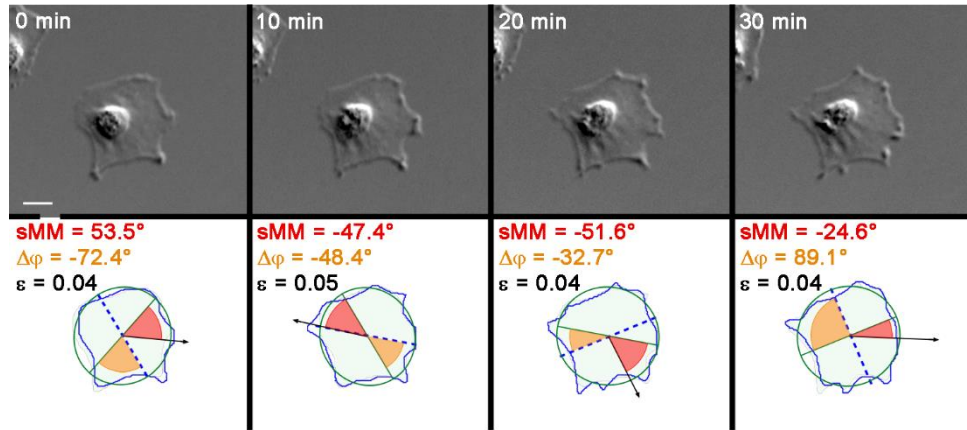


Figure 30. sMM angle and M.A. dynamics presented for the regularly shaped MEF 3T3 cell. Scalebar = 20 $\mu$ m. Adapted from <sup>234</sup>.

### 6.2.3. Morphomigrational description of selected cellular behaviors.

To show the application of morphomigrational description we have analyzed three exemplary cells that differed significantly in the type of migratory behavior: fish epithelial keratinocyte, MEF 3T3 cell and HEK293 cell. The time evolution of each morphomigrational building block is presented in Figure 31.

At first look, it is clear that the time series of the same parameters differ for each cell, reflecting the differences between their set of distinct behaviors. To give a better insight into the morphomigrational description, we have selected some fragments of time-lapse sequences of each examined cell for their further detailed description. Since the behavior of fish epithelial keratinocyte is quite steady, only one sequence (K1) was chosen. For the MEF 3T3 cell, we chose five behaviors that differ in the level of complexity (M1-M5). For HEK293 we chose 5 different fragments (H1-H5) to illustrate the variety of behaviors that are exhibited by this type of cell. The exact values of building blocks calculated for each behavior are shown in Table 9.

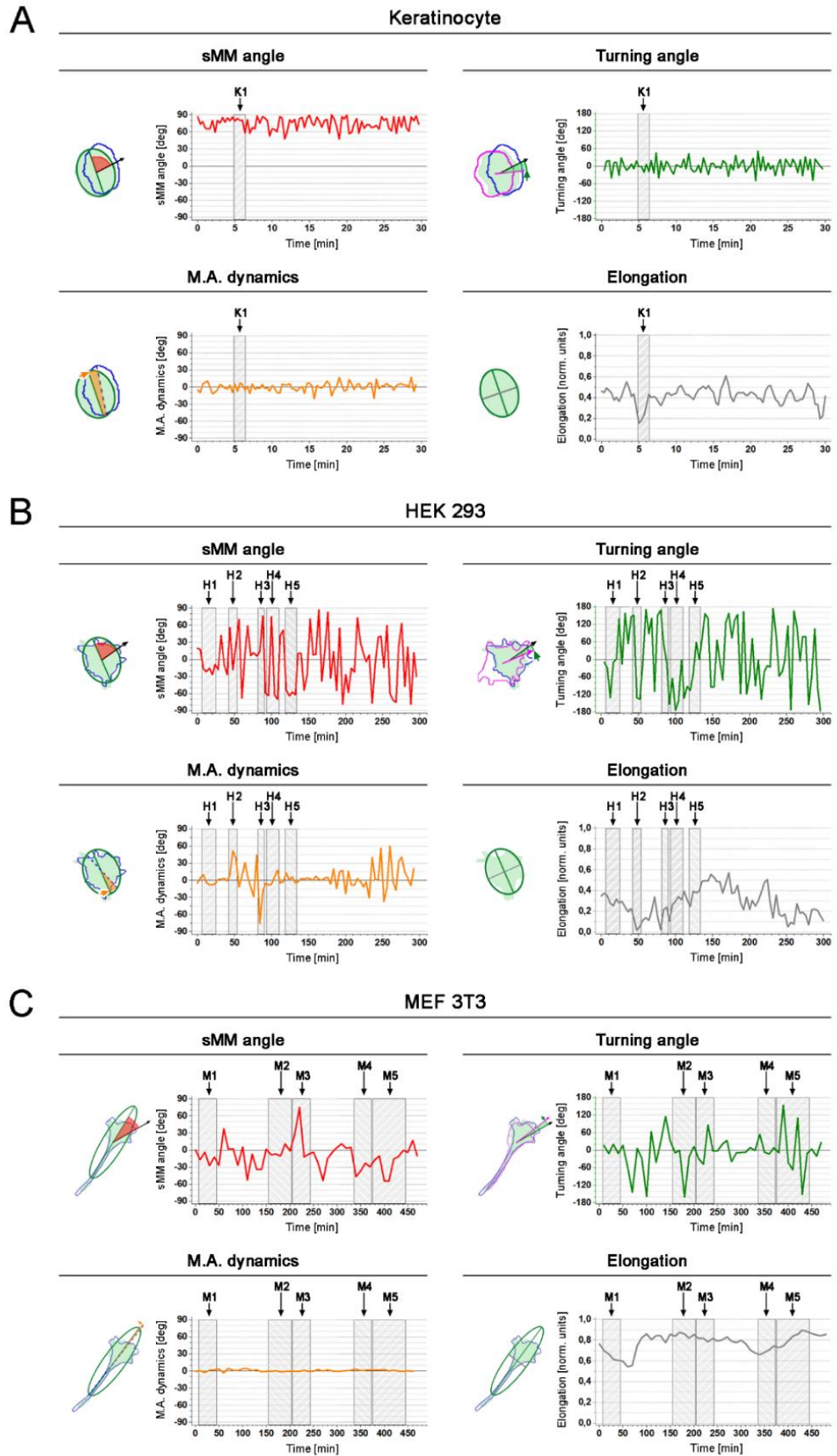


Figure 31. Time series plots of all four building blocks of morphomigrational description. **A:** Keratinocyte, **B:** MEF3T3 cell, **C:** HEK293 cell. Adapted from <sup>234</sup>.

Table 9. Exact values of fragments: K1, M1-M5, H1-H5 marked in Figure 31. Adapted from <sup>234</sup>.

Symbol	Frame	Time [min]	sMM		$\alpha$		$\Delta\varphi$		$\epsilon$	
			exact [deg]	Coarse-grain	exact [deg]	Coarse-grain	exact [deg]	Coarse-grain	exact [norm]	Coarse-grain
K1	16	5.0	78.6	high	-2.4	low	5.4	very low	0.15	moderate
	17	5.3	83.7	high	-0.5	low	-7.4	very low	0.18	moderate
	18	5.7	80.1	high	-21.1	low	7.3	very low	0.23	moderate
	19	6.0	80.8	high	5.9	low	4.1	very low	0.32	moderate
	20	6.3	58.0	moderate	-19.1	low	-6.0	very low	0.43	moderate
H1	3	8	-16.4	low	-28.7	low	10.1	low	0.35	moderate
	4	12	-21.7	low	-131.5	high	-4.1	very low	0.27	moderate
	5	16	-15.3	low	-11.6	low	-8.2	very low	0.25	moderate
	6	20	-26.7	low	2.5	low	-8.0	very low	0.32	moderate
	7	24	-8.9	very low	138.2	very high	-5.9	very low	0.28	moderate
H2	12	44	55.5	moderate	151.1	very high	10.2	low	0.14	moderate
	13	48	-18.3	low	-131.6	high	51.8	high	0.02	low
	14	52	25.0	low	-136.1	very high	39.2	moderate	0.05	low
H3	22	84	13.5	very low	53.1	low	-75.9	very high	0.22	moderate
	23	88	78.5	high	-12.7	low	-19.7	low	0.24	moderate
H4	24	92	-59.8	moderate	-154.2	very high	-5.4	very low	0.10	low
	25	96	-63.4	moderate	-65.3	moderate	-8.1	very low	0.26	moderate
	26	100	75.1	high	-174.8	very high	-7.1	very low	0.29	moderate
	27	104	-62.2	moderate	-143.8	very high	6.4	very low	0.34	moderate
	28	108	-70.4	high	-3.9	low	18	low	0.31	moderate
H5	31	120	-53.4	moderate	-107.0	high	12.6	low	0.25	moderate
	32	124	-64.1	moderate	-49.1	low	0.5	very low	0.39	moderate
	33	128	-57.3	moderate	59.2	low	5.9	very low	0.38	moderate
	34	132	-62.5	moderate	-0.7	low	-4.5	very low	0.4	moderate
M1	2	10	-16.7	low	16.6	low	0.6	very low	0.70	high
	3	20	-3.9	very low	-12.7	low	-2.4	very low	0.66	high
	4	30	-27.4	low	20.5	low	1.5	very low	0.61	high
	5	40	-12.1	very low	-12.4	low	2.1	very low	0.60	moderate
M2	17	160	-8.3	very low	-9.6	low	-0.8	very low	0.84	high
	18	170	-7.0	very low	-0.1	low	0.7	very low	0.87	high
	19	180	-10.4	very low	-161.6	very high	-1.0	very low	0.86	high
	20	190	10.7	very low	-22.7	low	-0.8	very low	0.82	high
	21	200	-1.8	very low	12	low	-0.6	very low	0.85	high
M3	22	210	26.7	low	-28.9	low	-0.7	very low	0.82	high
	23	220	74.8	high	-48.8	low	-0.5	very low	0.82	high
	24	230	-12.6	very low	85.8	moderate	1.1	very low	0.78	high
	25	240	-7.1	very low	-3.4	low	-0.4	very low	0.81	high
M4	35	340	-47.1	moderate	53.9	low	3.4	very low	0.66	high
	36	350	-36.9	low	-7.2	low	0.9	very low	0.68	high
	37	360	-22.8	low	-13.7	low	1.0	very low	0.71	high
	38	370	-29.5	low	7.8	low	2.0	very low	0.74	high
M5	39	380	-17.2	low	-10.3	low	1.1	very low	0.73	high
	40	390	-10.3	very low	153.5	very high	1.0	very low	0.74	high
	41	400	-53.9	moderate	-42.4	low	2.6	very low	0.79	high
	42	410	-55.2	moderate	-68.2	moderate	0.3	very low	0.84	high
	43	420	-15.5	low	-109.4	high	1.0	very low	0.85	high
	44	430	-11.5	very low	-151.9	very high	0.3	very low	0.90	high
	45	440	-0.5	very low	-10.6	low	-0.4	very low	0.88	high

### ***6.2.3.1. Perpendicular movement, movement askew, perpendicular and askew stretching***

Behaviors K1 of keratinocyte and H4 of HEK293 cell are presented in Figure 32 and Table 10. The analyzed keratinocyte migrated perpendicularly to its major axis, which is marked by high values of sMM angle of the same sign (K1 behavior in 5.00-6.00 min). The similar migration direction is marked by low values of turning angles. What is also interesting, the M.A. dynamics is very low, but its sign changes every 1-2 frames, which shows that fish epithelial keratinocyte was extending its lamellipodium sequentially on the right and left side, each after another. A similar perpendicular movement is also visible in the HEK293 cell, in the last frame of the H4 sequence (108 min), also illustrated by the high sMM angle and low turning angle.

The same cells can also migrate askew to the major axis, which is visible in the last frame of the K1 sequence (6.33 min) and 4<sup>th</sup> frame of the H4 sequence (104 min). However, the values of building blocks are quite different, which is the result of different context of movement. The askew movement of keratinocyte followed the perpendicular migration, and the movement proceeded in the same direction, which is marked by a moderate sMM angle (58°) and low turning angle (-19.1°). On the contrary, in the 4<sup>th</sup> frame of the H4 sequence we can see the moderate value of sMM angle (-62.2°) and a very high value of turning angle (-143.8°). The very high turning angle signifies that the movement askew in that frame was performed after the significant change of direction, therefore it occurred after the frame of different morphomigrational behavior. It is true indeed because the previous frames of the H4 sequence show perpendicular and askew stretching. By the term „stretching” we understand the protrusion extensions, that are performed in different directions one after another. These behaviors are also illustrated by the moderate and high turning angles.

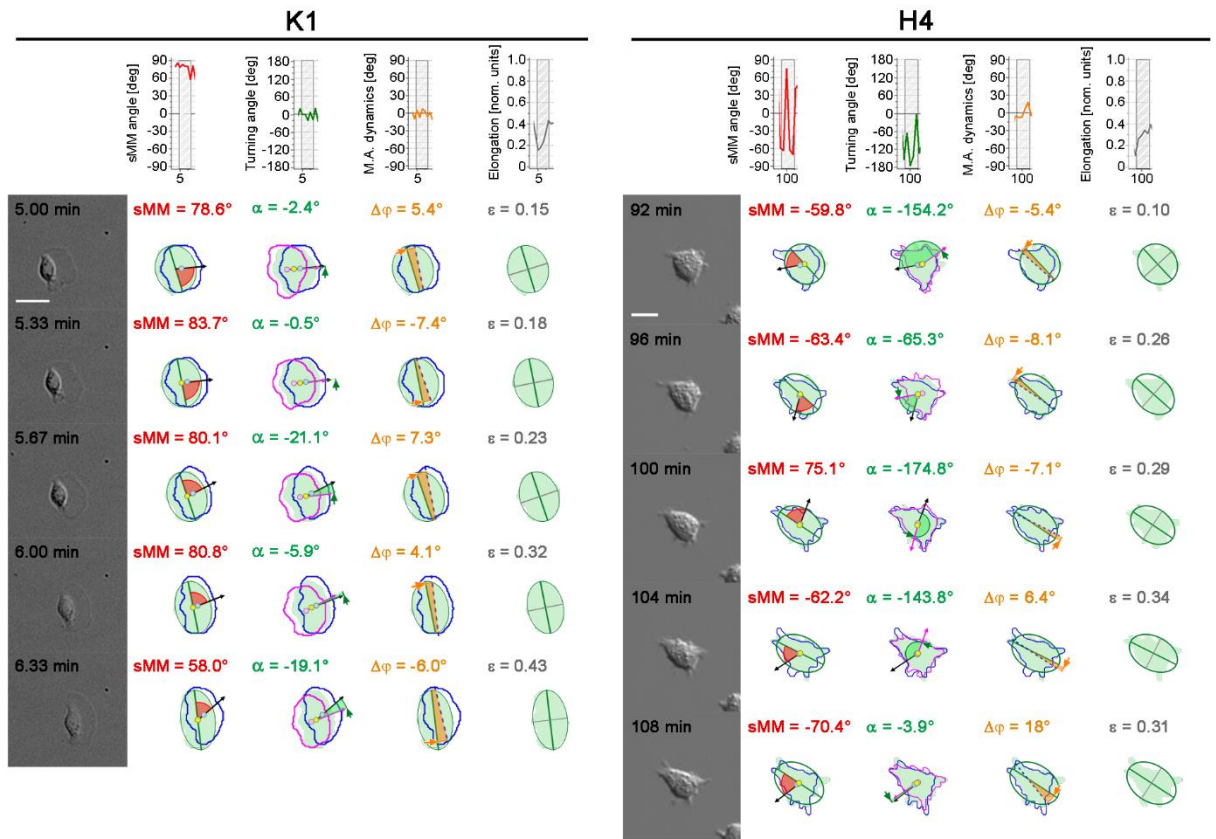


Figure 32. Illustration of all four building blocks of morphomigrational description of K1 and H4 fragments. Scalebar = 20μm. Adapted from <sup>234</sup>.

Table 10. Morphomigrational description of K1 and H4 fragments. Adapted from <sup>234</sup>.

Fragment of sequence	Parameter	Coarse-grain description of numerical values	What does the quantitative parameter inform about	Morphomigrational behavior
K1	sMM	Moderate and high, sign does not change	Displacement perpendicular to the major axis, always on the same side of it.	Perpendicular displacement [5.0-6.0 min] and askew displacement [6.3 min].
	α	Low, sign might change	Movement in a particular direction. Changing sign informs about no visible bias in the clockwise nor anti-clockwise direction.	
	Δφ	Very low, sign might change	No rapid changes of cell shape.	
	ε	Moderate, increasing.	Moderately elongated cell and slightly elongates itself.	
H4	sMM	Moderate and high, changing sign	Protrusions are created perpendicularly and askew to M.A. on both sides of it. The same sign at the end of the sequence indicates perpendicular displacement	Perpendicular/askew stretching ended with perpendicular displacement [92-108 min].
	α	Very high, moderate, and low, sign might change	Chaotic movement ended with directional movement	
	Δφ	Very low and low, changing sign	Shape slightly changes its arrangement first anti-clockwise and then clockwise.	
	ε	Moderate, increasing	Cell slightly stretches itself while still being moderately elongated	

To find similarities as well as differences between perpendicular and askew movements of keratinocyte and HEK293 cell we have analyzed all such behaviors in time sequences. Figure 33 shows the comparison of building blocks for each cell. To make description more intuitive, they

are described by elongation ( $\epsilon$ ) and absolute values of turning angle ( $|\alpha|$ ), sMM angle ( $|\text{sMM}|$ ), and M.A. dynamics ( $|\Delta\phi|$ ). For the perpendicular movement of keratinocyte, the values of all building blocks are consistent: low turning angles, high sMM angles, low M.A. dynamics, and moderate elongation. For the HEK293 cell, we can observe there are only three frames that are described with low turning angles, which suggests that such movement was performed after the askew or perpendicular movement as well (thus did not require the change of movement direction). The remaining frames show moderate and high turning angles that suggest that those frames followed different morphomigrational behaviors. The only frame characterized by the moderate M.A. dynamics shows that in this particular frame, the perpendicular movement was coupled with a significant rearrangement of the cell geometry. A similar situation is visible for the askew movement of two cells. Turning angles of keratinocyte are consistently low, while for HEK293 cell their values are moderate, high, and very high, indicating again the stability of the cellular behavior.

Besides the identification of the morphomigrational behaviors, these plots show the context in which those behaviors are located in a time sequence. For keratinocyte, the perpendicular and askew movements are persistent along their migration, while in the case of HEK 293 cell, they are rather random, being fitted between other types of behaviors. It also shows how much information about cellular dynamics might be described by the quantitative, morphomigrational description.

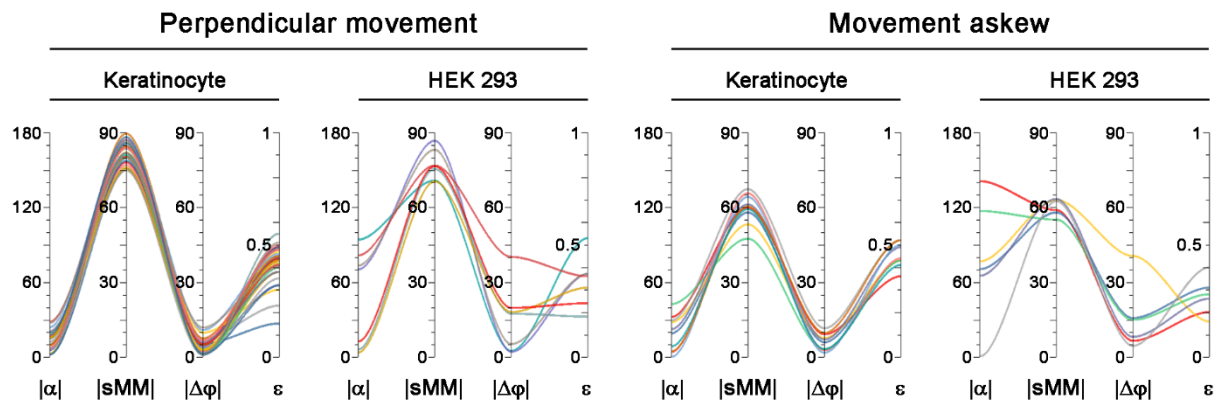


Figure 33. Similarities and differences between perpendicular movement and movement askew observed for keratinocyte and HEK 293 cell. Adapted from <sup>234</sup>.

### 6.2.3.2. Lateral movement, lateral U-turns

Another type of morphomigrational behavior identified in this thesis is the movement lateral to the major axis. This type of behavior is visible in fragments M1 and M4 which are shown in Figure 34 and described in Table 11. The lateral movement is described by very low and low sMM angles. The same sign of sMM angle suggests, that the lamellipodium is created



asymmetrically, which is especially visible in the M4 sequence that starts from one moderate sMM angle and then it keeps the low sMM angle of the same sign. Low M.A. dynamics means that the shape is stable along the time and does not perform rapid turns, however in sequence M4 there is a visible slight turn in the clockwise direction.

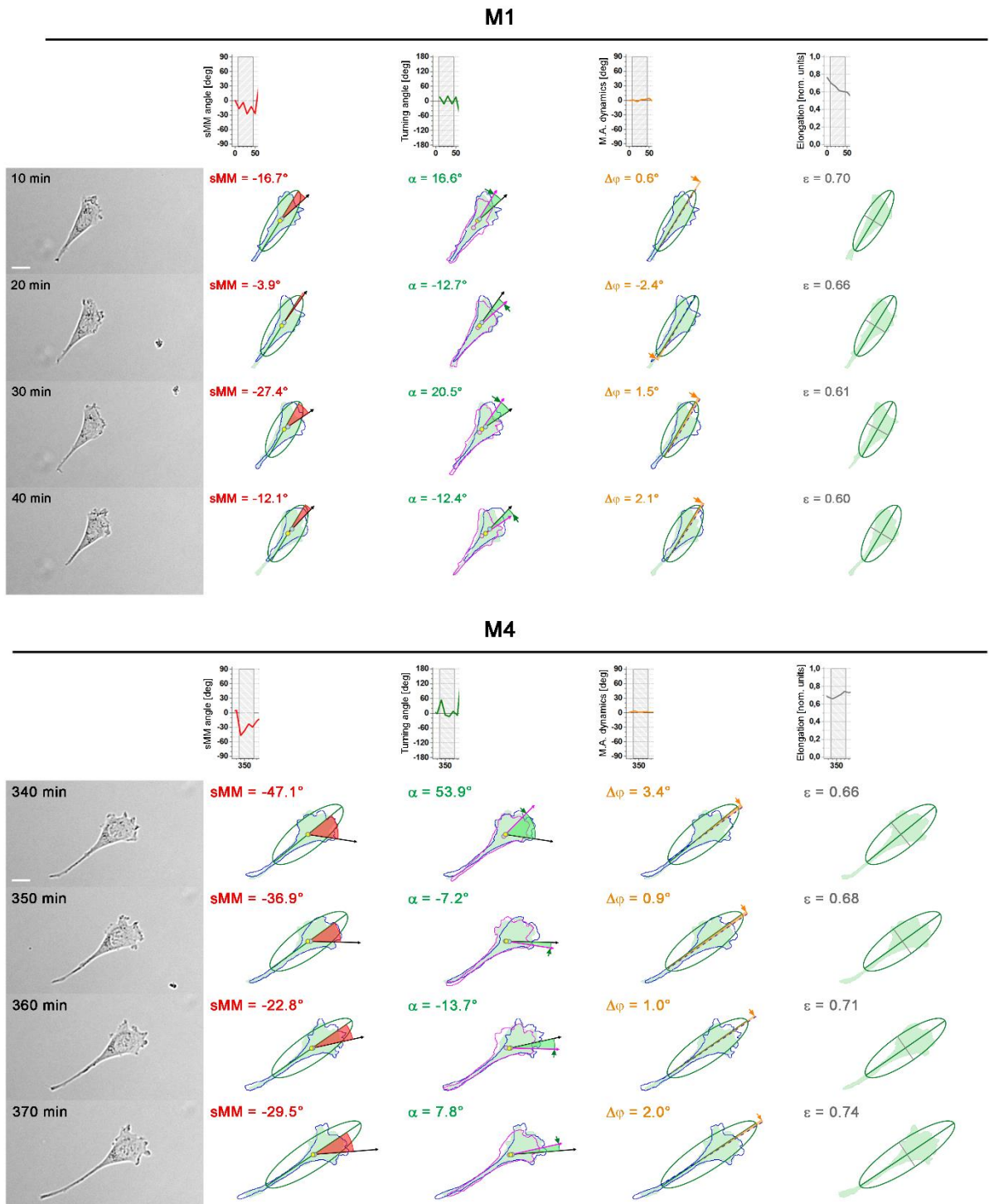


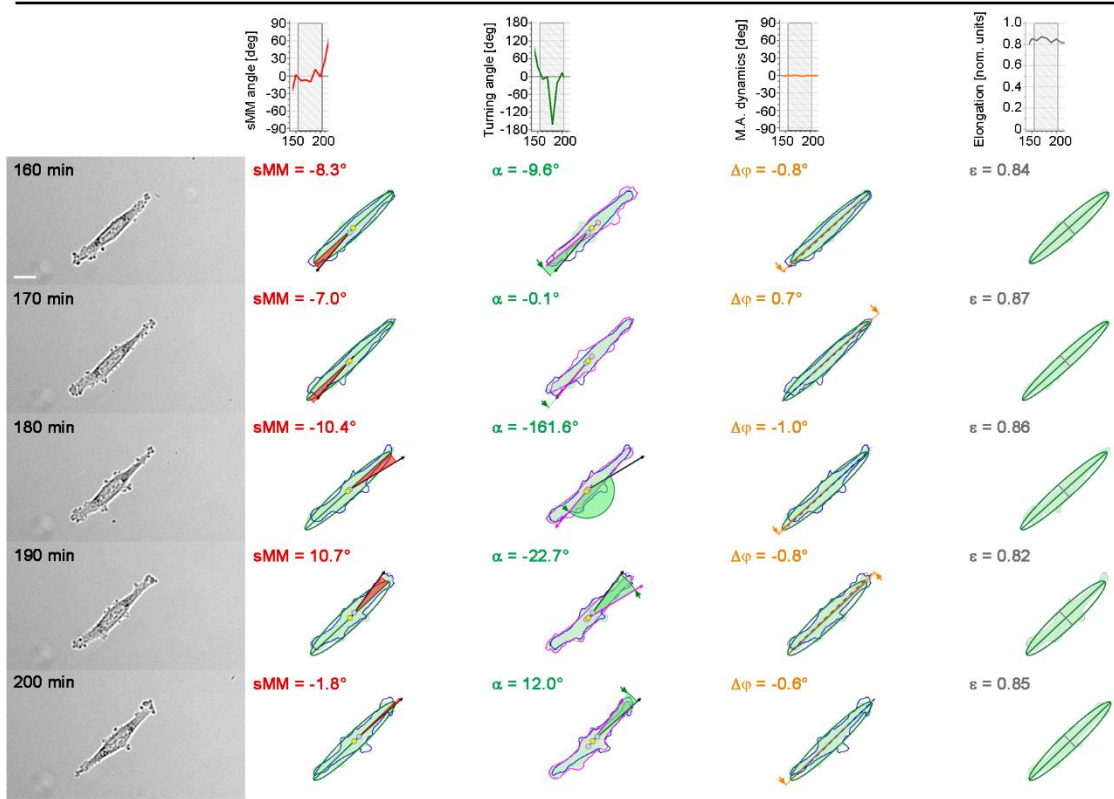
Figure 34. Illustration of all four building blocks of morphomigrational description of M1 and H4 fragments. Scalebar = 20 $\mu$ m. Adapted from <sup>234</sup>.

Table 11. Morphomigrational description of M1 and M4 fragments. Adapted from <sup>234</sup>.

Fragment of sequence	Parameter	Coarse-grain description of numerical values	What does the quantitative parameter inform about	Morphomigrational behavior
M1	sMM	Very low and low, sign does not change	Displacement along the major axis, lamellipodium created mostly on one side of M.A.	Lateral displacement [10-40 min.].
	$\alpha$	Low, sign might change	Movement in a particular direction. Changing sign informs about no visible bias in the clockwise nor anti-clockwise direction.	
	$\Delta\varphi$	Very low, sign might change	No rapid changes of cell shape.	
	$\varepsilon$	High and moderate, decreasing	Highly elongated cell that slightly reduces its length.	
M4	sMM	Low and moderate, the same sign	Cell creates protrusion on one side of M.A. (the same sign) rather on one of the cell's ends (moderate and low values) – lateral movement	Lateral displacement with lamellipodium on one side of M.A [340-370 min.].
	$\alpha$	Low, sign might change	Movement in a particular direction. Changing sign informs about no visible bias in the clockwise nor anti-clockwise direction.	
	$\Delta\varphi$	Very low, the same sign	Cell shape rotates slightly clockwise.	
	$\varepsilon$	High, increasing	Highly elongated shape, still elongating itself.	

Another fragments, i.e. the M2 and H1 are also partially described by the lateral movement as well, being described similarly to the M1 and M4 sequences (Figure 35, Table 12). However, the lateral movement is broken by the rapid U-turn of the MEF 3T3 and HEK 293 cells. In both cases, those behaviors are described by the incidental high or very high value of turning angle with the very low or low sMM angles. The parameter that differentiates those 2 cells is elongation, which just characterizes the differences in cell shape.

## M2



## H1

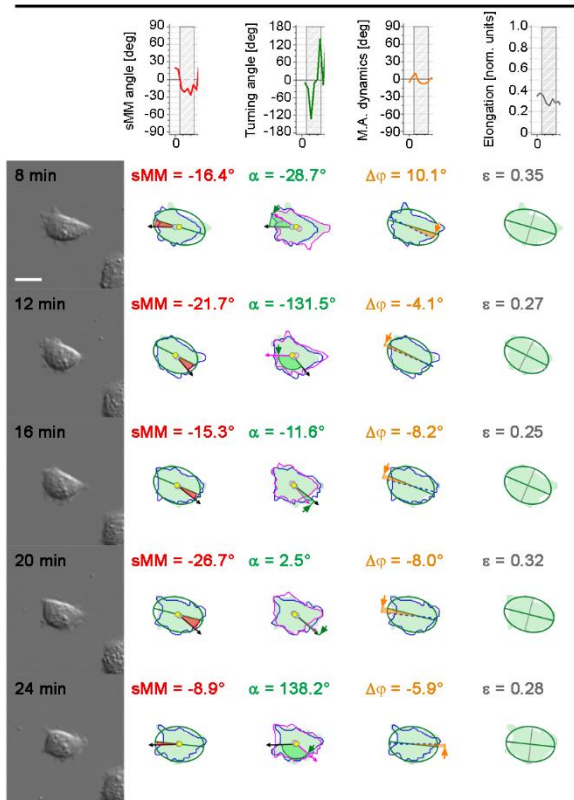


Figure 35. Illustration of all four building blocks of morphomigrational description of M2 and H1 fragments. Scalebar = 20 $\mu$ m. Adapted from <sup>234</sup>.

Table 12. Morphomigrational description of M2 and H1 fragments. Adapted from <sup>234</sup>.

Fragment of sequence	Parameter	Coarse-grain description of numerical values	What does the quantitative parameter inform about	Morphomigrational behavior
M2	sMM	Very low and low, sign does not change	Displacement along the major axis, lamellipodium created mostly on one side of M.A.	Lateral displacement [160-170 min and 190-200 min]
	$\alpha$	Low, sign might change	Movement in a particular direction. Changing sign informs about no visible bias in the clockwise nor anti-clockwise direction.	
	$\Delta\varphi$	Very low, sign might change	No rapid changes of cell shape.	
	$\varepsilon$	High, constant	Highly elongated cell that slightly reduces its length.	
	sMM	Very low and low, sign might change	Displacement along the major axis.	with lateral U-turn [180 min]
	$\alpha$	Low $\rightarrow$ high/very high $\rightarrow$ low, sign might change	Cell performs the turn back.	
	$\Delta\varphi$	Very low, sign might change	No rapid changes of cell shape.	
	$\varepsilon$	High, constant	Highly elongated cell.	
H1	sMM	Very low and low, sign does not change	Displacement along the major axis.	Lateral displacement [8 min and 16-20 min]
	$\alpha$	Low, sign might not change	Movement in a particular direction. Changing sign informs about no visible bias in the clockwise nor anti-clockwise direction.	
	$\Delta\varphi$	Very low and low, sign might not change	Cell shape rotates slightly anti-clockwise.	
	$\varepsilon$	Moderate, constant.	Moderately elongated cell.	with occasional lateral U-turns [12 min and 24 min]
	sMM	Very low and low, the same sign	Displacement along the major axis.	
	$\alpha$	High/very high, sign might change	Cell performs the turn back.	
	$\Delta\varphi$	Very low and low, the same sign	Barely noticeable anti-clockwise turn of the shape.	
$\varepsilon$	Moderate, constant	Moderately elongated cell.		

The comparison of lateral movements and lateral U-turns of MEF 3T3 cell and HEK293 cell is described in Figure 36. MEF 3T3 migrating laterally is described consistently by:  $|\alpha| < 60^\circ$ ,  $|\text{sMM}| < 45^\circ$ ,  $|\Delta\varphi| < 10^\circ$ , and  $\varepsilon > 0.5$ . HEK293 cell migrating laterally is also described by  $|\alpha| < 60^\circ$ ,  $|\text{sMM}| < 45^\circ$ , however, it shows higher M.A. dynamics, indicating lateral movement can be also connected here with the rearrangement of the cell on the 2D plane. This is especially visible for the frame of high M.A. dynamics and low sMM angle. Also, the lateral U-turns of HEK293 and MEF 3T3 cells are described in similar ways, even if in the case of the HEK293 cell the sMM angle is a bit higher than for MEF 3T3 cell. Again, we can observe higher M.A. dynamics and lower elongation, which means the less stable and more rounded shape of the HEK293 cell.

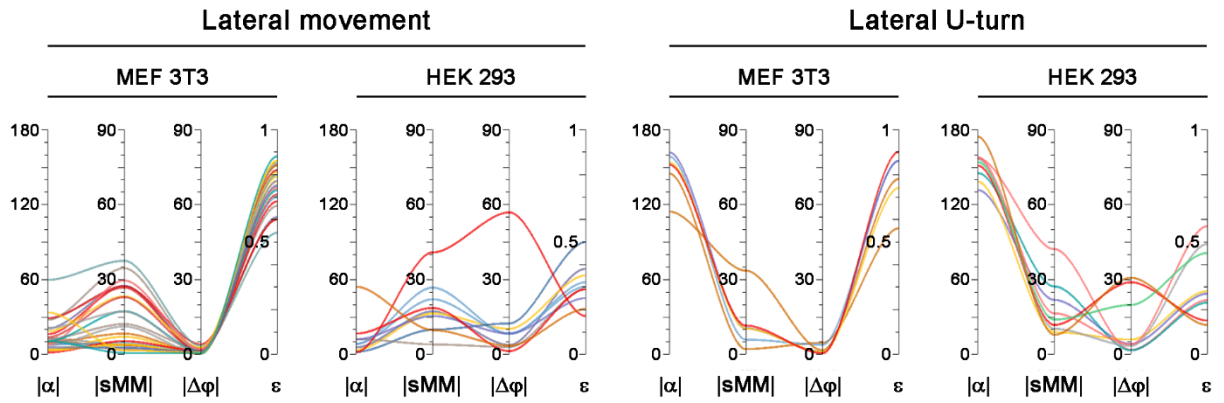


Figure 36. Similarities and differences between lateral movement and lateral U-turns, observed for keratinocyte and HEK 293 cell. Adapted from <sup>234</sup>.

### 6.2.3.3. Other examples of cellular behaviors and their morphomigrational description

Figure 37 and Table 13 show the remaining exemplary morphomigrational behaviors expressed by HEK293 cell. In behavior H2, the observed cell is rounded, which is described by the low elongation. Also, the M.A. dynamics is moderate and high, imposing the random orientation of the major axis. Those descriptors are paired with the high and very high turning angles, which suggests the chaotic movement of this rounded cell. Therefore, the sMM angle is not interpretable because of the random orientation of M.A. dynamics, while the remaining building blocks inform about the random cell displacement. The H3 fragment presents in more detail the process of tail retraction, that was already mentioned in Figure 29. At the beginning (84 min), the cell is stretched and its movement is performed along the major axis which is described by a very low value of sMM angle. A low value of turning angle also illustrates that the cell does not change its direction much. However, those values are paired with a very high M.A. dynamics, which suggests the significant reorientation of the cell. What is also important, the elongation clearly illustrates that this cell is not rounded as in the H2 sequence. This significant reorientation of the shape is confirmed in the next frame because even if the turning angle is still very low, the sMM angle increases to  $78.5^\circ$  which is characteristic for perpendicular movement. This set of building blocks clearly describes the process of tail retraction, which in this case might be identified quantitatively. In the last analyzed HEK293 sequence (H5), one can observe the cell stretching coupled with the askew and perpendicular movement of the cell body. The sequence starts from the high turning angle describing the significant change of direction after the previous behaviors. In all four frames (120-128 min) the cell extends its protrusions on the sides, which results in its forward movement. While the sMM angle has moderate values, the changing signs of turning angles show that the extensions are made first on one side of the cell and then on another one and the increasing elongation depicts cell stretching.

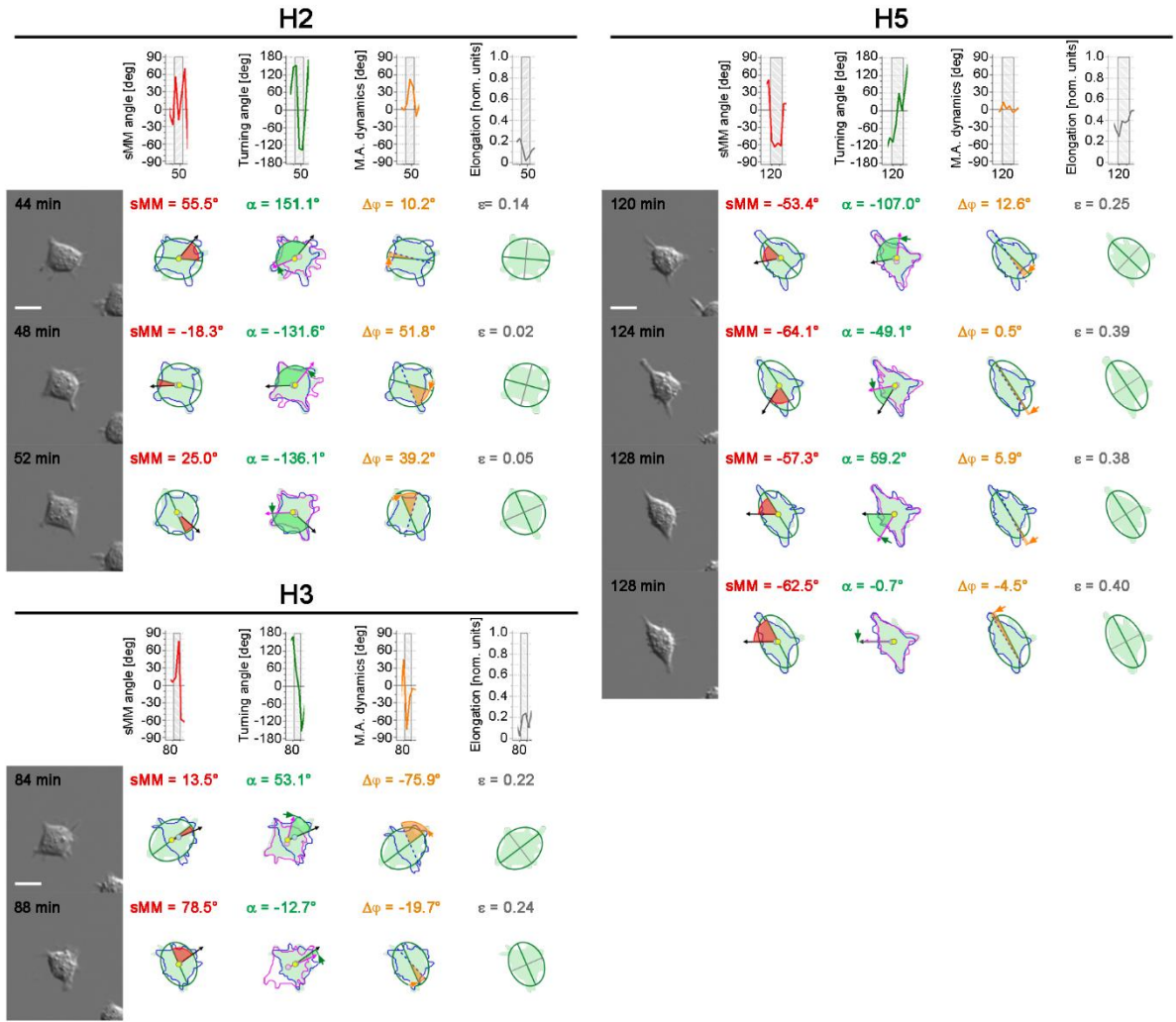


Figure 37. Illustration of all four building blocks of morphomigrational description of H2, H3 and H5 fragments. Scalebar = 20 $\mu$ m. Adapted from <sup>234</sup>.

Table 13. Morphomigrational description of H2, H3 and H5 fragments. Adapted from <sup>234</sup>.

Fragment of sequence	Parameter	Coarse-grain description of numerical values	What does the quantitative parameter inform about	Morphomigrational behavior
H2	sMM	Moderate and low, changing sign	Displacement in various directions regarding M.A.	Rounded cell with chaotic movement [44-52 min]
	$\alpha$	High and very high, changing sign	Nondirectional movement.	
	$\Delta\phi$	Low, moderate and high, the same sign	Shape changes its arrangement in a clockwise direction.	
	$\varepsilon$	Moderate and low, decreasing	Rounded or regular polygonal shape.	
H3	sMM	Low $\rightarrow$ high, the same sign	Rapid change of sMM from lateral to perpendicular movement.	Rear protrusion retraction with directional displacement. Cell geometry changes from parallel to perpendicular to the movement direction. [84-88 min]
	$\alpha$	Low, changing sign	Movement in a particular direction. Changing sign informs about no visible bias in the clockwise nor anti-clockwise direction.	
	$\Delta\phi$	High $\rightarrow$ low, the same sign	Incidental rotation of cell shape, further conservation of this arrangement on a 2D plane.	
	$\varepsilon$	Moderate, stable	Moderately elongated cell	
H5	sMM	Moderate, the same sign	Displacement askew to the major axis constantly on the same side of M.A.	Lateral stretching with perpendicular displacement [120-132 min]
	$\alpha$	High $\rightarrow$ low, changing sign	Cell first changes movement direction (high $\alpha$ ) and then stabilizes it (low $\alpha$ )	
	$\Delta\phi$	Low, mostly the same sign	Cell arrangement slightly changes in the beginning and stabilizes itself in the next frames.	
	$\varepsilon$	Moderate, increasing	Cell stretches itself.	

The interesting behavior of extending the short-living protrusion by MEF 3T3 is shown in Figure 38 and Table 14. At the beginning (210 min) we can observe the lateral movement, described by a low sMM angle, low turning angle, very low M.A. dynamics, and high elongation, just as in previous behaviors of MEF 3T3 cell. Afterward, at 220 min we can observe an incidental increase of sMM angle that is caused by the creation of perpendicular protrusion. However, this protrusion is not maintained in the perpendicular direction but is rather pushed to the front of the cell (230 min). This is described by a low sMM angle and moderate turning angle of the opposite sign than in the previous frame. The lateral movement is then maintained in the last frame (240 min) of the M3 sequence, being described, as previously, by very low sMM, low  $\alpha$ , very low M.A. dynamics, and high elongation.

### M3

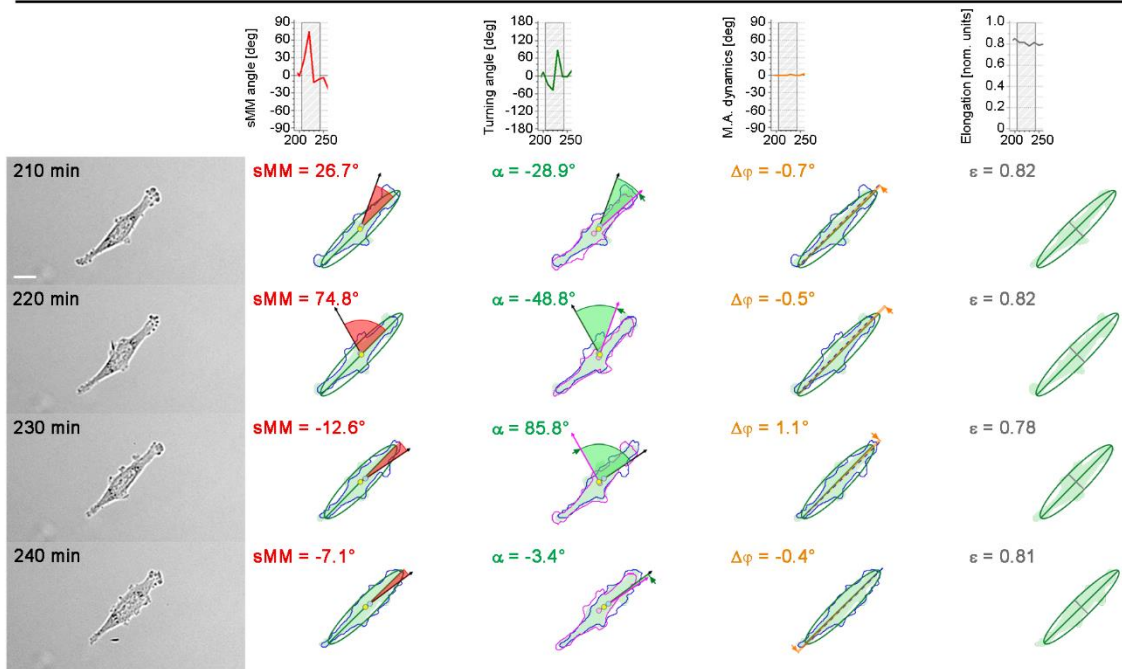


Figure 38. Illustration of all four building blocks of morphomigrational description of M3 fragment. Scalebar =  $20\mu\text{m}$ . Adapted from <sup>234</sup>.

Table 14. Morphomigrational description of M3 fragment. Adapted from <sup>234</sup>.

Fragment of sequence	Parameter	Coarse-grain description of numerical values	What does the quantitative parameter inform about	Morphomigrational behavior
M3	sMM	Low $\rightarrow$ high, sign does not change	Incidental displacement of centroid perpendicular to M.A. indicates perpendicular protrusion, roughly in the cell center	Lateral displacement with creation of small perpendicular protrusion in the central part [210-220 min]
	$\alpha$	Low, sign does not change	Displacement turned anti-clockwise according to creation of protrusion.	
	$\Delta\varphi$	Very low, sign might change	No rapid changes of cell shape.	
	$\epsilon$	High, constant	Highly elongated cell.	
	sMM	High $\rightarrow$ low, sign might change	Protrusion was not developed furtherly, cell continued previous lateral displacement.	followed by movement lateral to the major axis [230-240 min]
	$\alpha$	Moderate $\rightarrow$ low, sign changes	Cell goes back from creating perpendicular protrusion to previous stable directional movement.	
	$\Delta\varphi$	Very low, sign might change	No rapid changes of cell shape.	
	$\epsilon$	High, constant.	Highly elongated cell.	



One of the most complex behaviors presented in this work is shown in the M5 sequence, visualized in Figure 39 and described in Table 15. It starts from the lateral movement (380 min) which is followed by the lateral U-turn (290 min), described similarly as in previous examples. However, in the next two frames (400-410 min) the cell turns again, but this turn is performed in two frames with two moderate sMM angles as well as low and moderate turning angles of the same sign, one after another. Afterward, in 420-430 min there are two lateral U-turns, which are marked by low sMM angles and high to very high turning angles. Those sequential U-turns can be described also as the process of lateral stretching. All mentioned behaviors are followed by the lateral movement in the last frame (440 min) of this sequence.

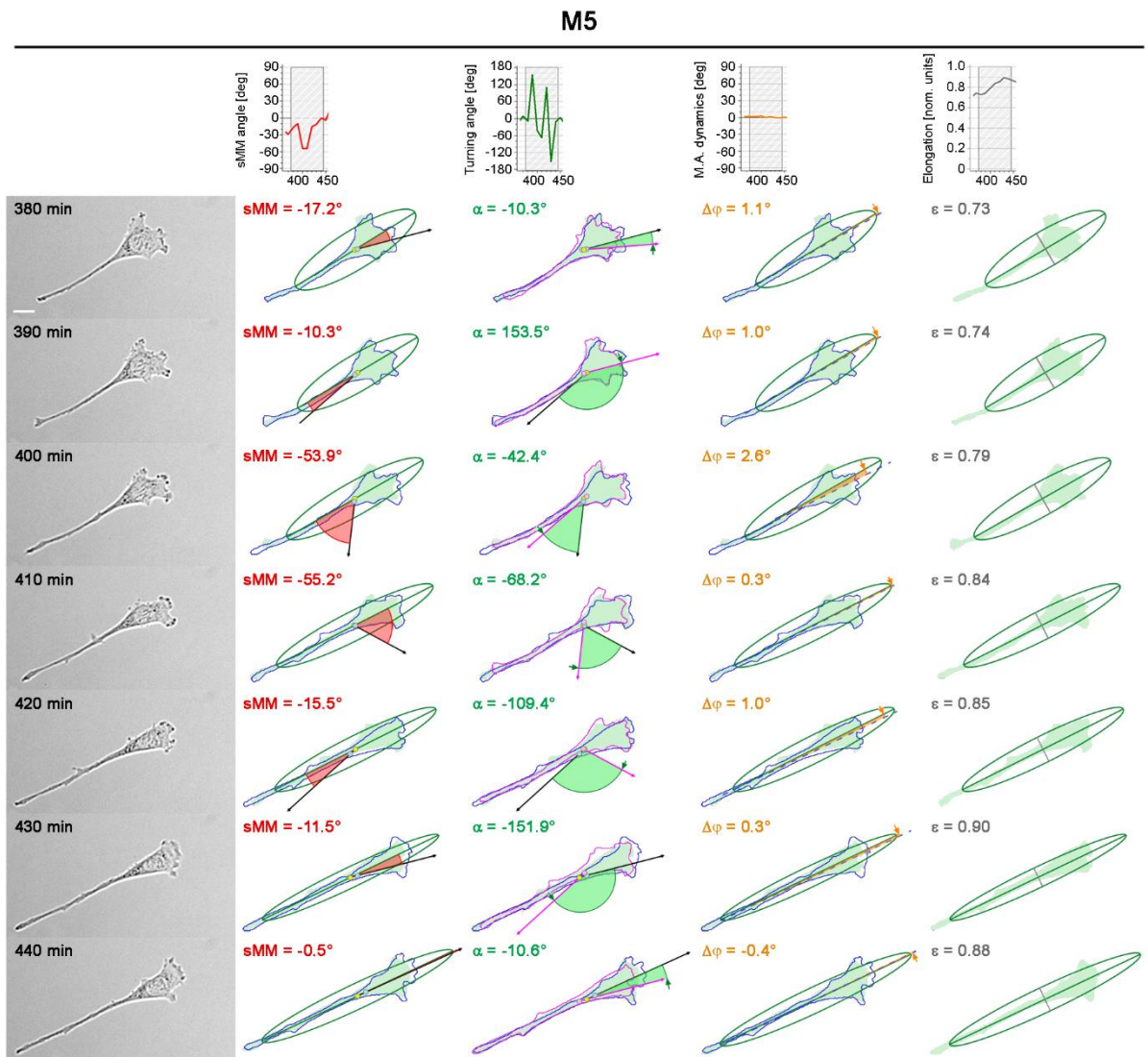


Figure 39. Illustration of all four building blocks of morphomigrational description of M5 fragment. Scalebar = 20 $\mu$ m. Adapted from <sup>234</sup>.

Table 15. Morphomigrational description of M5 fragment. Adapted from <sup>234</sup>.

Fragment of sequence	Parameter	Coarse-grain description of numerical values	What does the quantitative parameter inform about	Morphomigrational behavior
M5	sMM	Very low and low, sign might change	Displacement along the major axis.	Lateral displacement with lateral U-turn [380-390 min].
	$\alpha$	Low $\rightarrow$ high $\rightarrow$ low, sign might change	Cell performs the turn back.	
	$\Delta\varphi$	Very low, the same sign	Cell shape rotates slightly clockwise.	
	$\varepsilon$	High, increasing	Highly elongated shape, still elongating itself.	
	sMM	Moderate, likely the same sign	Cell slowly creates dominant protrusion on one side of M.A and on one of the cells' ends.	followed by a slow change of direction (restoration of lamellipodium in the previous direction) [400-410 min].
	$\alpha$	Low and moderate, likely the same sign	Slow change of displacement direction.	
	$\Delta\varphi$	Very low, the same sign	Cell shape rotates slightly clockwise.	
	$\varepsilon$	High, increasing	Highly elongated shape, still elongating itself.	
	sMM	Very low and low, sign might change	Displacement along the major axis.	and further lateral stretching (several direction reversals along the major axis) followed by directional migration [420-440 min].
	$\alpha$	High $\rightarrow$ high $\rightarrow$ low, sign might change	Two turn-backs (lateral stretching) followed by lateral movement	
	$\Delta\varphi$	Very low, sign changes	Stabilization of previous shape rotation.	
	$\varepsilon$	High, increasing.	Highly elongated shape, still elongating itself.	

#### 6.2.3.4. Summative image of morphomigrational building blocks

The summative characteristics of the cellular behavior that are observed with some specific sampling, can be considered as the set of cellular behaviors in time. Thus, the number of specific behaviors, their durations, their antecedence, and precedence will result in the different overall perception of cellular behavior. Such summative picture of three observed cells is shown in Figure 40. Distribution of each morphomigrational building block are presented in Figure 40 A, while the plots of turning angle, M.A. dynamics, and elongation against the sMM angle are shown in Figure 40 B. They give a bit less information than the previous analyses, however, they can serve as the visual aid in observing the overall cellular behavior, showing the similarities as well as differences between cells. It can be clearly seen that the behavior of the exemplary keratinocyte is described by some moderate and mostly high sMM angles of the same sign, representing perpendicular and askew movement, while low turning angles highlight the persistent migration direction. Different patterns are presented for the MEF 3T3 cell, for which most of sMM angles and turning angles are gathered around zero, with only a few points of higher values. This is the picture of lateral movement (low sMM angles and low turning angles) as well as lateral U-turns and lateral stretching (low sMM angles and high/very high turning angles). What is important, we are not able to properly assess in what order the behaviors occurred, therefore we would not distinguish the accidental U-turns from lateral stretching that is created by several U-turns each after another. The HEK293 cell exhibits a variety of morphomigrational behaviors that last

rather short times, which is represented by the chaotic pattern on the plot of sMM vs turning angle. Therefore, the turning angle and sMM angle have wide distributions, which describe lateral and perpendicular stretching and migration. What is interesting is that the distribution of M.A. dynamics for HEK293 and keratinocyte cells do not differ much from each other, which means that the stability of their shapes between frames is somehow similar. However, their arrangement in time sequence, as well as significant differences in the remaining building blocks (especially sMM angle), presenting their considerably different overall behavior. The proper understanding of histograms and patterns, as well as using them for complex conclusions will need further studies on a higher number of cells. However, they might be a useful tool to characterize different cell types based on their characteristic patterns.

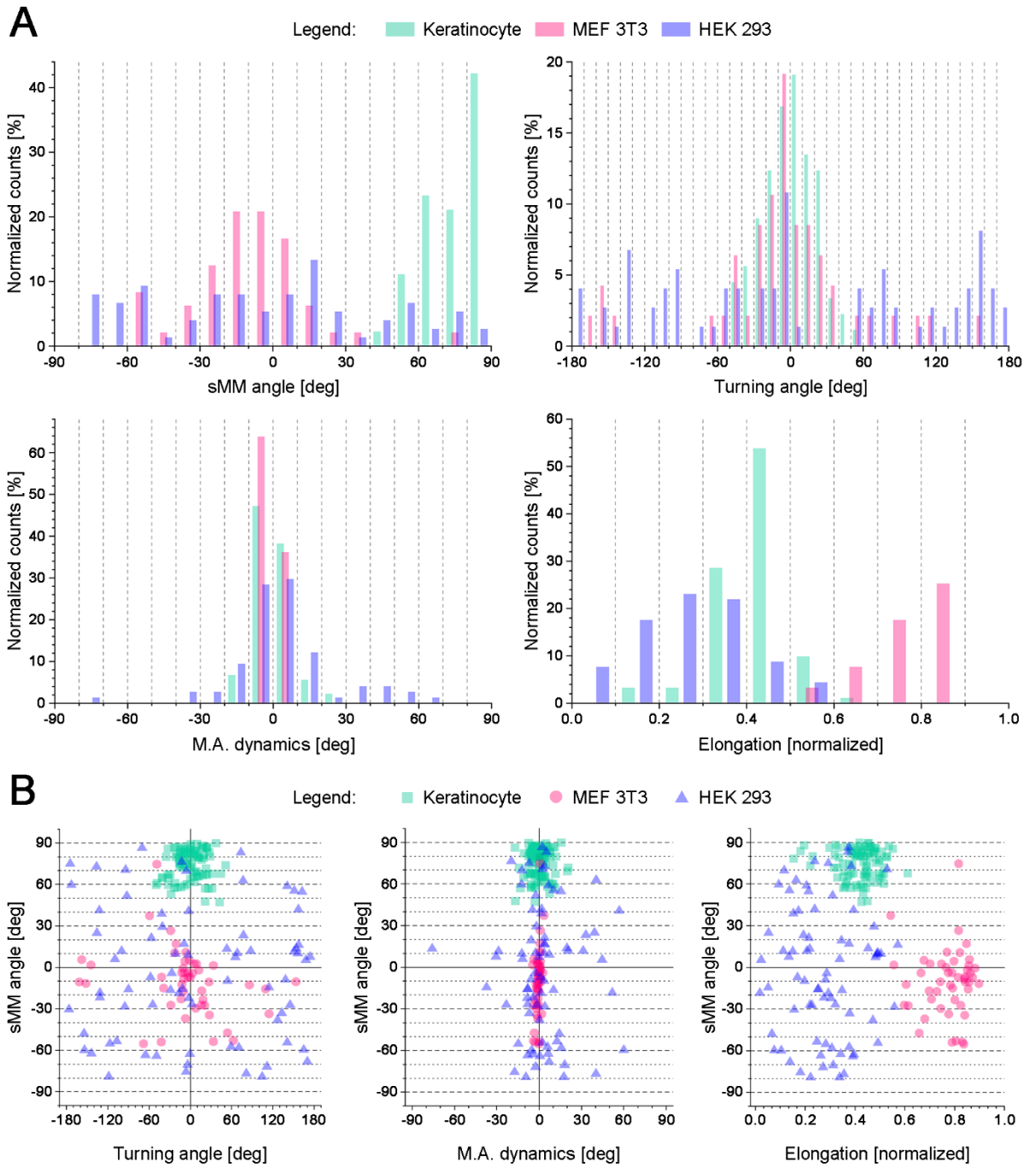


Figure 40. **A:** Histograms of all four building blocks calculated for three individual examined cells: keratinocyte, MEF 3T3 cell and HEK 293 cell. **B:** sMM angle plotted against turning angle, M.A. dynamics and elongation for three individual examined cells: keratinocyte, MEF 3T3 cell and HEK 293 cell. Adapted from <sup>234</sup>.

Table 16. Mean values of sMM angle, Turning angle, M.A. dynamics and Elongation for the three examined cells. Uncertainty was calculated as the standard deviation of each distribution. Adapted from <sup>234</sup>.

	sMM angle [deg]	Turning angle [deg]	M.A. dynamics [deg]	Elongation [normalized]
<b>Keratinocyte</b>	74.5 ± 10.8	-0.1 ± 21.6	0.1 ± 7.2	0.42 ± 0.08
<b>MEF 3T3</b>	-10.4 ± 23.9	-6.7 ± 62.6	-0.7 ± 1.6	0.77 ± 0.09
<b>HEK 293</b>	-4.9 ± 46.4	8.9 ± 114.7	0.4 ± 9.2	0.28 ± 0.14

#### 6.2.4. Summary of morphomigrational description

The signed morphomigrational angle (sMM) is to my knowledge the first such descriptor that links the orientation of cell shape (static descriptor in a specific time frame) with migration direction (dynamic descriptor that considers displacement between frames). The newly formulated parameters (sMM angle and M.A. dynamics) were combined with descriptors that already exist (turning angle and elongation) to create the new analytical method called *morphomigrational description*. It allowed for a quantitative description of cell migration and morphology, linking them under the one term of morphomigrational behavior, giving a chance to better understand cell dynamics. However, the three cells presented here are just early examples of the application of morphomigrational description, while the potential problems connected with the further analyses of whole populations are extensively analyzed in the discussion. Nevertheless, the creation of this new analytical method gives a great tool for further studies and comparative analysis of living cells in different experimental environments and stimulations.

### **6.3. Development of new experimental method for hybrid sensing of cellular traction forces and local temperature changes.**

The first two sections of results were focused on the analysis of biophysical aspects of cell migration and morphology, as well as the influence of elastic substrate on cancer heterogeneity. The third task of my thesis presents the development of a new method that allows for parallel measurements of cellular traction forces and relative local temperature, as yet another aspects of cell biophysics. The idea of incorporating the temperature measurements in the mechanobiology setup consisted of combining ODMR and TFM techniques, to perform the single ODMR-TFM experiments. Nevertheless, the experimental setup should also meet the three main objectives:

- Objective 1: the ODMR-TFM setup should be created with a standard wide-field inverted fluorescence microscope equipped with the CMOS camera and metal-halide fluorescence lamp. The reason behind this objective was the potential further application of similar setups in other life-science laboratories, without an expensive reconstruction of a microscope. Therefore, the resulting setup should not be made with additional light sources such as lasers.
- Objective 2: the accuracy of temperature measurement should be kept at ~1K level. Previous studies demonstrated an accuracy of 0.1K, which however required the confocal microscope or intensive laser illumination, and stayed in clear opposition to the first requirement. Therefore, the ~1K measurement accuracy was assumed to be useful in the live-cell imaging and mechanobiology studies, while being still possible to reach using the standard microscope setup.
- Objective 3: sample illumination and time of experiment should be as short as possible. The fluorescent light and microwaves can cause phototoxic effects, induce cell apoptosis and overheat the sample. Therefore, the decreased illumination and exposure to microwaves are crucial for a successful experiment. The expected time of a single ODMR measurement should be no longer than 5 seconds.

This part of the thesis was performed in the framework of the QUNNA Team-NET grant (POIR.04.04.00-00-1644/18). In this work, I was co-responsible for the study design, as well as for performing most of the experiments and data analysis, if not mentioned else.

#### **6.3.1. Experimental setup**

The experimental setup is presented in Figure 41 A. It consists of the inverted wide-field microscope with a large incubation chamber (I) and the external heating fan, which both maintain the specified temperature of the whole microscope environment. A 35-mm Petri dish

with an experimental sample (VI) is placed in the additional, on-stage mini-incubator (III), providing additional temperature stabilization. The sample is covered with a non-heated lid (IV) equipped with a window (VIII) for introducing a microwave antenna into the sample. Bulk temperature measurements are performed with the additional thermocouple placed inside the examined dish (V). The end of a thermocouple is placed on the left side of the inner well of the glass bottom dish, touching the surface of the well. A microwave antenna was made of a Cu rod of 0.2 mm diameter, creating a loop of 1mm inner diameter (X). The antenna was positioned  $\sim 250 \mu\text{m}$  above the substrate with living cells (IX) using the micromanipulator.

The simplified scheme of microwave equipment and its connection to the microscope setup is shown in Figure 41 B. Microwave generator serves as a source of microwaves as well as the camera trigger. Each new microwave signal triggers the next image of the time-lapse sequence, allowing the image acquisition. The ODMR signals, camera activity, and triggering signals were observed over the course of the experiment using the oscilloscope.

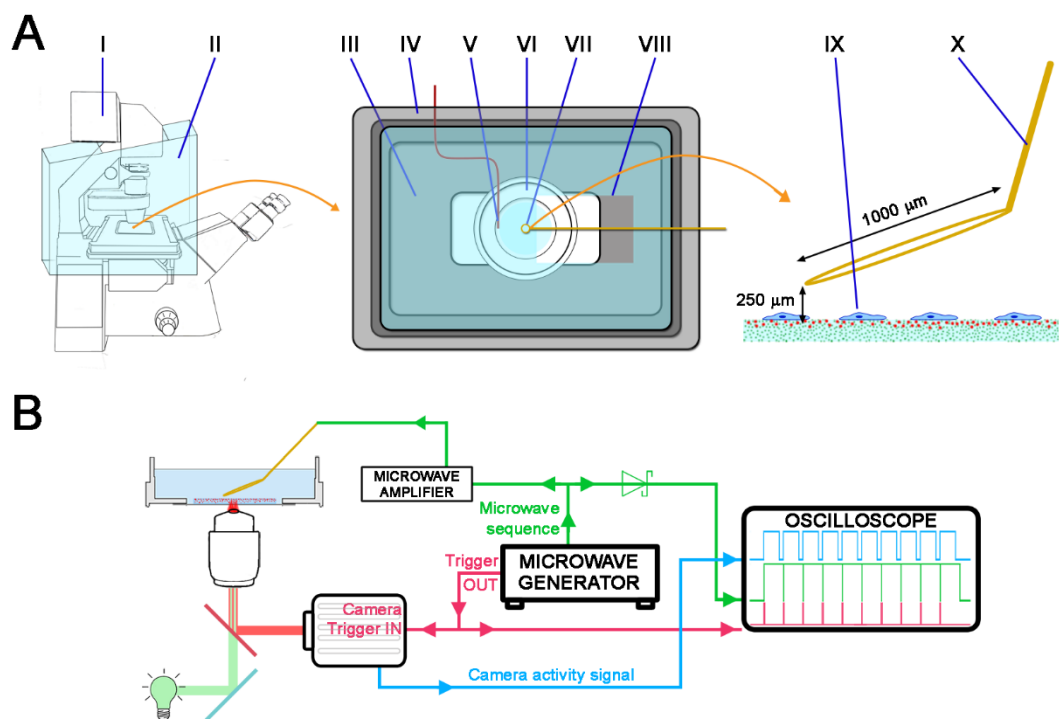


Figure 41. **A:** Scheme of cell incubation equipment and the microscope setup: I-Fluorescence microscope, II-large incubation chamber, III-on-stage mini-incubator (bottom), IV-incubator lid with (nonheated), V-thermocouple placed in the side of the inner well, VI-glass-bottom dish with a sample, VII-microwave (MW) antenna, VIII-window in the lid for the antenna, IX-cells, X- antenna (side view). **B:** Idea of microwave setup. Microwave generator serves as the microwave source as well as the camera trigger. All signals were observed with the oscilloscope.

The development of ODMR-TFM experiment consisted of three major stages: preparation of the suitable ODMR-TFM substrate, optimization of ODMR experimental conditions, and the final demonstration of ODMR-TFM proof-of-principle experiment.

### **6.3.2. Preparation and characterization of ODMR-TFM substrate.**

The ideal ODMR-TFM substrate should be characterized by the following properties:

- intensive fluorescence of NV<sup>-</sup> color centers for ODMR signal registration,
- properly visible TFM markers, low aggregation of diamond particles,
- presence of diamond particles in the top layer of the substrate,
- properly determined elasticity of the substrate for TFM calculations.

In this study, we decided to use microdiamonds of  $\sim 1 \mu\text{m}$  diameter instead of  $\sim 140 \text{ nm}$  diameter as shown in Figure 42 A. Microdiamonds contain many more color centers, which relates to their larger size. Therefore, they exhibit more intensive fluorescence and have better ODMR contrast. However, due to their size, microdiamonds are not suitable as TFM markers. Initially, the simple mixture of  $140 \text{ nm}$  diamonds (for TFM detection) and  $1 \mu\text{m}$  diamonds (for ODMR detection) was considered. Nonetheless, the intensive fluorescence of microdiamonds outshined the neighboring nanodiamonds and thus it was impossible to adjust the proper light balance of the TFM image, jeopardizing the TFM experiments. Therefore, we decided to register ODMR in the red channel and introduce green polystyrene (PS) beads for TFM detection.

The development of ODMR-TFM substrate started from the preparation of diamond suspension that could be introduced into the polyacrylamide (PA) polymerization mixture. Therefore, we examined microdiamonds with oxygenated (-O) and hydrogenated (-H) surface functionalization, which were further suspended in four different solvents to check for their potential aggregation. The first solvent was DI water which is also the solvent of the polymerization mixture. As a second solvent, we chose dimethyl sulfoxide (DMSO), which might work well with the hydrogenated surface due to the presence of methyl groups. What is more, it would be also miscible with aqueous solutions due to the presence of the S=O group. The two remaining solvents consisted of protein solutions: 2.5% Bovine Serum Albumin (BSA) solution in water and Fetal Bovine Serum (FBS) which is the protein cocktail used in cell culture media. Their use was inspired by previous work that reported the formation of protein corona on the surface of nanodiamonds when they were initially suspended in a protein solution. Such diamond preprocessing prevented them from aggregation<sup>235</sup>. The functionalization of diamond surface, as well as DLS measurements, were performed by Mateusz Ficek and Maciej Głowacki from the Department of Metrology and Optoelectronics, Faculty of Electronics,



Telecommunications and Informatics, Gdańsk University of Technology, Poland. Types of surfaces functionalization as well as solvents were chosen by the author of the thesis, after prior consultation with Maciej Głowacki (Gdańsk University of Technology), Mariusz Mrózek, Adam Wojciechowski (both from Photonics Department, Institute of Physics, Jagiellonian University) and Zenon Rajfur (thesis supervisor).

The initial screening was performed using non-fluorescent microdiamonds of similar size to the NV<sup>-</sup> diamonds. The application of non-fluorescent diamonds was dictated by their lower cost and thus the opportunity to prepare large sample volumes. Figure 42 B presents the hydrodynamic diameter distribution of oxygenated and hydrogenated diamonds. In Table 16 we can see the quantitative description of particles: Z-average diameter  $\pm$  SEM (see: Materials and methods) as well as 10<sup>th</sup>, 50<sup>th</sup>, and 90<sup>th</sup> percentiles. Among the oxygenated diamonds, the lowest  $Z_{Ave}$  diameter was observed for particles suspended in water, 2.5% BSA, and FBS. The lowest dispersion (SEM) and well as lowest percentiles were however observed for the water suspension. Among the hydrogenated particles, the ones suspended in DI water, DMSO, and 2.5% BSA have an acceptable  $Z_{Ave}$  diameter as well. However, due to the simplicity of the solvent, the combination of oxygenated surface and suspension in water was chosen for further studies. Even if the combination of oxygenated surface and protein solutions did also meet the criteria, they had to be also handled in sterile conditions, which would complicate the experimental procedure.

After the examination of nonfluorescent microdiamonds, the ultimate suspension of the oxygenated NV<sup>-</sup> microdiamonds in DI water (0.5 mg/ml) was prepared. Consistently with the results obtained for nonfluorescent  $\mu$ Ds, the hydrodynamic diameter of diamonds was sufficiently low (Figure 42 C, and Table 17). We could also see a low fraction of large aggregates (> 6  $\mu$ m), but they constituted less than 10% of the overall intensity measured by DLS. It is important to mention that the intensity plot does not measure the number of particles, but the percentage of light intensity reflected by particles of each size. Large aggregates reflect more light than smaller particles and thus the actual share of aggregates in the total suspension volume is expected to be even lower.

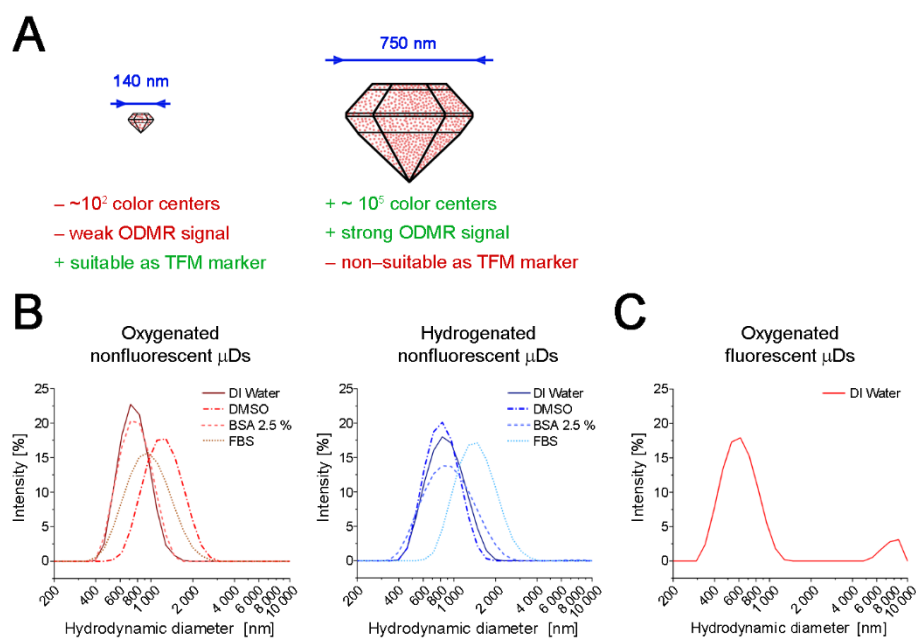


Figure 42. **A:** Comparison of nanodiamonds and microdiamonds. **B:** Hydrodynamic diameters of oxygenated and hydrogenated nonfluorescent microdiamonds suspended in different solvents. **C:** Hydrodynamic diameter of the final suspension of oxygenated NV<sup>-</sup> microdiamonds in deionized water.

Table 17. DLS characterization of hydrodynamic diameters of nonfluorescent (Non-NV<sup>-</sup>) and fluorescent (NV<sup>-</sup>) diamonds. Quantitative characterization presents the average hydrodynamic diameter ( $Z_{Ave}$ ), Standard Error of the Mean (SEM) as well as 10<sup>th</sup>, 50<sup>th</sup> and 90<sup>th</sup> quantiles ( $Di_{10}$ ,  $Di_{50}$ ,  $Di_{90}$ ).

NV <sup>-</sup> presence	Surface termination	Solvent	$Z_{Ave} \pm SEM$ [nm]	$Di_{10}$ [nm]	$Di_{50}$ [nm]	$Di_{90}$ [nm]
Non – NV <sup>-</sup>	-O	DI water	734 ± 88	546	754	1060
		DMSO	1145 ± 279	813	1220	1860
		BSA 2.5%	741 ± 108	540	767	1100
		FBS	887 ± 168	597	945	1540
	-H	DI water	818 ± 187	578	864	1310
		DMSO	798 ± 108	568	817	1200
		BSA 2.5%	851 ± 192	548	907	1570
		FBS	1267 ± 385	942	1430	2230
NV <sup>-</sup>	-O	DI water	734 ± 202	484	713	1260

The suspension of oxygenated NV<sup>-</sup> microdiamonds was used to prepare the elastic substrates of Young's modulus = 12 kPa. Elasticity, topography and the spatial distribution of fluorescence particles of substrates were characterized with AFM and confocal microscopy. Measurements of elasticity were performed for the blank substrates (without any additional particles), substrates with microdiamonds only, and the proposed ODMR-TFM substrate

(with microdiamonds and green fluorescent beads). The AFM experiments and their interpretation were performed by Agata Kubisiak from Department of Physics of Nanostructures and Nanotechnology, Institute of Physics, Jagiellonian University, while the substrate preparation was done by the author of the thesis.

As shown in Figure 43 A, the blank substrates show a similar elasticity ( $11.7 \pm 0.5$  kPa) to the one of similar composition that was found in the literature (12 kPa)<sup>208</sup>. This result proves the validity of the experimental protocol, allowing for reproducible results. Substrates with microdiamonds are slightly softer ( $E = 10.8 \pm 0.4$  kPa) and the addition of PS beads causes further softening of the substrate with the final elasticity of  $E = 9.6 \pm 1.6$  kPa. Therefore, the last of the mentioned values was taken into the TFM calculations. The lower value of Young's modulus is not the problem as far as it was validated experimentally and thus such substrate is suitable for further mechanobiology studies.

Another significant property of the substrate is the morphology of its surface. The AFM imaging revealed the presence of nanopits of with a depth <100 nm (Figure 43 B). We expect those wells to coincide with the presence of diamonds, which are placed in the top layer of the substrate. However, the verification of this hypothesis could be performed by further studies utilizing the combination of AFM and 3D superresolution microscopy. Considering the cellular scale, the nanopits are rather shallow, however, one can take them into account as an additional factor in further mechanobiology studies.

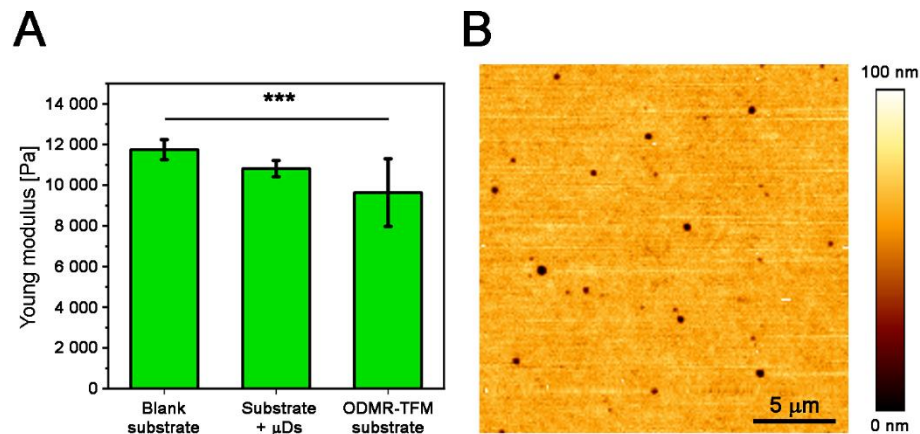
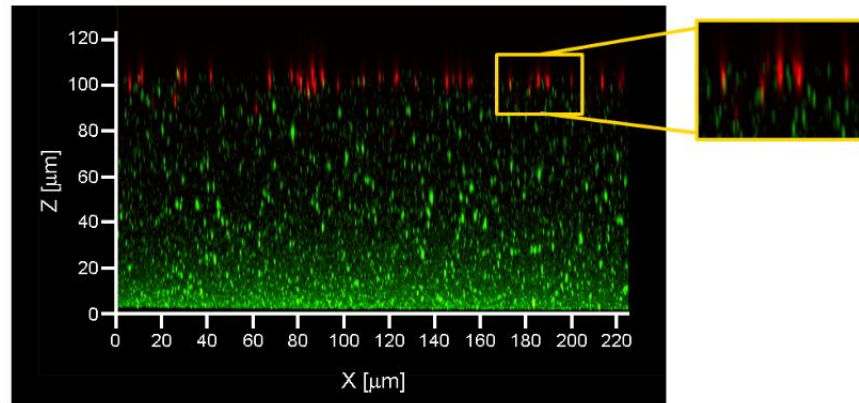


Figure 43. A: Young's moduli of different variants of elastic substrates. B: Surface morphology of the ODMR-TFM substrate

Figure 44 presents an exemplary Z-section 3D confocal scan of the ODMR-TFM substrate, showing that microdiamonds are positioned in the top layer of the substrate. However, they were not placed exactly at the same height, but their Z-position differs slightly from one another (see the magnified fragment). Such positioning was the result of upside-down substrate

polymerization that allowed for microdiamonds sedimentation. What is more, the light green fluorescent beads made of polystyrene could flow to the top of the polymerizing substrate, which resulted in their higher presence at the bottom of the substrate. Nevertheless, the number of beads in the top layer was sufficient for the TFM experiments.



*Figure 44. Cross section of ODMR-TFM substrate from a confocal scan.*

The whole characterization of the substrate proves that the first step consisting of ODMR-TFM substrate development was successful and therefore, it was possible to proceed with the second stage focused on the optimization of ODMR experiment conditions.

### **6.3.3. Optimization of ODMR experimental conditions.**

The next stage of the study consisted of the optimization of ODMR experimental conditions to decrease the sample illumination intensity and experiment time. In the first step, we examined how the method of data processing influenced the accuracy of temperature measurement. Figure 45 and Table 18 demonstrate that fitting two Lorentzian functions to the ODMR spectrum results in the less precise determination of ODMR central frequency (zero-field splitting value), than fitting only one Lorentzian function to the central part of data. Temperature uncertainty was calculated assuming the  $-74.2$  K/kHz relation of ODMR shift to the temperature change <sup>204</sup>.

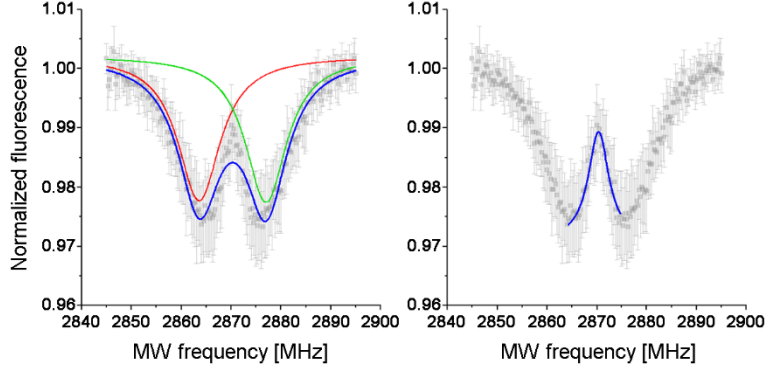


Figure 45. Comparison of fitting the same ODMR spectrum by two Lorentzian functions (left) and one Lorentzian function (right).

Table 18. Comparison of fitting procedure on the resulting temperature accuracy.

	2 Lorentzian functions	1 Lorentzian function
<b>Fitted peak center uncertainty</b>	$\Delta x_{c1} = 114.5 \text{ kHz}$ $\Delta x_{c2} = 111.4 \text{ kHz}$	$\Delta x_c = 55.0 \text{ kHz}$
<b>Averaged fitted peak center uncertainty</b>	$\overline{\Delta x_c} = 112.9 \text{ kHz}$	$\overline{\Delta x_c} = 55.0 \text{ kHz}$
<b>Expected temperature uncertainty</b>	$\Delta T = 1.52 \text{ K}$	$\Delta T = 0.74 \text{ K}$

This result opened the possibility of probing only the central region, between the two resonance peaks, which would shorten the microwave sequence and thus substantially decrease the experiment time. Because of that, the ODMR optimization started from developing of a so-called “Irregular Sequence” (abbrev: Irreg Sequence or Irreg Seq), which probes only the central peak in the range of 2864 – 2874 MHz with a 0.25 MHz frequency step, supplied with additional 6 out-of-resonance points that are used for signal normalization (3 points in the beginning and 3 points at the end of the sequence). The frequency range was chosen with the assumption, that potential live-cell imaging will be performed in the temperature range of 20°C - 45°C. Therefore, the chosen frequency range is related to the theoretical expectations of resonant frequencies in that temperature range. The regular ODMR sequence between 2845 and 2895 MHz with a 0.25 MHz step served as the reference and was further called the “Regular Sweep”, as mentioned in Materials and Methods.

Previous studies measured ODMR temperature shifts by fitting the whole ODMR spectrum<sup>236</sup> or, by contrast, reducing the ODMR spectrum acquisition into 6 points, symmetrically around the center, that were then processed by linear regression<sup>205,237</sup>. However, we observed that ODMR spectra averaged for several diamonds have the central peak sufficiently visible to fit there a single Lorentzian function. The method of analyzing ODMR spectra is shown in Figure 46. In the first step, the computer program retrieved all spectra that were available in the image. This program

was provided by Saravanan Sengottuvel from Photonics Department, Institute of Physics, Jagiellonian University. The second step relied on the selection of those ODMR spectra that met three quality criteria: 1) at least 1% of ODMR contrast (defined by fluorescence decrease), 2) the uncertainty of the fitted peak height should be lower than the peak height itself ( $\sigma H/H < 100\%$ ), and 3) the  $R^2$  factor of the fitted peak should be equal or greater than 0.5. These criteria were constructed to elucidate even the weakest ODMR spectra, in order to collect them from as many diamonds as possible. In the third step, the chosen spectra were averaged and fitted with Lorentzian function, to determine the relative temperature by comparing the resonance shift in the fourth step.

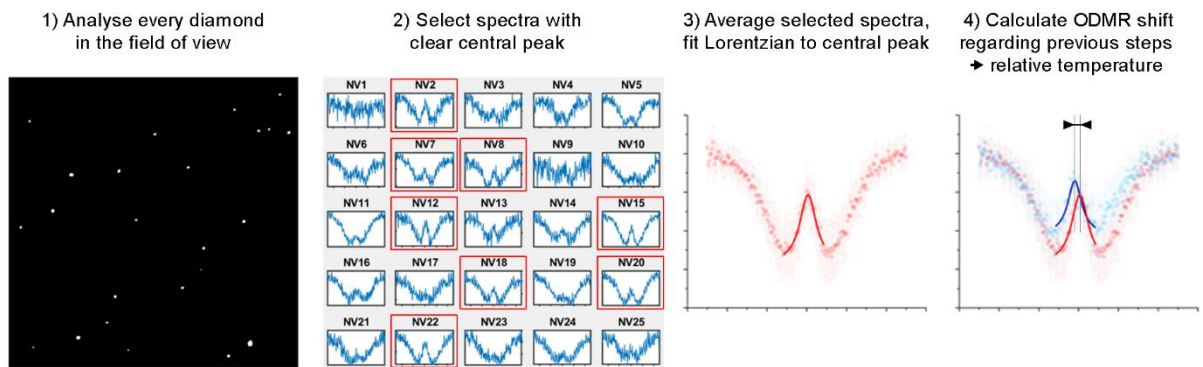


Figure 46. Idea of calculation the relative temperature that is averaged in a field of view.

In the further optimization of the ODMR experiment, we have considered the interplay of three parameters: 1) substrate thickness, 2) excitation intensity, and 3) type of microwave sequence (and thus the time of the experiment). These three factors were analyzed with regards to the accuracy of temperature measurement as well as the number of diamonds that were included in the analysis. The increased number of diamonds analyzed in each field of view should increase the reliability of the average temperature measurement because the information comes from more points across the substrate. Testing the substrate thickness consisted of three types of substrates: thin ones (20-40  $\mu\text{m}$  thickness) that are too thin for mechanobiology applications, medium ones (50-70  $\mu\text{m}$  thickness) that should be good enough for mechanobiology studies, and thick substrates (100-120  $\mu\text{m}$ ) that provide the comfortable experimental setup for mechanobiology studies. The excitation intensities were measured from the highest one obtained for this setup (25  $\text{W}/\text{cm}^2$ ) and then scaled down to the lower excitation intensities. We have also analyzed five microwave sequences: the Irregular Sequence averaged 1, 2, 3, and 4 times, as well as the Regular Sweep that serves as the reference measurement. These five microwave sequences determine the duration of the ODMR experiment for: 1.2 s, 2.4 s, 3.5 s, 4.7 s, and 5.1 s, respectively.

Figure 47 shows that the uncertainty of temperature measurement decreases with the increased thickness of the substrate, assuming the ODMR temperature response equal

to 74.2 kHz/K<sup>204</sup>. This might be caused by the fact, that substrates were produced in the glass-bottom dishes of #0 thickness (80  $\mu\text{m}$  - 130  $\mu\text{m}$ ), instead of #1.5 thickness (160  $\mu\text{m}$  - 190  $\mu\text{m}$ ). Therefore, the standard objective calibrated for the #1.5 thickness would lose some incoming light and therefore lower the ODMR quality. The satisfactory uncertainty of temperature measurement that met <1K accuracy including the error bar ( $0.76 \pm 0.16$  K) was found for the combination of 15W/cm<sup>2</sup> illumination and the Irregular Sequence averaged twice. Therefore, it was possible to decrease the ODMR collection down to 2.4 sec. Also, the number of diamonds (Figure 47, bottom row) for those conditions was found to be satisfactory ( $12.6 \pm 2.07$  diamond particles) and thus these experimental conditions were used in further work.

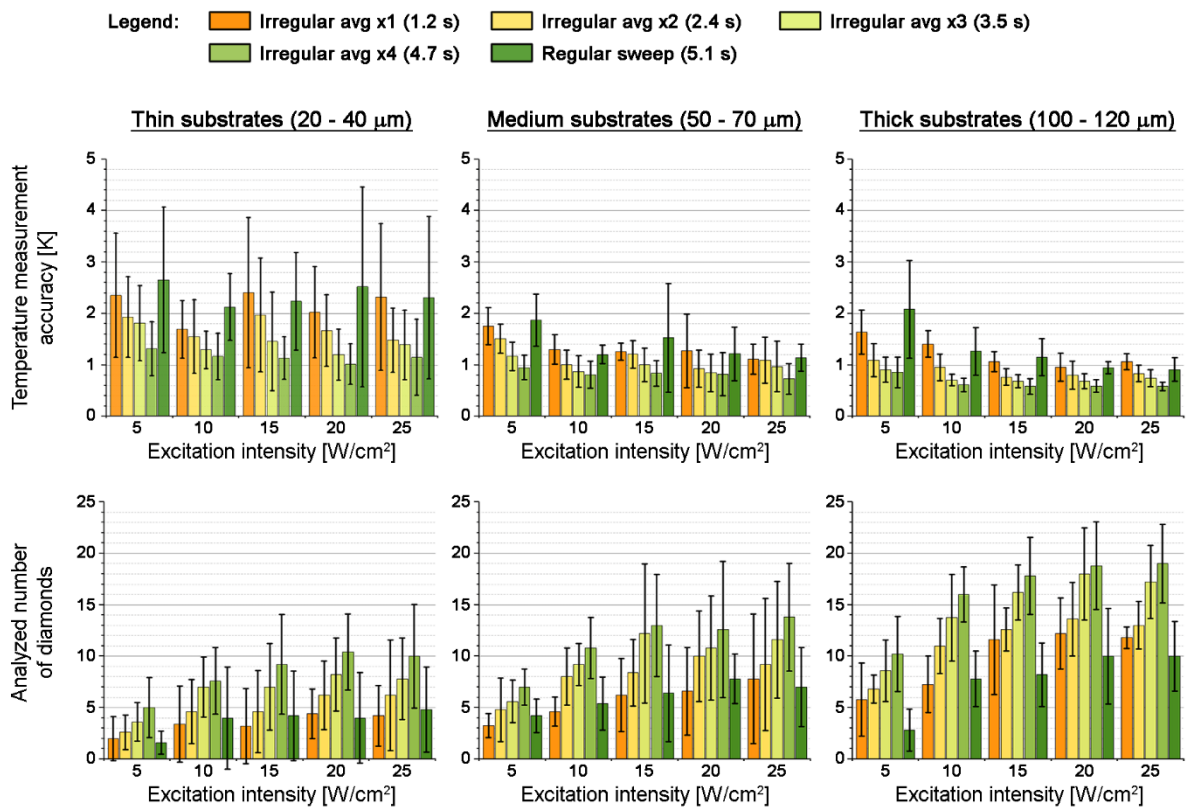


Figure 47. Optimization of ODMR experiment. Top row: influence of experimental parameters on the temperature measurement accuracy. Bottom row: influence of experimental parameters on the number of diamonds included in the analysis.

The last element of ODMR optimization required the temperature calibration of the ODMR resonance shift observed in our setup. The most commonly used value of ODMR temperature shift is -74 kHz/K around room temperature and comes from its experimental determination<sup>204</sup>. In Figure 48 we compared the Irregular Sequence that was chosen for further experiments with the Regular Sweep, to verify whether the use of our ODMR-TFM substrates enables the tracking of relative temperature changes accurately. Both slopes (Table 19) are close to the literature data, and therefore we can assume that our setup can properly measure the relative

temperature using microdiamonds and we can use the literature shift coefficient value in our experiments.

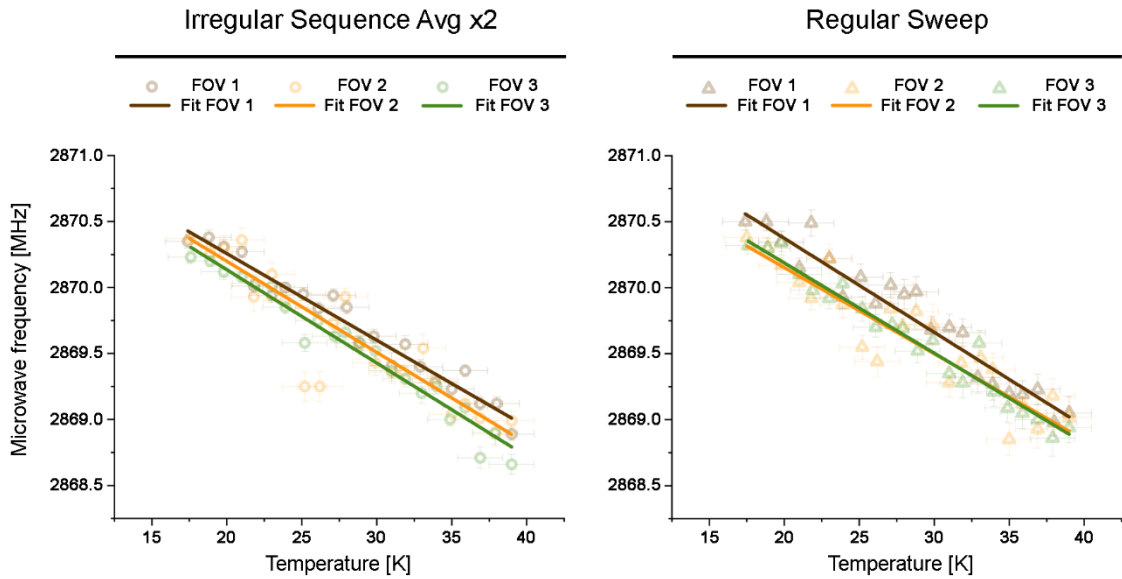


Figure 48. Temperature calibration of ODMR-TFM substrates. The chosen Irregular Sequence averaged twice and Regular Sweep were compared.

Table 19. Slopes of linear functions fitted to the temperature calibration data.

	Calibration slope [kHz/K]	
	Irregular Seq avg x2	Regular Sweep
Position 1	$-65.6 \pm 3.0$	$-71.2 \pm 3.8$
Position 2	$-69.0 \pm 5.3$	$-65.2 \pm 5.6$
Position 3	$-70.7 \pm 2.7$	$-68.3 \pm 3.2$
Averaged	$-68.4 \pm 3.6$	$-68.2 \pm 4.2$

### 6.3.4. Proof-of-principle ODMR-TFM experiments

The optimized experimental procedure was used in the proof-of-principle experiments that show the applicability of ODMR-TFM measurement for adherent cells subjected to cooling, heating, and maintenance of constant physiological temperature. Figure 49 A presents the relative temperature measured locally by the diamonds and globally by the thermocouple, as well as the mean traction forces in consecutive time frames. The three timepoints highlighted in the plot are presented in Figure 49 B-D. While the temperature decrease measured by the thermocouple seemed to be smooth, the temperature measurements registered by diamonds were characterized by the step-like decrease. This irregularity might have been caused by the method of cooling which consisted of placing refrigerated icepacks inside the chamber, to decrease the temperature around the sample. The timepoints in which the diamonds indicated the rapid drop of temperature



coincided with the moments of adding the next icepacks into the incubation chamber. The slower answer of the thermocouple might be caused by the fact that the dish was not cooled evenly in the whole volume, and the cell medium was cooled later than the substrate itself.

The mean cellular tractions initially decrease, then they increase, and consecutively decrease again, to recover for the second time at the end of the experimental sequence. Such fluctuation of cellular tractions in time is a standard feature of the cell and does not indicate any anomalous processes. The maps of unconstrained tractions show that cellular tractions are exerted in some defined parts of the cell, being also visibly distinct from the background, providing the proper quality of TFM measurement.

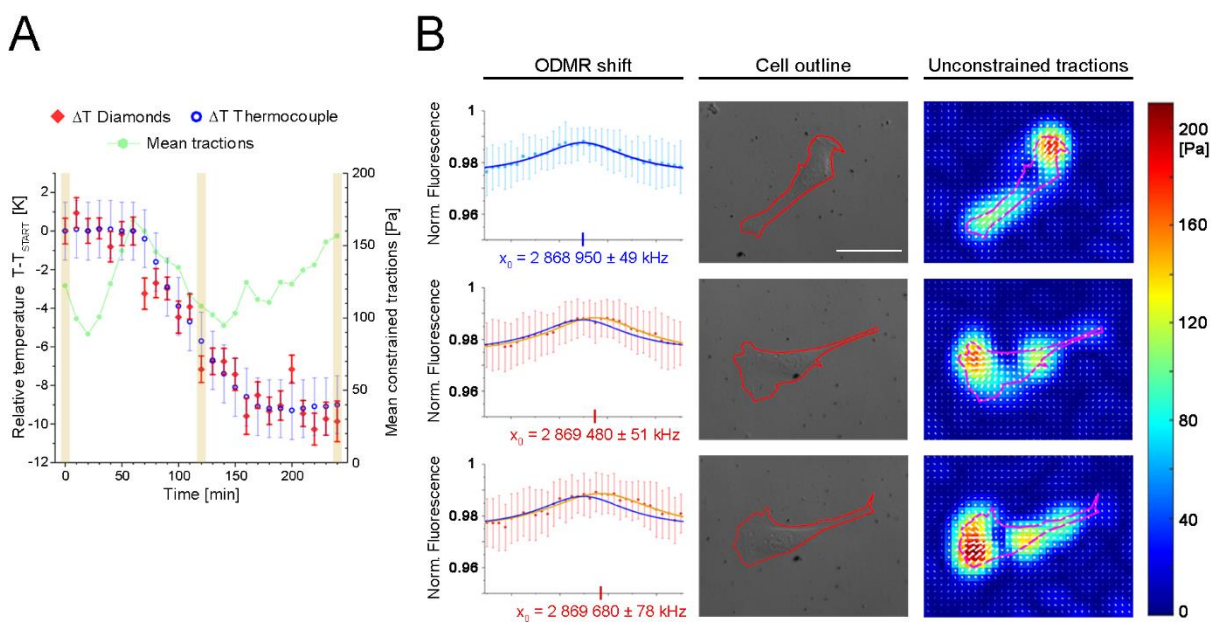


Figure 49. Proof-of-principle observation of cell cooling using the ODMR-TFM technique. **A:** Time evolution of relative temperature and cellular tractions. **B:** ODMR shift, cell outline and map of unconstrained tractions.

The exemplary application of the ODMR-TFM method for cell medium heating is shown in Figure 50. The temperature measured by diamonds and the thermocouple is more consistent than for cooling, which was possibly caused by the more stable method of sample heating that just required setting the incubator to the desired temperature. However, at some timepoints, there are some visible differences between temperature measurements which result from differences between global and local temperatures as well as the instantaneous reaction of diamonds to the changing temperature. What is more, the accuracy of diamond temperature measurement is significantly better than the one made by thermocouple. Cellular tractions fluctuate there as well, which is just a standard cellular behavior. The maps of unconstrained tractions confirm the proper quality of TFM measurement.

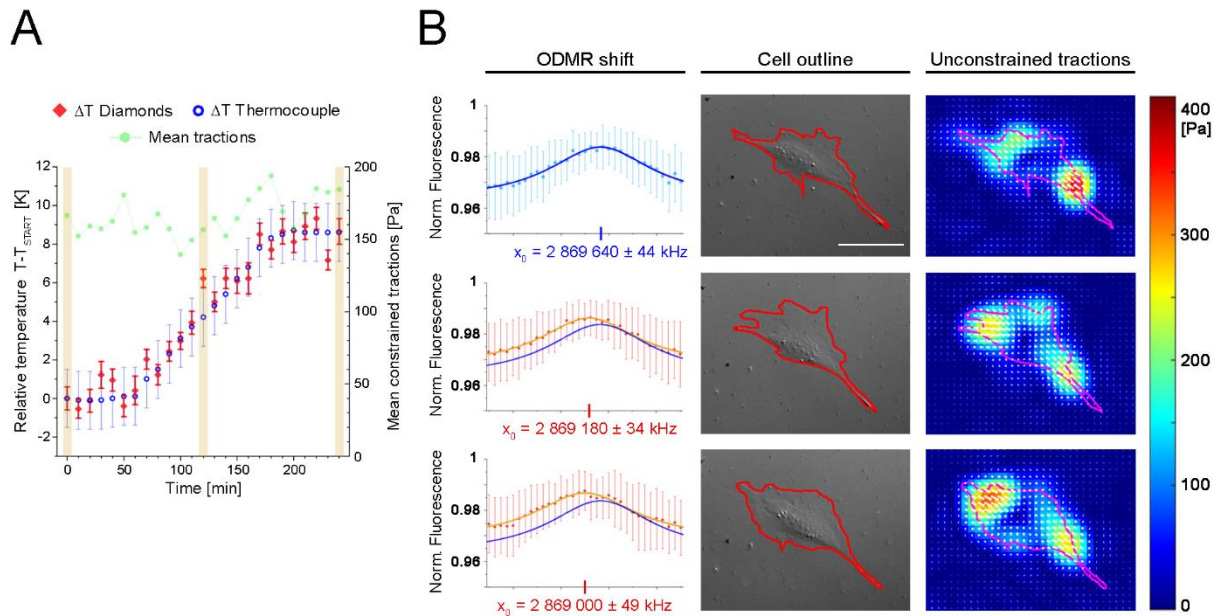


Figure 50. Proof-of-principle observation of cell heating using the ODMR-TFM technique. **A:** Time evolution of relative temperature and cellular tractions. **B:** ODMR shift, cell outline and map of unconstrained tractions.

Figure 51 presents the temperature measurement in the conditions of thermal stability. While the thermocouple readout seems to be stable, the temperature measurements done by diamonds reveal the local differences in the temperature. These changes can be observed due to the faster temperature readout by the diamonds, as well as the uneven heating of the sample. The map of traction forces again confirms the quality of TFM measurements. The lower quality of the DIC image of the cell was caused by the presence of antennae in the path of transmitted light, causing the formation of additional shades. The ODMR plots confirm the slight fluctuations of the resonance peak, which illustrate the temperature changes.

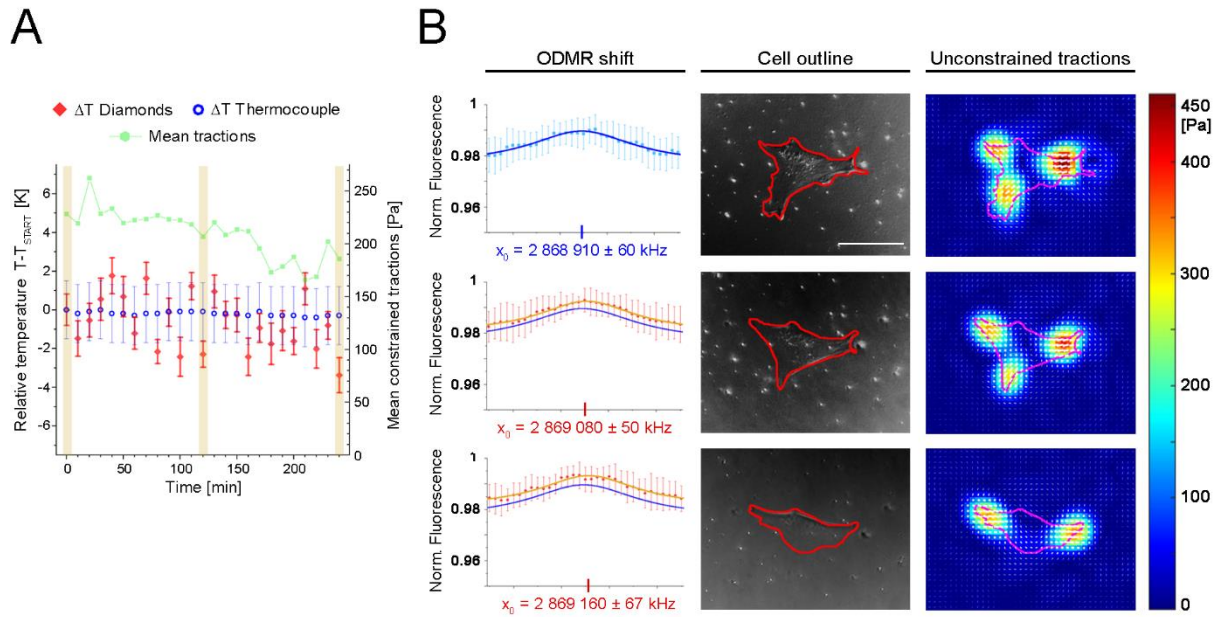


Figure 51. Proof-of-principle observation of cell in stable temperature using the ODMR-TFM technique. **A:** Time evolution of relative temperature and cellular tractions. **B:** ODMR shift, cell outline and map of unconstrained tractions.

### 6.3.5. Summary of the ODMR-TFM technique development.

In this chapter of results, we have aimed to incorporate the ODMR measurement of temperature into the mechanobiology studies. The first objective of the simplicity of the microscopic setup was achieved since the experimental setup was constructed on the standard wide-field fluorescence microscopy that is used routinely for live-cell imaging. The resulting elastic substrate had defined elastic properties and the diamonds were placed in the top layer of the substrate, just beneath the cells. The further optimization of ODMR experimental conditions allowed us to reach the  $<1$ K accuracy of temperature measurement as well. What is more, the exemplary proof-of-principle experiments of the ODMR-TFM technique were performed on living MEF 3T3 cells. Therefore, the combination of two existing methods required the optimization of several elements of ODMR and TFM techniques to make their applicable combination the live-cell imaging.

Nevertheless, this technique might be further improved by the next optimization steps, as well as the application of different types of objectives, detectors, microwave equipment, etc., which is described in the discussion section. However, the optimization of potentially harmful physical technique in microscopy experiments is a great achievement itself and opens new perspectives in mechanobiology by monitoring the temperature as an additional physical parameter.

## 7. Discussion

### 7.1. Application of time-lapse microscopy and biomimetic elastic substrates in cancer heterogeneity studies.

The first part of results shown how the application of time-lapse experiments, dynamic analysis of cellular subpopulations, and elastic polymer substrates were improved the understanding of heterogenous of adherent subline of WC256 cells.

The first consequence of the dynamic classification of WC256 subpopulations was the identification of a larger number of mesenchymal (lamellipodia-creating) than polygonal and bigonal (nonpolar) cells cultured on a glass substrate. This result stands in opposition to previous literature data <sup>211</sup> which reported the dominance of nonpolar cells. This difference might arise from the method of cell classification, since the previous study was based on the description of static images, without their dynamic context. In such classification, some mesenchymal cells with poorly distinguishable lamellipodia could be misleadingly classified as nonpolar cells. This fact highlights the usefulness of time-lapse observations and dynamic cellular classification in the studies of heterogenous of cells. However, this change might be also caused by the presence of fibronectin coating, which was applied here, but not in the previous work <sup>211</sup>. The current literature shows that the different protein coating can have a significant impact on cellular adhesion and morphology <sup>238,239</sup>.

Another novel and biologically significant result enabled by the dynamic approach was the observation of the dynamic heterogeneity of WC256 cells. It has shown that the given morphology and migration strategy do not need to be the constant feature of the population. The analyzed cells were capable of spontaneous transformation into different subpopulation and such transitions could occur several times for the same cells. Therefore, the existence of cellular subpopulations is the dynamic and reversible feature of WC256 cell line. Current studies provide several examples of AMT and MAT transitions. However, up to now their occurrence was always caused by the additional chemical or physical stimulation of cells, such as interfering with small GTPases, cytoskeleton, and cell-ECM interactions. Blocking of RhoA activity was shown to induce AMT transition <sup>240-243</sup>, while the activation of Rho-ROCK pathway as well as activation of RhoA caused MAT transition <sup>244-248</sup>. Another way of MAT transitions was to influence the actin network organization or the interactions between the actin cortex and plasma membrane in several ways: by the total disruption of actin cortex, <sup>249,250</sup>, weakening of actin cortex <sup>251-254</sup>, weakening the coupling between actin cortex and plasma membrane, or disrupting the direct attachment of the plasma membrane to an actin cortex <sup>255-258</sup>, as well as rapid contraction of myosin II <sup>106</sup>. The third way consisted of the modification of cytoskeleton-ECM interaction by increasing

the cortical tension<sup>130</sup>, alteration of ECM adhesiveness<sup>257</sup>, introducing the confinement combined with surface modification<sup>218</sup>, inhibition of Focal Adhesion Kinase<sup>259,260</sup>, modification of focal adhesions<sup>261-263</sup> and several other ways that were reviewed in the work of Alexandrova et al.<sup>91</sup>. The previous study of Sroka et al. showed that the stable shift from amoeboid to mesenchymal form required the long-term cell culture that caused the epigenetic modifications, not taking into account the fast changes between subpopulations<sup>211</sup>. Most of the transitions observed in this work were not the proper MAT or AMT, however many cells were able to significantly change their characteristics by losing or establishing polarization that resulted in more directional movement. However, the small fraction of cells, performed the proper AMT/MAT transition either by passing through the polygonal and bigonal subpopulation, as well as through the direct transition. To the best knowledge of the author, this is the first such observation of spontaneous AMT/MAT transitions in the two-dimensional *in vitro* culture. The reason behind observation of this phenomenon could also be a 4-hour observation period, which was densely sampled (each 90 seconds). Further time-lapse studies of migrating heterogeneous cancer cells might therefore be a significant way to increase the depth of understanding of cancer functioning.

What is more, the velocity of amoeboid subpopulation cultured on glass is lower than previously reported, while the velocity of mesenchymal cells is similar to the “lamellipodia-creating cells” measured in a previous study<sup>231</sup>. The dissimilarities between amoeboid cells can be explained by their different origin. In the previous study, they were derived directly from the non-adherent subline, which resulted in effective migration driven by frontal blebs. Alternatively, amoeboid cells in this study were already present in the adherent subline, constituting ~10% of the total population. Therefore, the epigenetic differences between non-adherent subline used before and the adherent subline used here might cause this difference. This hypothesis is also supported by the fact, that the mesenchymal cells in both studies have similar velocities.

Further studies on this newly described phenomenon of dynamic heterogeneity can be improved by increasing the number of measured cells, as well as extending the time of the experiment while keeping the dense sampling interval. However, this approach could meet a simple practical obstacle that comes from the current form of dynamic classification of subpopulations. As it was presented in Materials and Methods, the assignment of cell subpopulation for each frame was performed by the visual examination not only of the current frame but also evaluation of two precedent and following frames, and application of previously described qualitative criteria. As a result, several thousands of frames were analyzed here in order to elucidate significant biological information. Increasing the number of cells, as well as time length of the experiment will dramatically increase the number of frames subjected to further

analysis. Therefore, the progress in this field might be enabled by the development of the robust, automatic, and quantitative analysis of WC256 subpopulations that could work with large datasets of migrating cells.

The elastic polyacrylamide substrates of 40 kPa elasticity were used here as the biomimetic material to simulate the elasticity of breast tissues. It is an elasticity similar to the one found for the breast parenchymal tissue which elasticity lies between 30 and 50 kPa<sup>56</sup>. However, it is worth mentioning that the breast tissue itself is quite complicated from the physical point of view. It consists also of fat tissue ( $E \sim 7$  kPa), while the breast cancer cells can display a wide range of elasticities, between 10 and 100 kPa, depending on their malignancy<sup>56,57</sup>. However, as this type of cancer came from the rat mammary gland<sup>264</sup>, we decided to examine cells exposed to the substrate of 40 kPa elasticity. In this study, the elastic substrate influenced the WC256 cells in three different aspects: the occurrence of subpopulations, characteristics of subpopulational transitions, and the biophysical properties of subpopulations.

The mesenchymal subpopulation was the largest one found on the glass substrate, while on the PA substrate, the polygonal and bigonal cells constituted the majority of the sample. Also, the share of amoeboid subpopulation was higher on PA substrate than on glass. Therefore, it creates the picture of the specific “shift”, from the predominant mesenchymal subpopulation on glass substrate towards the polygonal or bigonal and amoeboid subpopulations predominant on elastic PA substrate. What is important, the total occurrence of amoeboid subpopulation was not only caused by the increased number of stable amoeboid cells but also by the transitions from other subpopulations to the amoeboid one. This “shift” towards amoeboid subpopulation can be possibly caused by the difficulty in the creation of cell-ECM adhesions on 40kPa substrate. Current literature shows that softer substrates can promote the pseudopodal and blebbing migration over the mesenchymal migration<sup>39</sup>. What is more, amoeboid cells play a significant role in cancer cell migration<sup>265</sup>. The indirect evidence suggests that the invasiveness and stemness of model cancer cell lines such as MDA-MB-231 (breast cancer) and A375M2 (melanoma) correlate with the PKC $\alpha$ -dependent amoeboid migration<sup>266</sup>. What is more, the amoeboid cells do not produce strong adhesions that can secrete metalloproteinases and therefore the switching between mesenchymal and amoeboid migration is one of the ways of avoiding the therapies targeted on the proteolytic enzymes<sup>267</sup>. Even more, the current models show that amoeboid migration can also be preferred in heterogeneous microenvironments, which are more common in vivo conditions<sup>268</sup>.

The application of PA substrate showed that the mechanical properties of microenvironment have a profound impact on the heterogeneity of the adherent subline of WC256 cells. Among the current reports, one can find that substrate elasticity alters various

processes in physiological and pathological cells, such as cell spreading <sup>269,270</sup>, morphology <sup>271–273</sup>, migration velocity <sup>134,269</sup> migration directionality <sup>134,274</sup>, cell proliferation <sup>68,270,272,275</sup> or actin organization <sup>269,274,276</sup>. The importance of substrate elasticity was also discussed in the context of tumor progression <sup>70,71,74,75,77,79,80,275,277</sup>. Parallely, many different factors were considered in the context of tumor heterogeneity, including epigenetic changes and genetic evolution <sup>278</sup>. However, there were no studies on the influence of the mechanical microenvironment on cellular heterogeneity yet. Our results showed that the application of biologically more relevant, biomimetic elastic substrate can influence the distribution of subpopulations and therefore the cancer heterogeneity. Therefore, as cellular heterogeneity is an important factor in oncological diagnosis and treatment <sup>221,278,279</sup>, further studies on subpopulational dynamics will give a better insight into the mechanism of cancer behavior. This is also an extremely important finding in the context of research on cancer cell migration which is an underlying mechanism of cancer metastasis.

Besides the subpopulation distribution, subpopulational transitions, and duration of subpopulations, PA substrate influenced also the morphology and migration of WC256 cells. However, its impact on biophysical parameters of migration and morphology was not uniform among investigated subpopulations as well as the whole cell population. The mesenchymal subpopulation was mostly affected in the context of cellular shape. These cells were rounder and smaller on elastic substrates, while their other quantitative descriptors were not altered much. The polygonal and bigonal subpopulation was not influenced in the context of its velocity, turning angles, and elongations, while the only difference was observed for cell area and perimeter/area ratio. In contrast, the amoeboid subpopulation velocities, turning angles, areas and perimeter/area ratios were highly influenced between different types of substrates. The current literature describes the influence of substrate micromechanics on cell area, velocities, or persistence that depend on elasticity <sup>68,134,269,270,274</sup>. However, the cell lines used in these studies were not heterogenous or the analysis of subpopulations was not the subject of the studies. What is important, the influence of the elastic substrates on different subpopulations does not need to be followed by the averaged image of the whole population, which in most cases was influenced differently that each subpopulation separately. This observation highlights the need for a separate analysis of each subpopulation in heterogenous cell lines, which was already proposed by Altschuler & Wu <sup>220</sup>.

To better understand the mechanism behind the shift towards the amoeboid subpopulation, as well as the reasons for subpopulational transitions, further studies should examine wider ranges of elasticities, various substrate surface protein coatings and dimensional constraints <sup>39</sup>. In this study, we employed polyacrylamide and glass substrates and covered them

with fibronectin at the same concentration. However, besides the substrate elasticity, the observed phenomena might also be dependent on other micromechanical factors. For example, the mechanisms of ECM binding to the PA and glass substrates differ, so even if a similar concentration of protein solution was provided, the resulting density of ECM might differ between samples. It is an important factor since the different concentrations of ECM can modify cell spreading<sup>238</sup>. The PA and glass substrates also differ in porosity. While glass is smooth, the PA gels have pores whose diameter can reach up to 45 nm for 30 kPa substrates<sup>280</sup> which are slightly softer than the ones used in our work. Since the 40 kPa substrate used here is slightly stiffer, the expected pore size might be even smaller. However, the reaction of living cells does not need to be influenced by substrate porosity, being predominantly dependent on elasticity<sup>280</sup>. Because of that, we assume that elasticity might be the main factor responsible for all differences in WC256 cells seeded on elastic substrates. However, further studies will need to take into account the aforementioned micromechanical factors in order to fully understand the reported phenomenon.

The discovery of the dynamic heterogeneity phenomenon was enabled by the application of the already known time-lapse observation method in the new subject, i.e. cancer heterogeneity. What is more, the application of the mechanically relevant elastic substrate showed the altered dynamics of cancer cells, giving a more reliable image of the processes that occur among the soft tissues in the organism. Therefore, the combination of the already existing techniques with a new subject lead to novel and significant conclusions that are of great importance for cancer biology.

## **7.2. Development of morphomigrational description**

In section 6.2 of results, cell migration and morphology were unified under one name: *morphomigrational behavior* which verbally describes the temporal cellular actions. To describe the morphomigrational behavior, we have built the quantitative *morphomigrational description* that introduces two novel parameters (sMM angle and M.A. dynamics) and combines them with the two already existing ones (turning angles and elongation). This combination made possible to describe four aspects of cellular behavior in a particular frame: (I) the direction of displacement regarding the cell shape, (II) dynamics of cell shape, (III) the magnitude of cell direction change and (IV) elongation of cell shape. These four building blocks were then used to assign the set of quantitative values to various morphomigrational behaviors, such as perpendicular or lateral migration, parallel stretching, turning back along the major axis, tail retraction, and many others. To my knowledge, the sMM angle is the first such parameter that links migration direction with cell morphology by coupling a static cell shape, with the displacement direction which is a dynamic parameter calculated between two frames.



There are some metrics that can be compared to sMM angle. The orientation of the cell regarding the patterned substrate links the cellular arrangement on a 2D plane with the extracellular topographical cues <sup>151,155</sup>, however, it does not consider the migration direction. Alternatively, the tensor of an individual moment of inertia shows the predominant migration direction on the 2D plane, while not linking it with the cell shape <sup>143,158</sup>. There were also some studies focused solely on the dynamics of cell shape. The Fourier descriptors of shape dynamics were introduced by Tweedy et al., while the VAR model in TSRVF-PCA space that quantifies the outline dynamics was introduced by Deng et al. <sup>157</sup>. Another approach was assumed by Harris et al. <sup>281</sup> who introduced the DECCA parameter (Dynamic Expansion/Contraction of Cell Area) that describes the “total amount of cell motion over time”. As was clearly stated by the authors of that work, DECCA is not able to distinguish between the migrating cell that changes its position from the non-motile cell that evince an intensive membrane ruffling. Nevertheless, neither of those dynamic descriptors of cell shape tried to couple migration direction with the cell shape, as sMM angle does. Therefore, the sMM angle parameter provides a new quantitative description that can be used for the accurate illustration and further identification of cellular behavior.

The plethora of current quantitative descriptors of cell migration and morphology provides the proper understanding of many different aspects of cellular functioning. However, they describe each aspect separately, giving significant, but still fragmentary information about: directionality of movement <sup>140,142</sup>, predominant migration direction <sup>143</sup>, velocity <sup>134</sup>, or shape properties <sup>145-147</sup>. These parameters can be then analyzed in the context of single cell, or cell population, to draw general conclusions about cellular behavior <sup>133</sup>. The morphomigrational description presents an alternative approach, where the combination of several quantitative descriptors creates a quantitative picture of cellular behavior in a specific moment. Similar, but qualitative attempts were already presented in the work of Shafquat-Abbasi et al., where some of the behaviors: lateral protrusion, lateral migration, tail retraction, and perpendicular migration were identified as the elements of “continuous” and “discontinuous” modes of cell migration. Cellular dynamics was initially examined visually and then classified using behavioral criteria, presenting a similar approach to the one used in this thesis in WC256 cells description. The behavioral criteria were presented in the form of intuitive images, that allowed the reader to understand the cellular processes. However, the mathematical description of cellular activities was not the subject of the study whatsoever <sup>282</sup>. At some point, the work presented in this thesis assumes a similar approach as it also starts from a visual inspection of cellular behaviors. Nonetheless, the morphomigrational description makes a step forward, by assigning quantitative values to those behaviors.

The benefit that comes from the connection of several quantitative descriptors in one frame is visible in the description of several cellular actions. For example, the separate analysis of simple behaviors such as constant lateral migration, the averaged turning angle and sMM angle may work fine. However, for the lateral U-turn, the separate analysis of turning angle informs only about changes in migration direction, while sMM angle is not changed at all, indicating the lateral displacements. Also, for any type of stretching, turning angles inform only about the chaotic displacement, while sMM angle informs about stretching direction, and M.A. dynamics together with elongation describe whether the cell keeps the same shape arrangement. Another type of behavior that has been already identified in the literature is the uropod retraction which can be described only partially by the membrane dynamics<sup>283</sup>, but it still would not provide whether the cell changed its arrangement, or even its migration direction, as can be done with four building blocks of morphomigrational description.

The overall behavior of the cell can be also reflected by the patterns of plots where sMM angle is plotted against turning angle, M.A. dynamics, and elongation. This image, however, is greatly simplified, because it does not show the temporal order of behaviors. If the particular cell exhibits a well-defined and rather constant behavior (such as keratinocyte and MEF3T3 cells presented here), the patterns of morphomigrational behaviors can cluster in some defined fragments of the plot. However, the more chaotic movement that consists of several short-living behaviors (such as HEK293 cell) results in the large spread of points on the sMM vs turning angle plot. In that case, the only parameter that separates HEK293 cell from other types of cells might be the elongation, which is specific for particular cell.

The creation of morphomigrational description aimed also at bridging the gap between the qualitative intuitive description of cell behaviors and the complicated mathematical models. On one hand, keratinocyte is widely recognized among many researchers as the model cell in migration studies. The shape and migration of keratinocytes are described verbally with “persistent motion” and “stable morphology”<sup>284</sup> as well as a “fan-like shape”<sup>97</sup>. This description seems to be valid, even the shapes of keratinocytes can vary under different conditions<sup>97,98</sup>. The fibroblasts are also widely recognized due to their elongated shape<sup>285</sup> with the lamellipodium on the front<sup>50</sup>. Therefore, keratinocytes and fibroblasts serve as archetypic cells and some studies use them to describe the appearance of other biological objects as “keratocyte-like” or “fibroblast-like”<sup>286–289</sup>. Therefore, the common understanding of cellular appearance seems to properly work among the scientific community, however, it still cannot be accounted as a quantitative classification. The drawback of such a description is that it requires the visual examination of samples, while the numerical or analytical methods are not able to classify cellular behavior using archetypic cells. The only reasonable way of using such a qualitative archetypal

description seems to be the utilization of machine-learning algorithms that can learn and distinguish different cellular behaviors from images. On the other hand, some complex analytical models describe the cellular shape and dynamics as well <sup>98,290</sup>. Also, the more sophisticated characteristics of cellular behavior, such as adhesiveness, contractility, occurring forces, or interactions of focal adhesions might be used to describe the cellular state <sup>39,291</sup>. The morphomigrational description may fill this gap, by assigning the quantitative information to the visually assessed phenomena that are intuitive to understand. What is more, such parameters can be easily calculated for any set of binary masks.

Since the sMM angle, turning angle and M.A. dynamics are calculated from two or three frames, the morphomigrational description naturally depends on the sampling interval <sup>136,140,292,293</sup>, which is caused by the fact that different morphomigrational behaviors can occur in different timescales. Therefore, modification of sampling interval would just change the type of phenomenon we are focused on in our studies, being also reflected in the quantitative description. It is easy to imagine that the analysis of densely sampled data would predominantly show the membrane dynamics, while the longer sampling intervals would register larger cell translocation. It is also reflected in the general observation that the cell movement observed in a short time-scale is more similar to diffusive dynamics, while observation of cells with sparse sampling draws it closer to ballistic motion <sup>140</sup>. Another issue that should be considered in further studies of morphomigrational description is the problem of oversampling. Regarding this problem, one can imagine the situation, in which the centroid displacement or the membrane displacement would be too little to be distinguished from the uncertainty of the cell outline acquisition. However, to my knowledge, this issue has not been properly resolved in the current literature up to now. Another issue connected with data sampling is the fact that the cell velocity does not need to be constant along the whole time sequence. Therefore, even for the properly long sampling one can observe some moments in which cells just stop for a while, causing the temporal oversampling. The potential solution to this problem may come from the different type of sampling in which the constant time sampling is replaced with the sampling of constant minimal centroid displacement <sup>292</sup>. This approach, however, would not solve the problem of the theoretical case of the ideally symmetric stretching, in which the centroid remains in the same place, but the membrane would extend symmetrically in two or more directions. In such case, the minimal centroid displacement sampling would discard such frame as completely non-motile. Therefore, the next sampling method could be potentially coupled with defining the minimal membrane displacement, however even after extensive research I was not able to find any method that would describe such approach. Moreover, to my knowledge, there is no universal formula or even a guide that optimizes the sampling interval of cell migration data. Therefore, the problem of sampling

provides an open question for further consideration and answering this question can be significant in the wider perspective of migrating cells or tracing any other objects that actively change their shapes.

The construction, meaning, and potential application of morphomigrational description were introduced here for three exemplary cells, that represent different morphomigrational behaviors. Further studies on this subject may be aimed at the analysis of whole cellular populations, to characterize them in different environmental conditions. However, this subject is not as trivial as it might be seen, which can be easily explained with an example of migrating MEF 3T3 cells, that are often used for a model of mesenchymal migration. In the classic model described in more detail in the introduction, mesenchymal cells have to create protrusion, produce adhesion sites, perform the actomyosin contraction, and detach the rear part, resulting in cell translocation. In real life, these steps might overlap, creating an even more complicated image, since different phases of mesenchymal migration will be described by distinct morphomigrational behaviors. The averaging of such behaviors in the whole sample would not make much sense, because each cell can function independently and therefore, various behaviors can potentially occur at the same time for different cells in the same population. To complicate this image even more, those behaviors can occur in different timescales as it was mentioned in the previous paragraph. Consequently, further studies on cell populations would also require the following steps: (I) creation of the library of morphomigrational behaviors and their quantitative morphomigrational descriptions, (II) determining the timescales of different behaviors, (III) detection and description of time patterns in which particular behaviors occur one after another for each type of cell and (IV) taking into account the aforementioned problem of data sampling. These issues require further extensive studies that will help in the wider application of morphomigrational description in the analysis of cellular dynamics. These are also the reasons, why the morphomigrational description was not applied for the classification of WC256 subpopulations yet, as this subject requires further extensive analyses. However, the morphomigrational description opens a new path for improving the quantitative understanding of many biological phenomena. The properly catalogued quantitative descriptions will also facilitate the process of robust automatic analysis of these behaviors by the proper future algorithms.

### **7.3. Development of ODMR-TFM technique for parallel measurements of temperature and cellular tractions.**

In the third chapter of results, the combination of two already existing methods was employed to create the method for parallel sensing of temperature and traction forces. The construction of new method consisted of several optimization steps. The first task consisted of optimization of the protocol for elastic substrate preparation, to make it suitable for both methods. In the second task, I have performed the optimization of ODMR experiment parameters, to decrease its potential negative effect on living cells. In the final step, the proof-of-principle ODMR-TFM experiment was conducted for heating, cooling, and constant temperature measurement, to present the final coupling of these methods.

In the first optimization step, we have created the elastic substrate that contained fluorescent beads for TFM measurements and microdiamonds for ODMR experiment. This substrate was tested in respect to its micromechanics and topography. These tests were the indispensable part of TFM optimization because the properly defined substrate elasticity is an essential factor in mechanobiology studies<sup>50,51</sup>, while the local topography can potentially bias cell behavior. In our case, the ODMR-TFM substrate differs in elasticity from the reference substrate produced without fluorescent markers. This difference could come from the fact that since standard TFM substrates are made with the use of buffers<sup>208</sup> in this study we aimed to avoid ionic solutions since they can induce diamond clustering<sup>235</sup>. The current literature shows that the acidic environment slows down the polyacrylamide polymerization reaction due to the protonation and oxidization of TEMED, which is one of the reaction catalysts<sup>294</sup>. This slightly acidic environment might be introduced by the carboxyl groups of green polystyrene beads, which in turn lead to the softening of the substrate. However, regardless of the cause of this effect, the ODMR-TFM substrate is still suitable to TFM experiments, as it still has a well-defined Young's modulus. It only raises the need of measuring the exact Young's modulus of polyacrylamide substrates of different elasticities produced that way.

Another issue that might be considered in further studies is the topography of the ODMR-TFM substrate. The presence of nanopits was shown to affect the cell spreading, adhesion, differentiation and osteogenic induction<sup>295-297</sup>. However, in these studies, nanopits were deeper (hundreds of nanometers) and were arranged in the form of dense matrices where nanopits were placed next to each other. In this work, the nanopits had different depths, (mostly less than 100 nanometers) and were located sparsely along the substrate. Nevertheless, this factor might potentially influence cellular behavior, which is the subject for further studies.

The second step encompassing optimization of the ODMR experiment was one of the most interesting parts of this research since the ODMR NV<sup>-</sup> microthermometry in living cells is a relatively novel subject and there is a limited number of studies that have already investigated it. Our aim was to decrease sample illumination and experiment time while keeping ~1 K temperature measurement accuracy. Here we should mention the two values that decide about the temperature measurement. The first is the temperature sensitivity that can be calculated by calibrating the ODMR shift regarding the temperature. Many studies assume the experimentally measured ODMR sensitivity around room temperature to be about -74 kHz/K<sup>204</sup>, however, the exact values slightly differ among literature sources from 65.4 kHz/K<sup>237</sup> to 84.4 kHz/K<sup>298</sup>. Therefore, it is possible to estimate the relative temperature from the ODMR shift. However, many studies perform separate calibrations to ensure the validity of the experimental procedure, as was done in this thesis. Another factor is the accuracy of temperature measurement, which comes from the determination of ODMR peak position. This value defines the final precision of the applied method in temperature measurements.

The already reported setups, experimental procedures, and methods of data analysis vary significantly between studies. Therefore, there is a visible gap regarding the systematic way of introducing ODMR experiments in live-cell imaging. The pioneering work of Kuckso et al.,<sup>205</sup> showed that the nanodiamonds were able to detect the local temperature change caused by the light-irradiated gold nanoparticles placed nearby. In their experiment microwave sequence consisted of the four frequencies that were chosen from the entire ODMR spectrum, of which two were placed on the descending and another two on ascending fragment of the ODMR spectrum. The accuracy of temperature measurement ranged from several to hundreds of millikelvins, depending on the experimental conditions and diamond type. That study however did not provide a separate temperature calibration, assuming the literature value of 77 kHz/K which seems to be the averaged value taken from two studies<sup>204,299</sup>. Their setup consisted of a sophisticated microscope with two independent excitation-collection paths (two laser beams) and fluorescence was collected by the avalanche photodiodes (APDs) that increased the readout accuracy. While the temperature measurement accuracy is impressive indeed, it is hard to compare it in the context of a methodological approach. The authors did not mention the number of averaging of the ODMR spectrum, type of the sequence (including the constant or pulsed MW), as well as the type of microwave antenna. On the other hand, since the confocal setup was used, one can assume that the point illumination should not induce negative phototoxic effects<sup>205</sup>.

A similar approach was employed by Fujiwara et al.,<sup>237</sup> who also used the confocal setup with APDs to investigate the temperature fluctuations in *C. Elegans* worm. What is interesting, the measurement was paired with the simultaneous tracking of nanodiamonds drift inside

the examined organism. In this work, the ODMR sequence also consisted of 4 points chosen from the whole spectrum (instead of the whole spectrum measurement), but authors introduced the additional corrections of ODMR acquisition frequencies due to the potential asymmetry of ODMR spectrum. The duration of a single measurement was not explicitly mentioned; however, the analysis of the experimental procedure suggests that the single ODMR measurement was done in the range of microseconds or milliseconds, which is quite impressive result. In that study, the ODMR was acquired for single nanodiamonds with a final accuracy of  $\pm 0.22$  K. However, that measurement was based on the constant temperature observation, where every single point could show the variability of a few Kelvins. The high accuracy of temperature measurement came from the process of smoothing of time-dependent temperature registration signal, performed with the moving average procedure from 20 experimental points. In that study, Fujiwara et al. performed the temperature calibration of diamonds, obtaining the result of  $-65.4$  kHz/K, which is lower than the aforementioned studies, however close to the value obtained in this thesis. What is more, the intensity of laser illumination was relatively high, between  $1$  and  $10$  kW/cm<sup>2</sup>. One can discuss again how much the point laser illumination can influence cellular processes; however, it also might be an issue for consideration in further studies <sup>237</sup>.

Another NV<sup>-</sup> temperature measurement on the confocal setup was done by Yukawa et al., <sup>236</sup> who used a similar setup with an APD detector, but the utilized laser power was much lower, estimated at  $4.7$  W/cm<sup>2</sup>. Instead of choosing only four points, the authors registered the whole ODMR spectrum from a single nanodiamond, similarly to the “Regular sweep” procedure used in our work. Therefore, data were fitted to the whole sweep by two or one Lorentzian function, depending on the analysis. The duration of experiment was however much longer, depending on the number of signal averaging and the duration of ODMR sweep that lasted between 3 and 6 minutes. The authors also provided the temperature calibration of ODMR, obtaining a result of  $-77.6 \pm 11$  kHz/K, which is similar to the literature sources. They had lower, but still reasonable accuracy of the temperature measurement at the level of 1 Kelvin <sup>236</sup>.

The study of Haechan et al. <sup>300</sup> also utilized the laser-power source, however, the type of microscope setup (confocal or wide-field) was not explicitly mentioned. The green laser beam ( $\lambda=520$  nm) had a power of 33 mW, but the authors did not recalculate it into the optical power density, therefore it is hard to directly compare this experimental condition. Fluorescence of nanodiamonds was collected with a single photon detector (SPD) and the ODMR sweep that lasted 83 seconds was used for the temperature measurements. The ODMR spectra were fitted with two Lorentzian functions to calculate the peak position. Nevertheless, the authors did not perform the temperature calibration of ODMR spectra, relying on the values presented

in the literature <sup>204</sup>. The long duration of experiment might be harmful to cells, especially in the wide-field configuration <sup>300</sup>.

The study that was most similar to the one presented in this thesis, was performed by Simpson et al. who used the wide-field fluorescence microscope with the sCMOS camera to register the temperature changes in living neurons <sup>206</sup>. Their main experiments consisted of the registration of a full sweep that lasted 12 seconds. During that time, they were able to register spectra of hundreds of nanodiamonds that were introduced to the neurons during their prior culturing. The accuracy of temperature measurement was in the range of tens to hundreds of millikelvins, which is an impressive result. This accuracy was enabled by the averaging of information from a large number of diamonds because as the authors showed, the accuracy of a single diamond measurement was estimated at  $\sim 1.2$  K. In our experiments, we first averaged the ODMR spectra to calculate the average relative temperature in the field of view. In that study, the relative temperature was calculated first, and the histogram collected from hundreds of cells allowed the precise estimation of temperature. However, they used an intensive laser light of  $3\text{kW}/\text{cm}^2$  optical power density that was illuminating the whole field of view. This illumination can be assumed to be intensive and might cause significant photodamage in observed cells, which together with the 12 seconds ODMR registration time might be harmful to cells. What is more, the authors did not provide the temperature calibration of ODMR spectra, assuming the literature value of  $-74.2$  kHz/K.

Compared to the aforementioned studies, the temperature calibration of our setup ( $68.4 \pm 3.6$  kHz/K) is similar to the ones found in the literature. The accuracy of temperature measurement achieved here ( $0.78 \pm 0.16$  K) is lower than in some other studies. However, it was accomplished with low level of illumination, a simple standard microscope setup, and a relatively short experiment duration. This level of precision still allows retrieving the useful information about the thermal environment of cells, while decreasing the potential negative effects of ODMR experiment. What is even more important, this work introduces temperature measurement into the field of mechanobiology, without the direct introduction of nano- or microdiamonds into the cells.

The optimization of ODMR experiment shows that the interplay between experimental parameters such as the type of the MW sequence, illumination intensity, and substrate height play a significant role in the resulting accuracy of temperature measurement. These experimental parameters might be even more improved in further studies, by testing other types of MW sequences, in order to decrease the time of ODMR experiment and the accuracy even more. Another potential improvement of this setup could be connected with a different application



of antenna, by placing it in the substrate or below the sample, to close the whole cellular environment from the top.

To sum up, the process of developing the ODMR-TFM experiment required the optimization of several experimental aspects, including substrate preparation and ODMR optimization. The resulting setup was prepared on the standard wide-field microscope and can be potentially adapted in other life-science laboratories. What is more, the proof-of-principle ODMR-TFM measurement showed that bulk temperature measurement may differ from the locally measured one, and it is possible to connect both of those techniques. Our data gives also a deeper insight into cell biophysics, by coupling two existing methods in new contexts.

## 8. Conclusions.

This thesis presents the development and application of novel biophysical methods to study cell behavior. The first method connected time-lapse experiments with the time-dependent (dynamic) analysis of the heterogenous WC256 cell line. The results revealed a new phenomenon – the dynamic subpopulational heterogeneity, demonstrating that particular morphology and migration mode do not need to be necessarily a constant feature of a single cell. On the contrary, cells can change their form to lose or establish a polarized migrating morphology. Observation of those cells in the more physiological mechanical environment – elastic polymer substrate with Young's modulus  $E=40$  kPa – resulted in modifications of the overall image of cell subpopulations distribution. While on stiffer substrates cells preferred the mesenchymal and nonpolar state, the elastic substrate caused the shift into the less adherent amoeboid form. Both of these results are of special importance in the context of cancer biology, since different cell subpopulations can react differently to the applied chemotherapeutics. It also shows the importance of the relevant micromechanical environment in the studies of heterogenous cell lines. The second part of results described the development of the new geometrical parameter that links the orientation of cell shape with displacement direction (*signed morphomigrational angle*) and further creation of *morphomigrational description*. This description combines cell shape and migration as one *morphomigrational behavior* and allowed to quantitatively describe several cellular activities such as lateral and perpendicular migration, cell stretching, and rear retraction, that up to now were predominantly described in a qualitative way. This is a unique method that unifies cell morphology with migration direction and can be utilized in various future applications, such as studies of directional stimulation of the cell, classification of different temporal behaviors of cells, as well as identifying behavioral cellular patterns in various physical and chemical environmental conditions. Therefore, the application of morphomigrational description may open new research paths in studies of cell dynamics. The third part of the results described the process of implementation of two experimental techniques: *Optically-Detected Magnetic Resonance (ODMR)* which utilized diamond color centers to measure relative temperature and *Traction Force Microscopy (TFM)* which measures cellular tractions. This process consisted of several steps, including: the production of proper diamond surface termination, incorporation of diamonds into the elastic substrates, verification of mechanical and optical properties of the substrate as well as optimization of the experiment duration and the sample illumination dose. These steps have to be performed in order to achieve the expected  $\sim 1$  K accuracy of temperature measurements while not harming living cells by the experimental procedure at the same time. This will enable the incorporation of the relative local temperature measurements into the field of mechanobiology

what to the author's knowledge is the first such known combination of research techniques and can open new paths in cell biology studies.

Relating to the Nobel prize talk of Frits Zernike, the three parts of this thesis were focused on new methodological approaches that "applied old ideas in new field", "invented new connections", and "saw the deeper connections". All of these developed and applied techniques already helped – or might help in the future – in a better understanding of cellular processes. Therefore, the results presented in this thesis might be useful for further researchers who will be interested in extending their research view and applying novel methods to discover yet unknown aspects of cellular processes, activities and regulatory paths.

## 9. Literature.

1. Zernike, F. How I Discovered Phase Contrast. *Science* **121**, 345–349 (1955).
2. Croft, W. J. *Under the microscope: a brief history of microscopy*. (World Scientific Publishing, 2006).
3. Wollman, A. J. M., Nudd, R., Hedlund, E. G. & Leake, M. C. From *Animaculum* to single molecules: 300 years of the light microscope. *Open Biol* **5**, 150019 (2015).
4. Hooke, R. *Micrographia: or, Some physiological descriptions of minute bodies made by magnifying glasses. With Observations and Inquiries Thereupon*. (J. Martyn and J. Allestry, 1665).
5. Masters, B. R. *Confocal Microscopy and Multiphoton Excitation Microscopy: The Genesis of Live Cell Imaging*. (SPIE, 2006).
6. Baker, H. & Leeuwenhoek, A. van. IX. An account of Mr. Leeuwenhoek's microscopes. *Philos Trans R Soc Lond* **41**, 503–519 (1740).
7. Leeuwenhoek, A. van & Hoole, S. *The select works of Antony van Leeuwenhoek : containing his microscopical discoveries in many of the works of nature*. (G. Sidney, 1800).
8. Masters, B. R. in *eLS* (Wiley, 2008).
9. Ribatti, D. Rudolf Virchow, the founder of cellular pathology. *Rom J Morphol Embryol* **60**, 1381–1382 (2019).
10. Smith, K. A. Louis Pasteur, the Father of Immunology? *Front Immunol* **3**, (2012).
11. Maxwell, J. C. *A Treatise on Electricity and Magnetism*. (1873).
12. Coico, R. Gram Staining. *Curr Protoc Microbiol* **00**, (2006).
13. Pluta, M. *Mikroskopia fazowo-kontrastowa i interferencyjna*. (Wydawnictwo Naukowe PWN, 1965).
14. Jablonski, A. Efficiency of Anti-Stokes Fluorescence in Dyes. *Nature* **131**, 839–840 (1933).
15. Minsky, M. Microscopy Apparatus. U.S. Patent no. 3013467. (1961).
16. Shimomura, O., Johnson, F. H. & Saiga, Y. Extraction, Purification and Properties of Aequorin, a Bioluminescent Protein from the Luminous Hydromedusan, Aequorea. *J Cell Comp Physiol* **59**, 223–239 (1962).
17. Chalfie, M., Tu, Y., Euskirchen, G., Ward, W. W. & Prasher, D. C. Green Fluorescent Protein as a Marker for Gene Expression. *Science* **263**, 802–805 (1994).
18. Heim, R., Prasher, D. C. & Tsien, R. Y. Wavelength mutations and posttranslational autoxidation of green fluorescent protein. *Proceedings of the National Academy of Sciences* **91**, 12501–12504 (1994).
19. Clegg, R. M. in *Reviews in Fluorescence 2006* 1–45 (Springer US, 2006).
20. Grecco, H. E. & Verveer, P. J. FRET in Cell Biology: Still Shining in the Age of Super-Resolution? *ChemPhysChem* **12**, 484–490 (2011).

21. Suhling, K., Hirvonen, L. M., Levitt, J. A., Chung, P.-H., Tregido, C., le Marois, A., Rusakov, D. A., Zheng, K., Ameer-Beg, S., Poland, S., Coelho, S. & Dimble, R. in *Advanced Time-Correlated Single Photon Counting Applications. Springer Series in Chemical Physics.* **111**, 119–188 (2015).
22. Jacobson, K., Wu, E. & Poste, G. Measurement of the translation mobility of concanavalin a in glycerol-saline solutions and on the cell surface by fluorescence recovery after photobleaching. *Biochimica et Biophysica Acta (BBA) - Biomembranes* **433**, 215–222 (1976).
23. Lippincott-Schwartz, J., Snapp, E. L. & Phair, R. D. The Development and Enhancement of FRAP as a Key Tool for Investigating Protein Dynamics. *Biophys J* **115**, 1146–1155 (2018).
24. Hell, S. W., Lindek, S., Cremer, C. & Stelzer, E. H. K. Confocal microscopy with an increased detection aperture: type-B 4Pi confocal microscopy. *Opt Lett* **19**, 222 (1994).
25. Hell, S. W. & Wichmann, J. Breaking the diffraction resolution limit by stimulated emission: stimulated-emission-depletion fluorescence microscopy. *Opt Lett* **19**, 780 (1994).
26. Dickson, R. M., Cubitt, A. B., Tsien, R. Y. & Moerner, W. E. On/off blinking and switching behaviour of single molecules of green fluorescent protein. *Nature* **388**, 355–358 (1997).
27. Betzig, E., Patterson, G. H., Sougrat, R., Lindwasser, O. W., Olenych, S., Bonifacino, J. S., Davidson, M. W., Lippincott-Schwartz, J. & Hess, H. F. Imaging Intracellular Fluorescent Proteins at Nanometer Resolution. *Science* **313**, 1642–1645 (2006).
28. Heilemann, M., van de Linde, S., Schüttelpelz, M., Kasper, R., Seefeldt, B., Mukherjee, A., Tinnefeld, P. & Sauer, M. Subdiffraction-Resolution Fluorescence Imaging with Conventional Fluorescent Probes. *Angewandte Chemie International Edition* **47**, 6172–6176 (2008).
29. Darnell, M. & Mooney, D. J. Leveraging advances in biology to design biomaterials. *Nat Mater* **16**, 1178–1185 (2017).
30. Brusatin, G., Panciera, T., Gandin, A., Citron, A. & Piccolo, S. Biomaterials and engineered microenvironments to control YAP/TAZ-dependent cell behaviour. *Nat Mater* **17**, 1063–1075 (2018).
31. Liu, Z., Tang, M., Zhao, J., Chai, R. & Kang, J. Looking into the Future: Toward Advanced 3D Biomaterials for Stem-Cell-Based Regenerative Medicine. *Advanced Materials* **30**, 1705388 (2018).
32. Alexander, C. & Shakesheff, K. M. Responsive polymers at the biology/materials science interface. *Advanced Materials* **18**, 3321–3328 (2006).
33. Alberts, B., Heald, R., Johnson, A., Morgan, D., Raff, M., Roberts, K. & Walter, P. in *Molecular Biology of the Cell, Seventh Edition* 873–948 (W. W. Norton & Company, 2022).
34. Bielfeldt, M., Rebl, H., Peters, K., Sridharan, K., Staehlke, S. & Nebe, J. B. Sensing of Physical Factors by Cells: Electric Field, Mechanical Forces, Physical Plasma and Light—Importance for Tissue Regeneration. *Biomedical Materials & Devices* (2022).
35. Choi, B., Kim, D., Han, I. & Lee, S.-H. in *Biomimetic Medical Materials. Advances in Experimental Medicine and Biology.* **1064**, 147–160 (2018).

36. Baker, B. M. & Chen, C. S. Deconstructing the third dimension – how 3D culture microenvironments alter cellular cues. *J Cell Sci* **125**, 3015–3024 (2012).
37. Zhang, Y. & Habibovic, P. Delivering Mechanical Stimulation to Cells: State of the Art in Materials and Devices Design. *Advanced Materials* **34**, 2110267 (2022).
38. Butcher, D. T., Alliston, T. & Weaver, V. M. A tense situation: forcing tumour progression. *Nat Rev Cancer* **9**, 108–122 (2009).
39. Friedl, P. & Wolf, K. Plasticity of cell migration: a multiscale tuning model. *Journal of Cell Biology* **188**, 11–19 (2010).
40. van der Meulen, M. C. H. & Huijkes, R. Why mechanobiology? *J Biomech* **35**, 401–414 (2002).
41. Vogel, V. & Sheetz, M. Local force and geometry sensing regulate cell functions. *Nat Rev Mol Cell Biol* **7**, 265–275 (2006).
42. Goelzer, M., Thompson, W. R. & Uzer, G. in *Mechanobiology* 79–98 (Elsevier, 2020).
43. Wang, J. H. C. & Lin, J. S. Cell traction force and measurement methods. *Biomech Model Mechanobiol* **6**, 361–371 (2007).
44. Balaban, N. Q., Schwarz, U. S., Riveline, D., Goichberg, P., Tzur, G., Sabanay, I., Mahalu, D., Safran, S., Bershadsky, A., Addadi, L. & Geiger, B. Force and focal adhesion assembly: a close relationship studied using elastic micropatterned substrates. *Nat Cell Biol* **3**, 466–472 (2001).
45. Ghibaudo, M., Saez, A., Trichet, L., Xayaphoummine, A., Browaeys, J., Silberzan, P., Buguin, A. & Ladoux, B. Traction forces and rigidity sensing regulate cell functions. *Soft Matter* **4**, 1836–1843 (2008).
46. Joshi, R., Han, S.-B., Cho, W.-K. & Kim, D.-H. The role of cellular traction forces in deciphering nuclear mechanics. *Biomater Res* **26**, 43 (2022).
47. Roca-Cusachs, P., Conte, V. & Trepats, X. Quantifying forces in cell biology. *Nat Cell Biol* **19**, 742–751 (2017).
48. Harris, A. K., Wild, P. & Stopak, D. Silicone Rubber Substrata: A New Wrinkle in the Study of Cell Locomotion. *Science* **208**, 177–179 (1980).
49. Pelham, R. J. & Wang, Y. Cell locomotion and focal adhesions are regulated by substrate flexibility. *Proceedings of the National Academy of Sciences* **94**, 13661–13665 (1997).
50. Dembo, M. & Wang, Y. L. Stresses at the cell-to-substrate interface during locomotion of fibroblasts. *Biophys J* **76**, 2307–2316 (1999).
51. Butler, J. P., Tolić-Nørrelykke, I. M., Fabry, B. & Fredberg, J. J. Traction fields, moments, and strain energy that cells exert on their surroundings. *American Journal of Physiology-Cell Physiology* **282**, C595–C605 (2002).
52. Landau L. D., Lifshitz, E. M., Kosevich, A. M. & Pitaevskii, L. P. *Theory of Elasticity*. (Elsevier, 1986).

53. Merkel, R., Kirchgeßner, N., Cesa, C. M. & Hoffmann, B. Cell force microscopy on elastic layers of finite thickness. *Biophys J* **93**, 3314–3323 (2007).
54. Sabass, B., Gardel, M. L., Waterman, C. M. & Schwarz, U. S. High resolution traction force microscopy based on experimental and computational advances. *Biophys J* **94**, 207–220 (2008).
55. Legant, W. R., Choi, C. K., Miller, J. S., Shao, L., Gao, L., Betzig, E. & Chen, C. S. Multidimensional traction force microscopy reveals out-of-plane rotational moments about focal adhesions. *Proc Natl Acad Sci U S A* **110**, 881–886 (2013).
56. Berg, W. A., Cosgrove, D. O., Doré, C. J., Schäfer, F. K. W., Svensson, W. E., Hooley, R. J., Ohlinger, R., Mendelson, E. B., Balu-Maestro, C., Locatelli, M., Tourasse, C., Cavanaugh, B. C., Juhan, V., Stavros, A. T., Tardivon, A., Gay, J., Henry, J.-P. & Cohen-Bacrie, C. Shear-wave Elastography Improves the Specificity of Breast US: The BE1 Multinational Study of 939 Masses. *Radiology* **262**, 435–449 (2012).
57. Athanasiou, A., Tardivon, A., Tanter, M., Sigal-Zafrani, B., Bercoff, J., Deffieux, T., Gennisson, J. L., Fink, M. & Neuenschwander, S. Breast lesions: Quantitative elastography with supersonic shear imaging - Preliminary results. *Radiology* **256**, 297–303 (2010).
58. Engler, A. J., Sen, S., Sweeney, H. L. & Discher, D. E. Matrix Elasticity Directs Stem Cell Lineage Specification. *Cell* **126**, 677–689 (2006).
59. *Mechanobiology: From Molecular Sensing to Disease*. (Elsevier, 2020).
60. Tonk, C. H., Witzler, M., Schulze, M. & Tobiasch, E. in *Essential Current Concepts in Stem Cell Biology. Learning Materials in Biosciences*. 21–39 (2020).
61. Xu, J., Sun, M., Tan, Y., Wang, H., Wang, H., Li, P., Xu, Z., Xia, Y., Li, L. & Li, Y. Effect of matrix stiffness on the proliferation and differentiation of umbilical cord mesenchymal stem cells. *Differentiation* **96**, 30–39 (2017).
62. Young, D. A., Choi, Y. S., Engler, A. J. & Christman, K. L. Stimulation of adipogenesis of adult adipose-derived stem cells using substrates that mimic the stiffness of adipose tissue. *Biomaterials* **34**, 8581–8588 (2013).
63. Olivares-Navarrete, R., Lee, E. M., Smith, K., Hyzy, S. L., Doroudi, M., Williams, J. K., Gall, K., Boyan, B. D. & Schwartz, Z. Substrate Stiffness Controls Osteoblastic and Chondrocytic Differentiation of Mesenchymal Stem Cells without Exogenous Stimuli. *PLoS One* **12**, e0170312 (2017).
64. Seib, F. P., Prewitz, M., Werner, C. & Bornhäuser, M. Matrix elasticity regulates the secretory profile of human bone marrow-derived multipotent mesenchymal stromal cells (MSCs). *Biochem Biophys Res Commun* **389**, 663–667 (2009).
65. Mao, A. S., Shin, J. W. & Mooney, D. J. Effects of substrate stiffness and cell-cell contact on mesenchymal stem cell differentiation. *Biomaterials* **98**, 184–191 (2016).
66. Lü, D., Luo, C., Zhang, C., Li, Z. & Long, M. Differential regulation of morphology and stemness of mouse embryonic stem cells by substrate stiffness and topography. *Biomaterials* **35**, 3945–3955 (2014).

67. Teixeira, A. I., Ilkhanizadeh, S., Wigenius, J. A., Duckworth, J. K., Inganäs, O. & Hermanson, O. The promotion of neuronal maturation on soft substrates. *Biomaterials* **30**, 4567–4572 (2009).
68. Tilghman, R. W., Cowan, C. R., Mih, J. D., Koryakina, Y., Gioeli, D., Slack-Davis, J. K., Blackman, B. R., Tschumperlin, D. J. & Parsons, J. T. Matrix rigidity regulates cancer cell growth and cellular phenotype. *PLoS One* **5**, (2010).
69. Tilghman, R. W., Blais, E. M., Cowan, C. R., Sherman, N. E., Grigera, P. R., Jeffery, E. D., Fox, J. W., Blackman, B. R., Tschumperlin, D. J., Papin, J. A. & Parsons, J. T. Matrix rigidity regulates cancer cell growth by modulating cellular metabolism and protein synthesis. *PLoS One* **7**, (2012).
70. Shukla, V. C., Higuera-Castro, N., Nana-Sinkam, P. & Ghadiali, S. N. Substrate stiffness modulates lung cancer cell migration but not epithelial to mesenchymal transition. *J Biomed Mater Res A* **104**, 1182–1193 (2016).
71. Zhao, D., Xue, C., Li, Q., Liu, M., Ma, W., Zhou, T. & Lin, Y. Substrate stiffness regulated migration and angiogenesis potential of A549 cells and HUVECs. *J Cell Physiol* **233**, 3407–3417 (2018).
72. Ulrich, T. A., de Juan Pardo, E. M. & Kumar, S. The Mechanical Rigidity of the Extracellular Matrix Regulates the Structure, Motility, and Proliferation of Glioma Cells. *Cancer Res* **69**, 4167–4174 (2009).
73. Pogoda, K., Bucki, R., Byfield, F. J., Cruz, K., Lee, T., Marcinkiewicz, C. & Janmey, P. A. Soft Substrates Containing Hyaluronan Mimic the Effects of Increased Stiffness on Morphology, Motility, and Proliferation of Glioma Cells. *Biomacromolecules* **18**, 3040–3051 (2017).
74. McGrail, D. J., Kieu, Q. M. N. & Dawson, M. R. The malignancy of metastatic ovarian cancer cells is increased on soft matrices through a mechanosensitive Rho-ROCK pathway. *J Cell Sci* **127**, 2621–2626 (2014).
75. Fan, Y., Sun, Q., Li, X., Feng, J., Ao, Z., Li, X. & Wang, J. Substrate Stiffness Modulates the Growth, Phenotype, and Chemoresistance of Ovarian Cancer Cells. *Front Cell Dev Biol* **9**, (2021).
76. Alexander, N. R., Branch, K. M., Parekh, A., Clark, E. S., Iwueke, I. C., Guelcher, S. A. & Weaver, A. M. Extracellular Matrix Rigidity Promotes Invadopodia Activity. *Current Biology* **18**, 1295–1299 (2008).
77. Peng, Y., Chen, Z., Chen, Y., Li, S., Jiang, Y., Yang, H., Wu, C., You, F., Zheng, C., Zhu, J., Tan, Y., Qin, X. & Liu, Y. ROCK isoforms differentially modulate cancer cell motility by mechanosensing the substrate stiffness. *Acta Biomater* **88**, 86–101 (2019).
78. Lin, F., Zhang, H., Huang, J. & Xiong, C. Substrate Stiffness Coupling TGF- $\beta$ 1 Modulates Migration and Traction Force of MDA-MB-231 Human Breast Cancer Cells in Vitro. *ACS Biomater Sci Eng* **4**, 1337–1345 (2018).
79. Li, Y., Randriantsilefisoa, R., Chen, J., Cuellar-Camacho, J. L., Liang, W. & Li, W. Matrix Stiffness Regulates Chemosensitivity, Stemness Characteristics, and Autophagy in Breast Cancer Cells. *ACS Appl Bio Mater* **3**, 4474–4485 (2020).



80. Qin, X., Lv, X., Li, P., Yang, R., Xia, Q., Chen, Y., Peng, Y., Li, L., Li, S., Li, T., Jiang, Y., Yang, H., Wu, C., Zheng, C., Zhu, J., You, F., Wang, H., Chen, J. & Liu, Y. Matrix stiffness modulates ILK-mediated YAP activation to control the drug resistance of breast cancer cells. *Biochimica et Biophysica Acta (BBA) - Molecular Basis of Disease* **1866**, 165625 (2020).
81. Syed, S., Schober, J., Blanco, A. & Zustiak, S. P. Morphological adaptations in breast cancer cells as a function of prolonged passaging on compliant substrates. *PLoS One* **12**, (2017).
82. L. Collins, J., van Knippenberg, B., Ding, K. & V. Kofman, A. in *Cell Culture* (IntechOpen, 2019).
83. Horwitz, R. & Webb, D. Cell migration. *Current Biology* **13**, R756–R759 (2003).
84. Lintz, M., Muñoz, A. & Reinhart-King, C. A. The Mechanics of Single Cell and Collective Migration of Tumor Cells. *J Biomech Eng* **139**, (2017).
85. Wedlich-Soldner, R. & Li, R. Spontaneous cell polarization: undermining determinism. *Nat Cell Biol* **5**, 267–70 (2003).
86. Parsons, J. T., Horwitz, A. R. & Schwartz, M. A. Cell adhesion: integrating cytoskeletal dynamics and cellular tension. *Nat Rev Mol Cell Biol* **11**, 633–43 (2010).
87. Swaney, K. F., Huang, C.-H. & Devreotes, P. N. Eukaryotic chemotaxis: a network of signaling pathways controls motility, directional sensing, and polarity. *Annu Rev Biophys* **39**, 265–89 (2010).
88. Cramer, L. P., Siebert, M. & Mitchison, T. J. Identification of novel graded polarity actin filament bundles in locomoting heart fibroblasts: implications for the generation of motile force. *J Cell Biol* **136**, 1287–305 (1997).
89. Svitkina, T. M. & Borisy, G. G. Arp2/3 complex and actin depolymerizing factor/cofilin in dendritic organization and treadmilling of actin filament array in lamellipodia. *J Cell Biol* **145**, 1009–26 (1999).
90. Block, J., Stradal, T. E. B., Hänisch, J., Geffers, R., Köstler, S. A., Urban, E., Small, J. V., Rottner, K. & Faix, J. Filopodia formation induced by active mDia2/Drf3. *J Microsc* **231**, 506–17 (2008).
91. Alexandrova, A. Y., Chikina, A. S. & Svitkina, T. M. in *Int Rev Cell Mol Biol* **356**, 197–256 (Elsevier Inc., 2020).
92. Zaidel-Bar, R., Ballestrem, C., Kam, Z. & Geiger, B. Early molecular events in the assembly of matrix adhesions at the leading edge of migrating cells. *J Cell Sci* **116**, 4605–4613 (2003).
93. Hotulainen, P. & Lappalainen, P. Stress fibers are generated by two distinct actin assembly mechanisms in motile cells. *Journal of Cell Biology* **173**, 383–394 (2006).
94. Vicente-Manzanares, M. & Horwitz, A. R. in *Cell Migration. Methods in Molecular Biology*. **769**, 1–24 (2011).
95. Calle, Y., Antón, I. M., Thrasher, A. J. & Jones, G. E. WASP and WIP regulate podosomes in migrating leukocytes. *J Microsc* **231**, 494–505 (2008).
96. Gimona, M., Buccione, R., Courtneidge, S. A. & Linder, S. Assembly and biological role of podosomes and invadopodia. *Curr Opin Cell Biol* **20**, 235–241 (2008).

97. Barnhart, E. L., Lee, K. C., Keren, K., Mogilner, A. & Theriot, J. A. An adhesion-dependent switch between mechanisms that determine motile cell shape. *PLoS Biol* **9**, (2011).
98. Keren, K., Pincus, Z., Allen, G. M., Barnhart, E. L., Marriott, G., Mogilner, A. & Theriot, J. A. Mechanism of shape determination in motile cells. *Nature* **453**, 475–480 (2008).
99. Lee, J. & Jacobson, K. The composition and dynamics of cell-substratum adhesions in locomoting fish keratocytes. *J Cell Sci* **110**, 2833–2844 (1997).
100. Lämmermann, T. & Sixt, M. Mechanical modes of ‘amoeboid’ cell migration. *Curr Opin Cell Biol* **21**, 636–644 (2009).
101. Charest, P. G. & Firtel, R. A. Big roles for small GTPases in the control of directed cell movement. *Biochemical Journal* **401**, 377–390 (2007).
102. Krummel, M. F. & Macara, I. Maintenance and modulation of T cell polarity. *Nat Immunol* **7**, 1143–1149 (2006).
103. Paluch, E., Piel, M., Prost, J., Bornens, M. & Sykes, C. Cortical Actomyosin Breakage Triggers Shape Oscillations in Cells and Cell Fragments. *Biophys J* **89**, 724–733 (2005).
104. Charras, G. T., Yarrow, J. C., Horton, M. A., Mahadevan, L. & Mitchison, T. J. Non-equilibration of hydrostatic pressure in blebbing cells. *Nature* **435**, 365–369 (2005).
105. Mitchison, T. J., Charras, G. T. & Mahadevan, L. Implications of a poroelastic cytoplasm for the dynamics of animal cell shape. *Semin Cell Dev Biol* **19**, 215–223 (2008).
106. Charras, G. T., Hu, C.-K., Coughlin, M. & Mitchison, T. J. Reassembly of contractile actin cortex in cell blebs. *Journal of Cell Biology* **175**, 477–490 (2006).
107. Fritz-Laylin, L. K., Riel-Mehan, M., Chen, B.-C., Lord, S. J., Goddard, T. D., Ferrin, T. E., Nicholson-Dykstra, S. M., Higgs, H., Johnson, G. T., Betzig, E. & Mullins, R. D. Actin-based protrusions of migrating neutrophils are intrinsically lamellar and facilitate direction changes. *Elife* **6**, (2017).
108. te Boekhorst, V. & Friedl, P. in *Adv Cancer Res* **132**, 209–264 (Academic Press Inc., 2016).
109. Trepap, X., Chen, Z. & Jacobson, K. in *Compr Physiol* 2369–2392 (Wiley, 2012).
110. Wu, J., Sheng, S., Liang, X. & Tang, Y. The role of tumor microenvironment in collective tumor cell invasion. *Future Oncology* **13**, 991–1002 (2017).
111. van Zijl, F., Krupitza, G. & Mikulits, W. Initial steps of metastasis: Cell invasion and endothelial transmigration. *Mutation Research/Reviews in Mutation Research* **728**, 23–34 (2011).
112. Bronsert, P., Enderle-Ammour, K., Bader, M., Timme, S., Kuehs, M., Csanadi, A., Kayser, G., Kohler, I., Bausch, D., Hoepfner, J., Hopt, U., Keck, T., Stickeler, E., Passlick, B., Schilling, O., Reiss, C., Vashist, Y., Brabletz, T., Berger, J., Lotz, J., Olesch, J., Werner, M. & Wellner, U. Cancer cell invasion and EMT marker expression: a three-dimensional study of the human cancer-host interface. *J Pathol* **234**, 410–422 (2014).

113. Friedl, P., Noble, P. B., Walton, P. A., Laird, D. W., Chauvin, P. J., Tabah, R. J., Black, M. & Zänker, K. S. Migration of coordinated cell clusters in mesenchymal and epithelial cancer explants in vitro. *Cancer Res* **55**, 4557–60 (1995).
114. Osswald, M., Jung, E., Sahm, F., Solecki, G., Venkataramani, V., Blaes, J., Weil, S., Horstmann, H., Wiestler, B., Syed, M., Huang, L., Ratliff, M., Karimian Jazi, K., Kurz, F. T., Schmenger, T., Lemke, D., Gömmel, M., Pauli, M., Liao, Y., Häring, P., Pusch, S., Herl, V., Steinhäuser, C., Kronic, D., Jarahian, M., Miletic, H., Berghoff, A. S., Griesbeck, O., Kalamakis, G., Garaschuk, O., Preusser, M., Weiss, S., Liu, H., Heiland, S., Platten, M., Huber, P. E., Kuner, T., von Deimling, A., Wick, W. & Winkler, F. Brain tumour cells interconnect to a functional and resistant network. *Nature* **528**, 93–98 (2015).
115. Haeger, A., Krause, M., Wolf, K. & Friedl, P. Cell jamming: Collective invasion of mesenchymal tumor cells imposed by tissue confinement. *Biochimica et Biophysica Acta (BBA) - General Subjects* **1840**, 2386–2395 (2014).
116. Denais, C. M., Gilbert, R. M., Isermann, P., McGregor, A. L., te Lindert, M., Weigel, B., Davidson, P. M., Friedl, P., Wolf, K. & Lammerding, J. Nuclear envelope rupture and repair during cancer cell migration. *Science* **352**, 353–358 (2016).
117. Friedl, P. & Gilmour, D. Collective cell migration in morphogenesis, regeneration and cancer. *Nat Rev Mol Cell Biol* **10**, 445–457 (2009).
118. Polyak, K. & Weinberg, R. A. Transitions between epithelial and mesenchymal states: acquisition of malignant and stem cell traits. *Nat Rev Cancer* **9**, 265–273 (2009).
119. Xu, R., Boudreau, A. & Bissell, M. J. Tissue architecture and function: dynamic reciprocity via extra- and intra-cellular matrices. *Cancer and Metastasis Reviews* **28**, 167–176 (2009).
120. Savagner, P. The epithelial–mesenchymal transition (EMT) phenomenon. *Annals of Oncology* **21**, vii89–vii92 (2010).
121. Aiello, N. M., Maddipati, R., Norgard, R. J., Balli, D., Li, J., Yuan, S., Yamazoe, T., Black, T., Sahmoud, A., Furth, E. E., Bar-Sagi, D. & Stanger, B. Z. EMT Subtype Influences Epithelial Plasticity and Mode of Cell Migration. *Dev Cell* **45**, 681–695.e4 (2018).
122. Grigore, A., Jolly, M., Jia, D., Farach-Carson, M. & Levine, H. Tumor Budding: The Name is EMT. Partial EMT. *J Clin Med* **5**, 51 (2016).
123. Yamaguchi, H., Wyckoff, J. & Condeelis, J. Cell migration in tumors. *Curr Opin Cell Biol* **17**, 559–564 (2005).
124. Matisse, L. A., Palmer, T. D., Ashby, W. J., Nashabi, A., Chytil, A., Aakre, M., Pickup, M. W., Gorska, A. E., Zijlstra, A. & Moses, H. L. Lack of transforming growth factor- $\beta$  signaling promotes collective cancer cell invasion through tumor-stromal crosstalk. *Breast Cancer Research* **14**, R98 (2012).
125. Wolfson, B. Adipocyte activation of cancer stem cell signaling in breast cancer. *World J Biol Chem* **6**, 39 (2015).
126. Goswami, S., Sahai, E., Wyckoff, J. B., Cammer, M., Cox, D., Pixley, F. J., Stanley, E. R., Segall, J. E. & Condeelis, J. S. Macrophages Promote the Invasion of Breast Carcinoma Cells via a

- Colony-Stimulating Factor-1/Epidermal Growth Factor Paracrine Loop. *Cancer Res* **65**, 5278–5283 (2005).
127. Wyckoff, J. B., Wang, Y., Lin, E. Y., Li, J., Goswami, S., Stanley, E. R., Segall, J. E., Pollard, J. W. & Condeelis, J. Direct Visualization of Macrophage-Assisted Tumor Cell Intravasation in Mammary Tumors. *Cancer Res* **67**, 2649–2656 (2007).
  128. Kumar, S., Kapoor, A., Desai, S., Inamdar, M. M. & Sen, S. Proteolytic and non-proteolytic regulation of collective cell invasion: tuning by ECM density and organization. *Sci Rep* **6**, 19905 (2016).
  129. Hegerfeldt, Y., Tusch, M., Bröcker, E.-B. & Friedl, P. Collective cell movement in primary melanoma explants: plasticity of cell-cell interaction, beta1-integrin function, and migration strategies. *Cancer Res* **62**, 2125–30 (2002).
  130. Bergert, M., Chandradoss, S. D., Desai, R. A. & Paluch, E. Cell mechanics control rapid transitions between blebs and lamellipodia during migration. *Proceedings of the National Academy of Sciences* **109**, 14434–14439 (2012).
  131. Chikina, A. S., Rubtsova, S. N., Lomakina, M. E., Potashnikova, D. M., Vorobjev, I. A. & Alexandrova, A. Y. Transition from mesenchymal to bleb-based motility is predominantly exhibited by CD133-positive subpopulation of fibrosarcoma cells. *Biol Cell* **111**, 245–261 (2019).
  132. Taddei, M. L., Giannoni, E., Morandi, A., Ippolito, L., Ramazzotti, M., Callari, M., Gandellini, P. & Chiarugi, P. Mesenchymal to amoeboid transition is associated with stem-like features of melanoma cells. *Cell Communication and Signaling* **12**, 24 (2014).
  133. Beltman, J. B., Marée, A. F. M. & De Boer, R. J. Analysing immune cell migration. *Nat Rev Immunol* **9**, 789–798 (2009).
  134. Dziob, D., Kołodziej, T., Nowak, J., Cyzio, P., Raczowska, J., Laska, J. & Rajfur, Z. Effect of substrate elasticity on macroscopic parameters of fish keratocyte migration. *Phys Biol* **13**, 054001 (2016).
  135. Masuzzo, P., Huyck, L., Simiczyjew, A., Ampe, C., Martens, L. & Van Troys, M. An end-to-end software solution for the analysis of high-throughput single-cell migration data. *Sci Rep* **7**, (2017).
  136. Loosley, A. J., O'Brien, X. M., Reichner, J. S. & Tang, J. X. Describing directional cell migration with a characteristic directionality time. *PLoS One* **10**, (2015).
  137. Lara Rodriguez, L. & Schneider, I. C. Directed cell migration in multi-cue environments. *Integrative Biology* **5**, 1306–1323 (2013).
  138. O'Brien, X. M., Loosley, A. J., Oakley, K. E., Tang, J. X. & Reichner, J. S. Technical Advance: Introducing a novel metric, directionality time, to quantify human neutrophil chemotaxis as a function of matrix composition and stiffness. *J Leukoc Biol* **95**, 993–1004 (2014).
  139. DiMilla, P. A., Quinn, J. A., Albelda, S. M. & Lauffenburger, D. A. Measurement of individual cell migration parameters for human tissue cells. *AIChE Journal* **38**, 1092–1104 (1992).

140. Thomas, G. L., Fortuna, I., Perrone, G. C., Glazier, J. A., Belmonte, J. M. & de Almeida, R. M. C. Parameterizing cell movement when the instantaneous cell migration velocity is ill-defined. *Physica A: Statistical Mechanics and its Applications* **550**, (2020).
141. Pijuan, J., Barceló, C., Moreno, D. F., Maiques, O., Sisó, P., Marti, R. M., Macià, A. & Panosa, A. In vitro cell migration, invasion, and adhesion assays: From cell imaging to data analysis. *Front Cell Dev Biol* **7**, (2019).
142. Wu, P.-H., Giri, A. & Wirtz, D. Statistical analysis of cell migration in 3D using the anisotropic persistent random walk model. *Nat Protoc* **10**, 517–527 (2015).
143. Banigan, E. J., Harris, T. H., Christian, D. A., Hunter, C. A. & Liu, A. J. Heterogeneous CD8+ T Cell Migration in the Lymph Node in the Absence of Inflammation Revealed by Quantitative Migration Analysis. *PLoS Comput Biol* **11**, e1004058 (2015).
144. Bear, J. E. & Haugh, J. M. Directed migration of mesenchymal cells: where signaling and the cytoskeleton meet. *Curr Opin Cell Biol* **30**, 74–82 (2014).
145. Lepekhin, E. A., Walmod, P. S., Berezin, A., Berezin, V. & Bock, E. in *Cytoskeleton Methods and Protocols. Methods in Molecular Biology™* (ed. Gavin R.H) **161**, 85–100 (Humana Press, 2001).
146. Lobo, J., See, E. Y.-S., Biggs, M. & Pandit, A. An insight into morphometric descriptors of cell shape that pertain to regenerative medicine. *J Tissue Eng Regen Med* **10**, 539–553 (2016).
147. Yu, H., Lim, K. P., Xiong, S., Tan, L. P. & Shim, W. Functional Morphometric Analysis in Cellular Behaviors: Shape and Size Matter. *Adv Healthc Mater* **2**, 1188–1197 (2013).
148. Mielnicka, A., Kołodziej, T., Dziob, D., Lasota, S., Sroka, J. & Rajfur, Z. Impact of Elastic Substrate on the Dynamic Heterogeneity of WC256 Walker Carcinosarcoma Cells. *Scientific Reports (Accepted Manuscript)* (2023).
149. Biela, S. A., Su, Y., Spatz, J. P. & Kemkemer, R. Different sensitivity of human endothelial cells, smooth muscle cells and fibroblasts to topography in the nano-micro range. *Acta Biomater* **5**, 2460–2466 (2009).
150. Bitar, M., Friederici, V., Imgrund, P., Brose, C. & Bruinink, A. In vitro bioactivity of micro metal injection moulded stainless steel with defined surface features. *Eur Cell Mater* **23**, 333–347 (2012).
151. Jana, A., Nookaew, I., Singh, J., Behkam, B., Franco, A. T. & Nain, A. S. Crosshatch nanofiber networks of tunable interfiber spacing induce plasticity in cell migration and cytoskeletal response. *FASEB Journal* **33**, 10618–10632 (2019).
152. Qin, S., Ricotta, V., Simon, M., Clark, R. A. F. & Rafailovich, M. H. Continual cell deformation induced via attachment to oriented fibers enhances fibroblast cell migration. *PLoS One* **10**, (2015).
153. Soltys, Z., Orzylowska-Sliwinska, O., Zaremba, M., Orłowski, D., Piechota, M., Fiedorowicz, A., Janeczko, K. & Oderfeld-Nowak, B. Quantitative morphological study of microglial cells in the ischemic rat brain using principal component analysis. *J Neurosci Methods* **146**, 50–60 (2005).

154. Mikli, V., Käerdi, H., Kulu, P. & Besterci, M. Characterization of powder particle morphology. *Proceedings of the Estonian Academy of Sciences. Engineering* **7**, 22 (2001).
155. Kaiser, J. P., Reinmann, A. & Bruinink, A. The effect of topographic characteristics on cell migration velocity. *Biomaterials* **27**, 5230–5241 (2006).
156. Kim, D. H., Han, K., Gupta, K., Kwon, K. W., Suh, K. Y. & Levchenko, A. Mechanosensitivity of fibroblast cell shape and movement to anisotropic substratum topography gradients. *Biomaterials* **30**, 5433–5444 (2009).
157. Deng, X., Sarkar, R., Labruyere, E., Olivo-Marin, J.-C. & Srivastava, A. Modeling Shape Dynamics During Cell Motility in Microscopy Videos. in *2020 IEEE International Conference on Image Processing (ICIP) 2020-October*, 2491–2495 (IEEE, 2020).
158. Tweedy, L., Meier, B., Stephan, J., Heinrich, D. & Endres, R. G. Distinct cell shapes determine accurate chemotaxis. *Sci Rep* **3**, (2013).
159. Somero, G. N. The cellular stress response and temperature: Function, regulation, and evolution. *J Exp Zool A Ecol Integr Physiol* **333**, 379–397 (2020).
160. Sonna, L. A., Fujita, J., Gaffin, S. L. & Lilly, C. M. Invited Review: Effects of heat and cold stress on mammalian gene expression. *J Appl Physiol* **92**, 1725–1742 (2002).
161. Kamei, Y., Suzuki, M., Watanabe, K., Fujimori, K., Kawasaki, T., Deguchi, T., Yoneda, Y., Todo, T., Takagi, S., Funatsu, T. & Yuba, S. Infrared laser-mediated gene induction in targeted single cells in vivo. *Nat Methods* **6**, 79–81 (2009).
162. Guo, M., Xu, Y. & Gruebele, M. Temperature dependence of protein folding kinetics in living cells. *Proceedings of the National Academy of Sciences* **109**, 17863–17867 (2012).
163. Knapp, B. D. & Huang, K. C. The Effects of Temperature on Cellular Physiology. *Annu Rev Biophys* **51**, 499–526 (2022).
164. Metzger, K., Dannenberger, D., Tuchscherer, A., Ponsuksili, S. & Kalbe, C. Effects of temperature on proliferation of myoblasts from donor piglets with different thermoregulatory maturities. *BMC Mol Cell Biol* **22**, (2021).
165. Clark, D. L., Coy, C. S., Strasburg, G. M., Reed, K. M. & Velleman, S. G. Temperature effect on proliferation and differentiation of satellite cells from Turkeys with different growth rates. *Poult Sci* **95**, 934–947 (2016).
166. Khachatryan, G., Holle, A. W., Ende, K., Frey, C., Schwederski, H. A., Eiseler, T., Paschke, S., Micoulet, A., Spatz, J. P. & Kemkemer, R. Temperature-sensitive migration dynamics in neutrophil-differentiated HL-60 cells. *Sci Rep* **12**, (2022).
167. Sen, A. & Ta, M. Altered Adhesion and Migration of Human Mesenchymal Stromal Cells under Febrile Temperature Stress Involves NF- $\kappa$ B Pathway. *Sci Rep* **10**, (2020).
168. Nakamura, T., Sakamoto, J., Okabe, K., Taniguchi, A., Yamada, T. G., Nonaka, S., Kamei, Y., Funahashi, A., Tominaga, M. & Hiroi, N. F. Temperature elevation detection in migrating cells. *Optics Continuum* **1**, 1085 (2022).
169. Umar, D., Das, A., Gupta, S., Chattopadhyay, S., Sarkar, D., Mirji, G., Kalia, J., Arimbasseri, A., Durdik, J. M., Rath, S., George, A. & Bal, V. Febrile temperature change modulates CD4 T cell

- differentiation via a TRPV channel-regulated Notch-dependent pathway. *IMMUNOLOGY AND INFLAMMATION* **117**, 22357–22366 (2020).
170. Wang, S., Cheng, F., Ji, Q., Song, M., Wu, Z., Zhang, Y., Ji, Z., Feng, H., Belmonte, J. C. I., Zhou, Q., Qu, J., Li, W., Liu, G.-H. & Zhang, W. Hyperthermia differentially affects specific human stem cells and their differentiated derivatives. *Protein Cell* **13**, 615–622 (2022).
  171. Shimoni, C., Goldstein, M., Ribarski-Chorev, I., Schauten, I., Nir, D., Strauss, C. & Schlesinger, S. Heat Shock Alters Mesenchymal Stem Cell Identity and Induces Premature Senescence. *Front Cell Dev Biol* **8**, (2020).
  172. Acharya, U. R., Ng, E. Y. K., Tan, J.-H. & Sree, S. V. Thermography Based Breast Cancer Detection Using Texture Features and Support Vector Machine. *J Med Syst* **36**, 1503–1510 (2012).
  173. Helmy, A., Holdmann, M. & Rizkalla, M. Application of Thermography for Non-Invasive Diagnosis of Thyroid Gland Disease. *IEEE Trans Biomed Eng* **55**, 1168–1175 (2008).
  174. Evans, S. S., Repasky, E. A. & Fisher, D. T. Fever and the thermal regulation of immunity: the immune system feels the heat. *Nat Rev Immunol* **15**, 335–349 (2015).
  175. Okabe, K., Sakaguchi, R., Shi, B. & Kiyonaka, S. Intracellular thermometry with fluorescent sensors for thermal biology. *Pflugers Arch* **470**, 717–731 (2018).
  176. Zohar, O., Ikeda, M., Shinagawa, H., Inoue, H., Nakamura, H., Elbaum, D., Alkon, D. L. & Yoshioka, T. Thermal Imaging of Receptor-Activated Heat Production in Single Cells. *Biophys J* **74**, 82–89 (1998).
  177. Suzuki, M., Tseeb, V., Oyama, K. & Ishiwata, S. Microscopic Detection of Thermogenesis in a Single HeLa Cell. *Biophys J* **92**, L46–L48 (2007).
  178. Homma, M., Takei, Y., Murata, A., Inoue, T. & Takeoka, S. A ratiometric fluorescent molecular probe for visualization of mitochondrial temperature in living cells. *Chemical Communications* **51**, 6194–6197 (2015).
  179. Gota, C., Okabe, K., Funatsu, T., Harada, Y. & Uchiyama, S. Hydrophilic Fluorescent Nanogel Thermometer for Intracellular Thermometry. *J Am Chem Soc* **131**, 2766–2767 (2009).
  180. Qiao, J., Qi, L., Shen, Y., Zhao, L., Qi, C., Shangguan, D., Mao, L. & Chen, Y. Thermal responsive fluorescent block copolymer for intracellular temperature sensing. *J Mater Chem* **22**, 11543 (2012).
  181. Qiao, J., Chen, C., Qi, L., Liu, M., Dong, P., Jiang, Q., Yang, X., Mu, X. & Mao, L. Intracellular temperature sensing by a ratiometric fluorescent polymer thermometer. *J. Mater. Chem. B* **2**, 7544–7550 (2014).
  182. Qiao, J., Hwang, Y.-H., Chen, C.-F., Qi, L., Dong, P., Mu, X.-Y. & Kim, D.-P. Ratiometric Fluorescent Polymeric Thermometer for Thermogenesis Investigation in Living Cells. *Anal Chem* **87**, 10535–10541 (2015).
  183. Okabe, K., Inada, N., Gota, C., Harada, Y., Funatsu, T. & Uchiyama, S. Intracellular temperature mapping with a fluorescent polymeric thermometer and fluorescence lifetime imaging microscopy. *Nat Commun* **3**, 705 (2012).

184. Hayashi, T., Fukuda, N., Uchiyama, S. & Inada, N. A Cell-Permeable Fluorescent Polymeric Thermometer for Intracellular Temperature Mapping in Mammalian Cell Lines. *PLoS One* **10**, e0117677 (2015).
185. McCabe, K. M., Lacherndo, E. J., Albino-Flores, I., Sheehan, E. & Hernandez, M. LaCl(Ts)-Regulated Expression as an In Situ Intracellular Biomolecular Thermometer. *Appl Environ Microbiol* **77**, 2863–2868 (2011).
186. Donner, J. S., Thompson, S. A., Kreuzer, M. P., Baffou, G. & Quidant, R. Mapping Intracellular Temperature Using Green Fluorescent Protein. *Nano Lett* **12**, 2107–2111 (2012).
187. Kiyonaka, S., Kajimoto, T., Sakaguchi, R., Shinmi, D., Omatsu-Kanbe, M., Matsuura, H., Imamura, H., Yoshizaki, T., Hamachi, I., Morii, T. & Mori, Y. Genetically encoded fluorescent thermosensors visualize subcellular thermoregulation in living cells. *Nat Methods* **10**, 1232–1238 (2013).
188. Nakano, M., Arai, Y., Kotera, I., Okabe, K., Kamei, Y. & Nagai, T. Genetically encoded ratiometric fluorescent thermometer with wide range and rapid response. *PLoS One* **12**, e0172344 (2017).
189. Yang, J.-M., Yang, H. & Lin, L. Quantum Dot Nano Thermometers Reveal Heterogeneous Local Thermogenesis in Living Cells. *ACS Nano* **5**, 5067–5071 (2011).
190. Haro-González, P., Ramsay, W. T., Maestro, L. M., del Rosal, B., Santacruz-Gomez, K., del Carmen Iglesias-de la Cruz, M., Sanz-Rodríguez, F., Chooi, J. Y., Sevilla, P. R., Bettinelli, M., Choudhury, D., Kar, A. K., Solé, J. G., Jaque, D. & Paterson, L. Quantum Dot-Based Thermal Spectroscopy and Imaging of Optically Trapped Microspheres and Single Cells. *Small* **9**, 2162–2170 (2013).
191. Maestro, L. M., Haro-González, P., Iglesias-de la Cruz, M. C., SanzRodríguez, F., Juarranz, Á., Solé, J. G. & Jaque, D. Fluorescent nanothermometers provide controlled plasmonic-mediated intracellular hyperthermia. *Nanomedicine* **8**, 379–388 (2013).
192. Tanimoto, R., Hiraiwa, T., Nakai, Y., Shindo, Y., Oka, K., Hiroi, N. & Funahashi, A. Detection of Temperature Difference in Neuronal Cells. *Sci Rep* **6**, 22071 (2016).
193. Chipaux, M., van der Laan, K. J., Hemelaar, S. R., Hasani, M., Zheng, T. & Schirhagl, R. Nanodiamonds and Their Applications in Cells. *Small* **14**, 1704263 (2018).
194. Prabhakar, N., Peurla, M., Koho, S., Deguchi, T., Näreoja, T., Chang, H. C., Rosenholm, J. M. & Hänninen, P. E. STED-TEM Correlative Microscopy Leveraging Nanodiamonds as Intracellular Dual-Contrast Markers. *Small* **14**, (2018).
195. Hsieh, F. J., Chen, Y. W., Huang, Y. K., Lee, H. M., Lin, C. H. & Chang, H. C. Correlative Light-Electron Microscopy of Lipid-Encapsulated Fluorescent Nanodiamonds for Nanometric Localization of Cell Surface Antigens. *Anal Chem* **90**, 1566–1571 (2018).
196. Sotoma, S., Iimura, J., Igarashi, R., Hirosawa, K. M., Ohnishi, H., Mizukami, S., Kikuchi, K., Fujiwara, T. K., Shirakawa, M. & Tochio, H. Selective labeling of proteins on living cell membranes using fluorescent nanodiamond probes. *Nanomaterials* **6**, (2016).



197. Hsieh, F. J., Sotoma, S., Lin, H. H., Cheng, C. Y., Yu, T. Y., Hsieh, C. L., Lin, C. H. & Chang, H. C. Bioorthogonal Fluorescent Nanodiamonds for Continuous Long-Term Imaging and Tracking of Membrane Proteins. *ACS Appl Mater Interfaces* **11**, 19774–19781 (2019).
198. Petrakova, V., Benson, V., Buncek, M., Fiserova, A., Ledvina, M., Stursa, J., Cigler, P. & Nesladek, M. Imaging of transfection and intracellular release of intact, non-labeled DNA using fluorescent nanodiamonds. *Nanoscale* **8**, 12002–12012 (2016).
199. Chan, M. S., Liu, L. S., Leung, H. M. & Lo, P. K. Cancer-Cell-Specific Mitochondria-Targeted Drug Delivery by Dual-Ligand-Functionalized Nanodiamonds Circumvent Drug Resistance. *ACS Appl Mater Interfaces* **9**, 11780–11789 (2017).
200. Fang, C. Y., Vaijayanthimala, V., Cheng, C. A., Yeh, S. H., Chang, C. F., Li, C. L. & Chang, H. C. The exocytosis of fluorescent nanodiamond and its use as a long-term cell tracker. *Small* **7**, 3363–3370 (2011).
201. Wu, T. J., Tzeng, Y. K., Chang, W. W., Cheng, C. A., Kuo, Y., Chien, C. H., Chang, H. C. & Yu, J. Tracking the engraftment and regenerative capabilities of transplanted lung stem cells using fluorescent nanodiamonds. *Nat Nanotechnol* **8**, 682–689 (2013).
202. Purdey, M. S., Capon, P. K., Pullen, B. J., Reineck, P., Schwarz, N., Psaltis, P. J., Nicholls, S. J., Gibson, B. C. & Abell, A. D. An organic fluorophore-nanodiamond hybrid sensor for photostable imaging and orthogonal, on-demand biosensing. *Sci Rep* **7**, (2017).
203. Doherty, M. W., Manson, N. B., Delaney, P., Jelezko, F., Wrachtrup, J. & Hollenberg, L. C. L. The nitrogen-vacancy colour centre in diamond. *Phys Rep* **528**, 1–45 (2013).
204. Acosta, V. M., Bauch, E., Ledbetter, M. P., Waxman, A., Bouchard, L.-S. & Budker, D. Temperature Dependence of the Nitrogen-Vacancy Magnetic Resonance in Diamond. *Phys Rev Lett* **104**, 070801 (2010).
205. Kucsko, G., Maurer, P. C., Yao, N. Y., Kubo, M., Noh, H. J., Lo, P. K., Park, H. & Lukin, M. D. Nanometre-scale thermometry in a living cell. *Nature* **500**, 54–58 (2013).
206. Simpson, D. A., Morrisroe, E., McCoey, J. M., Lombard, A. H., Mendis, D. C., Treussart, F., Hall, L. T., Petrou, S. & Hollenberg, L. C. L. Non-Neurotoxic Nanodiamond Probes for Intraneuronal Temperature Mapping. *ACS Nano* **11**, 12077–12086 (2017).
207. Sekiguchi, T., Sotoma, S. & Harada, Y. Fluorescent nanodiamonds as a robust temperature sensor inside a single cell. *Biophys Physicobiol* **15**, 229–234 (2018).
208. Serra-Picamal, X., Conte, V., Vincent, R., Anon, E., Tambe, D. T., Bazellieres, E., Butler, J. P., Fredberg, J. J. & Trepap, X. Mechanical waves during tissue expansion. *Nat Phys* **8**, 628–634 (2012).
209. Raval, N., Maheshwari, R., Kalyane, D., Youngren-Ortiz, S. R., Chougule, M. B. & Tekade, R. K. in *Basic Fundamentals of Drug Delivery* 369–400 (Elsevier, 2019).
210. Visser, T. D. & Om, J. L. Volume Measurements in Three-Dimensional Microscopy. *Scanning* **16**, 198–200 (1994).
211. Sroka, J., von Gunten, M., Dunn, G. A. & Keller, H. U. Phenotype modulation in non-adherent and adherent sublines of Walker carcinosarcoma cells: the role of cell-substratum contacts

- and microtubules in controlling cell shape, locomotion and cytoskeletal structure. *Int J Biochem Cell Biol* **34**, 882–899 (2002).
212. Wang, Y.-L. & Pelham, R. J. in *J (Basel)* **68**, 489–496 (1998).
  213. Beningo, K. A., Lo, C.-M. & Wang, Y.-L. in *Methods Cell Biol* **69**, 325–339 (2002).
  214. Seroussi, I., Veikherman, D., Ofer, N., Yehudai-Resheff, S. & Keren, K. Segmentation and tracking of live cells in phase-contrast images using directional gradient vector flow for snakes. *J Microsc* **247**, 137–146 (2012).
  215. Entenberg, D. & Condeelis, J. ROI Tracker. *The ROI\_Tracker software was supplied by David Entenberg and John Condeelis as supported by CA100324 and GM064346*
  216. Alexandrova, A. Y., Arnold, K., Schaub, S., Vasiliev, J. M., Meister, J.-J., Bershadsky, A. D. & Verkhovsky, A. B. Comparative Dynamics of Retrograde Actin Flow and Focal Adhesions: Formation of Nascent Adhesions Triggers Transition from Fast to Slow Flow. *PLoS One* **3**, e3234 (2008).
  217. Lauffenburger, D. A. & Horwitz, A. F. *Cell Migration: Review A Physically Integrated Molecular Process. Cell* **84**, (1996).
  218. Liu, Y. J., Le Berre, M., Lautenschlaeger, F., Maiuri, P., Callan-Jones, A., Heuzé, M., Takaki, T., Voituriez, R. & Piel, M. Confinement and low adhesion induce fast amoeboid migration of slow mesenchymal cells. *Cell* **160**, 659–672 (2015).
  219. Welch, D. R. Tumor Heterogeneity—A ‘Contemporary Concept’ Founded on Historical Insights and Predictions. *Cancer Res* **76**, 4–6 (2016).
  220. Altschuler, S. J. & Wu, L. F. Cellular Heterogeneity: Do Differences Make a Difference? *Cell* **141**, 559–563 (2010).
  221. Flashner-Abramson, E., Vasudevan, S., Adejumobi, I. A., Sonnenblick, A. & Kravchenko-Balasha, N. Decoding cancer heterogeneity: Studying patient-specific signaling signatures towards personalized cancer therapy. *Theranostics* **9**, 5149–5165 (2019).
  222. Dagogo-Jack, I. & Shaw, A. T. Tumour heterogeneity and resistance to cancer therapies. *Nat Rev Clin Oncol* **15**, 81–94 (2018).
  223. Lim, Z.-F. & Ma, P. C. Emerging insights of tumor heterogeneity and drug resistance mechanisms in lung cancer targeted therapy. *J Hematol Oncol* **12**, 134 (2019).
  224. Findlay, J. M., Castro-Giner, F., Makino, S., Rayner, E., Kartsonaki, C., Cross, W., Kovac, M., Ulahannan, D., Palles, C., Gillies, R. S., Macgregor, T. P., Church, D., Maynard, N. D., Buffa, F., Cazier, J. B., Graham, T. A., Wang, L. M., Sharma, R. A., Middleton, M. & Tomlinson, I. Differential clonal evolution in oesophageal cancers in response to neo-adjuvant chemotherapy. *Nat Commun* **7**, (2016).
  225. Gallaher, J. A., Enriquez-Navas, P. M., Luddy, K. A., Gatenby, R. A. & Anderson, A. R. A. Spatial heterogeneity and evolutionary dynamics modulate time to recurrence in continuous and adaptive cancer therapies. *Cancer Res* **78**, 2127–2139 (2018).
  226. McEuen, C. S. Effect of Hypophysectomy on Growth of the Walker Rat Tumor. *Exp Biol Med* **30**, 928–929 (1933).

227. Chew, E. C. The fine structure of walker 256 carcinoma cells. *Experientia* **32**, 1192–1194 (1976).
228. Magro, C., Orr, F. W., Manishen, W. J., Sivananthan, K. & Mokashi, S. S. Adhesion, chemotaxis, and aggregation of Walker carcinosarcoma cells in response to products of resorbing bone. *J Natl Cancer Inst* **74**, 829–38 (1985).
229. Manishen, W. J., Sivananthan, K. & Orr, F. W. Resorbing bone stimulates tumor cell growth. A role for the host microenvironment in bone metastasis. *Am J Pathol* **123**, 39–45 (1986).
230. Simpkins, H., Lehman, J. M., Mazurkiewicz, J. E. & Davis, B. H. A morphological and phenotypic analysis of Walker 256 cells. *Cancer Res* **51**, 1334–8 (1991).
231. Sroka, J., Krecioch, I., Zimolag, E., Lasota, S., Rak, M., Kedracka-Krok, S., Borowicz, P., Gajek, M. & Madeja, Z. Lamellipodia and Membrane Blebs Drive Efficient Electrotactic Migration of Rat Walker Carcinosarcoma Cells WC 256. *PLoS One* **11**, e0149133 (2016).
232. Veronika, M., Welsch, R., Ng, A., Matsudaira, P. & Rajapakse, J. C. Correlation of cell membrane dynamics and cell motility. *BMC Bioinformatics* **12**, (2011).
233. Friedl, P. Prespecification and plasticity: shifting mechanisms of cell migration. *Curr Opin Cell Biol* **16**, 14–23 (2004).
234. Kołodziej, T., Mielnicka, A., Dziob, D., Chojnacka, A. K., Rawski, M., Mazurkiewicz, J. & Rajfur, Z. Morphomigrational description as a new approach connecting cell's migration with its morphology. *Scientific Reports (Accepted Manuscript)* (2023).
235. Hemelaar, S. R., Nagl, A., Bigot, F., Rodríguez-García, M. M., de Vries, M. P., Chipaux, M. & Schirhagl, R. The interaction of fluorescent nanodiamond probes with cellular media. *Mikrochim Acta* **184**, 1001–1009 (2017).
236. Yukawa, H., Fujiwara, M., Kobayashi, K., Kumon, Y., Miyaji, K., Nishimura, Y., Oshimi, K., Umehara, Y., Teki, Y., Iwasaki, T., Hatano, M., Hashimoto, H. & Baba, Y. A quantum thermometric sensing and analysis system using fluorescent nanodiamonds for the evaluation of living stem cell functions according to intracellular temperature. *Nanoscale Adv* **2**, 1859–1868 (2020).
237. Fujiwara, M., Sun, S., Dohms, A., Nishimura, Y., Suto, K., Takezawa, Y., Oshimi, K., Zhao, L., Sadzak, N., Umehara, Y., Teki, Y., Komatsu, N., Benson, O., Shikano, Y. & Kage-Nakadai, E. *Real-time nanodiamond thermometry probing in vivo thermogenic responses*. *Sci. Adv* **6**, (2020).
238. Engler, A., Bacakova, L., Newman, C., Hategan, A., Griffin, M. & Discher, D. Substrate Compliance versus Ligand Density in Cell on Gel Responses. *Biophys J* **86**, 617–628 (2004).
239. Deeg, J. A., Louban, I., Aydin, D., Selhuber-Unkel, C., Kessler, H. & Spatz, J. P. Impact of Local versus Global Ligand Density on Cellular Adhesion. *Nano Lett* **11**, 1469–1476 (2011).
240. Sahai, E. & Marshall, C. J. Differing modes of tumour cell invasion have distinct requirements for Rho/ROCK signalling and extracellular proteolysis. *Nat Cell Biol* **5**, 711–9 (2003).
241. Wilkinson, S., Paterson, H. F. & Marshall, C. J. Cdc42-MRCK and Rho-ROCK signalling cooperate in myosin phosphorylation and cell invasion. *Nat Cell Biol* **7**, 255–61 (2005).

242. Sanz-Moreno, V., Gadea, G., Ahn, J., Paterson, H., Marra, P., Pinner, S., Sahai, E. & Marshall, C. J. Rac activation and inactivation control plasticity of tumor cell movement. *Cell* **135**, 510–23 (2008).
243. Yamazaki, D., Kurisu, S. & Takenawa, T. Involvement of Rac and Rho signaling in cancer cell motility in 3D substrates. *Oncogene* **28**, 1570–83 (2009).
244. Ruprecht, V., Wieser, S., Callan-Jones, A., Smutny, M., Morita, H., Sako, K., Barone, V., Ritsch-Marte, M., Sixt, M., Voituriez, R. & Heisenberg, C.-P. Cortical contractility triggers a stochastic switch to fast amoeboid cell motility. *Cell* **160**, 673–685 (2015).
245. Sahai, E., Garcia-Medina, R., Pouyssegur, J. & Vial, E. Smurf1 regulates tumor cell plasticity and motility through degradation of RhoA leading to localized inhibition of contractility. *J Cell Biol* **176**, 35–42 (2007).
246. Laser-Azogui, A., Diamant-Levi, T., Israeli, S., Roytman, Y. & Tsarfaty, I. Met-induced membrane blebbing leads to amoeboid cell motility and invasion. *Oncogene* **33**, 1788–98 (2014).
247. Pietrovito, L., Leo, A., Gori, V., Lulli, M., Parri, M., Becherucci, V., Piccini, L., Bambi, F., Taddei, M. L. & Chiarugi, P. Bone marrow-derived mesenchymal stem cells promote invasiveness and transendothelial migration of osteosarcoma cells via a mesenchymal to amoeboid transition. *Mol Oncol* **12**, 659–676 (2018).
248. Wyse, M. M., Lei, J., Nestor-Kalinoski, A. L. & Eisenmann, K. M. Dia-interacting protein (DIP) imposes migratory plasticity in mDia2-dependent tumor cells in three-dimensional matrices. *PLoS One* **7**, e45085 (2012).
249. Keller, H. U. Redundancy of lamellipodia in locomoting Walker carcinosarcoma cells. *Cell Motil Cytoskeleton* **46**, 247–56 (2000).
250. Sedzinski, J., Biro, M., Oswald, A., Tinevez, J.-Y., Salbreux, G. & Paluch, E. Polar actomyosin contractility destabilizes the position of the cytokinetic furrow. *Nature* **476**, 462–6 (2011).
251. Chikina, A. S., Svitkina, T. M. & Alexandrova, A. Y. Time-resolved ultrastructure of the cortical actin cytoskeleton in dynamic membrane blebs. *J Cell Biol* **218**, 445–454 (2019).
252. Chikina, A. S., Rubtsova, S. N., Lomakina, M. E., Potashnikova, D. M., Vorobjev, I. A. & Alexandrova, A. Y. Transition from mesenchymal to bleb-based motility is predominantly exhibited by CD133-positive subpopulation of fibrosarcoma cells. *Biol Cell* **111**, 245–261 (2019).
253. Bergert, M., Chandradoss, S. D., Desai, R. A. & Paluch, E. Cell mechanics control rapid transitions between blebs and lamellipodia during migration. *Proceedings of the National Academy of Sciences* **109**, 14434–14439 (2012).
254. Derivery, E., Fink, J., Martin, D., Houdusse, A., Piel, M., Stradal, T. E., Louvard, D. & Gautreau, A. Free Brick1 is a trimeric precursor in the assembly of a functional wave complex. *PLoS One* **3**, e2462 (2008).
255. Obeidy, P., Ju, L. A., Oehlers, S. H., Zulkhernain, N. S., Lee, Q., Galeano Niño, J. L., Kwan, R. Y., Tikoo, S., Cavanagh, L. L., Mrass, P., Cook, A. J., Jackson, S. P., Biro, M., Roediger, B., Sixt, M. &

- Weninger, W. Partial loss of actin nucleator actin-related protein 2/3 activity triggers blebbing in primary T lymphocytes. *Immunol Cell Biol* **98**, 93–113 (2020).
256. Beckham, Y., Vasquez, R. J., Stricker, J., Sayegh, K., Campillo, C. & Gardel, M. L. Arp2/3 inhibition induces amoeboid-like protrusions in MCF10A epithelial cells by reduced cytoskeletal-membrane coupling and focal adhesion assembly. *PLoS One* **9**, e100943 (2014).
  257. Yip, A. K., Chiam, K.-H. & Matsudaira, P. Traction stress analysis and modeling reveal that amoeboid migration in confined spaces is accompanied by expansive forces and requires the structural integrity of the membrane-cortex interactions. *Integr Biol (Camb)* **7**, 1196–211 (2015).
  258. Diz-Muñoz, A., Krieg, M., Bergert, M., Ibarlucea-Benitez, I., Muller, D. J., Paluch, E. & Heisenberg, C.-P. Control of Directed Cell Migration In Vivo by Membrane-to-Cortex Attachment. *PLoS Biol* **8**, e1000544 (2010).
  259. Weng, N. J.-H., Cheung, C. & Talbot, P. Dynamic blebbing: A bottleneck to human embryonic stem cell culture that can be overcome by Laminin-Integrin signaling. *Stem Cell Res* **33**, 233–246 (2018).
  260. Logue, J. S., Cartagena-Rivera, A. X. & Chadwick, R. S. c-Src activity is differentially required by cancer cell motility modes. *Oncogene* **37**, 2104–2121 (2018).
  261. Gao, Y., Wang, Z., Hao, Q., Li, W., Xu, Y., Zhang, J., Zhang, W., Wang, S., Liu, S., Li, M., Xue, X., Zhang, W., Zhang, C. & Zhang, Y. Loss of ER $\alpha$  induces amoeboid-like migration of breast cancer cells by downregulating vinculin. *Nat Commun* **8**, 14483 (2017).
  262. Tozluoglu, M., Mao, Y., Bates, P. A. & Sahai, E. Cost-benefit analysis of the mechanisms that enable migrating cells to sustain motility upon changes in matrix environments. *J R Soc Interface* **12**, (2015).
  263. Carragher, N. O., Walker, S. M., Scott Carragher, L. A., Harris, F., Sawyer, T. K., Brunton, V. G., Ozanne, B. W. & Frame, M. C. Calpain 2 and Src dependence distinguishes mesenchymal and amoeboid modes of tumour cell invasion: a link to integrin function. *Oncogene* **25**, 5726–5740 (2006).
  264. Stewart H. L., Snell, K. C., Dunham L. J. & Schiven S.M. *Atlas of Tumor Pathology Sect. XII Fase. 40*. (Air Force Institute of Pathology, 1959).
  265. Graziani, V., Rodriguez-Hernandez, I., Maiques, O. & Sanz-Moreno, V. The amoeboid state as part of the epithelial-to-mesenchymal transition programme. *Trends Cell Biol* **32**, 228–242 (2022).
  266. Vaškovičová, K., Szabadosová, E., Čermák, V., Gandalovičová, A., Kasalová, L., Rösel, D. & Brábek, J. PKC $\alpha$  promotes the mesenchymal to amoeboid transition and increases cancer cell invasiveness. *BMC Cancer* **15**, (2015).
  267. Wolf, K., Mazo, I., Leung, H., Engelke, K., Von Andrian, U. H., Deryugina, E. I., Strongin, A. Y., Bröcker, E. B. & Friedl, P. Compensation mechanism in tumor cell migration: Mesenchymal-amoeboid transition after blocking of pericellular proteolysis. *Journal of Cell Biology* **160**, 267–277 (2003).

268. Talkenberger, K., Cavalcanti-Adam, E. A., Voss-Böhme, A. & Deutsch, A. Amoeboid-mesenchymal migration plasticity promotes invasion only in complex heterogeneous microenvironments. *Sci Rep* **7**, 9237 (2017).
269. Adlerz, K. M., Aranda-Espinoza, H. & Hayenga, H. N. Substrate elasticity regulates the behavior of human monocyte-derived macrophages. *European Biophysics Journal* **45**, 301–309 (2016).
270. Reimer, M., Petrova Zustiak, S., Sheth, S. & Martin Schober, J. Intrinsic Response Towards Physiologic Stiffness is Cell-Type Dependent. *Cell Biochem Biophys* **76**, 197–208 (2018).
271. Peyton, S. R., Ghajar, C. M., Khatiwala, C. B. & Putnam, A. J. The emergence of ECM mechanics and cytoskeletal tension as important regulators of cell function. *Cell Biochem Biophys* **47**, 300–320 (2007).
272. Skardal, A., Mack, D., Atala, A. & Sokern, S. Substrate elasticity controls cell proliferation, surface marker expression and motile phenotype in amniotic fluid-derived stem cells. *J Mech Behav Biomed Mater* **17**, 307–316 (2013).
273. Yeung, T., Georges, P. C., Flanagan, L. A., Marg, B., Ortiz, M., Funaki, M., Zahir, N., Ming, W., Weaver, V. & Janmey, P. A. Effects of substrate stiffness on cell morphology, cytoskeletal structure, and adhesion. *Cell Motil Cytoskeleton* **60**, 24–34 (2005).
274. Trichet, L., Le Digabel, J., Hawkins, R. J., Vedula, R. K., Gupta, M., Ribault, C., Hersen, P., Voituriez, R. & Ladoux, B. Evidence of a large-scale mechanosensing mechanism for cellular adaptation to substrate stiffness. *PNAS* **109**, (2012).
275. Fritsch, A., Höckel, M., Kiessling, T., Nnetu, K. D., Wetzels, F., Zink, M. & Käs, J. A. Are biomechanical changes necessary for tumour progression? *Nat Phys* **6**, 730–732 (2010).
276. Ladoux, B., Mège, R.-M. & Trepast, X. Front–Rear Polarization by Mechanical Cues: From Single Cells to Tissues. *Trends Cell Biol* **26**, 420–433 (2016).
277. Katira, P., Bonnacaze, R. T. & Zaman, M. H. Modeling the Mechanics of Cancer: Effect of Changes in Cellular and Extra-Cellular Mechanical Properties. *Front Oncol* **3**, (2013).
278. Qian, M., Wang, D. C., Chen, H. & Cheng, Y. Detection of single cell heterogeneity in cancer. *Semin Cell Dev Biol* **64**, 143–149 (2017).
279. Marusyk, A., Janiszewska, M. & Polyak, K. Intratumor Heterogeneity: The Rosetta Stone of Therapy Resistance. *Cancer Cell* **37**, 471–484 (2020).
280. Wen, J. H., Vincent, L. G., Fuhrmann, A., Choi, Y. S., Hribar, K. C., Taylor-Weiner, H., Chen, S. & Engler, A. J. Interplay of matrix stiffness and protein tethering in stem cell differentiation. *Nat Mater* **13**, 979–987 (2014).
281. Harris, M. P., Kim, E., Weidow, B., Wikswo, J. P. & Quaranta, V. Migration of isogenic cell lines quantified by dynamic multivariate analysis of single-cell motility. *Cell Adh Migr* **2**, 127–136 (2008).
282. Shafqat-Abbasi, H., Kowalewski, J. M., Kiss, A., Gong, X., Hernandez-Varas, P., Berge, U., Jafari-Mamaghani, M., Lock, J. G. & Strömblad, S. An analysis toolbox to explore mesenchymal

- migration heterogeneity reveals adaptive switching between distinct modes. *Elife* **5**, (2016).
283. Kowalewski, J. M., Shafqat-Abbasi, H., Jafari-Mamaghani, M., Ganebo, B. E., Gong, X., Stromblad, S. & Lock, J. G. Disentangling membrane dynamics and cell migration; differential influences of F-actin and cell-matrix adhesions. *PLoS One* **10**, (2015).
  284. Cao, Y., Ghabache, E. & Rappel, W.-J. Plasticity of cell migration resulting from mechanochemical coupling. *Elife* **8**, (2019).
  285. Mogilner, A. & Keren, K. The Shape of Motile Cells. *Current Biology* **19**, R762–R771 (2009).
  286. Jacquel, A., Obba, S., Boyer, L., Dufies, M., Robert, G., Gounon, P., Lemichez, E., Luciano, F., Solary, E. & Auberger, P. Autophagy is required for CSF-1-induced macrophagic differentiation and acquisition of phagocytic functions. *Blood* **119**, 4527–4531 (2012).
  287. Ma, X., Chen, J., Xu, B., Long, X., Qin, H., Zhao, R. C. & Wang, X. Keloid-derived keratinocytes acquire a fibroblast-like appearance and an enhanced invasive capacity in a hypoxic microenvironment in vitro. *Int J Mol Med* **35**, 1246–1256 (2015).
  288. Zhu, S., Mc Henry, K. T., Lane, W. S. & Fenteany, G. A chemical inhibitor reveals the role of Raf kinase inhibitor protein in cell migration. *Chem Biol* **12**, 981–991 (2005).
  289. Zhukova, Y., Hiepen, C., Knaus, P., Osterland, M., Prohaska, S., Dunlop, J. W. C., Fratzl, P. & Skorb, E. V. The Role of Titanium Surface Nanostructuring on Preosteoblast Morphology, Adhesion, and Migration. *Adv Healthc Mater* **6**, (2017).
  290. Zhong, Y. & Ji, B. Impact of cell shape on cell migration behavior on elastic substrate. *Biofabrication* **5**, (2013).
  291. Mogilner, A. & Keren, K. The Shape of Motile Cells. *Current Biology* **19**, R762–R771 (2009).
  292. Codling, E. A. & Hill, N. A. Sampling rate effects on measurements of correlated and biased random walks. *J Theor Biol* **233**, 573–588 (2005).
  293. Rosser, G., Fletcher, A. G., Maini, P. K. & Baker, R. E. The effect of sampling rate on observed statistics in a correlated random walk. *J R Soc Interface* **10**, (2013).
  294. Zhang, J., Daubert, C. R. & Foegeding, E. A. Characterization of polyacrylamide gels as an elastic model for food gels. *Rheol Acta* **44**, 622–630 (2005).
  295. Dalby, M. J., Gadegaard, N., Tare, R., Andar, A., Riehle, M. O., Herzyk, P., Wilkinson, C. D. W. & Oreffo, R. O. C. The control of human mesenchymal cell differentiation using nanoscale symmetry and disorder. *Nat Mater* **6**, 997–1003 (2007).
  296. McMurray, R. J., Gadegaard, N., Tsimbouri, P. M., Burgess, K. V., McNamara, L. E., Tare, R., Murawski, K., Kingham, E., Oreffo, R. O. C. & Dalby, M. J. Nanoscale surfaces for the long-term maintenance of mesenchymal stem cell phenotype and multipotency. *Nat Mater* **10**, 637–644 (2011).
  297. Allan, C., Ker, A., Smith, C. A., Tsimbouri, P. M., Borsoi, J., O'Neill, S., Gadegaard, N., Dalby, M. J. & Dominic Meek, R. M. Osteoblast response to disordered nanotopography. *J Tissue Eng* **9**, (2018).

298. Chen, X.-D., Dong, C.-H., Sun, F.-W., Zou, C.-L., Cui, J.-M., Han, Z.-F. & Guo, G.-C. Temperature dependent energy level shifts of nitrogen-vacancy centers in diamond. *Appl Phys Lett* **99**, 161903 (2011).
299. Toyli, D. M., Christle, D. J., Alkauskas, A., Buckley, B. B., Van de Walle, C. G. & Awschalom, D. D. Measurement and Control of Single Nitrogen-Vacancy Center Spins above 600 K. *Phys Rev X* **2**, 031001 (2012).
300. An, H., Yin, Z., Mitchell, C., Semnani, A., Hajrasouliha, A. R. & Hosseini, M. Nanodiamond ensemble-based temperature measurement in living cells and its limitations. *Meas Sci Technol* **32**, 015701 (2021).